Università degli Studi di Milano & Università Cattolica del Sacro Cuore
Scuola di Dottorato in Fisica, Astrofisica e Fisica Applicata
Dipartimento di Matematica e Fisica

Corso di Dottorato in Fisica, Astrofisica e Fisica Applicata
Ciclo XXIV

Models of turbulence. Applications to particulate mixing induced by traffic flow in urban areas.

Settore Scientifico Disciplinare FIS/07

Tutore: Professor Fausto BORGONOVI

Co-Tutore: Professoressa Roberta VECCHI

Coordinatore: Professor Marco BERSANELLI

Tesi di Dottorato di:
Abramo AGOSTI

Anno Accademico 2012-2013

Commission of the final examination:

President:
Professor Timothy R. GINN

First Member:
Professor Ezio G. BOLZACCHINI

Second Member:
Professor Edie MIGLIO

First Expert:
Professor Ghislain DE MARSILY

Final examination:

Date 13/02/2013

Università degli Studi di Milano, Dipartimento di Fisica, Milano, Italy

Contents

1 Introduction

The scientific community is devoting an increasing effort to investigate the emission sources of traffic-related fine particulate matter (mainly as PM10) and its possible effects on living organisms [Davidson et al., 2005], [Pope, Dockery, 2006], [Stone, Donaldson, 1998], [Penttinen et al., 2001], [Nel et al., 2006]. In particular, actual research focuses on the biological interactions of fine and ultrafine particulate matter (micrometer and nanometer scale) in their impacts on human health [Stone, Donaldson, 1998]. PM10 particulate matter consists in a set of liquid and solid particles, having a diameter less than 10 micrometer, which are suspended in the atmosphere and who originate from emission processes, such as combustion and erosion, as well as from chemical transformation processes in the atmosphere. The chemical and physical properties of PM10, as well as their toxic nature, depend on the dimensions of the particles, on the type of emission sources, on the transport phenomena and chemical transformations taking place in the atmosphere. The capacity of particulate matter to penetrate the organism and to interact with biological tissues varies with the dimension of the particles: in particular, it has been demonstrated that particles having a size of the order of one micrometer can enter and follow the human respiratory apparatus until the pulmonary alveoli, inducing inflammatory responses and cellular death processes (depending on the chemical composition) [Penttinen et al., 2001]. Furthermore, the theoretical models suppose that particles having a size of the order of one nanometer can end up in the blood and in the organs, thereby causing a systematic harm [Nel et al., 2006].

Accordingly, the legislators and policy-makers are striving to figure out the most effective measures capable to reduce PM atmospheric ground-level concentration, mainly in urban areas where the population exposure is more alarming.

Most, if not all, of these policies are currently based on emissions reduction and control, on the assumption that the prevailing contribution of the observed PM concentration is due to the direct emission sources of primary PM or its secondary component's precursors.

In the European urban areas, the dominant emission source of PM10 and PM2.5 (the two fractions of particulate matter presently monitored according to the EU regulation) is represented by the vehicular traffic, whose contribution to the total PM concentration varies from 30 % to more than 50 % [CAFE, 2005], [Wong et al., 2003]. The European legislation on air pollution has implemented, in the last two decades, an increasing body of regulations aimed at reducing vehicles emission factors and establishing national emission ceilings to be gradually attained by the member states.

As a consequence, many primary air pollutants have been continuously diminishing and have now met, in most of the European regions, the required air quality standards [Pey et al., 2009]. However, the PM10 and PM2.5 levels

have not decreased significantly, at least in the last decade, in most urban areas [EEA, 2007] [EEA, 2006].

This phenomenon could be explained, at least theoretically, by an increase of secondary PM photochemical formation induced by the ongoing climate change, and by a parallel decrease of the PM deposition rate caused by land use changes which have converted natural and agricultural soils into artificial surfaces [De Leeuw, 2002].

Another tentative explanation of the observed decoupling between PM emissions trend (primary and secondary) and its ground level concentrations could arise by the fact that a considerable fraction of the traffic-related PM is attributable to non-exhaust phenomena, like brake abrasion, tire and road wear and turbulent resuspension of particles previously deposited on the road surfaces [Dunbar, 1976] [Giovannini, Grechi, 2003] [Empa, 2009]. Furthermore, the vehicle-generated air turbulence due to increased traffic flows can transfer larger amounts of kinetic energy to the air-borne PM, so contributing to its wider and faster transport. Such non-exhaust PM component may even overwhelm the contribution from the engine's combustion exhaust, especially when high loads of PM are present on the road surfaces and depending on peculiar traffic and asphalt features. If these conditions get worse, the final effect, at least at a local scale, could overcompensate the improvement of emission factors derived from new engine technologies.

Under this assumption, in this work we address our attention to a better estimate of the contribution of non-exhaust sources to the final PM air concentration and particularly we focus our investigation on the resuspension of PM deposited on road pavement surfaces and raised by the air turbulence produced by the vehicle flux, under urban and extra-urban traffic conditions.

Phenomenological emissive models [Dunbar, 1976] [Giovannini, Grechi, 2003] and statistical analysis on experimental data measured in particular traffic conditions [Empa, 2009] have shown that the resuspension fraction is about ~ 50 % of the total PM10 vehicle emission. Our approach to the problem is based on modeling techniques. We mainly refer to the data reported in [Empa, 2009] to determine the selected empirical parameters contained in our models. We use suitable analytical and numerical models to describe the turbulence field generated inside a canyon street by an external wind at roof level and by vehicles of simplified geometrical shapes in open streets and urban canyon streets. In particular, analytical models, based on algebraic eddy diffusivity hypothesis for the description of turbulence, enables us to describe the mean statistical component of flow generated by air recirculation inside a canyon and by the far-wake structure besides moving vehicles. The far-wake structure is the region of the vehicle wake in which unstable motions, caused by the deceleration of the boundary layer at the rear slant face of the vehicle, have been dissipated and a mean structure, with self-similar properties, reattaching to the ground level has been created. The analysis of the far wake solutions is suitable to the description of vehicle wakes interaction, which

permit to apply our analysis to different driving cycles condition. Numerical simulations based on finite element discretization of suitable two-equation turbulence models have been employed to describe near-wake structure, i.e. the region behind a vehicle in which turbulence kinetic energy is strongly produced, which causes the strongest mixing of atmospheric pollutants and resuspension of road dust. These different components of turbulence fields at different scales of the street geometry are composed to define an operational model for the dispersion of two classes of PM10 pollutants, those corresponding to the two dominant dimensional modes in the mass distribution of exhaust and non-exhaust emissions. The deposition and the resuspension of pollutants are suitably described by resistance models and filtration models on porous asphalts, which enable to consider the physics beyond the processes, described by suitable parameters combined in adymensional groups. The corresponding terms are then inserted in the dispersion equations, as suitable boundary conditions on the ground. The emission from exhaust tailpipes and from wear components of the vehicles are obtained through the use of EMEP-CORINAIR methodology, which is an emission inventory methodology for road transport developed by the EEA. Road dust composition and concentration are deduced from experimental data. The resuspension fraction of traffic-related PM10 emissions at the tailpipe, for typical urban and extra-urban driving cycles, has thus been estimated, through a simplified linear-emission model, considering representative data describing traffic statistics coming from the Artemis project [André, 2004].

Profile laws of resuspension factors have been drawn, for different vehicles geometries and velocities, and how resuspension changes with different asphalt characteristics.

Lastly, the results have been applied to typical traffic situations in the city of Milan, relying on data provided by the Agenzia Mobilità Ambiente Territorio (AMAT), [AMAT, 2008], [AMAT, 2010], and studying the effect of implementations of different reduction scenarios to the total amount of traffic-related PM10 emissions.

In Chapter 2 we will introduce the physical models which we have used to describe the deposition and resuspension fluxes, depending on turbulent quantities, on particles inertia and on asphalt characteristics. A simple tailpipe emission model, based on this physical models and on traffic emission data given in literature, will be used to set up important parameters of the models by comparison with empirical results. An application of the results to the case of Milan will be shown, and possible preventive strategies for pollutant airborne concentration reduction will be analysed.
In Chapter 3 the modelling approach will be described. A set of operational and simplified numerical models for the dispersion dynamics at the canyon scale will be introduced. These canyon-scale models allow us to describe the dispersion processes associated to complex urban traffic situations, characterised by vehicle wake interactions, which would be difficult to describe

with numerical simulations for the dispersion dynamics associated to each single vehicle. These models require analytical solutions in order to describe the vehicle wake interactions effects and the effects of the flow recirculation inside the street canyon. Moreover, results from numerical simulations of the flow in the near wake of each vehicle are needed in order to obtain suitable parametrizations of the deposition and resuspension fluxes, to be used at the canyon scale.
In Chapter 4 we will derive the analytical solutions required by the canyon-scale dispersion models, remanding some calculation to the Appendix, and we will show the simulation results for the near wake Turbulence structure, for different vehicle categories and driving conditions, and will define all the parametrizations of the deposition and resuspension terms derived from the numerical results. Finally, we will apply one of the dispersion operational models introduced in Chapter 3 to the case of a congested urban traffic configuration in a canyon street.

2 Traffic emissions in urban areas

Atmospheric aerosols (generally referred to as the particulate component of a suspension of solid or liquid particles in a gas) are particles that range in size from a few nanometers (nm) to tens of micrometers (μm) in diameter. They are directly emitted in the atmosphere as particles (primary aerosol), or formed by gas-to-particle conversion processes. Particulate matter (PM) is usually divided into a discrete set of dimensional classes: the *nucleation* mode, which comprises particles with equivalent diameter up to 10 nm; the *Aitken* mode, which ranges from 10 to 100nm; the *accumulation* mode, extending from $0,1\mu m$ to $2,5\mu m$; the *coarse* mode, which comprises particles with diameter $> 2,5\mu m$. Particles with diameter less than $2,5\mu m$ are called *fine* particles, and particles with diameter less than $0,1\mu m$ are called *ultra-fine*. The atmospheric aerosol mass ditribution is dominated in most areas by the *accumulation* and the *coarse* mode; the *accumulation* mode accounts for most of the aerosol surface area; the number distribution is dominated by the *nucleation* and the *Aitken* mode. [Seinfeld, Pandis, 2006]. The processes that influence the formation, size and composition of airborne particles are defined here below:

- Nucleation: the formation of stable clusters of a solid or a liquid phase in a super-saturated vapor phase, in absence (homogeneous) or in presence (heterogeneous) of condensation nuclei of a foreign substance. This is the main process for the transfer of mass from the gaseous to the particulate phase.

- Condensation and evaporation: the condensation of a vapor on the particle surface or the evaporation of material into the vapor phase. The rate of growing of particles by condensation depends on the saturation ratio and on their dimension relative to the mean free path of the gas; for sufficiently grown particles (with a diameter of the order of $\sim 0,5\mu m$), the rate of diffusion of vapor molecules on the particle surface induce a negligible change of volume with respect to the volume of the particle, and the PM population does not change appreciably under this transformation.

- Coagulation: the process of transformation of particles size distribution induced by particles collisions, generated by their Brownian motion or by advection and mixing in a wind field.

- Chemical reaction: atmospheric reactions involving gaseous precursors and organic compounds.

- Removal processes: deposition at the Earth's surface (dry deposition) and incorporation into cloud droplets during the formation of precipitation, snow and fog (wet deposition).

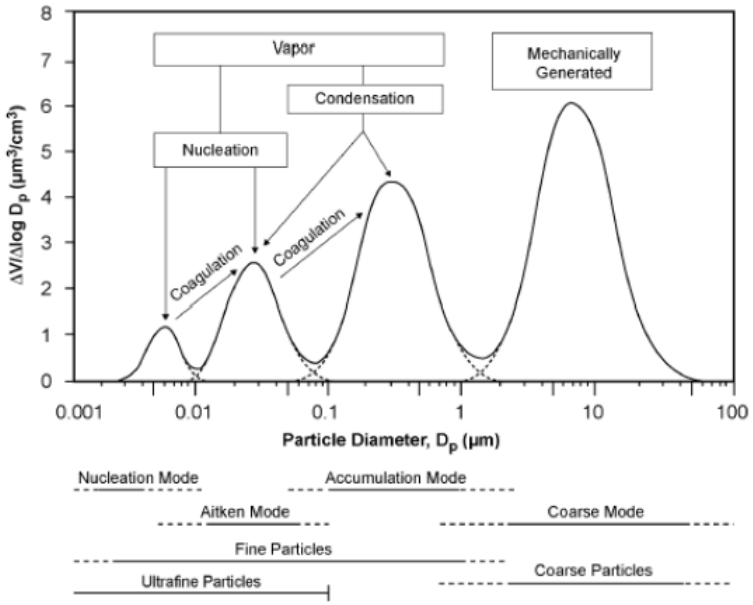

Figure 1: Scheme of the principal modes, sources, particle formation and removal mechanisms, for the volume distribution of an atmospheric aerosol [Seinfeld, Pandis, 2006].

Particles in the *nucleation* mode are formed from condensation of hot vapors during combustion processes and from the nucleation of atmospheric gases. Particles in the *Aitken* mode are mainly formed during high-temperature combustion processes. The dominant dispersion mechanism is Brownian motion, and their dominant removal process is coagulation with larger particles. Due to the fast time-scale of the dispersion and removal process for these two PM classes, their mixing time and lifetime in atmosphere is of the orders of few seconds [Seinfeld, Pandis, 2006]. The source of particles in the *accumulation* mode is the coagulation of smaller particles and vapor condensation onto existing particles, with relative surface growth. The dispersion mechanism of Brownian diffusion is less efficient for this mode, and removal mechanisms (mainly wet deposition) have a low time-scale, and cause the lifetime in this regime to be of the order of the weeks. The *coarse* mode is formed by mechanical processes, and consists of windblown human-made and natural dust (soil particles), pollens, plant fragments, seasalt. Their atmospheric dispersion is guided by inertial forces, and the dominant removal process is gravitational sedimentation. The time-scale of the removal process cause this mode to have a lifetime of the order of few minutes. In figure 1 the phenomena that influence particle volume distribution are schematically shown.

Urban aerosols are mixtures of primary particulate emissions from industries, nonindustrial fugitive sources (soil dust, construction), transportation, fuel combustion for power generation, natural sources and secondary PM. The number distribution of PM is dominated by particles smaller than $0,1\mu m$, whereas the surface area distribution is dominated by particles in the $0,1-0,5\mu m$ range. The Urban aerosol mass distribution has two distinct modes [Seinfeld, Pandis, 2006], one in the submicrometric regime (*accumulation* mode) and the other in the *coarse* mode. Next to trafficated roads there is an increase in mass concentrations of roughly $10-20\%$ with respect to the urban background; the concentrations of these particles decays by dilution in a characteristic distance of roughly $100m$ from the road. Coarse particles near road sources are generated mainly by mechanical processes of vehicles and road wear, resuspended by traffic flow; accumulation mode contains primary particles from the combustion processes (mainly Soot - elemental Carbon) and secondary aerosol material, coming from coagulation and condensation of particles from Aitken and nucleation mode, formed through nucleation in the atmosphere after rapid cooling and dilution of vehicle emissions (mainly Sulfates, Nitrates, Ammonium and gaseous organic precursors). Coagulation among accumulation mode particles is a slow process and does not transfer particles to the coarse mode.

We considered the case of the city of Milan. Milan is a huge city, characterized by highly dense residential and commercial edifices and a very high volume of vehicular traffic. It is located in the centre of the Po Valley, the most industrialized area of Northern Italy. Because of the topography of the city and the meteorological conditions that characterize the Po Plain, higher concentrations of suspended PM10 and PM2.5 are registered in winter than in summer [Marcazzan et al., 2001]. In summertime, the higher average wind velocity and the broader mixing layer improve the dispersion of pollutants in the atmosphere. In winter, very frequent and persistent thermal inversions and fog situations at ground level cause a considerable amount of air pollutants to accumulate in the lower layers of the atmosphere. The monthly-averaged values of PTS (Total Suspended Particulate - PM with an equivalent diameter $\leq 50\mu m$) and PM10 concentrations for january between year 1977 and 2009 are shown in figure 2.

The temporal series of PM10 and PM2.5 concentrations data are well correlated [Marcazzan et al., 2001], with an almost constant ratio between the two fractions ($0,61$ in summer, $0,63$ in winter). It is evident that PM2.5 is a substantial part of PM10; the mass of fine particles is nearly twice as much as the mass of particles with equivalent diameter between $2,5$ to $10\mu m$. Through a mass-closure approach [Vecchi et al., 2004] it is possible to determine the average elemental compositions of the detected elements in the two PM fractions. We report in figure 3 the elemental analysis, with relative values of concentration, conduced for PM2.5 composition in the year 2004 and for PM10 composition for the year 2009, for winter and summer,

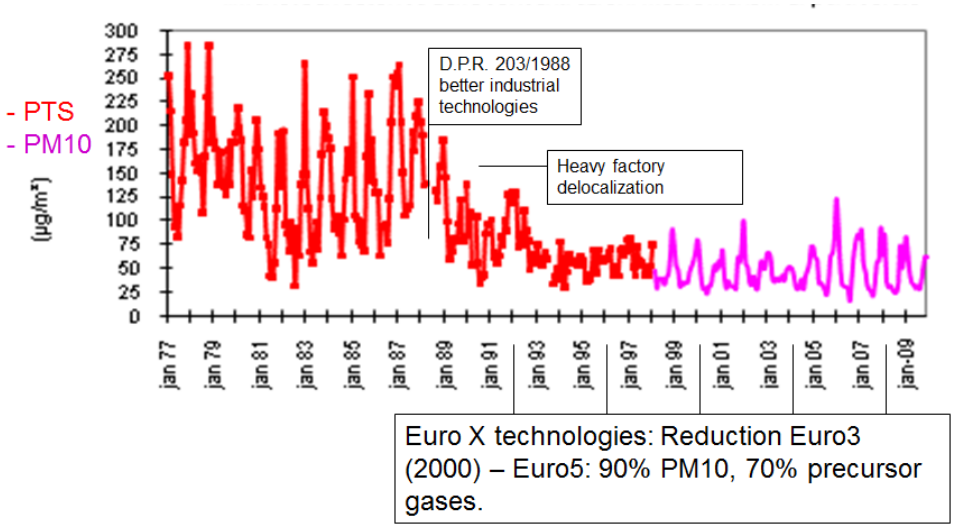

Figure 2: Historical series of PTS and PM10 january average concentrations for the city of Milan. The different strategies pursued to reduce PM concentrations are reported.

for the city of Milan.

We can see that carbon compounds fraction goes from 35% to 50% of the total mass fraction, being more concentrated in the fine fraction; Sulfate and inorganic ions are increased in the fine fraction; the mineral oxides (crustal elements), which define a mineral dust component through the use of a "preferential oxides" algorithm [Marcazzan et al., 2001], and heavy metals are more concentrated in the $2,5 - 10\mu m$ fraction, in which they amount to the 8% of the total mass in winter and to the 20% in summer (this is due to a greater soil dryness and to the increase of mean wind speed). The principal component analysis conduced in [Marcazzan et al., 2001] identifies four factors, which are able to explain the main part of the variance of the concentrations data set for both PM10 and PM2.5 fractions: the first factor identifies a traffic source, related to car exhaust emissions, while the second identifies a generic soil dust source, which can be decomposed into soil particles, resuspended by the action of the wind, and wear components of tyres, breaks and roads, resuspended by traffic. The third factor identifies an industrial source, and the fourth identifies a sulphur contribution of secondary origin, ascribed not only to local sources, but also to a contribution at the mesoscale. A proper multilinear regression model between the concentrations of PM and the concentrations of proper tracers of the identified sources and subsources shows a contribution of $\sim 30\%$ to the total PM10 concentration from traffic (exhaust + wear contribution), and a contribution of $\sim 50\%$ from secondary aerosols. Traffic contributions consists of an exhaust and a non-exhaust component. In principle it is not possible to separate the con-

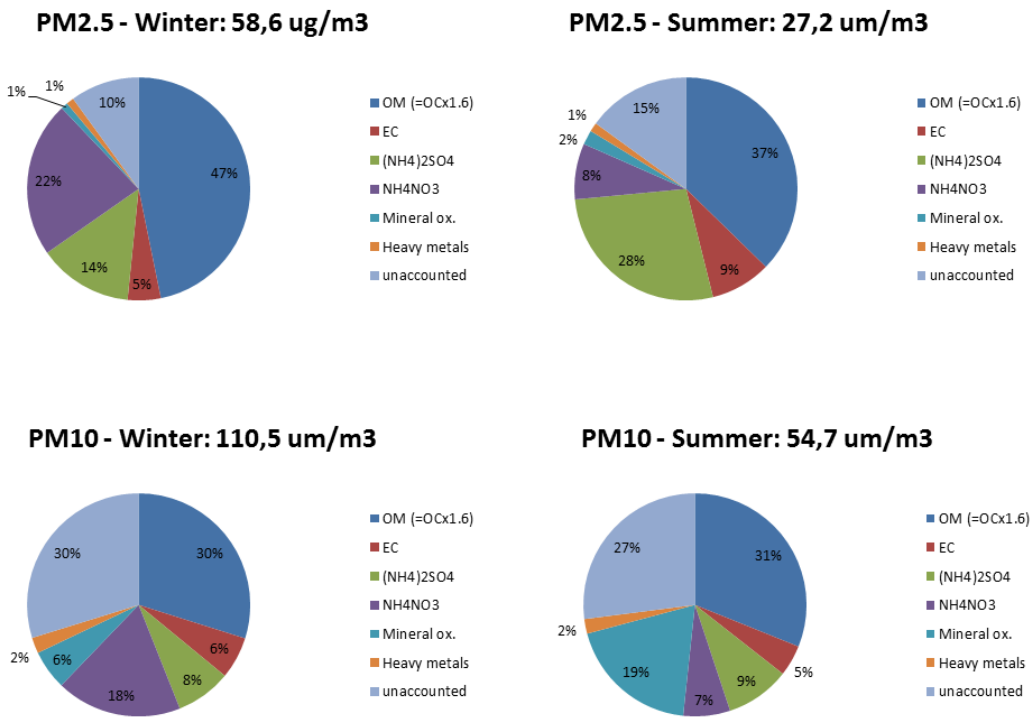

Figure 3: Concentration values and elemental compositions for PM2.5 (year 2004) and PM10 (year 2009), for winter and summer, for the city of Milan

Source typology	Primary PM10 (t/y)	%
Energy production	0,84	0,12
Non industrial combustible	75,53	10,86
Industrial combustible	20,43	2,94
Productive processes	15,56	2,24
Combustible extraction	0,00	0
Solvents usage	25,13	3,61
Road transport	445,81	64,12
Other mobile sources	39,04	5,61
Garbage disposal	2,90	0,42
Agriculture	2,91	0,42
Other sources	67,14	9,66
Total	695,29	

Table 1: Primary PM10 emission estimations for 11 macrosectors for the city of Milan. Data: INEMAR 2008

tribution of wear processes from that of resuspension of deposited road dust, since they have the same tracers and the same temporal profiles. Details on the method to isolate these components will be shown in next paragraphs. In order to update the source apportionment contribution of PM10 to more recent emission scenarios, we analyze the emission data of primary PM10 in Milan city, for the year 2008, reported by INEMAR (INventario delle EMissioni in ARia). In table 1 we report INEMAR elaboration of the source apportionment for the concentration of primary PM10 (expressed as tons per year), considering 11 macrosectors of possible sources.

Road transport is the predominant source of primary PM10 atmospheric concentrations. Its emission contributions can be disaggregated into the different parts coming from exhaust and wear processes, for each vehicle category. Results are reported in table 2.

Diesel motor vehicles, Light Duty Vehicles (LDV) and Heavy Duty Vehicles (HDV) contribute to $\sim 60\%$ of the total road traffic PM10 primary emissions; wear components contribute to $\sim 30\%$ of the total. Diesel engines dominate in large vehicle applications because of their improved fuel efficiency and torque characteristics over gasoline engines. Lately though, an increasing shift to diesel engines is observed also for passenger cars, which now correspond to the highest share of new passenger car registrations in several European countries, with shares reaching as high as 70% for some countries [EMEP/CORINAIR, 2007].

Current European legislation addresses total PM10 mass concentration limits as daily and 1 year averages, and imposes year averages limits to reach in two steps within 2015 and 2020 for the total PM2.5 mass concentrations.

Vehicle typology	Emission typology	%
motor vehicle	unleaded gasoline	$0,68$
	GPL	0
	natural gas	0
	diesel	$18,78$
	wear	$15,34$
LDV	unleaded gasoline	$0,08$
	diesel	$30,21$
	wear	$9,33$
HDV + autobus	unleaded gasoline	$0,00$
	diesel	$11,54$
	wear	$5,59$
moped	unleaded gasoline	$3,77$
	wear	$0,51$
motorcycles	unleaded gasoline	$2,66$
	wear	$1,11$

Table 2: Primary PM10 percentages of emission for the different vehicle categories, separated between exhaust and wear components, for the city of Milan. LDV: Light Duty Vehicles ($< 3,5t$). HDV: Heavy Duty Vehicles ($> 3,5t$). Data: INEMAR 2008

	PM10	**PM2.5**
Stage 1	from 1/1/2005	within 1/1/2015
Annual average	$40\mu m/m^3$	$25\mu m/m^3$
Daily average	$50\mu m/m^3$ (not more than 35 times/year)	
Stage 2	from 1/1/2010	within 1/1/2020
Annual average	$20\mu m/m^3$	$20\mu m/m^3$
Daily average	$50\mu m/m^3$ (not more than 7 times/year)	

Table 3: EU legislation on PM10 and PM2.5 limit atmospheric concentrations.

In Table 3 we report the limits imposed on PM mass concentrations by European legislation.

Figure 2 shows the historical trend of the monthly averages of PM10 concentrations for the city of Milan. PM10 concentrations have not decreased significantly, at least in the last decade, despite the introduction of Euro X engine technologies associated with national emission ceilings, and are often above the limit of EU legislation (we must note that the emission control technologies of diesel light duty vehicles, which contribute the most to primary PM emissions, as seen in Table 2, generally follows the technology of passenger cars with a delay of 1-2 years). High PM10 pollution levels are constantly observed in street canyons. This suggests that a tentative explanation of the observed decoupling between PM emissions trend and its ground level concentrations could arise by the fact that a considerable fraction of the traffic-related PM is attributable to non-exhaust and resuspension phenomena.

2.1 Exhaust emissions

Traffic exhaust (coming from fossil fuels combustion processes) emissions consists of primary particles, Greenhouse gases, CO, NO_x and Hydrocarbons. The combustion process produces CO_2 and H_2O as the main products. Combustion also produces several by-products which either originate from incomplete fuel oxidation (CO, hydrocarbons, particulate matter) or from the oxidation of non-combustible species present in the combustion chamber (NO_x, of which more than 90% is in the form of NO, from N_2 in the air, SO_x from S in the fuel and lubricant, etc...). A wide range of unburned and chemically transformed hydrocarbons (e.g. benzene, toluene, ethane, ethylene, pentane, etc.) is emitted by motor vehicles through a number of different processes (e.g. evaporation, fuel tank displacement, oil seep, etc...). Finally, primary particles of condensed carbonaceous material are emitted mainly by diesel and poorly maintained petrol vehicles. Vehicles with spark-ignition engine are considered as negligible sources of primary particulate

emissions. For old generation gasoline vehicles, not equipped with a three-way catalyzer, emission of primary particles, constituted by Soot and Pb compounds, are comparable with diesel vehicle emissions. New generation gasoline vehicles with direct injection and lean-burn combustion technologies have comparable Soot emissions with diesel vehicles too. Diesel vehicles exhaust emissions are constituted by sulfates, nitrates, organic compounds and carbonaceous (soot and/or ash) agglomerates, on which organic compounds are adsorbed.

Organic compounds belong to the nucleation mode; they are primarily composed of readily volatile components derived from unburned fuel and lubricant oil (i.e. the solvent organic fraction: n-alkanes, alkenes, alkyl-substituted cycloalkanes, and low molecular weight poly-aromatic hydrocarbon compounds).

Carbonaceous agglomerates are accumulation mode particles. They derive mainly from the combustion of engine fuel and lubricant oil by diesel-fuelled or direct injection petrol-fuelled vehicles, as well as from the coagulation of nucleation mode particles. Most of these particles are formed in the combustion chamber (or shortly thereafter), in the central zone of the non homogeneous spray where the air/combustible ratio is low and far from the values at which the mixture bursts. Soot particles are initially generated by condensation of products of partial oxidation and of pirolysis; poly-aromatic hydrocarbon compounds are the main precursors. Oxidation processes at the tailpipe generate CO and CO_2 from Soot particles.

Exhaust primary particulate is thus mainly constituted by small spherical particles, with a diameter between 10 and 80 nm, which form agglomerates and chains characterized by a fractal dimension. The size distribution of this emission source has a principal mode in the accumulation mode, corresponding to the accumulation mode dominant in the mass distribution of urban aerosol.

Exhaust particles dispersion and transformation processes. Particles dispersion at urban scales develops at different spatial scales. The vehicle wake is the first spatial scale where the emitted particles disperse into the ambient environment. It consists of two regions [Kumar et al., 2011]: the near wake and the mean (or far) wake. In the near wake region the number and size distributions of particles change rapidly, due to the influences of various transformation processes induced by turbulent mixing and dilution. The faster of these transformations are homogeneous nucleation, condensation and coagulation (characteristic times of these transformations go from the order of nanoseconds to microseconds [Kumar et al., 2011]). These transformations does not influence the distribution of mass of dispersed particles: nucleation and growth through condensation are competing processes in the nucleation mode happening in the few milliseconds directly after the exhaust

is released, and can be regarded as part of the emission process, in the case it is described by an effective vehicle emission factor; coagulation between nucleation mode particles preserves the total mass of the submicrometric mode, and coagulation between accumulation mode particles is a slow process with respect to dilution, deposition and resuspension processes. Particles are removed at an air surface interface by dry deposition as a result of particle Brownian diffusion. This can remove the smaller particles (i.e. nucleation mode) more efficiently due to their higher diffusion coefficient compared with that for larger particles (i.e. accumulation mode), (gravitational settling is a weak process for exhaust particles). The deposition velocity will be relatively high for small particles and for high friction velocities. In the far wake region the rate of evolution is much slower because vehicle-produced turbulence decays with the increasing distance from the tailpipe and atmospheric turbulence influences the mixing processes. Effects of vehicle wakes interaction on the dispersion evolution must be considered at this spatial scale. Driving cycles determine vehicles reciprocal distances and velocities. The emitted parcel of exhaust is further spread within the street canyon. Depending on the atmospheric stability, on the geometric characteristics of the canyon (such as the aspect ratio W/H, as will be explained in Sections 3.4, 4.1 and 4.2) and the intensity and direction of the roof-level wind, different components of mean recirculation develop at this scale, which influence the pollutant dispersion. After the street scale, the parcel of exhaust can be assumed to be advected in the neighbourhood through a network of streets, and further to be extended to the city scale. In our work we consider pollutant dispersion until the spatial scale of the street canyon. Nucleation and coagulation processes are nearly complete within the near-wake regions behind the vehicular exhaust tailpipe, and dilution then spreads the particles which are carried by advection from the near wake to the far wake. In the far-wake region, particles can still grow by condensation but the growth rates decrease with distance away from the tailpipe due to decreasing dilution factor and concentrations of condensable species.

The dilution is the most important parameter and should be considered appropriately in dispersion models. It is so fast in the near-wake of a moving vehicle that the competing effects of the transformation processes are nearly over within $1s$ after emission. Particles processes may last up to $10s$ in the far wake region, depending on canyon geometry and meteorological conditions. Dry deposition is an important process for both wake regions.

Exhaust particles health effects. Numerous studies conclude that road vehicles are a major source of nanoparticles in urban areas. Their contribution can be up to 86% of total particle number concentrations [Kumar et al., 2011]. The ultrafine size range of nanoparticles has the potential for the largest deposition rates in the lungs. They can enter the body through the skin, lung

and gastrointestinal tract and can also penetrate epithelial cells and accumulate in lymph nodes (Nel et al., 2006). Besides this, particles in the accumulation mode, having the highest surface area to mass ratio, allows greater contact for adsorbed compounds to interact with biological surfaces. The studies suggest that particle number concentrations are an important metric to represent the toxic effects. Atmospheric particles are currently regulated in terms of mass concentrations in the size ranges $\leq 10\mu m$ and $\leq 2.5\mu m$ but this does not address particle number concentrations. Thus the major proportion of vehicle emissions that contribute significantly to number concentrations remains unregulated through ambient air quality standards.

In order to comply with emission legislation, vehicle manufacturers have been installing after treatment devices, such as catalytic converters and diesel particle filters, to suppress byproduct emission. Catalytic converters are not able to bring down NO_x and carbonaceous fraction emissions; such devices may also produce small quantities of pollutants such as NH_3 , N_2O and sulfates. There are currently new technologies available, which aim at decreasing both energy consumption and pollutant emissions by (for diesel engines) increasing the air/combustible ratio, the pressure of fuel injection, the regulation of ignition timing (a shorter ignition timing causes lower soot but higher NO_x emissions) and exhaust gas recirculation. . Those technologies include new fuels (CNG, Reformulated grades, eventually H2) and alternative powertrains (hybrids – meaning a combination of internal combustion engine and electric motor, fuel cell vehicles, etc.). Particle mass emissions from bio-fuelled vehicles have decreased significantly, but possibly at the expense of an increase in particle number emissions.

Description of the transport dynamics for the Soot component. As we are interested in mass distribution trend for vehicle exhaust and non-exhaust emissions, we consider exhaust emitted particles in the accumulation mode (where there is a dominant peak in urban aerosol mass distribution). The transformation processes which are dominant in the different spatial scales of dispersion after emission (from vehicle wake to canyon street) for accumulation particle dispersion are emission, dilution and dry deposition. Near wake turbulent quantities are anyhow important to describe resuspension phenomenon, as will be described in Section 4.3. We do not need to gain detailed insight into near wake transformation processes, as they does not influence the distribution of mass of dispersed accumulation particles with respect to dilution. This mode does not interact with the coarse mode of road dust emissions, as we have already explained. We will consider Soot as the main tracer of primary exhaust emissions, and will express PM10 primary exhaust emission factors of diesel powered vehicles as Soot emission factors in the simulation of particles mass concentration via advection-diffusion equations. We will consider specific emission factors of different vehicle cat-

Soot	Agglomerate diameter	Agglomerate density
	$40nm$	$900\frac{kg}{m^3}$
	$100nm$	$500\frac{kg}{m^3}$
	$300nm$	$200\frac{kg}{m^3}$

Table 4: Soot agglomerates diameters and densities.

egories, as given by emission inventories, in the determination of tailpipe PM10 emission for the case of Milan.

The equation for the statistically averaged concentration evolution C (mg/m^3) of Soot or road dust component is:

$$\frac{\partial C}{\partial t} + \vec{U} \cdot \vec{\nabla} C = \vec{\nabla} \cdot ((D + D_T)\vec{\nabla} C), \tag{2.1}$$

where D is the Einstein diffusion coefficient for the particles in the considered mode, and D_T is the turbulent diffusion coefficient. This is an advection-diffusion equation for the dispersion of the pollutant, advected by the wind field $\vec{U}$ at the different spatial scales of dispersion. This equation will be treated both analytically and numerically in the next chapters. In a context of an operational dispersion model, it will be approximately solved by a superposition of puff solutions, with advection and turbulent dispersive parameters coming from the combination of the vehicle and canyon scales (for different traffic conditions and canyon geometries). In a context of a finite element discretization approach, it will be numerically solved in a street canyon or open street domain, with proper wind field description and parameterization of turbulent diffusivity for different traffic conditions. Soot is constituted by fractal-like agglomerates, in the accumulation mode, of carbon primary spheres of diameter $10 - 20nm$. The effective density of agglomerates decreases as the diameter increases with a power law of the form [Keskinen et al., 2010]:

$$\rho_P \propto d_P^{d_F - 3},$$

where d_P is the agglomerate maximum diameter, and d_F is its fractal dimension. According to this law and to the data reported in [Keskinen et al., 2010], we have used the following values for three kind of stable Soot agglomerates in our dispersion solutions:

Soot particles with a diameter of $\sim 40nm$ are characteristics of diesel Euro 3 vehicle (without DPF) emissions; the other two Soot diameters are characteristics of diesel Euro 4 vehicle with DPF emissions. [Avella, Faedo, 2008]. Soot dispersion in air takes place in the transition regime [Seinfeld, Pandis, 2006]: particles diameter are comparable with the mean free path of air (equal to $\lambda = 60nm$ at $298K$ and $1atm$). In this regime continuum conservation equa-

tions can be considered, if slip correction factors C_C is introduced in the force balance equations for particle motion. Einstein diffusion coefficients is:

$$D = \frac{kTC_C}{3\pi\mu d_P}, \quad C_C = 1 + \frac{2\lambda}{d_P}\left[1.257 + 0.4\exp\left(-\frac{1.1d_P}{2\lambda}\right)\right] \tag{2.2}$$

Brownian diffusion of Soot particles, described by the diffusive flux determined by Einstein coefficient, is an important process, with respect to turbulent diffusion and gravitational settling, in the far-wake and canyon regions, and in boundary layers next to rigid boundaries. Deposition and resuspension processes are described by Neumann boundary conditions for the normal flux of particles at the road surface, written as a dynamical balance between deposition and resuspension (for road dust) fluxes (see later paragraphs). Exhaust emission processes, which we insert as a linear source of emission in the operational model or as a source on a small circular surface in the base rear face of the vehicle in numerical simulations, are given in terms of emission values, depending on vehicle velocities and thermal conditions of the engine, vehicle category and technology, according to EMEP CORINAIR emissive methodology [EMEP/CORINAIR, 2007].

Description of the emission factors. The EMEP CORINAIR methodology gives particulate emissions from the vehicle exhaust in the PM2.5 size range. The calculated emission factors must be multiplied by Soot/PM2.5 ratios, given by the same methodology for different vehicle technologies, in order to obtain Soot emission factors. For an Euro3 passenger car, the fraction of Soot to PM2.5 is 85%. For an Euro4 passenger car with DPF, the fraction is 10%. From the data on Soot concentrations we can obtain the values for primary Organic Matter concentrations, by multiplying the Soot fraction by given OM/Soot factors for each vehicle categories. Primary organic material is in this case the mass of primary organic carbon corrected for the hydrogen content of the organic species collected. This method does not account for additional quantities of aerosol carbon, usually small, which may exist either as carbonates or CO_2 adsorbed onto Soot particles. Nitrates and sulphates constitute the remaining fraction when Soot and OM do not sum up to 100% of total PM2.5 exhaust emissions. From values of primary OM and data on total OM (obtainable for example by multiplying the primary OM by a factor 1.5 [Seinfeld, Pandis, 2006]) we should obtain values of secondary OM emitted by traffic, through the use of Soot tracier method: $[OC]_S = [OC]_{Tot} - (OM/Soot)[Soot]$. In general, we are not interested in secondary components in this work. PM2.5 emission factors for EuroX gasoline passenger cars are given as fixed values (expressed in mg/km) for each kind of road relative to different driving cycles: urban, rural and highway. PM2.5 emission factors for Euro1,2,3,4 diesel passenger cars are calculated as a function of speed V. The value introduced for speed should correspond

to the average speed during travelling and not to the instantaneous speed. The generic function used is:

$$e_{hot} = a + bV + cV^2$$

whith a, b, c suitable constants. PM2.5 emission reduction percentage for Euro 5 and 6 diesel passenger cars applied to vehicles complying with Euro 4 standards is 95%. For example, the Soot emission factors $e_{hot}(g/km)$ for a diesel Euro 4 with DPF and a diesel Euro 3 without DPF motor vehicle in a urban driving cycle, in thermally stabilised engine operation (hot), moving at an average velocity of $42km/h$, are:

$$e_{hot} = 1,7mg/km \quad [Euro4] \qquad e_{hot} = 17,66mg/km \quad [Euro3]$$

These factor are a little different from those reported in Parfil project report [Avella, Faedo, 2008]. This is due to the fact that in Parfil project a mean emission factor for each driving cycle is reported, and a different ratio between Soot and total primary exhaust PM for the Euro4 vehicle with DPF is found (pactically negligible Soot fraction with the DPF device for Parfil project, 10% fraction for EMEP-CORINAIR methodology). PM emissions from gasoline LDV can be considered similar to passenger cars. Diesel LDV emission factors are calculated as a function of speed for conventional and Euro1 vehicles, and by means of reduction percentages for Euro 2,3,4,5 vehicles. Diesel autobus and HDV are calculated as functions of speed, depending also on load factor. GPL and Gas passenger cars, LDV and autobus, and gosoline motorcycles emission factors are given as fixed values for each kind of road relative to different driving cycles. Factors in mg/km can be transformed in units mg/m^3 or mol/m^3 by dividing for 1000· area of the circle of the tailpipe emission and by 1000· the molar mass (in u) of the pollutant furthermore.

Driving cycles. Typical driving cycles, obtained through a clustering statistical analysis on speed *vs* acceleration distribution of representative segments of data describing vehicles instantaneous speed profiles, are given in the context of the Artemis project [André, 2004]. European driving conditions are divided in 12 kinematical representative classes, reported in the Table in Figure 4 with their kinematical characteristics.

The urban and the motorway (extra-urban) driving cycles, obtained by juxtaposing representative kinematic segments of driving classes, covers a lenght of $3,4km$ and $82km$ respectively, and are composed by the representative classes reported in Table 5, with relative percentages of the total covered mileage

Data of urban driving cycle will be considered as input data on vehicle velocity, accelerations and covered mileage in the analysis of pollutant tailpipe

Classes of driving conditions and their description			Percentage of total mileage	Running speed (km/h)	Average speed (km/h)	Stop duration (in %)	Stop rate (stop/km)	Average positive acceleration (m/s^2)
1	congested urban	high stop duration	3.7	25.9	10.2	60.8	3.9	0.87
2			5.9	23.6	15.9	32.7	3.0	0.81
3		low steady speeds	2.4	16.5	13.2	19.5	3.4	0.67
4	free-flow urban		5.1	28.0	26.1	6.7	0.97	0.65
5		unsteady speeds	12.2	35.6	32.3	9.1	0.98	0.81
6	secondary roads	unsteady speeds	10.8	52.2	48.8	6.6	0.41	0.75
7			8.8	45.5	43.8	3.7	0.39	0.63
8		steady speeds	7.2	65.0	64.0	1.5	0.15	0.55
9	main roads	unsteady speeds	11.8	75.0	72.5	3.3	0.15	0.67
11			6.2	86.1	85.7	0.4	0.04	0.48
10	motorways	unsteady speeds	10.4	115.6	114.9	0.7	0.03	0.53
12			15.6	123.8	123.7	0.1	0.01	0.40

Figure 4: European driving conditions for 12 typical classes, obtained by automatic clustering of speed profiles recorded on-board vehicles [André, 2004]

Urban driving cycle	%	**Motorway driving cycle**	%
Congested, stops	14		3
Urban dense	22		2
Congested, low speed	10		1
Free-flowing	14		2
Free-flowing, unsteady speed	23		5
Secondary roads, unsteady speed	5		6
Secondary roads	7		3
Secondary roads, steady speed	1		4
Main roads, unsteady speed	2		12
Main roads	0		6
Motorway, unsteady speed	1		20
Motorway	0		36

Table 5: Urban and Motorway (extra-urban) driving cycles described in function of its structure under typical driving conditions

emissions in a urban area. Canyon street geometry will be considered for urban and main roads, whereas open street geometry will be considered for secondary and motorway roads.

2.2 Non-exhaust emissions - Definition of road dust

Non-exhaust particles, which contribute to the coarse mode of urban aerosol mass distribution, are produced as a result of the interaction between a vehicle tyre and the road surface, and also when the brakes are applied to decelerate the vehicle. In both cases, the generation of shear forces by the relative movement of surfaces is the main mechanism for particle production. A secondary mechanism involves the evaporation of material from surfaces at the high temperatures developed during contact. The other component is coming from wear processes and resuspension processes of deposited road dust on road surface. Tyre and road surface interactions generate about 70% of particles by mass mainly in the $2.5-10\mu m$ size range [EMEP/CORINAIR, 2007].

Experimental characterization. The APART (Abrasion PArticles produced by Road Traffic) project [Empa, 2009], held by the swiss research organization Empa and by PSI (Paul Scherrer Institut), through a series of measures in different street configurations (urban canyon and extra-urban road) in the city of Zurich, has identified and quantified, by using proper statistical analysis on collected data, the traffic related non exhaust PM10 fraction, both for the entire vehicle fleet and for LDV and HDV vehicles separately. Principal Component Analysis is applied to the chemical dataset to identify the most significant factors responsible for the variance of chemical species in PM10 road dust. Antimony (Sb) and other traciers are correlated to traffic emissions coming from brake wear. Other typical traciers for this emissive component are steel, which is the support material of brake pads, Cu, Mo, Sn, Sb and Ba. Specifical traciers for tyre wear component are Zn and black carbon. Factor analysis cannot distinguish between vehicle and road wear and road dust resuspension emissions, due to their similar chemical composition and to their strongly correlated temporal variation. One way to proceed, once identified the principal factors of the component analysis, should be to write a multilinear regression model with autocorrelation terms for the concentration data (finite difference stochastic model whith autoregressive terms), and to quantify the resuspension source through the strenght of autocorrelation terms. In [Empa, 2009] the different emission factors for road wear and resuspension sources are obtained through the analysis of data obtained in laboratory experiments by using two different mobile load simulators (wheel devices which reproduce the loads and wheel flow of LDV and HDV vehicles on roads with different pavements).

Both in the case of street canyon and extra-urban motorway, the brake wear component is characterised by a pattern of Fe, Cu, Zn, Mo, Zr, Sn,

Sb and Ba. Its size distribution is in the range $\geq 1\mu m$ for LDV vehicles, whereas more than 75% of brake wear particles coming from HDV vehicles are in the coarse mode in the range $2,5 - 10\mu m$.

Tyre wear component is not quantitatively important in PM10 fraction, whereas in $> 10\mu m$ size fraction it constitutes a contribution of $5 - 10\%$ to TPS.

The Zurich road dust consists mainly of two components : a) roughly 50% of the mass is crustal material (SiO_2, CaO), b) carbonaceous matter, being the sum of $OM + EC$ and comprising also about 35% of mass. It is generated mainly by mineral sources, building materials and deposited wear components from traffic.

The PM10 area deposition of road dust determined for the Zürich sites in February 2008 varied within a range of $0.2 - 3.0mg/m^2$, according to increasing traffic density. The maximum concentration is for a street canyon with a heavy traffic load, an old surface with many repair patches (asphalt concrete). A value of $0.5mg/m^2$ is measured in an open intersection road with new porous asphalt surface.

The mass fraction of dominant components of PM10 road dust and the size distribution obtained during the analysis of the abrasion particles produced by a cycle of operation of a mobile load simulator are shown in figure 5.

A comparison between road dust analysis for the city of Barcellona can be made [Amato et al., 2009]. The city centre showed values of PM10 road dust within a range of $3-23mg/m^2$, whereas levels reached $24-80mg/m^2$ in locations affected by transport of uncovered heavy trucks. The largest dust loads were measured in the proximity of demolition/construction sites with values up to $328mg/m^2$. The city centre road dust profiles were enriched in OC, EC, Fe, S, Cu, Zn, Mn, Cr, Sb, Sn, Mo, Zr, Hf, Ge, Ba, Pb, Bi, SO42, NO3, Cl and NH4, but several crustal components such as Ca, Ti, Na, and Mg were also considerably concentrated. Locations affected by construction and demolition activities had high levels of crustal components such as Ca, Li, Sc, Sr, Rb and also As whereas ring roads, characterized by a higher load of uncovered heavy trucks showed an intermediate composition.

Constituents with the highest average concentrations are SiO_2 $(18,8\%)$, Ca $(12,8\%)$ and OC $(10,7\%)$. Averaging the concentration of trace elements in all the collected samples, the highest elements were found to be Ti, Zn, Ba, Cu, and Mn. The chemical results highlighted the importance of distinguishing four categories in order to shed light on how local factors influence sediment properties, classifying the sites according to the type of environments. City centre locations show similar elemental components and concentrations of road dust as in the Zurich experiment.

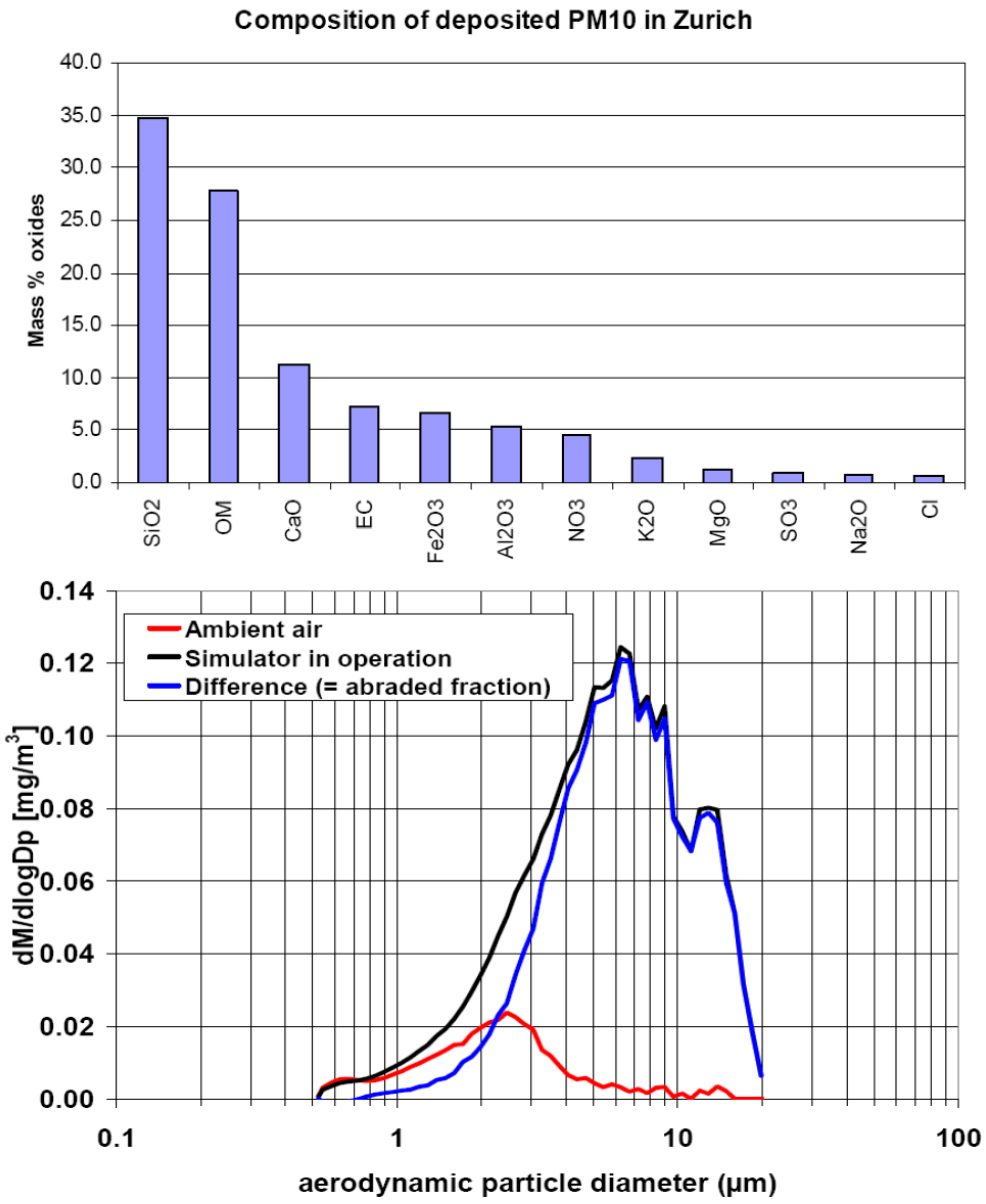

Figure 5: Mass fraction of dominant components of Zurich PM10 road dust and size distribution for an experiment with mobile load simulator [Empa, 2009]

Road dust component definition. As we have from experimental data, even if the different wear processes are characterized by specifical traciers of different chemical compositions (mainly Fe, Cu and Sb for break wear components, silicon, carbon and mineral compounds for road wear and resuspension components, and Zn for tyre wear components), their components are all distributed in the coarse mode, and can be characterised in principle by a single mode, with a size corresponding to the dominant peak in an analysis of road dust, and with a density calculated by a "preferential oxides" like algorithm, derived by the analysis of the fractions of the dominant components of road dust. As we don't dispose of direct measures of Milan road dust, we refer to measures coming from APART project [Empa, 2009], as representative data on a urban typical sample of road dust, with a weak influence of building works and external sources.

We will consider in our simulations initial road dust concentrations with the same values as those reported in APART data, and a single coarse component describing all wear and resuspension of road dust processes, with an average diameter and a density equal to (see Figure 5):

Road dust	
Average diameter	$7\mu m$
Density	$0,36\,\rho_{\mathbf{SiO_2}} + 0,28\,\rho_{\mathbf{OM}} + 0,125\,\rho_{\mathbf{CaO}} + 0,075\,\rho_{\mathbf{Soot}}$ $+0,075\,\rho_{\mathbf{Fe_2O_3}} + 0,06\,\rho_{\mathbf{Al_2O_3}} = 2361,72\frac{km}{m^3}$

Table 6: Road dust average diameter and density.

We have considered a road dust component composed of chemical constituents in the proportions reported in Figure 5, and reference values for the oxides densities. The organic component OM of ambient particles is a complex mixture of hundreds of organic compounds. We consider as the dominant OM tracier of road dust styrene butadiene coming from tyre wear [EMEP/CORINAIR, 2007]. Other dominant components, such as benzopyren hidrocarbons, should be associated to exhaust emissions in the accumulation mode. We could consider different classes of coarse particles for each different wear process as well, but in that case it would be difficult to characterise the single component of resuspended road dust. Simulating the dispersion process of this coarse component we consider as sources all emission contributions given by the different wear processes, by background and initial road dust concentrations.

Description of the emission factors. Emission factors, depending on vehicle velocity, vehicle category, driving cycle, are calculated by means of EMEP CORINAIR emissive methodology [EMEP/CORINAIR, 2007]. Road wear emission factor for a new or a damaged asphalt are extrapolated by data

taken from [Empa, 2009]. We report here the procedure used to determine wear emission factors, as derived from EMEP-CORINAIR methodology. Receptor modelling is the widely-used technique for determining particle emission rates for tyre wear. Another method is to record wear rates of particles by periodic weighing of tyres, and then to deduce an emission factor by assuming that a fraction of this wear is airborne. Particle emission factors from tyre wear are expressed in term of Total Suspended Particles (TSP) in the following way:

$$e_{tyre} = e_{TSP} \cdot f_{Ti} \cdot S_T(V)$$

where e_{TSP} is TSP mass emission factor from tyre wear $[mg/km]$, given for the different vehicle categories; f_{Ti} is the mass fraction of tyre-wear TSP that can be attributed to the considered particle size class i (0.6 for the PM10 class); $S_T(V)$ is the tyre-wear correction factor for a mean vehicle travelling speed V, expressed as a linear function of V. The TSP emission rates do not assume that all tyre wear material is transformed into suspended particulate, as a large fraction may be produced as dustfall particles. From literature we deduce a fraction of TSP which is directly airborne equal to 50% [Hedalen, 1994]. The determination of particle emissions from brake wear is obtained by direct measurement using a simulated wheel or brake operation in the laboratory (the simulation of brake operation in the laboratory is straightforward). Similarly to tyre wear, brake wear emissions can be calculated as:

$$e_{brake} = e_{TSP} \cdot f_{Ti} \cdot S_T(V)$$

The mass fraction of brake-wear TSP that can be attributed to the PM10 class is $0,98$. A $55-70\%$ of the total wear material is in the form of airborne particles; experimental studies reported in [EMEP/CORINAIR, 2007] identify that $3-30\%$ of brake debris falls on the road, $16-22\%$ is retained on the wheel, and $8-25\%$ is retained on the brake and steering and suspension equipment. The wear rate of asphalt, at least in terms of airborne wear particles, is even more difficult to quantify than tyre and brake wear, partly because the chemical composition of bitumen is too complex for quantification with receptor modeling, and partly because primary wear particles mix with road dust and resuspended material. Therefore, wear rates and particle emission rates for road surfaces are highly uncertain. Emission rates from asphalt wear are calculated through the formula:

$$e_{asphalt} = e_{TSP} \cdot f_{Ti}$$

The mass fraction of asphalt-wear TSP that can be attributed to the PM10 class is $0,50$. As for the tyre wear component, the fraction of road wear TSP which is directly airborne is 50% [Hedalen, 1994]. For the heavy-duty truck case, emission factor needs to take vehicle size into account, in

term of the number of truck axles and load factor. According to EMEP-CORINAIR values of e_{TSP}, tyre wear emissions for an HDV are ~ 2 times the emissions for a passenger car (depending on the load factor), brake wear are ~ 3 times and road wear are ~ 6 times the corresponding emissions for a passenger car.

2.3 Deposition and Resuspension

By analysing the diurnal variation profiles of NO_x, Soot and CO_2 reported in [Empa, 2009], we can see that they are strongly correlated to HDV and LDV frequency profiles, whereas Sb and coarse Si profiles show a distinct peak at midday, correlation with wind velocity and no significant correlation with daily traffic frequency profiles. An explanation to these behaviours is that NO_x, Soot and CO_2 emission processes are dominated by vehicle exhaust emissions, whereas Sb and coarse Si, which are traciers of brake wear and resuspended road dust respectively, are correlated to wind velocity in its effect on increase of resuspension intensity. We see that resuspension is an important process for road dust component dynamics, but is negligible for pollutant dispersion in the accumulation mode. Thus we consider a total removal of Soot component when deposited on road surface.

Dry deposition and resuspension processes are described by a Neumann boundary condition for the normal flux of particles at road surface, written as a dynamical balance between deposition and resuspension fluxes (we don't consider deposition on the vehicle boundary and on the walls of the canyon). Following [Seinfeld, Pandis, 2006], dry deposition flux is directly proportional to the local concentration C of depositing pollutant at some reference height z above the surface:

$$F(z) = -v_d(z)C(z)$$

The proportionality constant v_d (for z fixed) between dry deposition flux F and pollutant concentration is the deposition velocity. The process of dry deposition is viewed as consisting of three steps: the particle is first vertically transported through the logarithmic boundary layer via turbulent transport to a thin viscous sublayer adjacent to the boundary; as a second step the particle is transported by Brownian diffusion and sedimentation across the viscous sublayer to the boundary itself; lastly the particle is uptaken at the boundary. In the modelization, the transport in the buffer sublayer (the transition layer between the logarithmic and the viscous sublayers, in which the eddy diffusivity is described by Van-Driest law [Wilcox, 1998], as we will explain later) is not considered. This is not a problem, as the parametrisation of the three processes are determined from experimental data fitting based on the dominant dimensionless groups considered above. The deposition velocity is modelled using the concept of the resistance analogue, in which the transport of the pollutant to the surface is assumed to be governed by a

sequence of three resistances in series, representing aerodynamic resistance in the logarithmic BL, resistance to transfer across the viscous sublayer, resistance to surface uptake, and one in parallel, representing gravitational settling. In figure 6 we report a scheme for the three resistances in series.

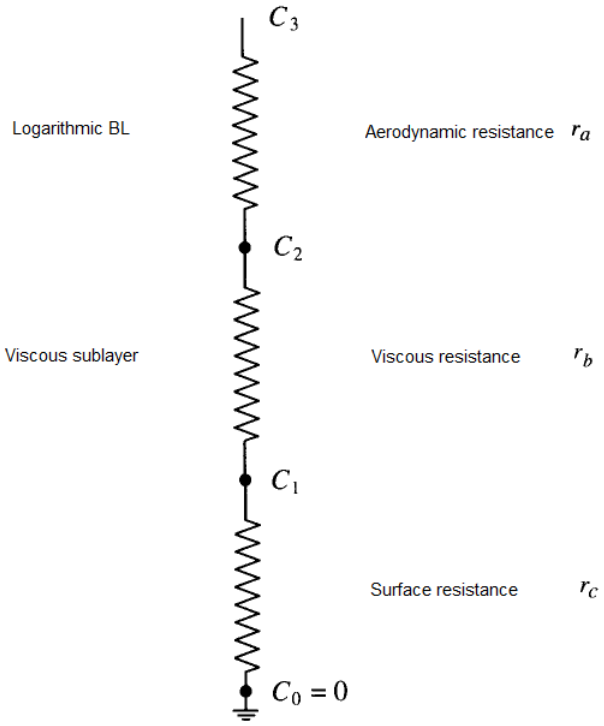

Figure 6: Resistance model for dry deposition

C_3 is the pollutant concentration at the top of the logarithmic BL; C_2 that at the top of the viscous sublayer; C_1 at the bottom of the viscous sublayer; C_0 that at the surface boundary. Particle settling operates in parallel with the three resistances in series. It is assumed that particles adhere to the surface on contact, so that the surface resistance is 0. Particle sedimentation processes are inserted in viscous resistance. At steady state it is assumed that the total flux F is constant and equal across the different sublayers. The deposition flux is:

$$F(z) = \frac{C_3(z)}{r_{tot}(z)} = C_3(z)v_d(z) = \frac{C_3 - C_2}{r_a} + v_s C_3 = \frac{C_2}{r_b} + v_s C_2$$

so that:

$$v_d(z) = \frac{1}{r_a + r_b + r_a r_b v_s} + v_s$$

where v_s is the particle settling velocity, dependent on particle density and diameter, on acceleration of gravity and on air viscosity:

$$v_s = \frac{\rho_p d_p^2 g C_c}{18\mu}$$

The aerodynamic resistance is calculated on the basis of gradient transport theory and similarity between mass transfer and momentum transfer. For momentum transfer, vertical turbulent transport is determined by the z component of Reynolds stress tensor in the direction parallel to the wall, which can be written, in the logarithmic BL, in terms of the vertical gradient of parallel velocity multiplied by an eddy diffusivity proportional to the distance from the wall (details will be shown in next chapters). In analogy with momentum transfer, aerodynamic resistance for mass transfer can be written as:

$$r_a = \frac{1}{k u_*}\left[\log\left(\frac{z}{z_0}\right) + \Phi_M(\zeta)\right]$$

where z_0 is the roughness length of the boundary surface, k is Von-Karman constant, $\Phi_M(\zeta)$ is linked to integrals of empirically determined functions of the dimensionless variable $\zeta = z/L$, with L the Monin-Obukhov length (representing the ratio between buoyancy and mechanical turbulence), which take into account the thermal stability of the atmosphere [Seinfeld, Pandis, 2006]. In the case of neutral stability of the atmosphere, $\Phi_M(\zeta) = 1$.

The resistance to transfer in the viscous layer depends on viscous diffusivity and on surface characteristics (in the hypothesis that particles deposition on surface elements by impaction and interception are considered as occurring in the viscous sublayer, with a surface resistance equal to zero and $C_0(0) = 0$):

$$r_b = \frac{1}{3u_*(E_b + E_{IM} + E_{IN})R_1}$$

Semi-analytical descriptions of particle collection efficiencies are largely derived from wind tunnel studies [Slinn, 1982], adapted here for small collectors constituted by asphalt collectors (with average diameter d_c) with negligible form drag (only viscous drag is relevant for asphalt collectors). E_b is the collection efficiency from brownian diffusion, expressed in terms of Schmidt number $Sc = \frac{\nu}{D}$ as:

$$E_b = Sc^{-2/3}$$

E_{IM} is the collection efficiency from impaction, governed by the dimensionless Stokes number $St = v_s u*/g d_c$, which represents the ability of a particle to deviate from the flow streamline. It is expressed as:

$$E_{IM} = \frac{St^2}{1 + St^2}$$

The efficiency of particle collection by interception depends on the particle diameter and the average dimension of the collectors. It can be expressed as:

$$E_{IN} = \frac{d_p}{d_p + d_c}$$

A variety of expressions have been proposed in literature for all the collection efficiency parameters. R_1 is a sticking coefficient, representing the fraction of particles, once in contact, that stick to the surface. It can be expressed as:

$$R_1 = \exp\left(-\sqrt{St}\right)$$

As $St \to 0$, $R_1 = 1$, which means that small particles do not possess sufficient inertia to bounce off from a surface. We must observe that the values of u_*, for different vehicle categories, road type and driving conditions, must be given from our results of vehicle wake and canyon solutions. The adopted methodologies will be shown in Section 4.3. We only note that, due to stability and convergence issues of the discretized turbulence model which we will consider, turbulence equations will be integrated starting from the logarithmic BL, in the adjacent discretization cells to the surface boundaries; the resistance model of deposition velocity usefully reintroduces the viscous layer physics in the dispersion equation for the pollutant. By considering the case of the far-wake (at a distance 15 times the height of the vehicle, on the centerline of the road) of a sedan vehicle flowing at $40km/h$ in a street canyon, with $d_c = 11,2mm$, we obtain (see Section 4.3 for details and values of deposition velocities for other cases) a value of $u_* = 0,26m/s$, and the following values for v_d for a Soot particle and a road dust particle:

Particle type	v_d $[cm/s]$
Soot	$0,25$
Road dust	$0,51$

Table 7: Values of v_d for a sedan vehicle flowing at $40km/h$ in a street canyon

These should be compared to the values obtained in [Pryor et al., 2008] for a urban environment:

There are differences, as we are considering different density particles and very small collectors. For the dispersion of the Soot particles, we consider a complete removal of the deposited particles on the road surface. The deposition flux must be expressed at the road level $z = 0$, as we don't know

Particle diameter $[\mu m]$	v_d $[cm/s]$
$0,1-0,2$	$1,3-3,0$
$0,2-0,5$	$0,1-1,5$
$0,5-2$	$0,3-0,8$

Table 8: Data of v_d in a urban context for different particle dimension ranges [Pryor et al., 2008]

in advance the value of the pollutant concentration $C(z)$ in the logarithmic BL: imposing a flux condition based on the previous parametrizations of the deposition flux would be difficult in the context of a finite element method. In order to obtain a form for the deposition velocity at the street level $v_d(0)$, we have to integrate the conservation equation for C in the vertical direction from the logarithmic BL to the surface:

$$\frac{d}{dz}\left((D+K(z))\frac{dC}{dz}\right)+v_s\frac{dC}{dz}=\frac{dF(z)}{dz}=0$$

where $K(z)$ is the vertical eddy diffusivity. Let us write the deposition velocity as:

$$v_d(z)=\frac{F(z)}{C(z)}=v_s+(D+K(z))\left(\frac{C'}{C}\right)$$

$$\longrightarrow C(z)=C(0)\exp\left[\int_0^z\frac{1}{D+K(z')}(v_d(z')-v_s)\,dz',\right]$$

Substituting into the conservation equation, we obtain the Bernoulli equation:

$$v_d'+\frac{1}{D+K(z)}v_d(v_d-v_s)=0$$

Let us also consider an eddy diffusivity of the kind $K(z)=ku_*z$ (we are neglecting again the buffer sublayer). This is a Cauchy problem; as $z>0$, there is no divergence of the equation coefficients ($u_*>0$ for the turbulent boundary layer), which are C^∞ in the considered interval, and a unique solution exists for $z\geq 0$. It's simple, by changing first $v_d\to v_d^{-1}$ in the previous equation, to find its general solution dependent on $v_d(0)$. Inverting the dependence in the solution we obtain:

$$v_d(0)=\left[\frac{1}{ku_*}+\left(\frac{1}{v_d(z)}-\frac{1}{ku_*}\right)\left(1+\frac{ku_*z}{D}\right)^{\frac{v_s}{ku_*}}\right]^{-1},$$

where $v_d(z)$ is the deposition velocity obtained in the resistance model framework, and z is to be chosen in the logarithmic BL. The logarithmic law of momentum transfer is valid for a turbulent boundary layer from $u_*z/\nu=$

$z^+ = 30$ to 100 and more. We can choose a value of $z^+ = 50$. The road surface boundary condition for Soot dispersion is thus:

$$N = -v_d(0)C, \tag{2.3}$$

where N is the normal flux of particles concentration C at the road boundary. For road dust dispersion, we must consider the resuspension phenomenon. Road dust Deposition and Resuspension processes are described by a Neumann boundary condition for the normal flux of particles (a Robin boundary condition for C) at road surface in the description of the dispersion equation, written as a dynamical balance between deposition and resuspension fluxes:

$$\begin{cases} N = -\dfrac{v_d(0)}{\theta_0} C(\theta_0 - c_s) + k_{res} c_s \\ \dfrac{\partial c_s}{\partial t} + v_v \dfrac{\partial c_s}{\partial x} = \dfrac{v_d(0)}{\theta_0} C(\theta_0 - c_s) - (k_{res} + f_x n_v) c_s + S(t), \end{cases} \tag{2.4}$$

where N is the normal flux of particles concentration C at the road boundary, c_s is the road dust concentration, $v_d(0)$ is the deposition velocity, calculated as for the case of Soot deposition, k_{res} is the resuspension rate (in units of $1/s$), θ_0 is the maximum capacity of road dust concentration entrainment of the surface (calculated by means of asphalt parameters, as shown in the Section 2.4) and $S(t)$ is a source term corresponding to the road and vehicle wear components. All terms in equations (2.4) have dimensions of $[\frac{mg}{sm^2}]$: the balance equation is considered in a $2D$ road surface. The influence of road thickness is treated through the influence of a dimensionless parameter representing the filtration dynamics, as will be explained in a moment. In a dispersion equation for road dust in which traffic is considered as a linear emissive source, $S(t)$ is the fraction of vehicle and road wear which is not airborne, but is directly deposited on the road boundary, as expressed in previous paragraphs (airborne vehicle wear fractions are inserted as linear emissions at the height of the tyres). In a dispersion simulation in the wake of a vehicle, total tyre wear emissions should be inserted as Dirichlet conditions on tyre boundaries, whereas total road wear emission should be inserted as in (2.4). $S(t)$ must be transformed in an emission rate with units $[mg/sm^2]$ from emission data expressed in $[mg/km]$, by considering vehicle velocity and road width. Note that, since equations are written in the vehicle system of reference, the road dust concentration c_s must translate along the road with velocity opposite to the vehicle velocity v_v. The term $f_x n_v$ takes into account the mechanism for sticking of material to the outer surface of the wheels; road dust is thus carried along the road by this mechanism. This effect can be described through proper empiric parametrizations, such as those given in [Patra et al., 2008], in which the fraction of material removed from a road segment along the road by one vehicle is determined through a street canyon series of measurments in central London to be $f_x = 3,9\,10^{-4}[v^{-1}]$.

By multiplying this factor by the traffic flow rate $n_v[vs^{-1}]$ and road dust concentration c_s, we obtaine the desired removal flux. We must observe that the particles sticked to tyre surfaces can be emitted again during the vehicle flow; this effect is implicitly described by EMEP-CORINAIR emission rates for tyre and road wear, which are determined by receptor analysis of real-world traffic emissions data (and not laboratory data).

Through dimensional group analysis [Stull, 1989] [Seinfeld, Pandis, 2006], we describe the resuspension rate as dependent on Schmidt number, friction velocity, particles Stokes number, asphalt bulk porosity θ and surface porosity θ_S (defined as the void area fraction around the surface of the particles in a concrete asphalt), surface roughness z_0 and average collectors diameter d_c. Resuspension rate has the dimension of $1/s$. For the case of a concrete asphalt, it can be dimensionalized as:

$$k_{res} \sim \frac{u_* z_0}{(1-\theta_S)A^2},$$

where A is a collection efficiency diameter, determined by the average grain dimension of the components of concrete asphalt. For the case of a porous asphalt, it can be dimensionalized as:

$$k_{res} \sim \frac{u_* z_0}{(1-\theta_S)(d_c)^2}$$

To determine the resuspension phenomenon dependence on physical processes in the boundary layer, we could proceed in two different ways:

- consider, as before, no surface resistance, and all processes of surface interactions with deposited road dust happening in the viscous sublayer. C_2 in figure 6 is the effective concentration c_s at the road surface. In the case of the deposition velocity, the empirical parameterization was based on the consideration of the effect of transport in the logarithmic and in the viscous layers, so it was possible to neglect the buffer sublayer resistance. For resuspension there is no available empirical parameterization, so the viscous sublayer must be joined to the bottom of the buffer layer, where the semi-empirical Van-Driest law [Wilcox, 1998] for the eddy diffusivity is valid:

  $$\nu_T = k u_* z \left(1 - e^{-\frac{z^+}{26}}\right)$$

  Particles in the buffer sublayer are transported by turbulent diffusion with a turbulent diffusivity $D_T = \nu_T$. The bottom of the buffer sublayer is at $z^+ \sim 5$ [Wilcox, 1998]. $ku_*z = \nu_{T(log)}$ is the value of eddy viscosity in the logarithmic layer; in our analytical and numerical solutions, we will start to integrate the equations from the logarithmic layer, and we will be able to express ku_*z in terms of boundary values

of other quantities (such as $ku_*z = \frac{k}{\omega}$ at the surface boundary for the $k-\omega$ turbulence model - see next chapters for details). We have at the bottom of the buffer sublayer:

$$\nu_T = \nu_{T(log)}\left(1 - e^{-\frac{5}{26}}\right)$$

Diffusion in the viscous sublayer will dipend on a dimensionless Schmidt turbulence number:

$$Sc = \frac{\nu}{D + D_T}$$

We now suppose that diffusion efficiency E_b will be expressed by the same function as those considered in the parameterization of viscous resistance r_b, being considered a universal dependence of diffusion phenomenon on the main dimensional parameters on which it scales:

$$E_b = Sc^{-2/3}$$

- apply the gradient transport theory and the mass transfer/momentum transfer similarity, in the hypothesis that at the steady state the flux across the different sublayers is constant, through buffer and viscous sublayers. The flux is given by:

$$F = C_2 \int_0^z \frac{\phi_M(\zeta)}{\nu + ku_*z\left(1 - e^{-\frac{z^+}{26}}\right)}\, dz$$

This integral is not exactly solvable, but can be approximated with a power series.

We choose to use the first method, which is simpler and more immediate. In the case of porous asphalt, filtration of particles inside the asphalt medium influence the surface pollutant concentration. To obtain the dependence on asphalt characteristics of a dimensionless factor E_f which describes filtration in asphalt medium, we use the solution of a filtration equation [Logan et al., 1995] obtained from a mass balance for a scalar c across a layer in a packed bed:

$$\frac{\partial c}{\partial t} - u\frac{\partial c}{\partial z} + D\frac{\partial^2 c}{\partial z^2} = \frac{3}{2d_c}\frac{1-\theta}{\theta}(\alpha_f \eta)uc,$$

where u is the interstitial velocity (equal to $v_d(0)$, as air velocity is supposed to be zero in the medium), D is particles diffusivity, and the term on the right represent the removal of particles by collectors: η is a collector efficiency factor, and α_f an adhesion coefficient for filtration. Neglecting diffusion and considering a stationary process, integrating over the thickness L of the porous medium both in the direction of deposition and resuspension (with an

elastic condition at the bottom side) we obtain for the effluent concentration c in terms of the incoming c_0:

$$c = c_0 E_f = c_0 exp\left[-3\frac{(1-\theta)}{d_c\theta}\alpha_f \eta L\right]$$

We can suppose that the concentration of road dust c_s at the surface boundary is reduced by a factor of E_f when filtration in a porous asphalt is ongoing. We must observe that the parameter L should depend on the accumulation of c_s inside the medium, making the E_f highly non-linear in c_s, and so introducing difficulties in analysing the boundary condition (2.4). The effect of the accumulation of road dust in the road medium is expressed by the introduction of the θ_0 term in the budget equations (2.4). The collector efficiency factor η is equal to [Logan et al., 1995]:

$$\eta = 4\left(\frac{v_d(0)d_c}{D}\right)^{-2/3} + \frac{3}{2}\left(\frac{d_p}{d_c}\right)^2$$

where the first term indicate removal by diffusion (this term can be neglected here) and the second removal by interception (the only term to be considered). The forms of resuspension rate for concrete asphalt $k_{res,c}$ and for porous asphalt $k_{res,f}$ are thus:

$$k_{res,c} = \alpha_c \frac{u_* z_0 E_b}{(1-\theta_S)A^2},$$

$$k_{res,f} = \frac{u_* z_0 E_b E_f}{(1-\theta_S)(d_c)^2}$$

The adhesion constants α_c and α_f in the resuspension rate must be adjusted in order to fit the experimental results reported in [Empa, 2009]. (A complete model should incorporate electrostatic and London-Van der Walls forces between particles and collectors to describe the attachment process. PM surface electrostatic potentials are a difficult to find, and the attachment process is here quantized through measurements). Surface roughness z_0, as represented by the International Roughness Index (IRI), is taken from [Sayers, Karamihas, 1998], for different conditions of asphalt maintenance (new, average and damaged asphalts) and for a dense bituminous and a porous asphalt. IRI is a mathematical transform of the true sampled elevation profile of a road, in units of slope $[m/k]$, which is a profile index for road roughness (intended as the deviation of a pavement surface from a true planar surface with characteristic dimensions that affect vehicle dynamics and wear processes). Different roughness indexes are associated with different wavelengths associated to a spectral decomposition of the elevation profile. To obtain the IRI value, the profile is filtered with a moving average

(low-pass filter) with a $250mm$ base lenght. Successive filters are applied to correlate the profile index to the output of response-type road roughness measuring systems (for example devices which measure the suspension deflection of simulated passenger cars). Concrete and porous asphalt profiles show different undulations and different power spectra, but can have similar IRI. IRI is influenced by wavelengths ranging from $1,5$ to 30 m (corresponding to the peaks in power spectra of elevation profiles of a porous and a bituminous asphalt respectively, considering the range of wavelengths passed after applying the IRI filters). We multiply IRI values by a wavelength relevant to deposition and resuspension processes ($1m$), with a weight factor determined by the relative intensities of power spectra of the true elevation profiles (i.e. with no filter applied, as reported in [Sayers, Karamihas, 1998] for a typical porous and concrete asphalt) at that wavelenght to obtain z_0. Values for different asphalt types will be reported in the next paragraph. The parameter L, which describes the depth of the porous medium in which the deposited particles filter, can be defined by means of the lift-thickness parameter [Blades, Kearney, 2004], introduced as the depth of the porous asphalt wear layer, whose value is approximately four times the diameter of the nominal top size asphalt aggregate (when the minimal requirements on the porous asphalt permeability are satisfied [Hardiman, 2004]). The surface porosity θ_S is calculated from the bulk porosity θ as in [Ouchlyama, Tanaka, 1984], For the particular case of the packing of uniformly sized spheres:

$$\theta = 1 - \frac{1}{8}\left[1 + \frac{13}{2}(1 - \theta_s)\right]$$

For the case of dense asphalts (such as asphalt concrete), the resuspension factor depends only on θ_S, which can be calculated by the nominal value of the bulk porosity θ given in the asphalt technical papers [SPENS, 2009]. In this sense we consider the bulk porosity as not defined for an asphalt concrete.

2.4 Asphalt parameters and characteristics

A range of asphalt based and concrete based road surfaces are in use throughout Europe, with block paving being used in many urban areas. Concrete surfaces are composed of coarse aggregate, sand and cement. Asphalts are mixtures of mineral aggregate, sands, filler, and bitumen binder, though the composition can vary widely both from country to country and within countries. Generally, the stone content is around $90 - 95\%$ and the bituminous binder around $5 - 10\%$. The properties of asphalt can be modified by additives such as adhesives, polymers, and different types of filler.

In this work we consider four types of asphalt mixtures:

- AC11: this is an asphalt concrete mixture. AC11 is the asphalt mixture

constituting the road surface in the urban canyon frame considered in Ref. [Empa, 2009].

- PA11: this is a porous asphalt mixture. PA11 is the asphalt mixture constituting the road surface in the freeway frame considered in Ref. [Empa, 2009].

- Porous asphalt obtained by a grading design as in [Hardiman, 2004]. In [Hardiman, 2004] a grading design is obtained by firstly varying the percentage of aggregate with maximum size of 20, 14, 10 and 5 mm, and compacting the aggregates, in order to achieve a minimum dry aggregate porosity and a stable aggregate matrix. Fine aggregate fractions are then added, with a binder content of $4,5\%$, in order to achieve a target porosity and Marshall stability and permeability requirements. We consider a porous asphalt mixture constituted by the stable coarse aggregates matrix.

- Optimal porous asphalt. We consider a stable coarse aggregate matrix, as found in [Hardiman, 2004], and consider the addition of fractions of fine aggregates, in order to reduce porosity while keeping the average grain size as high as possible; this leads to the minimization of the value of the resuspension factor. The porosity depends on the coarse component and the fine aggregate fractions by means of a random packing theory of spherical spheres with discrete size distribution $d_i = 1, \ldots, n$, with fractions f_i relative to each component of the mixture and average size $\bar{d}$ [Ouchlyama, Tanaka, 1984]:

$$\theta = 1 - \frac{\sum_{i=1}^{n} d_i^3 f_i}{\sum_{i=1}^{n} (d_i - \bar{d})^3 f_i \; + \frac{1}{\bar{n}} \sum_{i=1}^{n} [(d_i + \bar{d})^3 - (d_i - \bar{d})^3] f_i}$$

where:

$$\bar{n} = 1 + \frac{4}{13}(7 - 8\theta_*)\bar{d} \frac{\sum_{i=1}^{n} (d_i + \bar{d})^2 \left(1 - \frac{3}{8}\frac{\bar{d}}{\bar{d}+d_i}\right) f_i}{\sum_{i=1}^{n} [d_i^3 - (d_i - \bar{d})^3] f_i}$$

θ_* is the porosity value obtainable in the packing of uniformly sized spheres, which, for a random packing, is equal to $0,399$. We must observe that such an aggregate may not satisfy Marshall stability requirements; in this case it should be necessary to use emulsion binders to increase the stability properties of the aggregate [Blades, Kearney, 2004], which should cause a raise in the asphalt production costs.

To calculate z_0 of the two design mixtures, we observe that by increasing the values of the average diameter of the particles composing the mixture (without changing surface porosity), IRI, and so surface porosity, increases by the

same amount [Sayers, Karamihas, 1998]. This increase must be weighted by the relative values of surface porosity between the design mixture and the reference mixture (PA11). θ_0, the maximum capacity of road dust concentration entrainment of the surface, can be calculated as the total mass of road dust which can be entrained in a volume $1[m^2] * (L + z_0)[m])$ of road, considering the obstruction to entrainment in the total volume at disposal by interception of road dust particles to asphalt collectors (expressible as the ratio of their diameters, as expressed previously):

$$\theta_0 = (\theta L + \theta_s z_0)\left(\frac{d_p}{d_c}\right)\rho_p$$

The term θL should not be considered for a concrete asphalt. In the next Table we show the values of the parameters for the different types of asphalt.

	θ	z_0 good $[mm]$	z_0 damaged $[mm]$	d_C max $[mm]$	d_C average $[mm]$	θ_0 good $[mg/m^2]$	θ_0 damaged $[mg/m^2]$
CA11	$0,05$	$1,26$	$4,00$	$8,00$	$5,43$	$59,06$	$187,51$
PA11	$0,25$	$2,18$	$6,00$	$11,20$	$9,89$	$19552,88$	$21025,71$
Design	$0,35$	$2,28$	$6,00$	$20,00$	$12,55$	$37953,03$	$39687,27$
Optimal	$0,26$	$2,08$		$20,00$	$12,50$	$28178,00$	

Note that the maximum capacity of road dust for a porous asphalt is greater than the largest dust loads measured in the proximity of demolition/construction sites in Barcellona (reported in Section 2.2). Considering road dust initial concentration loads for urban and extra-urban streets with the same values as those measured in Zurich (which vary in the range $0,2 - 3mg/m^2$), we should not be aware of surface dust overload, in which case we should change the modelization for the dynamical budget (2.4).

2.5 Non-Exhaust estimates in literature

In literature there is an empiric model, developed by the US-EPA, called "Paved Roads", which estimates the quantity of particulate emissions from resuspension of loose material on the road surface, due to vehicle travel on a dry paved road, using the following empirical expression:

$$E = k(Sl)^{0,91}(W)^{1,02}$$

where E is the particulate emission factor (in units $[gv^{-1}/km]$); k is a particle size multiplier for particle size range ($0,62[gv^{-1}/km]$ for PM10; $0,15[gv^{-1}/km]$ for PM2.5); Sl is road surface silt loading; W is the average weight of the vehicles traveling the road. In [Giovannini, Grechi, 2003]

Source	Quantification	Method	EF Fleet mgv^{-1}/km	EF LDV mgv^{-1}/km	EF HDV mgv^{-1}/km
PM10	Measures	CMB	71	24 ± 8	498 ± 86
Brake wear	PMF	MR	15	8 ± 4	81 ± 39
Exhaust	PMF	MR	29	15 ± 6	155 ± 67
Resuspension	PMF	CMB	27	1 ± 11	262 ± 115
Road wear	MLS			$< 3_{a,d}$	$7_a\, 80_b$
Resuspension	MLS			$5_d\, 76_a$	$110_c\, 660_b$

Table 9: Emission Factors (EF) for the individual sources of traffic-related PM10 for the urban canyon case in Zurich. $_a$ = AC new; $_b$ = bad condition AC; $_c$ = good condition AC; $_d$ = PA new. PMF = Positive Matrix Factorization; CMB = Chemical Mass Balance; MR = Multilinear Regression. Fleet is 10% HDV

results are reported of the application of the "Paved Roads" model to the estimation of the resuspension contribution to traffic-related PM10 emission in the Florence urban area (year 2000). The result was that $\sim$ 60% of all traffic-related emissions was emitted by resuspension process.

In the context of the APART project [Empa, 2009], evaluation of non-exhaust contributions to traffic-related PM10 tailpipe emissions have been conduced for different street configurations and vehicle categories. In table 9 we show the results for the estimation of the tailpipe emission factors for the individual sources valid for a urban street canyon with heavy traffic in Zurich, and for different type of asphalts in the mobile load simulator (MLS) experiments, with the indication of the method adopted to obtain them.

In this case 38% of fleet-related PM10 tailpipe emissions comes from resuspension; resuspension fraction of total emissions is 4% for the LDV and 53% for the HDV case. These difference in resuspension fractions for the LDV and the HDV cases is due to the fact that road dust is resuspended and kept suspended in the atmosphere mainly by HDV generated turbulence, and LDV resuspension emissions are limited by the low road dust concentration deposited on the road surface. The $mg\, v^{-1}/km$ unit is not the most appropriate unit to define the resuspension emission factor; the most appropriate unit would be mg/sm^2.

In Table 10 we show the results for the estimation of the tailpipe emission factors for the individual sources valid for an extra-urban freeway (Reiden), with the indication of the method adopted to obtain them.

In this case 55.8% of fleet-related PM10 tailpipe emissions comes from resuspension; resuspension fraction of total emissions is 56% for the LDV and 55.6% for the HDV case. A quantification of the resuspension factor associated to the resuspension process was not possible, due to the lack of a chemical profile analysis of the road dust deposited on the road surface

Source	Quantification	Method	EF Fleet mgv^{-1}/km	EF LDV mgv^{-1}/km	EF HDV mgv^{-1}/km
PM10	Measures	MR	86	50 ± 13	288 ± 72
Brake wear	PMF	MR	3	$1,6 \pm 1,1$	9 ± 7
Exhaust	PMF	MR	35	$20,4 \pm 7$	119 ± 38
Unexplained (Resuspension)		CMB	48	28 ± 14	160 ± 82

Table 10: Emission Factors (EF) for the individual sources of traffic-related PM10 for the freeway case in Reiden. PMF = Positive Matrix Factorization; CMB = Chemical Mass Balance; MR = Multilinear Regression. Fleet is 15% HDV

for the case of the freeway in Reiden. In order to investigate the influence of asphalt porosity on the resuspension phenomenon, a quantity of $10g$ of sampled road dust has been placed on an AC and on a PA asphalt before the start of a road simulator ride. In Figure 7 we show a comparison between PM10 emission factors profiles in time for the two cases.

The graphs show that resuspension emission is dominant for at least the first 30 minutes. The emission factor in the case of the AC asphalt are greater than those relative to the PA case: a porous surface retain the deposited road dust more efficiently than a dense (concrete) one. We will show in next paragraphs how resuspension is affected by asphalt parameters in the context of our modelization.

2.6 Tailpipe emissions for urban and extra urban driving cycles

We now introduce a model to determine the tailpipe emissions of traffic-related PM10 for particular traffic configurations. Total traffic-related PM10 emission factors (E_{tot}, in $\frac{mg}{hours \cdot km}$) at the tailpipe are given by:

$$E_{tot} = E_{exhaust} + E_{wear} + E_{resusp},$$

The exhaust emissions are expressed as a sum of the contribution from the thermal stabilized phase of engine operation (E_{hot}) and from the engine warming phase (E_{cold}).

$$E_{hot,jk} = N_j e_{hot,jk},$$

where $E_{hot,jk}$ is the total hot emission at the tailpipe relative to a vehicle of category j on a road branch of type k; N_j is the number of vehicles of category j per hour on the road branch k; $e_{hot,jk}$ is the hot PM10 emission factor in mg/km depending on vehicle category and road type, determined

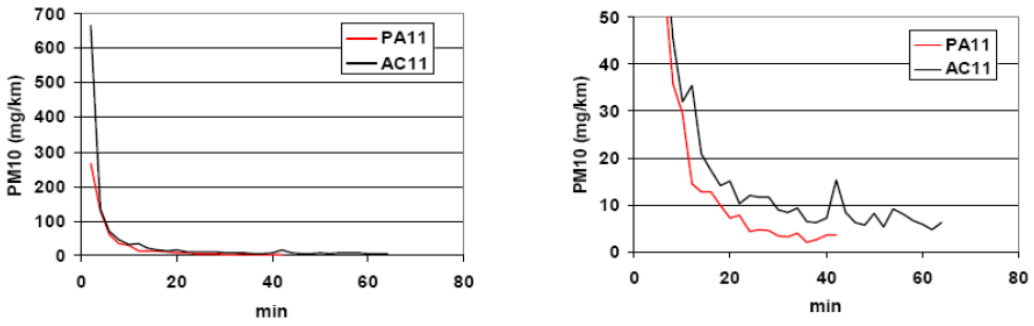

Figure 7: Road dust resuspension emission factors *vs* time in the case of road simulator ride on AC11 and PA11 asphalts. Left panel: graph at full scale. Right panel: zoom on the y axis.

through EMEP-CORINAIR emissive methodology, as expressed in Section 2.1. A sum on all j categories must be performed in order to obtain the total exhaust emissions per hour on a road branch of type k. Multiplying these emission factors by the length in km covered by vehicles of category j on arch type k, M_k, and summing on all arch types composing a typical driving cycle or real traffic data, we would obtain the total hot exhaust emission factor in mg/h:

$$E_{hot,jk} = N_j M_k e_{hot,jk}.$$

For the engine warming phase contribution:

$$E_{cold,jk} = \beta_j N_j e_{hot,jk} \left(\frac{e_{cold}}{e_{hot}} \bigg|_j - 1 \right),$$

where $E_{cold,jk}$ is the total cold emission at the tailpipe in $\frac{mg}{hkm}$ relative to a vehicle of category j on a street arch of type k; β_j is the fraction of the vehicle route driven in the warming phase of the engine. The β parameter depends on ambient temperature and on trip length with specified functions. An average trip length must be used when we are not working with a specific driving cycle, in which total trip mileage for a single vehicle is known. A European value of $12,4km$ has been established for the average trip length value [EMEP/CORINAIR, 2007]. Cold start over-emission is attributed to urban driving only. The correction factor $\frac{e_{cold}}{e_{hot}}\Big|_j$ is determined for each vehicle category through EMEP-CORINAIR emissive methodology.

E_{wear}, in $\frac{mg}{hkm}$, is calculated by summing the emission contributions from each wear process $i = 1, 2, 3$, corresponding to tyre, brake and asphalt wear processes:

$$E_{wear,ijk} = N_j e_{wear,ijk} f_{air,i}$$

$e_{wear,ijk}$ values are given through EMEP-CORINAIR methodology, depending on vehicle velocity and category, road type and asphalt conditions, as expressed in Section 2.2. $f_{air,i}$ is the fraction of wear emission which is airborne, whose value for each wear process is reported in Section 2.2. The resuspension emission factors, in $\frac{mg}{hkm}$, are given by:

$$E_{resusp,jk} = N_j r_{s,jk} P_d(t) = r_{s_{tot},jk} P_d(t),$$

where $r_{s,jk}$ is the fraction of road dust that is resuspended due to the passage of one vehicle. $N_j r_{s,jk} = r_{s_{tot},k}$ is the total resuspension rate (in $1/h$) due to the passage of all vehicles of category j (summing on all j) for a given road type k. The fraction of road dust that is resuspended due to the passage of one vehicle in $1h$ is related to the emission rates (in $1/s$) introduced in equation (2.4) by the relation:

$$r_{s,jk} = k_{res,jk} \left[\frac{1}{s}\right] \cdot 3600[s]$$

The resuspension emissions depend on the quantity of road dust available at the road surface $P_d(t)$ for a given road framework. To obtain the linear concentration $P_d(t)$ in mg/km it's necessary to multiply the road dust concentrations, as reported in [Empa, 2009] in mg/m^2, by a factor $1000 \cdot W$, where W is the width of the road (in m). To determine the evolution in time of road dust quantity for each road type, we recall equation (2.4), and solve a balance equation:

$$\frac{dP_d(t)}{dt} = \frac{P_k}{\theta_0}(\theta_0 - P_d(t)) - r_{s_{tot},k} P_d(t),$$

where P_k is the road dust production term, expressed as the fraction of wear emissions from each vehicle that are not directly emitted in air but deposited on road surface plus a deposition component:

$$P_k = N_j e_{wear,ijk}(1 - f_{air,i}) + \ deposition$$

The solution of this equation is (in mg/km):

$$P_d(t) = \frac{P_k \theta_0}{P_k + r_{s_{tot},k}\theta_0} + \left[P_d(0) - \frac{P_k \theta_0}{P_k + r_{s_{tot},k}\theta_0}\right] exp\left[-\left(\frac{P_k}{\theta_0} + r_{s_{tot},k}\right)t\right] \tag{2.5}$$

At the equilibrium, the stationary road dust concentration (in mg/km) for a road framework of type k is:

$$P_d(t) = \frac{P_k \theta_0}{P_k + r_{s_{tot},k}\theta_0} = \frac{E_{resusp,jk}}{r_{s_{tot},jk}} \tag{2.6}$$

From equation (2.5) or (2.6) we can calculate the values of the adhesion constants α_c and α_f in the resuspension rates $k_{res,c}$ and $k_{res,f}$, by considering experimental data and numerical results. In [Empa, 2009] road wear and road dust emission rates were derived from measurements with two different types of mobile load simulators on different types of road pavement (asphalt concrete, porous asphalt) with different conditions of conservation. The experimental set-up allowed for a separate characterisation of the emissions caused by fresh in-situ abrasion and by resuspension of previously deposited dust. These estimates are more accurate than specific quantification of PM10 emissions due to abrasion and resuspension from road pavement obtained by PMF analysis on roadside measurements. Equation (2.5) should be applied to the time profile of road dust emission rates obtained during the operation of road simulators; unfortunately, no measurement on initial road dust concentrations was taken in the experiment, and equation (2.5) cannot be applied to identify the values of the adhesion constants in the emission rates. Another approach is to consider the application of equation (2.6) to data coming from roadside measurements in the urban canyon and in the freeway case. Data on road dust concentrations, averaged between the values obtained at different samples at each site (8 primary and secondary roads in the urban area of Zurich have been considered to sample and analyse deposited road dust concentrations) for three consecutive days at the end of a dry period, show an overall stationarity of average values. Road dust analysis has not been performed for the case of the freeway; anyhow, a secondary road framework in Zurich with similar traffic regime, the same porous asphalt and similar street geometry as the freeway case has been considered for road dust sampling (Hardstrasse). We use the value of stationary road dust concentration relative to this secondary road site in Zurich as the value of the stationary concentration in the freeway case. Data of resuspension emission factors for LDV and HDV, traffic statistics and street geometry are reported in [Empa, 2009] for the two cases. We summarize them in Table 11.

Let us rewrite equation (2.6) as:

$$EF_{resusp,jk} N_j = PC_d(t) \cdot 1000 \cdot WN_j(k_{res,jk}) \cdot 3600,$$

where $EF_{resusp,jk}$ is the resuspension emission factor (in $[mg/km]$) as expressed in Table 11 for vehicle category j and road type k, and $PC_d(t)$ is the stationary road dust concentration, in mg/m^2, for each road type.

Let us start from the Urban case. We consider the HDV resuspension

Street type	Width m	Asphalt	Traffic statistics $[v/h]$	Road dust $[mg/m^2]$	Resuspension emission $[mg/km]$
Urban	20	AC11 Bad condition	LDV: 1132$[v/h]$ HDV: 96$[v/h]$ $v = 30[km/h]$	3	LDV: 1 ± 11 HDV: 262 ± 115
Extra Urban	24 4 lanes	PA11 New	LDV: 2550 $[v/h]$ HDV: 310 $[v/h]$ $v = 120[km/h]$	$0,5$	LDV: 28 ± 14 HDV: $160 \pm 81,8$

Table 11: Data of resuspension emission factors for LDV and HDV, traffic statistics and street geometry for the Urban and Extra-Urban cases.

emission, since it has a lowest relative error derived from the PMF analysis. Substituting values and expressions, we have:

$$261,8\left[\frac{mg}{km}\right] = 3\left[\frac{mg}{m^2}\right] \cdot 1000\left[\frac{m}{km}\right] \cdot 20[m]\left(\alpha_c \frac{u_* z_0 E_b}{(1-\theta_S)A^2}\left[\frac{1}{s}\right] \cdot 3600[s]\right)$$

We need to know the average value of the factor $u_* E_b$ for an HDV vehicle flowing at $30km/h$ in a canyon street (in urban dryving cycle) in order to obtain the value of α_c. We suppose that the average resuspension effect induced by the vehicle is determined mainly inside its near-wake. We can define the following average value, obtained as a result of our turbulence simulations (see Chapter 4):

$$\frac{1}{W l_\omega}\int_\omega u_* Sc^{-2/3}\, dxdy = 5,3129\left[\frac{m}{s}\right] \qquad \text{from simulations}$$

where the integral is over the road surface in front, under and behind the vehicle extending for the lenght of its developed near-wake (indicated as ω in the domain of integration), and l_ω is the longitudinal dimension of the domain (considered as 8 times the vehicle length behind the vehicle, and 1 time the vehicle length in front of it). Considering the values of z_0, θ_s and A for an AC11 in bad condition, as reported in Section 2.4, we obtain:

$$\alpha_c = 1,676 \cdot 10^{-9} \tag{2.7}$$

Note that in this case the resuspension rate and the sticking rate of road dust to the vehicle tyres are:

$$k_{res,c} = 1,21 \cdot 10^{-6}[1/s]$$
$$f_x n_v = 10,4 \cdot 10^{-6}[1/s]$$

The sticking rate to tyre surfaces is dominant over the resuspension rate in removing deposited road dust. We must observe that we are considering HDV vehicle moving at $30\,km/h$. For an HDV moving at $100\,km/h$ the average value of $u_* E_b$, calculated in the context of our turbulence simulations, is equal to $41,86\,[m/s]$, so that $k_{res,c} = 9,56 \cdot 10^{-6}$, and become comparable to tyre sticking rate. (All these conclusions are to be intended as order of magnitude estimates, since measures are lacking and incomplete). From equation (2.6) we can estimate an average deposition rate in the given road framework. We have:

$$P_d(t) = \frac{(\sum_{ij} N_j e_{wear,ijk}(1 - f_{air,i}) + \ deposition)\theta_0}{(\sum_{ij} N_j e_{wear,ijk}(1 - f_{air,i}) + \ deposition) + (\sum_j N_j k_{res,jk} \cdot 3600)\theta_0}$$

Substituting the values for θ_0 relative to a damaged AC11 asphalt, values for wear emission processes estimated through the PMF analysis of data measurment (with the associated f_i factors), data on traffic counting and on the average resuspension factor for both LDV and HDV vehicles moving at $30\,km/h$, we obtain:

$$deposition\left[\frac{mg}{km\,h}\right] = 11251$$

The deposition rate is comparable with the component of P_k coming from wear processes, which in this case is $\sum_{ij} N_j e_{wear,ijk}(1 - f_{air,i}) = 13954 \frac{mg}{km\,h}$.

Let us now consider the Extra-Urban case, and the LDV resuspension emission.

$$28\left[\frac{mg}{km}\right] = 0,5\left[\frac{mg}{m^2}\right] \cdot 1000\left[\frac{m}{km}\right] \cdot 24[m]\left\{\frac{u_* z_0 E_b \exp\left[-3\frac{(1-\theta)}{d_c\theta}\alpha_f \eta L\right]}{(1-\theta_s)(d_c)^2}\left[\frac{1}{s}\right] \cdot 3600[s]\right\}$$

The average value of the factor $u_* E_b$ for an LDV vehicle flowing at $120 km/h$ in an open street framework (in extra-urban dryving cycle) is:

$$\frac{1}{W l_\omega}\int_\omega u_* Sc^{-2/3}\,dxdy = 10.2051\left[\frac{m}{s}\right] \qquad \text{from simulations}$$

We note that this value is lower than the value associated to an LDV vehicle moving at $120 km/h$ in a street canyon (due to urban driving cycle and canyon geometry): $u_* E_b / W l_\omega = 11.5167[m/s]$. Considering the values of z_0, θ, θ_s and d_c for a new PA11, as reported in Section 2.4, we obtain:

$$\alpha_f = 606193 \tag{2.8}$$

Note that in this case the resuspension rate and the sticking rate of road dust to the vehicle tyres are:

$$k_{res,c} = 6,48 \cdot 10^{-7}[1/s]$$
$$f_x n_v = 27,6 \cdot 10^{-5}[1/s]$$

The sticking rate to tyre surfaces is high and dominant over the resuspension rate in removing deposited road dust due to the high vehicle frequency (heavy traffic). We should point out that the estimates of the f_x term in [Patra et al., 2008] are obtained in the context of the analysis of roadside data for a urban primary road in London with heavy traffic, and don't distinguish between LDV and HDV. By considering HDV moving at an average velocity of $90km/h$ in the freeway (open street geometry), $u_* E_b = 24,41\,[m/s]$, we can substitute in the formula for $k_{res,c}$ (with the α_f just calculated), and compare the two rates for the HDV case:

$$k_{res,c} = 6,08 \cdot 10^{-6}[1/s]$$
$$f_x n_v = 3,36 \cdot 10^{-5}[1/s]$$

We highlight the fact that by calculating $k_{res,c}$ by starting with the data of HDV resuspension emission rates in equation (2.6), we obtain $k_{res,c} = 3,70 \cdot 10^{-6}[1/s]$. A propagation of the errors associated to the data given in [Empa, 2009] shows that this value and the value calculated from the α_f determined with LDV data have overlapping intervals of confidence. Calculation of the deposition rate is not possible for the extra-urban case, as a separation of road dust emission between a resuspension component and road wear component is not available.

With different vehicle velocities the resuspension factors $k_{res,c}$ and $k_{res,f}$, for each vehicle category and for different driving conditions, (which has been determined here for the reference velocities of traffic condition analysed in the experiments in [Empa, 2009]), vary according to power laws, (determined by our numerical simulations results by considering the variation of the term $u_* E_b$ with vehicle velocity), introduced in Section 4.3. We write:

$$k_{res,jk} = k_{res,jk(ref)} \left(\frac{v}{v_{ref}} \right)^{n_{jk}} \tag{2.9}$$

and this must be substituted in the form of $E_{resusp,jk}$ in the tailpipe emission model.

The tailpipe emissive model

$$E_{tot} = E_{exhaust} + E_{wear} + E_{resusp}$$

has been applied to estimate traffic-related PM10 emission contributions, from each traffic source, in the case of the typical urban and extra-urban

Road dust resuspension factor	*SV*	*LDV*	*HDV*
Extra Urban cycle	40 %	46 %	48 %
Urban cycle	26 %	38 %	53 %

Table 12: Resuspension factors of Road dust as percentage of the total traffic - related PM10 emissions in a typical urban and extra - urban guide cycles for SV, LDV and HDV.

driving cycles. Data on traffic statistics are reported in [André, 2004], and briefly summarised in Table 5. We use as initial data of road dust concentration, for urban and extra-urban roads, the values sampled in APART project for the Urban and the Extra-Urban case, and consider AC11 asphalt in good condition for urban and PA11 in good condition for extra-urban streets. The velocity variations of the moving vehicles and traffic densities influence the emission processes as explained previously. We show in Table 12 only the resuspension emissions percentage of the total tailpipe PM2.5 + Road Dust traffic related emissions. Details on the emission rates values, in $[mg/h]$, will be shown for the case of Milan in Section 2.8 .

We see from these results how resuspension emission is an important process to determine the traffic-related PM10 concentrations at urban scale. These data are in line with the measurements and the phenomenological model already described [Empa, 2009] [Giovannini, Grechi, 2003]. Sedan resuspension factor is lower than that of LDV and HDV vehicles, in line with results in [Empa, 2009], previously reported. The reason is that much of the available road dust is kept in resuspension by turbulence generated by LDV and mainly HDV (The mass budget for $P_d(t)$ in the tailpipe emission take in consideration all the contributions from SV, LDV and HDV vehicles at a time). This effect is greater in the case of Urban guide cycle, where interactions between turbulent wakes must be taken into account. For extra urban guide cycle the wake of the vehicles are considered non-interacting, and moreover open road conditions enhance deposition of resuspended road dusts.

2.7 Preventive and mitigative reduction strategies

Different reduction strategies of the total quantity of traffic-related PM10 emissions are being employed by legislators, in different urban contexts. We can distinguish between preventive and mitigative reduction strategies. Mitigative measures aim at reducing the impact of traffic-related urban pollution by lessening PM10 concentrations already emitted in urban air. These can consist in traffic control and traffic pollution charges, in street surfaces washings and in other control measures on the existing PM10 urban sources.

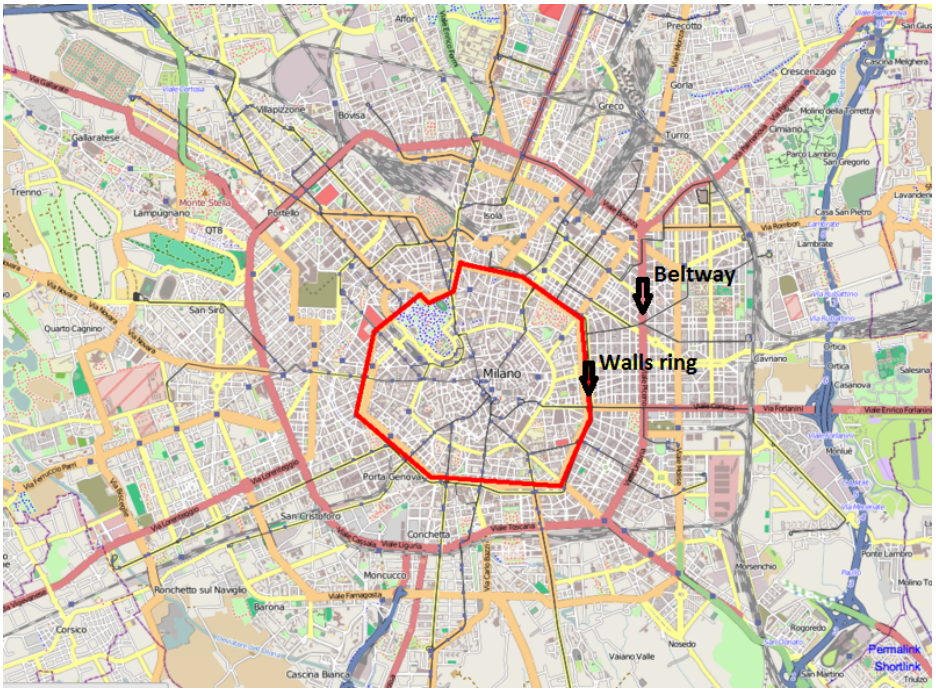

Figure 8: Map of the urban centre of Milan. ECOPASS area (inside the red contour) occupies a surface of $8,2km^2$. The total urban surface is $181km^2$.

Preventive measures aim at reducing the impact of traffic-related urban pollution by proper design technologies which ensure lower emission loads of urban sources before they are emitted.

The effect of cyclic road washings with pressurized water and mechanical sweeping washing actions has been studied in [Amato et al., 2009], carried out in one of the busiest roads of the city centre of Barcelona during hours at night. It has been found that these actions correspond to a reduction of road dust initial concentration at morning of 93% of the total. An example of a mitigative strategy consisting of traffic control is the Ecopass urban toll, implemented in Milan. ECOPASS is a traffic-congestion charge (through toll-pay barriers), in force since january 2008, extended to the urban area within the city's ancient Walls ring, which imposes an entry toll to drivers of private vehicles of the most pollutant technologies, in order to enter a traffic-limited zone inside the center of Milan, delimited by an ECOPASS (the Bastioni) circle. In Figure 8 we show a topographic map of the urban centre of Milan, with evidence of the traffic-limited zone (red ring). Effects of this reduction strategy will be derived in the next Section.

An example of a preventive reduction strategy for traffic exhaust emissions is the design of new engine technologies in order to comply with the European legislation on air pollution. As a possible preventive reduction strategy for traffic non-exhaust emissions, we consider the choice of opti-

mal geometric parameters of the asphalt in order to minimize resuspension factor. The resuspension factor, as written in Section 2.3, is a function of the geometric parameters: bulk porosity θ, surface porosity θ_S, average diameter of asphalt grains (asphalt aggregate) d_c and surface roughness z_0. These parameters can vary in an asphalt according to the aggregate grading, the different technology used to compact and bind asphalt grains and to the maintenance condition of the asphalt surfaces (a damaged asphalt has a greater z_0). We choose the values of these parameters which characterize AC11, PA11, design and optimal asphalts as introduced in Section 2.4 . In order to characterize the resuspension factor dependence on asphalt parameters, let's define the quantity R_{AB}, which is the percentage of reduction of the road dust resuspension factor when changing two different types of asphalt (from A to B). Table 13 shows the values of R_{AB}, considering a dense asphalt (concrete asphalt AC11), two porous asphalts characterized by two different values of bulk porosity θ (a porous asphalt PA11, with $\theta = 0,25$, and a porous asphalt obtained by a grading design, with $\theta = 0,35$), and an optimal asphalt, as introduced in paragraph 2.4. Different conditions of asphalt maintenance (asphalt in good condition and damaged asphalt, expressed in terms of different values of surface roughness z_0), are considered.

Asphalt A	*Asphalt B*	*good*	*damaged*
concrete	$\theta = 0,25$	$R_{AB} = 33,4\%$	$R_{AB} = 42,3\%$
$\theta = 0,25$	$\theta = 0,35$	$R_{AB} = 22,6\%$	$R_{AB} = 26,0\%$
$\theta = 0,25$	*optimal*[a]	$R_{AB} = 39,2\%$	
$\theta = 0,35$	*optimal*[a]	$R_{AB} = 21,4\%$	

Table 13: R_{AB} for different kinds of asphalt and different conditions of asphalt maintenance. [a]For optimal asphalts we consider only good conditions of maintenance.

According to the results obtained in [Empa, 2009] and shown in figure 7, the resuspension factor for a porous asphalt is smaller than that for a concrete asphalt by a factor of $\sim 40\%$. Changing a damaged into a good-condition AC asphalt, a resuspension factor reduction of $\sim 76\%$ has been obtained. This is in accordance with results obtained in road simulators experiments for an HDV vehicle in [Empa, 2009] and reported in Table 9: HDV resuspension emission rate for an AC asphalt in bad condition is reduced by a factor of 83% when passing to a good condition AC11 asphalt. This is an important check of our parametrization of the resuspension factor in function of geometrical parameters of the asphalt.

2.8 Application to the case of Milan

Lastly, we apply the tailpipe emissions analysis to typical traffic situations in the city of Milan, relying on data provided by the Agenzia Mobilità Ambiente Territorio (AMAT), [AMAT, 2008], [AMAT, 2010], and studying the effect of implementations of different reduction scenarios to the total amount of traffic-related PM10 emissions. Vehicular traffic data collected by AMAT [AMAT, 2008] are available until the 2006 inventory. These data give a synthetic description of the Milan road network, constituted by an oriented graph, determined by road branches between net junctions. For each road branch are specified the following data:

- length
- road branch typology (highway, principal or secondary road, local road)
- jurisdiction
- free stream velocity along the road branch
- road branch capacity in equivalent vehicles
- free stream curve parameters

Data are given on traffic fluxes in terms of equivalent vehicles per hour for different time slots, distinguished between light vehicles (sedan vehicles and motor cycles) and heavy vehicles (heavy trucks). Throughout equivalence coefficients, specified by AMAT in its vehicle counting methodology, and data on vehicle fleet relative to Milan, we obtain the number of vehicles per category and technology passed along the road branch. Free stream curve can be used to obtain the effective velocity of vehicles.

Here we show a sample data analysis on traffic counting data for a given road branch inside the Bastioni circle for the year 2006, for a typical weekday in the morning rush hour ($7:30-8:30$ am). Let us first notice that the Milan road network description given in AMAT files is constituted by data on more than 23000 road branches, and total traffic counting for a weekday rush hour covers, when compared with AMAT statistical investigation on people mobility in Milan areas [AMAT, 2008], ~ 70 % of all people mobility. Raw data from AMAT counting are in the format given in Table 14, where, together with the identification numbers of junctions determining the road branch, the numbers of equivalent LV, HV and total fleet vehicles (EV) per hour are given. V is the free-stream velocity, C the road branch capacity in equivalent vehicles; $dist$ is the length of the given road branch; α and β are the free-stream curve parameters. The equivalence coefficients are reported in the Table 15, where LDV truck stands for a weight smaller than 3,5 tons; HDV truck for a weight smaller than 7,5 tons; Truck trailer for a weight

Node A	**Node B**	**LV**	**HV**	**EV**	**type**	**V** (km/h)	**C**	**dist** (km)	α	β
31055	31256	317	63	376	secondary	40	601	0,23	1,46	3

Table 14: AMAT counting data

LV	*Motorcycle*	*Motor vehicle*	*LDV truck*
	0,7	1	1
HV	*HDV truck*	*Truck trailer*	*Bus*
	1,5	2	2

Table 15: equivalence coefficients

more than 7,5 tons.
From data on vehicle fleet composition in the city of Milan, relative to 2006, we obtain the percentages of vehicles per category and engine technology. In Table 16 we report the data on vehicle category composition.

Motor vehicles	**Motorcycles**	**LDV trucks**	**HDV trucks**	**Trucks trailer**	**Buses**
$78,71\%$	$13,88\%$	$6,21\%$	$0,22\%$	$0,68\%$	$0,29\%$

Table 16: percentages of vehicles per category for the year 2006 in the city of Milan

Data on engine technologies composition has been extrapolated as well. From the percentages of vehicle categories in fleet composition we can extrapolate the "average" proportions of vehicle categories in a single vehicle counting along a road branch. For the case of LV counting, proportions of Motor vehicles (Mv), Motorcycles and LDV trucks can be expressed as:

$$\textbf{Motor vehicles}/1 = \textbf{Motorcycles}/0,17 = \textbf{LDV trucks}/0,08.$$

For the case of HV counting, proportions of HDV trucks, Truck trailers and Buses can be expressed as:

$$\textbf{HDV trucks}/0,32 = \textbf{Truck trailers}/1 = \textbf{Buses}/0,43.$$

From the number of LV equivalent vehicles ($\#LV$) we can get the number of total Motor vehicles ($\#Mv$) by considering the previous proportions and the equivalence coefficients:

$$\#Mv = \left(\frac{\#LV}{1+0{,}08+(0{,}7*0{,}17)}\right)$$

From this number ($\#Mv$) we can get the numbers of total LDV trucks and Motorcycles multiplying by the proportions introduced previously. The same goes for the analysis of HV equivalent vehicles data. In Table 17 we show the data elaboration conduced on the given road branch data.
Multiplying the data of vehicles counting relative to the rush hour of the morning by the temporal expansion coefficients, we obtain the number of vehicles per hour for the three different reference time slots for a typical weekday. The temporal expansion coefficients are reported in Table 18.
From free-stream curve we obtain the effective velocity v_{eff} of vehicles along the road branch. Free-stream curve is the relation:

$$v_{eff} = V(1 - \alpha\left(\frac{\#EV}{C}\right)^{\beta}),$$

where V is free-stream velocity, C is the road branch capacity and $\#EV$ is the number of equivalent vehicles counted. For the case of the given road branch analysed here, $v_{eff} = 25,7\, km/h$.

Starting from the traffic data for a typical weekday in the year of 2006, we obtain, using ECOPASS monitoring data [Automobile Club Italia, 2010], a suitable description of traffic conditions during the time of application of the ECOPASS toll. Toll-free private vehicles are gasoline vehicles with technologies Euro III, IV and V; diesel vehicles with Euro IV and V with Anti Particulate Filter; hybrid vehicles, electric vehicles, GPL and Methane engined vehicles; motorcycles.

ECOPASS monitoring data, divulged by AMAT, give, for the year of 2010, the traffic reduction scenario inside the ECOPASS area given in the Table 19.
Considering data on vehicle fleet composition for the year of 2010, and considering traffic variations induced by the application of ECOPASS toll on the road branches inside ZTL and on those crossing the Bastioni circle, we can update traffic data relative to a typical weekday for the year of 2006. We add the amount of toll-subjected vehicles removed from the road branches crossing the Bastioni circle to those passing along and around the Bastioni circle (which automatically increases traffic congestion on the latter road branches), in order to conserve traffic fluxes. In the case of the particular road branch considered, which is inside the ZTL, the new traffic data are reported in Table 20.
Data on vehicles technologies are then extrapolated, considering the variations induced by the application of the ECOPASS toll.

We apply the tailpipe emission model previously introduced to Milan data, under different traffic-related emission scenarios, in order to evaluate more appropriate PM10 reduction strategies. Figure 9 shows the estimated emissions (as percentages) from different traffic-related sources (for a typical weekday morning , from 7 to 10 am) as a function of different asphalt

	Mv	LDV tr.	HDV tr.	Tr. trailer	Motorcycles	Buses	Tot
	259	20	5	17	45	7	353
Gasoline	181	2	0	0		0	
Euro0	32	0	0	0	20	0	
Euro1	23	0	0	0	11	0	
Euro2	59	0	0	0	10	0	
Euro3	32	0	0	0	2	0	
Euro4	32	0	0	0	0	0	
Euro5	0	0	0	0	0	0	
GPL	2	0	0	0		0	
Euro0	0	0	0	0		0	
Euro1	0	0	0	0		0	
Euro2	0	0	0	0		0	
Euro3	0	0	0	0		0	
Euro4	0	0	0	0		0	
Euro5	0	0	0	0		0	
Methane	0	0	0	0		0	
Euro0	0	0	0	0		0	
Euro1	0	0	0	0		0	
Euro2	0	0	0	0		0	
Euro3	0	0	0	0		0	
Euro4	0	0	0	0		0	
Euro5	0	0	0	0		0	
Diesel	74	17	4	17		6	
Euro0	4	2	2	8		1	
Euro1	1	1	0	1		0	
Euro2	10	4	0	3		2	
Euro3	36	7	0	3		2	
Euro4	20	0	0	0		0	
Euro5	0	0	0	0		0	

Table 17: data elaboration conduced on the given road branch data

Time slot	*Expansion coefficient*
$07-10$ h	2,33
$10-16$ h	6
$16-20$ h	3,52

Table 18: temporal expansion coefficients

		LDV,HDV	**Mv**	**total**
toll-subjected	variation	-60,4 %	-71,2 %	-68,4%
toll-free	variation	+74,9 %	+24,0 %	+27,2%
total	variation	-26,1 %	-10,8 %	-13,0%

Table 19: ECOPASS monitoring data

conditions, before the enforcement of the traffic-restriction regulation named ECOPASS. The estimated emission rates are given in the next Table.

Emission rates $[mg/h]$	Total	Exhaust	Wear	Resuspension
Pre Ecopass	11177992	4479230	1682976	5015786
Pre Ecopass - new asphalts	8653037	4479230	1275357	2898431
Pre Ecopass - damaged asphalts	15899178	4479230	1682976	9736972
Pre Ecopass - optimal asphalts	6624614	4479230	1275377	870007

By considering the contributions in the different time slots, we can obtain total emission per day, for a typical weekday. In the afternoon and evening time slot, the resuspension rate is 20% and 19% of the total respectively. The emission data can be disaggregated per vehicle category and technology (for the exhaust emission), per wear process and per road type. For example, in the pre-Ecopass case, the wear processes, in the morning time slot, contribute to the total PM10 emission rates by the factor: 32% from the tyre component; 39% from the brake component; 29% from the asphalt component. The contribution of the resuspension component to the total PM10 emissions rises from 19% for an optimal asphalt to 61% for a damaged one. On the other hand, comparing a standard pre-ECOPASS asphalt condition with a new asphalt cover, the resuspension-linked emissions decrease from 45% to 33%. Table 21 reports estimates of PM10 emission reduction (expressed as percentage), under a set of selected scenarios based on different asphalt characteristics (pre-ECOPASS situation).
Quite surprisingly, a damaged asphalt extended to all the road branches causes a rise in PM10 resuspension of more than 90%, while an optimal asphalt produces a drop higher than 80%. Therefore, impressive reductions of

Mv	LDV tr.	HDV tr.	Tr. trailer	Motorcycles	Buses	Tot
240	8	4	13	42	8	315

Table 20: Updated traffic data for the considered road branch

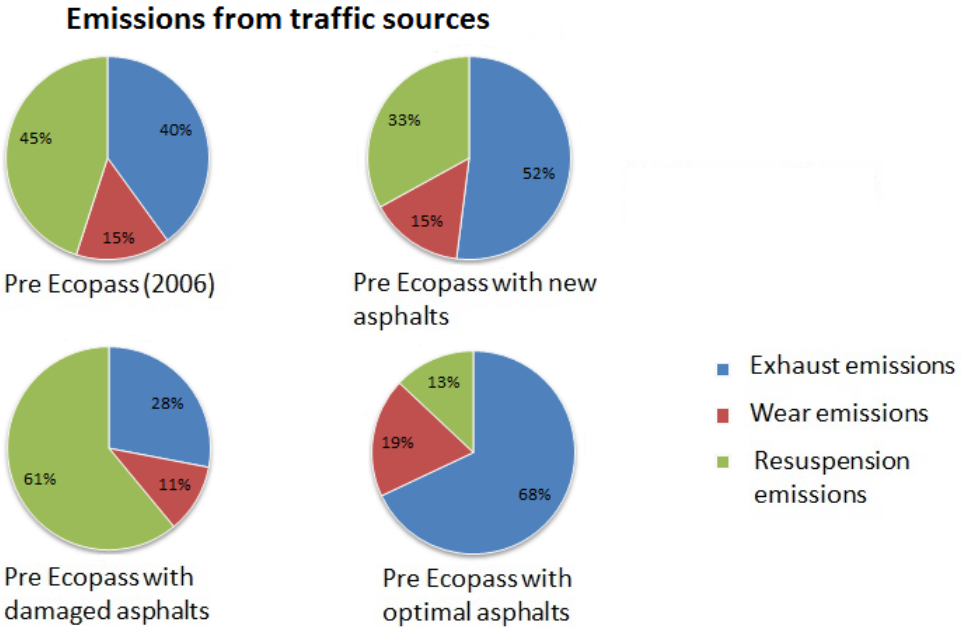

Figure 9: Emission (percentages) from different traffic-related PM10 sources in different asphalt conditions.

	Total	*Exhaust*	*Wear*	*Resuspension*
pre-Ecopass + new asphalts				
Emission reduction from pre-Ecopass	-22,58 %	+0,0 %	-24,21 %	-42,21 %
pre-Ecopass + damaged asphalts				
Emission reduction from pre-Ecopass	+42,23 %	+0,0 %	+0 %	+94,12 %
pre-Ecopass + optimal asphalts				
Emission reduction from pre-Ecopass	-40,73 %	+0,0 %	-24,21 %	-82,65 %

Table 21: Estimation of PM10 emission reductions for different scenarios depending on asphalt characteristics.

PM10 emissions would be expected if these asphalt-based reduction strategies were applied to the whole urban street network , which is, however, quite unlikely. In Table 22, the effects of four different PM10 reduction strategies are compared, namely (i) the implementation of the ECOPASS traffic-congestion charge (through toll-pay barriers) extended to the urban area within the city's ancient Walls ring (red ring in figure 8), (ii) a frequent road washing applied to the outer urban area comprised between the Walls ring and the external beltway (pink ring in figure 8), (iii) road washing applied to all the secondary roads in the urban area of Milan and (iv) the simultaneous adoption of both measures. (We characterize the effect of road washing as a reduction of initial concentrations of road dust by a factor of 93%, corresponding to the results reported in [Amato et al., 2009].
The estimated emission rates in mg/h are:

Emission rates $[mg/h]$	Total	Exhaust	Wear	Resuspension
Ecopass	9688600	3473559	1629436	4585605
pre-Ecopass + street washing (ii)	10780295	4479230	1682976	4618089
pre-Ecopass + street washing (iii)	8269788	4479230	1682976	2107583

As the results of Table 22 point out, not even the joint application of both measures is so effective as a preventive policy based on appropriate asphalt structure and maintenance (the reduction scenario of all secondary roads washing is unrealistic). Accordingly, a more effective PM10 emission control strategy (limited to traffic sources) should be addressed mainly to the

	Total	*Exhaust*	*Wear*	*Resuspension*
Ecopass scenario				
Emission reduction from pre - Ecopass	-13,3 %	-22,5 %	-3,2 %	-8,6 %
pre-Ecopass + street washing (ii)				
Emission reduction from pre - Ecopass	-3,55 %			-7,92 %
pre-Ecopass + street washing (iii)				
Emission reduction from pre - Ecopass	-26,02 %			-57,98 %
Ecopass + street washing (ii)				
Emission reduction from pre - Ecopass	-16,28 %	-22,45 %	-3,2 %	-15,17 %

Table 22: Estimation of PM10 emission reductions for ECOPASS application and street washing.

selection and employment of suitable road asphalts and their accurate maintenance. A more thorough investigation on realistic asphalt maintenance strategies applied to selected urban streets, inclusive of economic evaluations of the connected investment and management costs, is currently in progress.

3 CFD approach

The adopted modelization technique consists of a Computational Fluid Dynamics (CFD) approach, to model the air flow in an open street or a street canyon with traffic fluxes, coupled to a dispersion model for the two classes of non-interacting pollutants (Soot and road dust) introduced in Chapter 2, which are the traciers of traffic related exhaust and non-exhaust emissions (here we call generally the coupled modelization of air flow and pollutant dispersion as CFD approach). The dispersion model is described by an advection-difussion equation, assuming that both Soot and Road dust are passive traciers which do not influence the air flow. This represents a reasonable hypothesis: Soot dispersion ($d_p \sim 100nm$) takes place in the transition regime, whereas road dust ($d_p = 7\mu m$) takes place in the continuum regime [Seinfeld, Pandis, 2006]. This means that in both the dispersion cases the equations of continuum mechanics can be applied. Moreover, the effect of induced fluid motion by the motion of PM10 particles is negligible [Seinfeld, Pandis, 2006]. A CFD model consists of:

- **Turbulence modeling**: Turbulence is an irregular process, characterized by the presence of a large range of excited length and time scales, extending on a continuum spectrum from the mean scales in which energy is injected to the viscous scales in which it is dissipated; it is fully three-dimensional and it is characterized by spatial and temporal instabilities. Virtually all flows of engineering interest are turbulent. The transition to turbulence is driven by the instabilities of laminar flows when the Reynolds number is large. For a given turbulent flow application, the physically meaningful flow properties are usually related to statistically averaged (mean) or smoothed quantities, rather than to the complete time history over all spatial scales until the dissipative ones. Turbulence modeling is the mathematical description of turbulence which gives the desired flow properties or statistics starting from the Navier Stokes (NS) equations of fluid dynamics.

- Determination of **analytical solutions**: in the case of the simpler Turbulence models and geometries, analytical solutions for the averaged flow quantities can be derived. This solutions can serve as useful operational tools to calibrate more complex Turbulence models and their numerical resolution.

- **Numerical resolution**: the discretization of Turbulence models poses specific problems on grid generation and solver algorithm development.

As seen in Chapter 2, the turbulent quantities needed to describe the dominant dynamical processes of Soot and road dust dispersion are the friction velocity u_* and turbulent diffusivity D_T at the mean spatial scales of the

near-wake regiond behind a moving vehicle. This quantities are related to the mean statistical averages of the turbulent flow properties, and can be described by a statistical approach to Turbulence modeling. We will treat standard algebraic and $2-$ equations models of turbulence, obtained by statistically averaging the NS equations and making suitable hypothesis on the Turbulence enhanced diffusivity. Algebraic models, for the different geometries considered, will lead to analytical solutions, used both to define the dispersion models and to calibrate the $2-$ equations Turbulence models used to describe the friction velocity and the turbulent diffusivity in the near-wake region of a moving vehicle.

3.1 Turbulence modeling

Since Turbulence consists of random fluctuations of the various flow properties, a statistical approach has been devised by Reynolds in order to introduce a Turbulence modeling, in which all quantities are expressed as the sum of statistical mean and fluctuating parts [Wilcox, 1998]. For stationary Turbulence, Reynolds averaging consists in a *time averaging* $U(\mathbf{x})$ of an instantaneous quantity $u(\mathbf{x}, t)$:

$$U(\mathbf{x}) = \lim_{T\to\infty} \frac{1}{T} \int_t^{t+T} u(\mathbf{x}, t)\, dt$$

Other averaging concepts are *spatial averaging*, suitable for homogeneous Turbulence, and *ensemble averaging*, defined in terms of measurements from N identical realizations of the turbulent flow. In the ergodic hypothesis, ensemble averaging is equal to time and spatial averaging in the case of a stationary and homogeneous Turbulence. We express the instantaneous $i-$ component of velocity as the sum of a mean and a fluctuating part:

$$u_i(\mathbf{x}, t) = U_i(\mathbf{x}, t) + u_i'(\mathbf{x}, t)$$

In order to have a practical definition of the time averaging operation, a time T which is very long compared to the maximum period of the velocity fluctuations is chosen. For flows in which the mean and the fluctuating components are correlated, this procedure is ill-defined, and ensemble averaging must be considered [Wilcox, 1998]. The Reynolds-averaged incompressible NS equations are:

$$\begin{cases} \dfrac{\partial U_i}{\partial x_i} = 0 \\ \dfrac{\partial U_i}{\partial t} + U_j \dfrac{\partial U_i}{\partial x_j} = -\dfrac{1}{\rho}\dfrac{\partial \overline{p}}{\partial x_i} + \dfrac{\partial}{\partial x_j}\left(2\nu S_{ij} - \overline{u_i' u_j'}\right) \end{cases} \tag{3.1}$$

where the overbar indicates the averaging operation, ρ is the fluid density, S_{ij} is the mean strain rate tensor

$$S_{ij} = \frac{1}{2}\left(\frac{\partial U_i}{\partial x_j} + \frac{\partial U_j}{\partial x_i}\right),$$

and

$$\tau_{ij} = -\overline{\rho u_i' u_j'}$$

is called the *Reynolds stress tensor*. It is a second order correlation of turbulent quantities coming from the averaging operator acting on the non-linear advective term of the NS equations. The Reynolds stress tensor is a symmetric tensor, and thus has six independent components: Reynolds averaging has produced six new unknown variables. We have four equations (for an incompressible fluid without the effect of buoyancy, the NS equations for the velocity field is decoupled from the energy equation), and ten unknowns, so that the problem is under-determined. Taking moments of the NS equations and Reynolds averaging the result, we can determine the dynamic equation for the Reynolds stress tensor:

$$\frac{\partial \tau_{ij}}{\partial t} + U_k \frac{\partial \tau_{ij}}{\partial x_k} = -\tau_{ik}\frac{\partial U_j}{\partial x_k} - \tau_{jk}\frac{\partial U_i}{\partial x_k} + \epsilon_{ij} - \Pi_{ij} + \frac{\partial}{\partial x_k}\left[\nu \frac{\partial \tau_{ij}}{\partial x_k} + C_{ijk}\right] \quad (3.2)$$

where:

$$\epsilon_{ij} = \overline{2\mu \frac{\partial u_i'}{\partial x_k}\frac{\partial u_j'}{\partial x_k}};$$

$$\Pi_{ij} = \overline{p'\left(\frac{\partial u_i'}{\partial x_j} + \frac{\partial u_j'}{\partial x_i}\right)};$$

$$C_{ijk} = \overline{\rho u_i' u_j' u_k'} + \overline{p' u_i'}\delta_{jk} + \overline{p' u_j'}\delta_{ik}.$$

The phisical meaning of this terms will be explained later. In general, a conservation equation for a second moment quantity contains the material derivative term, a production term, a dissipation term, and a viscous plus a turbulent transport term. We have now ten equations, but we have introduced twenty-two new unknowns (coming from the third order correlation tensor and the two new second order correlation tensors). This illustrates the closure problem of Turbulence: because of the non linearity of the NS equations, taking higher and higher statistical moments, we generate new unknowns at each level. Turbulence modeling has the function to introduce approximations for the unknown correlations in terms of the mean flow properties that are already known, thus closing the system.

Reynolds Averaged Navier Stokes (RANS) equations describe the turbulent flow at the level of its stationary mean components. This components

correspond to spatial scales at which energy is introduced into the flow (integral scales, i.e. the scales of the order of magnitude of the correlation length of the velocity). Turbulence field at the dissipative and the inertial scale (i.e. the scale at which energy is transferred from the integral to the dissipative scales), as well as instantaneous fields, are not described. The ratio between the integral (l_0) and the dissipative (l_D) length scales is given by [Wilcox, 1998]:

$$\frac{l_0}{l_D} = \left(\frac{l_0 v_0}{\nu}\right)^{3/4} = Re^{3/4}$$

where v_0 is a characteristic velocity of the flow, generally identified with the square root of the mean square of velocity, and Re is Reynolds number. The two scales are more separated, and so the inertial range is more developed, for greater Reynolds number. A typical length scale for the inertial range is the Taylor length λ:

$$\lambda = \sqrt{5} l_0^{1/3} l_D^{2/3}$$

In the context of a numerical solution of the discretized 3-D NS equations, direct numerical simulations would require a number of collocation points $\sim Re^{9/4}$ in order to resolve all the turbulent scales. This is only affordable, with modern computation machines, only for laminar flows or flows with an homogeneous and isotropic Turbulence. RANS models resolve the mean stationary scales, and all sub-grid physics is described by the hypothesis of enhanced diffusivity. Large Eddy Simulation (LES) models resolve the instantaneous Turbulence field at the inertial scales, leaving to sub-grid modelization the task of modeling the turbulent diffusivity at the viscous scales. Details will be given in a moment. The simplest RANS Turbulence models are known as **algebraic models**. These models use the Boussinesq eddy-viscosity approximation to compute the Reynolds stress tensor as the product of an eddy viscosity ν_t and the mean strain rate tensor. The Boussinesq approximation is formulated by an analogy with momentum transport at the molecular level. In the latter context, the instantaneous flux of $x-$ directed momentum across a surface element in the plane $y = 0$, for a shear flow in which the mean velocity $U(y)$ is in the $x-$ direction, is:

$$dp_{xy} = \rho\big(U + u''\big)v'' dS$$

where u'' and v'' represent random molecular motion. Performing a statistical average on the instantaneous quantity, we have for the viscous stress tensor acting on $y = 0$:

$$t_{xy} = \overline{-\rho u'' v''}$$

This resembles the Reynolds stress tensor: a stress that is generated from a momentum flux can always be written in this form. The only difference is that, at the macroscopic level, turbulent fluctuations $u^{'}$ and $v^{'}$ appear in place of the random molecular fluctuations. Referring to arguments from the kinetic theory of gases, we can express the shear stress as:

$$t_{xy} \approx \frac{1}{2}\rho v_{th} l_{mfp} \frac{dU}{dy} = \mu \frac{dU}{dy}$$

where v_{th} is the thermal velocity, and l_{mfp} is the mean free path of the perfect gas. The $\approx$ is due to the fact that a momentum deficit

$$m\big[U(0) - U(-l_{mfp})\big] \approx l_{mfp} \frac{dU}{dy}$$

is associated to each molecule starting from a point below the $y = 0$ plane. This approximation is valid if:

$$\frac{l_{mfp}}{L} \ll 1 \qquad where \qquad L = \frac{|dU/dy|}{|d^2U/dy^2|}$$

Another approximation is introduced, in order to assume that $u^{''}$ remains Maxwellian even in the presence of shear:

$$l_{mfp} \ll \frac{v_{th}}{|dU/dy|},$$

which means that molecules experience many collisions on the time scale of the mean flow. In analogy with molecular transport of momentum, Prandtl introduced the *mixing length hypothesis*: in turbulent fluid motion fluid particles coalesce into lumps that cling together and move as a unit. In this context, for a mean shear flow $U(y)$, we can write the Reynolds stress in the form:

$$\tau_{xy} = \frac{1}{2}\rho v_{mix} l_{mix} \frac{dU}{dy} \tag{3.3}$$

with a mixing length l_{mix} replacing l_{mfp}. For the mixing length velocity v_{mix}, analogous to the thermal velocity of a pure gas, Prandtl postulated the form:

$$v_{mix} = constant \cdot l_{mix} \left| \frac{dU}{dy} \right| \tag{3.4}$$

This can be seen as the first order approximation of the Taylor expansion of the velocity fluctuation. The mixing length is not an intrinsic property of the fluid, but depends on the particular flow in consideration. It must be specified in advance, as part of the Turbulence modeling. For this reason algebraic models are *incomplete* models of Turbulence. We can absorb the

constant in Equations (3.3) and (3.4) in the definition of l_{mix}, and write for the Reynolds stress tensor:

$$\tau_{xy} = \mu_T \frac{dU}{dy} \qquad with \qquad \mu_T = \rho l_{mix}^2 \left| \frac{dU}{dy} \right| \tag{3.5}$$

For a general flow, the mean strain rate tensor must be considered in the definition of the Reynolds stress tensor in Equation (3.5). Prandtl postulated that for flows near solid boundaries the mixing length is proportional to distance from the surface. This is a reasonable assumption, which leads to the determination of the law of the walls (logarithmic profiles in scaled distance from the wall), as will be shown in the context of analytic solutions of algebraic Turbulence models. For free shear flows, a mixing length proportional to the width of the layer δ is usually assumed. In the context of a wake solution over a solid boundary, different prescription for the mixing length have to be made in different regions of the domain, and matching between the different solutions, in the context of a singular perturbation theory, must be performed. Details will be shown in Section 4.1. Prandtl also proposed a simpler eddy viscosity model for free shear flows:

$$\mu_T = \alpha \rho \big[U_{max}(x) - U_{min}(x) \big] \delta(x) \tag{3.6}$$

where x is the direction parallel to the flow, α is an empirical constant, U_{max} and U_{min} are the maximum and minimum values of the mean velocity in the layer, and δ is the width of the layer. For a wake solution in presence of a boundary layer, the $\big[U_{max}(x) - U_{min}(x)\big]$ term should be substituted by the value of the velocity external to the layer.

Concerning the Boussinesq approximation, closed to a solid boundary we have [Wilcox, 1998]

$$\frac{l_{mix}}{L} \approx k \qquad ; \qquad l_{mix} \sim \frac{v_{mix}}{|dU/dy|}$$

where $k = 0,41$ is the Von Karman constant. Thus, the theoretical foundation of the mixing-length model is weak; despite this, algebraic models of Turbulence give results which reproduce well the experimental measurements [Wilcox, 1998], when suitably calibrated with empirical results. Besides this, algebraic models of Turbulence usually lead to analytical solutions for the description of the considered flow in particular regimes (for example when self-similarity laws and separated solutions are valid, and when the properties of the flow are slowly varying), which can be used to calibrate more complex Turbulence models for complex flows, and to build up operational tools for dispersion modeling. Different algebraic Turbulence model will be introduced Section 4.1, in the context of finding analytical solutions for flow in the case of the canyon geometry and of the vehicle geometry.

More complex Turbulence models are based upon the equation for the turbulent kinetic energy k. These Turbulence models are usually solved in their discretized counterparts via numerical simulations. We will treat and use the two standard 2− equation models, i.e. the $k-\epsilon$ and the $k-\omega$ models. In one equation models, a characteristic velocity scale for the Turbulence mixing is given by the square root of k, so that the eddy viscosity is given by:

$$\mu_T = constant \cdot \rho k^{1/2} l \tag{3.7}$$

where l is a turbulent length scale. The Boussinesq eddy viscosity approximation is assumed, and the model is again incomplete, since l must be related to some typical flow dimension. An equation for k is obtained by taking the trace of Equation (3.2), and observing that $\tau_{ii} = -2\rho k$:

$$\rho\frac{\partial k}{\partial t} + \rho U_j \frac{\partial k}{\partial x_j} = \tau_{ij}\frac{\partial U_i}{\partial x_j} - \rho\epsilon + \frac{\partial}{\partial x_j}\left[\mu\frac{\partial k}{\partial x_j} - \frac{1}{2}\rho\overline{u_i' u_i' u_j'} - \overline{p' u_j'}\right] \tag{3.8}$$

The various terms in Equation (3.8) represent physical processes occurring as Turbulence is transported through the given flow. The term on the right hand side is the Eulerian derivative of k, giving its rate of change as the fluid moves in a x_i sistem of reference; the first term on the right hand side is the *production* term, and represents the rate at which work is done by the mean strain rate against the Turbulence stresses; the second term on the right and side is the *dissipation* term, represented by the mean rate at which work is done by the fluctuating part of the strain rate against the fluctuating viscous stresses; the third term on the right hand side is the *molecular diffusion* plus the *turbulent transport* plus the *pressure diffusion* term. The production, dissipation, turbulent transport and pressure diffusion terms involve unknown correlations, and must be represented as known mean quantities by suitable Turbulence modeling. Prandtl established the closure of each term of Equation (3.8) on the basis of dimensional analysis and empirical data, assuming a Turbulence flow in an equilibrium regime. This closure process is not a rigorous one, and in [Wilcox, 1998] it is calles *drastic surgery* of the exact equation. For the production term, a closure prescription comes from the Boussinesq approximation:

$$\tau_{ij} = 2\mu_T S_{ij} - \frac{2}{3}\rho k \delta_{ij},$$

with μ_T given in Equation (3.7), and the second term on the right hand side added in order to have the proper trace of τ_{ij}. For the turbulent transport term, the standard approximation is that of gradient-diffusion, in analogy with molecular transport processes of scalar quantities. The pressure diffusion term is generally grouped with the turbulent transport term:

$$\frac{1}{2}\rho\overline{u_i' u_i' u_j'} + \overline{p' u_j'} = -\frac{\mu_T}{\sigma_k}\frac{\partial k}{\partial x_j}$$

Again, the main effect of Turbulence on the transport process is that of enhanced diffusivity. σ_k is a closure coefficient, which must be obtained in the context of the Turbulence model calibration on empirical data. The dissipation term is determined by dimensional arguments. The two unknown parameters of the model are l and ϵ; if we assume they are function of the Turbulence, and do not depend on fluid properties such as molecular viscosity, we have by dimensional arguments:

$$\epsilon = C_D \frac{k^{3/2}}{l},$$

where C_D is another closure coefficient to be determined by the calibration of the model on empirical data. In this one equation Turbulence model, the length scale of Turbulence l must be prescribed, and the model is incomplete. In the case of equilibrium flows, i.e. the flows for which production and dissipation of k balance, the mean flow and the turbulent scales are proportional [Wilcox, 1998], and the prescription $l = l_{mix}$ is possible (the mean flow quantities specify the Reynolds stress factor in the production term, and the turbulent quantities specify the dissipation term). We see that for an equilibrium turbulent flow (i.e. a flow with slowly varying mean properties) the RANS model describes the evolution of the mean statistical quantities, at the integral scale. In non-equilibrium flows, an unknown mixing of scales is present, and RANS closure is not possible.

Two-Equations RANS models are complete models, i.e. no turbulent structure information for a particular flow configuration must be inserted in the model. In these models, a second transport equation is introduced to determine the length scale l throughout the flow. Standard two-equations model introduce transport equations for ϵ ($k-\epsilon$ model) or for ω ($k-\omega$ model), defined as the dissipation per unit turbulence kinetic energy. On dimensional grounds, we have:

$$\mu_T \sim \rho\frac{k^2}{\epsilon} \qquad ; \qquad l = \frac{k^{3/2}}{\epsilon}$$

for the $k-\epsilon$ model, and:

$$\mu_T \sim \rho\frac{k}{\omega} \qquad ; \qquad l = \frac{k^{1/2}}{\omega} \qquad ; \qquad \epsilon = \omega k$$

for the $k-\omega$ model. These prescriptions are suitable for calibration with empirical data, in order to find proper closure coefficients of the models. As for the case of the one-equation model, the ratio of Reynolds stresses to mean strain rate components depends only on the turbulent parameters, such as k, l, ϵ, ω, for equilibrium flows, for which mean flow and turbulent

scales are proportional. The transport equations for the turbulent quantities ϵ and ω are derived in a similar procedure as that involved to determine the k equation (3.8), i.e. by describing the physics related to each term of the exact equations by means of dimensional analysis based on the relavant turbulent-mean parameters of the process [Wilcox, 1998]. The standard $k-\epsilon$ model is:

$$\begin{cases} \mu_T = \rho C_\mu \dfrac{k^2}{\epsilon} \\ \rho \dfrac{\partial k}{\partial t} + \rho U_j \dfrac{\partial k}{\partial x_j} = \tau_{ij} \dfrac{\partial U_i}{\partial x_j} - \rho\epsilon + \dfrac{\partial}{\partial x_j}\left[\left(\mu + \dfrac{\mu_T}{\sigma_k}\right)\dfrac{\partial k}{\partial x_j}\right] \\ \rho \dfrac{\partial \epsilon}{\partial t} + \rho U_j \dfrac{\partial \epsilon}{\partial x_j} = C_{\epsilon 1} \dfrac{\epsilon}{k} \tau_{ij} \dfrac{\partial U_i}{\partial x_j} - C_{\epsilon 2} \rho \dfrac{\epsilon^2}{k} + \dfrac{\partial}{\partial x_j}\left[\left(\mu + \dfrac{\mu_T}{\sigma_\epsilon}\right)\dfrac{\partial \epsilon}{\partial x_j}\right] \end{cases} \tag{3.9}$$

where the closure coefficients must be determined by calibration of the model on empiric data.

The Wilcox $k-\omega$ model is:

$$\begin{cases} \mu_T = \rho \dfrac{k}{\omega} \\ \rho \dfrac{\partial k}{\partial t} + \rho U_j \dfrac{\partial k}{\partial x_j} = \tau_{ij} \dfrac{\partial U_i}{\partial x_j} - \beta^* \rho k \omega + \dfrac{\partial}{\partial x_j}\left[\left(\mu + \sigma^* \mu_T\right)\dfrac{\partial k}{\partial x_j}\right] \\ \rho \dfrac{\partial \omega}{\partial t} + \rho U_j \dfrac{\partial \omega}{\partial x_j} = \alpha \dfrac{\omega}{k} \tau_{ij} \dfrac{\partial U_i}{\partial x_j} - \beta \rho \omega^2 + \dfrac{\partial}{\partial x_j}\left[\left(\mu + \sigma \mu_T\right)\dfrac{\partial \omega}{\partial x_j}\right] \end{cases} \tag{3.10}$$

where the closure coefficients must be determined by calibration of the model on empiric data. Calibration consists in setting the values of closure coefficients to assure agreement with observed properties of Turbulence. By applying the models to decaying homogeneous, isotropic Turbulence, lead to a constraint on the values of the closure coefficients in order to have a solution that reproduces experimental observations [Wilcox, 1998]. We must note that for atmospheric flows a much larger length-scale interval is available than for wind-tunnel flows, which means that for the same dissipation and turbulence stress, the turbulent kinetic energy will usually be much larger in the atmosphere than in a tunnel simulation. This lead to different values of the closure coefficients for the two cases (e.g. the coefficient C_μ is smaller for the atmospheric case). Anyway, the consequences of trying the models with both coefficients often seem small [Berkowicz, Kearney, 2004]. Concerning the $k-\omega$ model, this lead to an imposed relation on the ratio β^*/β. Values for the other coefficients can be established by the application of singular perturbation analysis to the boundary layer solutions of the models. Singular perturbation analysis consists in developing a solution to the transport equations in the form of an asymptotic expansion in terms of a parameter, the error being small for small values of the parameter. Experimental

observations provide a strong argument for using singular perturbation analysis [Wilcox, 1998]: different scales are dominant in different regions of the domain; in the case of the turbulent boundary layer, different scales and physical processes are dominant in the inner (near-wall) and outer (wake region) part of the layer. We observe that closed to a solid boundary, the law of the walls holds, which can be written as (in the case of two dimensions, with x parallel and y orthogonal coordinates to the wall):

$$U(x,y) = u_*(x) f\left(\frac{u_* y}{\nu}\right),$$

where u_* is the square root of the wall tangential stress divided by density, defined as the *friction velocity*. The main body (wake region) of the turbulent boundary layer behaves according to Clauser defect law [Wilcox, 1998]:

$$U(x,y) = U_\infty - u_* F\left(\frac{y}{\Delta}\right) \qquad , with \qquad \Delta = \frac{U_\infty \delta}{u_*},$$

where U_∞ is the external (freestream) velocity to the boundary layer, and δ is the wake width. This law consists of a small perturbation from the freestream value. The solutions of the transport equations, developed as asymptotic expansions in the stretched variables defined in the previous empirical laws, are not uniformly valid on the whole domain: the wall solution, if it is consistent with the measurements, is logarithmically divergent with distance from the surface, as $u_* y/\nu \to \infty$; the outer solution, in the defect law form of a small perturbation from the freestream value, cannot satisfy the no-slip boundary condition at the wall. A matching procedure must be employed, in order to match the two solutions in the limits:

$$\frac{u_* y}{\nu} \to \infty \qquad , \qquad \frac{y}{\Delta} \to 0$$

Each of the two stretched variables are finite in their respective domain (near wall and wake region), and are infinite and infinitesimal respectively in the matching region. Details will be shown in Section 4.1, in the case of singular perturbation solutions for the canyon geometry and the vehicle geometry. Solving the equations for the two Turbulence models in the near-wall region in the limit $y^+ = u_* y/\nu \to \infty$, through a singular perturbation expansion in powers of the stretched variable $y^+ = u_* y/\nu$, and imposing a logarithmic behaviour for velocity, we obtain (see [Wilcox, 1998]) other constraints for two of the closure coefficients (e.g. β^* and α for the $k-\omega$ model), and the

laws (valid in the log-layer region):

$$\begin{cases} U = \dfrac{u_*}{\mathtt{k}} \log(y^+) + C, \quad k = \dfrac{u_*^2}{\sqrt{C_\mu}}, \quad \epsilon = \dfrac{u_*^3}{\mathtt{k}y} & \mathbf{k-\epsilon\ model} \\ U = \dfrac{u_*}{\mathtt{k}} \log(y^+) + C, \quad k = \dfrac{u_*^2}{\sqrt{\beta^*}}, \quad \omega = \dfrac{u_*}{\sqrt{\beta^*}\mathtt{k}y} & \mathbf{k-\omega\ model} \end{cases} \tag{3.11}$$

where C is an integration constant, with an empirical value of 5.0 in the case of no pressure gradient for the freestream flow, and we have written $\mathtt{k}$ for the Von-Karman constant, to avoid confusion with turbulent kinetic energy k. By performing a matching with the outer layer solutions for the two models, and comparing the velocity profile, the derived friction velocity and wake-related parameters [Wilcox, 1998] with corresponding experimental data, the $k-\omega$ model yields solution close to measurements (with an error of the order of 3%), whereas the $k-\epsilon$ model show greater differences and poor performance (with a $50-100\%$ error) in the case of freestream adverse pressure gradients. What can be seen [Wilcox, 1998] is that the $k-\epsilon$ model predicts a turbulence length scale which is too large in the near wall region, overestimating it in the region of boundary-layer separation; this region is induced by the presence of external adverse pressure gradient, in which the Reynolds-stress is frozen to its upstream value and advected in a recirculation zone [Batchelor, 1967]. The manner in which the $k-\omega$ model achieves smaller values of l than does the $k-\epsilon$ model can be shown by taking the change of variable $\epsilon = \beta^*\omega k$ in the equation for ω in the case of the stationary boundary layer approximation:

$$U\frac{\partial \epsilon}{\partial x} + V\frac{\partial \epsilon}{\partial y} = (1+\alpha)k\left(\frac{\partial U}{\partial y}\right)^2 - (1+\beta/\beta^*)\frac{\epsilon^2}{k} + \frac{\partial}{\partial y}\left[\sigma\nu_T\frac{\partial \epsilon}{\partial y}\right] - 2\sigma\nu_T\frac{\partial k}{\partial y}\frac{\partial \epsilon/k}{\partial y}$$

The only different term with respect to the $k-\epsilon$ model is the last one. This term is called the *cross-diffusion* term. Since, for flows with adverse pressure gradient, this term is nonvanishing as $y/\Delta \to 0$ [Wilcox, 1998], its effect is to suppress the rate of increase of l close to the surface. By integration of the Turbulence models equations in the viscous sublayer (i.e. for y^+ finite), imposing boundary conditions valid on the surface and in the log-layer, and comparing the derived velocity profiles with corresponding measurements, we find the constraints for the other two closure constants. We must observe that, except that for some flow typology described by the $k-\omega$ model [Wilcox, 1998], all two-equations model require Reynolds number dependent corrections to the values of the closure coefficients, in order to yield realistic sublayer solutions and correct transition from laminar to turbulent regime in the domain of the flow (e.g. the transition from a wake zone to the external freestream flow). These corrections are avoided by integrating the

2−equations model starting from the log-layer adjacent to a solid boundary, and, in the case of the wake simulation for the vehicle geometry, by calibrating the model in order to give results comparable with the analytical solutions for the far-wake region. Details will be shown in Section 3.4. When applied to free-shear layer flows, the $k-\omega$ model gives results which predict the correct values of measurement data only for specified values of the freestream boundary condition on ω [Wilcox, 1998]. For example, in the case of the wake flow in a region in which self-similar solutions are valid (far-wake solution; see Sections 3.4, 4.1 and 4.2 for details), the most sensible boundary conditions are those corresponding to vanishing turbulence at the turbulent-non turbulent interface, i.e. k, ω and ϵ vanishing at the edge of the shear layer. As it turns out, the $k-\epsilon$ model predictions are unaffected by finite values of k and ϵ in the freestream, whereas the $k-\omega$ solutions are very sensitive to the freestream value of ω (ω_∞). In the case of the far-wake solution, it predicts the correct experimental behaviours for $\omega_\infty = 0.4$. For $\omega_\infty = 0$, computed quantities exceed measurments by up to 37% [Wilcox, 1998]. There are different ways to overcame this difficulties:

- Use more detailed Turbulence models, which introduce dispersion equations for other turbulent quantities, in order to describe the length scale of the recirculation zone induced by the adverse pressure gradient. One of this is the $k-\epsilon-v^2-f$ model introduced by Durbin [Durbin, 1995], in which it is supposed that the normal Reynolds stress perpendicular to the wall in the separation zone, $\overline{v'^2}$, plays the most important role in determining the mixing length and the eddy viscosity near the wall. In this model the normal stress dynamics is resolved, along with the dynamics for k and ϵ, modified in order to introduce the turbulent scale associated to $\overline{v'^2}$. An equation for the pressure strain is introduced (the f part), in order to describe wall reflection and integrate the model in the viscous sublayer. Another possibility is to solve a transport equation for the full Reynolds stress (SSG models [Wilcox, 1998]), or to use hybrid RANS - LES models (e.g. Detached Eddy Simulations models [Martinat et al., 2008]), which use one-equation model which transform to LES model near a solid boundary, by introducing a dependence of the eddy viscosity on the grid spacing. We do not enter in the details of these models, but will cite their results in comparison with the results obtained by our 2-equations model in the case of the flow over the vehicle.

- To develop a $k-\omega$ model that has no sensitivity to the freestream value of ω. To obtain this purpose, Menter has included a cross-diffusion term in the ω equation [Wilcox, 1998]:

$$\rho\frac{\partial\omega}{\partial t}+\rho U_j\frac{\partial\omega}{\partial x_j}=\alpha\frac{\omega}{k}\tau_{ij}\frac{\partial U_i}{\partial x_j}-\beta\rho\omega^2+\frac{\partial}{\partial x_j}\left[\left(\mu+\sigma\mu_T\right)\frac{\partial\omega}{\partial x_j}\right]+\sigma_d\frac{\rho}{\omega}\frac{\partial k}{\partial x_j}\frac{\partial\omega}{\partial x_j}$$

The last term is the cross-diffusion term; since k decreases approaching the shear layer edge, the effect of this term is to make the effective entrainment velocity positive (or less negative), making ω diffusing from the turbulent into the non-turbulent region. In this way the freestream value of ω has no effect on the solution [Wilcox, 1998]. Clearly, the cross-diffusion term introduced by Menter cancels out the effect of the cross diffusion term which allows the $k-\omega$ model to achieve smaller value of l than the $k-\epsilon$ model in the wall region. Thus a blending function must be introduced, which makes $\sigma_d=0$ close to a solid boundary. Wilcox [Wilcox, 1998] introduces the function:

$$\sigma_d=\begin{cases}0, & \dfrac{\partial k}{\partial x_j}\dfrac{\partial\omega}{\partial x_j}\leq 0\\[2ex] \sigma, & \dfrac{\partial k}{\partial x_j}\dfrac{\partial\omega}{\partial x_j}>0\end{cases}$$

To understand this prescription, observe that k increases and ω decreases in the viscous sublayer [Wilcox, 1998].

- To consider ω_∞ as an adjustable empirical parameter in the model. In the case of strong separation in the vehicle wake simulations, we will use this approach, starting from a $k-\omega$ model, with standard calibration for the closure coefficients, additionally calibrated in the ω_∞ parameter in order to obtain far-wake solutions which reproduce analytic solutions results obtained through algebraic Turbulence models. It is assumed [Wilcox, 1998] that the optimum values of ω_∞ for the self-preserving case (far-wake solution) gives good result for non-preserving cases (near-wake solution).

The standard closure coefficients, for wind tunnel Turbulence, for the $k-\epsilon$ and the $k-\omega$ model are [Wilcox, 1998]:

RANS models are thus Turbulence models which describe, once calibrated on empirical data, the statistical mean of a particular flow structure; in the context of a discretization of the equations, a grid cell must have dimensions of the order of the integral scales of the flow (with exceptions for grid convergence considerations and numerical stabilities of boundary conditions near solid boundaries, as will be shown in Section 3.4). As we have seen, this results in a reasonable descriptions for equilibrium Turbulence, in which the mean and the turbulent scales, described by the transport equations of the model, are proportional. We cite here another the Large Eddy

$\mathbf{k}-\epsilon$	*model*	$\mathbf{k}-\omega$	*model*
$C_{\epsilon 1}$	1.44	α	5/9
$C_{\epsilon 2}$	1.92	β	3/40
C_{μ}	0.09	β^*	9/100
σ_k	1.0	σ	1/2
σ_{ϵ}	1.3	σ^*	1/2

Table 14: Standard closure coefficients for the $k-\epsilon$ and the $k-\omega$ model.

Simulation (LES) Turbulence modeling approach. It consists of a filtering operation over the governing NS equations. LES models give a description of an instantaneous realization of a filtered flow; this description must be three dimensional and unsteady, realistic Turbulence structures must be given as initial conditions, and the spatial resolution must capture all the energetic scales until the Taylor length λ, in order to describe the dominant coherent structures and local bifurcations of the flow which do not decay with viscous dissipation. The filtering operation is defined as a convolution of a filter kernel G and a turbulent quantity on the whole domain of the flow:

$$\overline{f(\mathbf{x},t)} = \int_D f(\mathbf{x}-\mathbf{r},t)G(\mathbf{r},\mathbf{x})\,d\mathbf{r}$$

The amplitude of the filter is of the order of λ, and determines the discrete grid spacing. The sub-grid shear stress tensor is again described by the Boussinesq approximation, and the turbulent viscosity is proportional, in the Smagorinsky model analogous to Prandtl mixing length model, to the square of the filter amplitude multiplied by the norm of the filtered strain rate tensor [Wilcox, 1998]. Dynamical procedures are available to determine the mixing length value as a step of the model resolution. We will not enter in the details of LES formulation.

Since for the description of the resuspension phenomenon and of the dispersion of Soot and Road dust we are interested in mean scale quantities, as expressed in Chapter 2, we will use RANS algebraic and 2- equations Turbulence models. We are interested in describing two kind of turbulent flows: i) the flow which develops inside a canyon street, forced by an external wind at the roof level; ii) the flow which develops in the near-wake and in the far-wake of a moving vehicle, both in the case of an open street and a street canyon geometry. We will define these cases in later chapters. The initial and boundary conditions specification of the problem, its discretization, grid generation and solver algorithm development will be briefly shown in Section 3.4.

3.2 Dispersion models

The equation for the dispersion of a passive scalar is given by a material balance of its concentration c taken over a volume element:

$$\frac{\partial c}{\partial t} + \frac{\partial}{\partial x_j}(u_j c) = D\frac{\partial^2 c}{\partial x_j \partial x_j} + S \tag{3.12}$$

where u_j is the $j-$ component of the fluid velocity, D is the molecular diffusivity and S is a source term. The molecular diffusivity is given by Formula (2.2), with the slip correction factor C_c in the case of the dispersion of the Soot component, in order to take into account non-continuum effects, and without it in the case of the road dust component.

In the context of a RANS description of turbulent flows, the fluid velocity is a random function of space and time, represented as the sum of a mean component and a fluctuating part. Accordingly, c is a random variable, and only the determination of certain statistical properties of c can be performed. Expressing c as the sum of a statistical mean C and a fluctuating part $c^{'}$:

$$c = C + c^{'}$$

and taking a statistical average of the dispersion equation (3.12), we obtain:

$$\frac{\partial C}{\partial t} + \frac{\partial}{\partial x_j}(U_j C) = D\frac{\partial^2 C}{\partial x_j \partial x_j} - \frac{\partial}{\partial x_j}(\overline{u_j^{'} c^{'}}) + S \tag{3.13}$$

This equation contains three new variables, given by the correlations of the fluctuating concentration with the three components of fluctuating velocity, and a closure problem is at hand. The mixing length hypothesis is the most common way to close the problem, expressing the turbulent fluxes $\overline{u_j^{'} c^{'}}$ in terms of the mean concentration C:

$$\overline{u_j^{'} c^{'}} = -K_{jk}\frac{\partial C}{\partial x_k},$$

where K_{jk} is the eddy diffusivity tensor, generally considered diagonal in the coordinate axes system. The equation for the pollutant dispersion in an incompressible turbulent fluid now becomes Equation (2.1):

$$\frac{\partial C}{\partial t} + U_j\frac{\partial C}{\partial x_j} = \frac{\partial}{\partial x_j}\left[(D + K_{jj})\frac{\partial C}{\partial x_j}\right] + S \tag{3.14}$$

This is an advection-diffusion equation, and must be solved with suitable initial and boundary conditions. In particular, since we are integrating the Turbulence equations from the logarithmic layer, the dispersion equation is integrated from there too, and the molecular diffusion is negligible compared with the turbulent diffusion. All the effects of molecular diffusivity are included in the boundary conditions form, described, in the case of the

deposition flux and in the case of the deposition + resuspension flux at the road boundary, by Equations (2.3) and (2.4) respectively. Usually, in the case of isotropic Turbulence, the eddy diffusivity tensor for the pollutant dispersion is expressed as the eddy viscosity ν_T:

$$K = \nu_T,$$

where ν_T is described in the context of the Turbulence model solution to which the pollutant dispersion is coupled. In the cases in which the atmospheric stratification is important, the eddy diffusion coefficient is considered as the sum of a component associated to the reference atmospheric state, described by similarity theory [Eskridge et al., 1979], and a component associated to the mechanical Turbulence. In particular cases analytical solutions of the dispersion equation (3.14) exist. These analytical models can be used to set up operational models for the pollutant dispersion in street geometries. The Gaussian analytical model [Seinfeld, Pandis, 2006] is derived in the hypothesis of:

- a stationary dispersion process;
- an homogeneous and plain domain;
- a constant velocity field U in the x direction;
- the advection component is dominant with respect to the turbulent diffusion component in the x direction (*slender plume approximation*);
- the turbulent diffusion coefficients K_{yy} and K_{zz} are constants;
- the source term is given by

$$S = Q\delta(x) \cdot \delta(y) \cdot \delta(z)$$

Besides these assumptions, the pollutant is assumed as chemical inert. With this conditions, the dispersion equation is exactly solvable, and the Gaussian model solution is:

$$C = \frac{Q}{2\pi V \sigma_y \sigma_z} \exp\left[-\frac{1}{2}\left(\frac{y^2}{\sigma_y^2} + \frac{z^2}{\sigma_z^2}\right)\right] + C(0),$$

where $C(0)$ is the concentration at $x = 0$, and the dispersion coefficients are defined as:

$$\sigma_y^2 = 2K_{yy}\frac{x}{V} \qquad ; \qquad \sigma_z^2 = 2K_{zz}\frac{x}{V}$$

The Gaussian model describes a stochastic process, associated with the concentration distribution, with a Gaussian probability density function. The

dispersion parameters σ_y and σ_z are given by empirical parametrizations, depending on the atmospheric stability [Seinfeld, Pandis, 2006], or by the corresponding forms in terms of K_{yy} and K_{zz}. The Gaussian models can be extended to non-homogeneous and non stationary dispersion processes by considering the pollutant dispersion as given by a superposition of discrete *puff* solutions in space and time, which are Gaussian solutions valid in specific regions of the domain, in which the dispersion parameters can be approximately considered constant (for each time step). We will extend this approach in Section 3.5 to set up an operational model for the dispersion of Soot and road dust, in an open and a canyon street, considering the deposition and the resuspension process.

Let us introduce two important quantities which characterize the dispersed pollutant distribution in time and space: the **lifetime** and the **mixing time**. The lifetime is an average residence time for the pollutant in the atmosphere, telling on average how long a representative particle of the substance will stay in the atmosphere before it is removed [Seinfeld, Pandis, 2006]. It thus depends on the nature of emission and removal processes of the pollutant in the atmosphere. By integrating in a volume of air V the conservation of mass equation we obtain a balance equation for the total mass of pollutant Q in the considered spatial volume:

$$\frac{dQ}{dt} = \big(F_{in} - F_{out}\big) + \big(P - R\big),$$

where F_{in} and F_{out} are the mass fluxes of substance out of the considered region, integrated over the surface across which the flux is calculated, and P and R are the emission and removal rates of pollutant. In an equilibrium balance condition $dQ/dt = 0$, and we can define the average residence time τ (in $[s]$) as:

$$\tau = \frac{Q}{R + F_{out}} = \frac{Q}{P + F_{in}} \tag{3.15}$$

In the case of the Soot dispersion, F_{in} and R are zero, and we consider the proces of deposition at the road surface in the definition of τ. In the case of road dust dispersion, we will consider $F_{in} = k_{res} c_s$ in the definition of τ. Details will be given in Section 4.4. The characteristic mixing time τ_M for a pollutant in a volume of the atmosphere is defined as the time needed to mix the pollutant in that region of air. Its value depends on the dynamics of the turbulent mixing processes which the particles undergo in the considered region of space. The considered region of the atmosphere is well mixed for a particular pollutant if:

$$\tau_M \ll \tau$$

In order to introduce the relevant turbulent length scales in the definition of τ_M, we refer to the statistical study of a pollutant concentration distribution

reported in Ref. [Davidson, 2004]. The mixing time is defined as the characteristic time for the destruction of the variance of C, which is a measure of the non-uniformity of the pollutant distribution. Assuming a statistical homogeneous and isotropic distribution for C, we can obtain an equation for the variance $\overline{C^2}$ by multiplying the dispersion equation (3.14) by C and taking a statistical average of the result:

$$\frac{1}{2}\frac{d\overline{C^2}}{dt} = -\overline{\frac{\partial C}{\partial x_j}\frac{\partial K_{jj} C}{\partial x_j}}$$

We can define the average destruction rate ϵ_C of the variance of C in terms of the average eddy diffusion coefficient over the considered volume of air K:

$$\epsilon_C = K\overline{\frac{\partial C}{\partial x_j}\frac{\partial C}{\partial x_j}}$$

Introducing the characteristic length scale η_C of the rapid variations of C, $(\delta C)_{\eta_C}$, we can write:

$$\epsilon_C \sim K\left[\frac{(\delta C)_{\eta_C}}{\eta_C}\right]^2$$

We can consider η_C and ϵ_C as the analogous of the dissipative length l_D and the turbulent dissipation ϵ for the Turbulence field: the fluctuations of C are transported through the integral scales to the dissipative scale η_C, where they are dissipated at a rate ϵ_C. The analogous of the two-thirds law of Kolmogorov [Davidson, 2004] for the two-points correlation function S_2^C can be obtained by dimensional analysis, considering that it depends only on ϵ, ϵ_C and r in the isotropic inertial range:

$$S_2^C := \overline{\big(C(x+r) - C(x)\big)^2} = \overline{\big(\delta C\big)^2} \sim \epsilon_C \epsilon^{-1/3} r^{2/3}$$

Assuming that $l_c < l_0$:

$$\epsilon_C = \big(\overline{C^2}\big)_{\eta_C} V l_0^{-1/3} l_C^{-2/3},$$

where V is the characteristic velocity of the large-scale vortices, and the relation $\epsilon \sim V^3/l_0$ has been used. The length scale l_C can be calculated in analogy with the integral length scale l_0 starting from the knowledge of η_C:

$$l_C = (Pe)^{3/4}\eta_C \tag{3.16}$$

where Pe is the Peclet number:

$$Pe = \frac{v_0 l_C}{D}$$

and v_0 is the fluid velocity. Once η_C is known, l_C is determined through an iterative procedure applied to Equation (3.16). We note that the analogy with the Turbulence field applied to the result (3.16) is equivalent to assuming that:

$$\left(\frac{l_C}{l_0}\right)^{1/4}\left(\frac{\nu}{D}\right)^{1/2} \sim 1,$$

and the latter relation can be used to obtain the order of magnitude of l_C too. The values of η_C are given from theoretical and numerical considerations [Davidson, 2004]:

$$\begin{cases} \eta_C \sim l_D\left(\dfrac{\nu}{D}\right)^{-1/2} & \text{for} \quad \nu > \mathrm{D} \\ \\ \eta_C \sim l_D\left(\dfrac{\nu}{D}\right)^{-3/4} & \text{for} \quad \nu < \mathrm{D} \end{cases}$$

The value of V is determined as:

$$V = \frac{K}{l_{mix}},$$

where l_{mix} is an average value of the mixing length associated to the prescription used in the definition of the eddy diffusion coefficient. Finally, we have:

$$\frac{1}{2}\frac{d\overline{C^2}}{dt} \sim -V l_0^{-1/3} l_C^{-2/3}\overline{C^2},$$

so that the operative definition of the characteristic mixing time is:

$$\tau_M \sim \frac{l_0^{1/3} l_C^{2/3}}{V} \tag{3.17}$$

3.3 Turbulent boundary layer solutions

The turbulent boundary layer solutions are analytic solutions of the Turbulence equations obtained in special limiting cases. Singular perturbation analysis [Wilcox, 1998] is applied to the RANS equations, which consists in developing a solution in the form of an asymptotic expansion in terms of a parameter ϵ, uniformly valid for different regions of the domain, the error being small for small values of the parameter. The singular behaviour of the laws of the turbulent boundary layer, described in Section 3.1, is generated by the imposition of the no-slip boundary condition on the wall and by the presence of the turbulent-non turbulent interface in the wake region. The coordinate orthogonal to the boundary must be stretched in terms of the small

parameter ϵ, which represent the dominant physical scale in each of the two regions. In the near-wall region, the small parameter is the reciprocal of the Reynolds number; in the wake region, the small parameter is u_*/U_∞, where the friction velocity represents the intensity of the perturbation from the external velocity U_∞. Each of the two stretched variables are finite in their respective domain, and are infinite and infinitesimal in the matching region respectively. The thickness of the two layers determines the mixing length in the definition of the eddy diffusivity for the two regions. The transport equations, in the turbulent boundary layer form, are approximated to leading order terms in the perturbation expansion, considering that the thickness of the layers are small parameters with respect to the longitudinal mean dimensions of the domain. The solutions have a self-preserving (or self-similar) form, i.e. it can be written in a separated form, such as:

$$u(x,y) = u_*(x) f\left[\frac{y}{\epsilon(x)}\right],$$

where x is the longitudinal and y the orthogonal coordinate (considering for simplicity a two-dimensional flow), $\epsilon(x)$ is a generic stretching, and the term $f[y/(\epsilon(x)]$ depends only on the ratio $y/(\epsilon(x)$ and not on x. A well celebrated hypothesis of Prandtl states that such a self-preserving form of the solution always exists for the boundary layer approximations of the NS equations, which, to leading orders in the expansion parameter, must not contain divergent terms and admit separated solutions in both the inner and the outer layers. We will test this hypothesis in the case of the singular perturbation analysis applied to the canyon geometry. Another context in which a self-preserving form of the solution is supposed is the case of turbulent free-shear layers [Wilcox, 1998], i.e. flows not bounded by solid flows. In the case of the flow in the wake of an object, the free-shear layer regime is situated far enough downstream that the effects of the no-slip boundary conditions on the object boundaries have been dissipated and become unimportant. In such a regime the flow is supposed to approach a self-preserving form, with $\epsilon(x)$ the layer thickness. The boundary layer approximations are applicable asymptotically: even if a solid wall is not present, vorticity is generated at the turbulent - non turbulent interface, and the streamwise gradient of vorticity is small compared with that in the orthogonal direction (considering a two-dimensional wake). It can be still assumed that the departure from the free-stream velocity is small in the far-wake, since the frictional forces tend to make the velocity uniform, and the boundary layer NS equations assume the form of the Oseen equations [Batchelor, 1967].

We will search boundary layer analytical solutions for two kind of flows: the flow in a canyon geometry and the flow in the far wake of a moving vehicle in an open or a canyon street. These analytical solutions will be used to set up the pollutant dispersion models at the canyon scale. Besides this, the analytical solutions for the moving vehicle will be used to calibrate

the Turbulence models numerically solved to describe the near-wake region, to determine critical dimensions for the grid cells near solid boundaries and initial conditions on turbulent quantities (see Sections 3.4, 4.2 for details).

Canyon geometry The flow within a street canyon generated by the wind blowing at the roof level plays an important role in determining pollutant concentrations within a urban street. There have been numerous studies aimed at studying the transport and dispersion of pollutants in individual streets. Most of the studies have been devoted to the particular case of a wind blowing perpendicular to the street axis, where the formation of a wind vortex is observed from wind measurements [Nakamura, Oke, 1988], which generally causes concentration levels greater for the leeward than for the windward side of the canyon [Berkowicz, Kearney, 2004]. Wind tunnel data [Hussain, Lee, 1980] give a systematic classification of flow into three regimes in urban street canyons, based on the canyon geometry: *isolated roughness* flow, *wake interference* flow and *skimming* flow. The canyon geometry is defined by the ratio H/W, where H is the average height of the canyon walls and W is the canyon width. For widely spaced buildings ($H/W < 0.3$), the flow fields associated with the buildings do not interact, which results in the isolated roughness flow regime. At closer spacing ($0.3 < H/W < 0.7$) the wake created by the upwind building is disturbed by the downwind building, creating a downward flow along the windward face of this building. This is the wake interference flow. Even closer spacing results in the skimming flow regime. In this case a stable circulatory vortex is established in the canyon and the ambient flow is decoupled from the street flow. Hotchkiss and Harlow [Hotchkiss, Harlow, 1973] found an analytical solution for the case of wind blowing perpendicularly to an infinitely long canyon with lateral walls of equal height, by solving a diffusion equation for the vorticity in two dimensions with constant turbulent diffusion, without sources or sinks of vorticity inside the domain, and imposing slip-conditions on the velocity at the side walls. This solution, representing one vortex with the kernel in the centre of the two dimensional canyon, is suitable only to describe the skimming flow regime [Berkowicz, Kearney, 2004]. Numerical simulations using 2− equation Turbulence models show the presence of secondary vortices near the corners of the canyon [Berkowicz, Kearney, 2004]. Street pollution models based on dispersion into Puffs (operational models) of the vehicles pollutant emissions inside the canyon, such as the OSPM (Operational Street Pollution Model) [Berkowicz, Kearney, 2004], are based on the Hotchkiss and Harlow or other simplified solutions of the flow, which describe the Puff advection and the dispersion parameters (with suitable parameterization to describe traffic produced turbulence and the thermal state of the atmosphere). In [Soulhac et al., 2008] an analytical solution based on an algebraic turbulence model is found for the case of a wind flowing parallel

to the axis of a symmetric canyon, and numerical simulations are used to study the flow generated by an external wind with any angle relative to the axis of the flow. The algebraic model used in [Soulhac et al., 2008] is based on an eddy viscosity which scales as the distance from the wall in the whole domain of the canyon, with an ad-hoc separation of the domain in order to match the different regions of influence of the side walls.

In Section 4.1 we will study new analytical solutions, based on different algebraic turbulence models for the wall and the wake regions (with a matching naturally incorporated in the turbulence model used), and singular perturbation theory, for both the case of an external wind flowing parallel and perpendicular to the axis of the canyon, for a symmetric (i.e. equal height side walls) canyon with infinite length (homogeneous in the direction along the street axis). We will then characterize the case of arbitrary external angle as in Ref. [Soulhac et al., 2008]. These solutions will be used in the set up of the street pollution dispersion models. In the Appendix the analytical details of the solutions are reported.

Vehicle geometry A model for investigating the behaviour of the far-wake of a vehicle-like geometry will be studied in Section 4.1. In Ref. [Eskridge et al., 1979] a self-preserving solution is obtained in terms of stretched variables with the wake thickness, imposing no-slip boundary conditions at the road boundary. The initial conditions for the wake are determined by integral properties of the flows close to the vehicle, determined by the couple acting on it (the effect, on the downstream motion, of the pressure gradient along the trailing vortices which form in the near wake is shown to be negligible, except in the case of significant shears in the approaching wind, and the vehicle is effectively considered as a point source of momentum). We will consider the so called **Ahmed body** geometry as a simplified geometry to describe different categories of vehicles, as will be shown in Section 3.4. We will use the Eskridge far-wake solutions, driven by an initial integral condition determined by the draft coefficient of the Ahmed body, as measured in wind-tunnel experiments, to set up the pollutant dispersion model at the canyon scale. The effect of the vehicle far-wake interactions will be described through modifications of the initial integral conditions; this will let us to describe traffic situations associated with heavy traffic, and to determine the initial values of turbulent intensity at the inlet boundary for near-wake simulations. In order to calibrate the $k-\omega$ Turbulence model, by choosing the appropriate value of ω_∞ which reproduces the far-wake structure characteristics obtained by the analytical solution of the algebraic model, we will modify the Eskridge solutions, considering a matching with the logarithmic law of the wall as the road surface boundary condition. This will give appropriate values of u_*, which will be used to determine the appropriate dimensions of the first cells of the computational grid near the solid boundary for both the

$k-\epsilon$ and $k-\omega$ Turbulence models.

3.4 Canyon and Wake simulations

Canyon simulations. We will compare our analytical results with numerical simulations of the flow in the canyon, in order to validate the model, using a suitable 2− equation RANS model. The geometry of the canyon is reported in Figure 10, in the case of $W = H = 12m$. In the case of an external wind orthogonal to the street axis ($\theta = \pi/2$), for a street canyon extending to Infinity in the longitudinal direction, the flow is two dimensional (as will be shown in Section 4.1).

Following the classification reported in Ref. [Hussain, Lee, 1980], the isolated roughness flow regime is equivalent to a backward step flow, with adverse pressure gradient of the external stream and strong boundary separation. This flow structure should be described, in the context of RANS simulations, by a Turbulence model which introduces the dynamical description for the length scale of separation, or through a calibrated $k-\omega$ model. As this flow regime is rarely occurring in realistic urban street canyon geometries, we will not consider it. In the wake interference and in the skimming flow regime, a stable vortex is estabilished in the canyon, and the flow separation is driven by the length scales of the canyon (W and H). The $k-\epsilon$ Turbulence model performs well for this kind of flows [Berkowicz, Kearney, 2004], so we choose it to describe the street canyon wind field (the $k-\epsilon$ is more stable and need less computational sources than the $k-\omega$ [Wilcox, 1998] model, whose ω conservation equation has stronger non-linearities than the ϵ equation, and introduces the process of cross-diffusion). We thus consider the stationary solution of the $k-\epsilon$ Turbulence model of Equations (3.1), (3.9), with the closure coefficients given in Table 14, for canyon geometries with aspect ratios $H/W = 1/2; 1; 2$, with a width of $W = 12m$,for different intensities of the external velocity (ranging from 0.5 to 3 m/s).

We now schematically show the setting of boundary conditions, grid generation, discretization and solver procedure for the considered problems.

Boundary conditions and grid generation. At the **wall boundaries** of the canyon, the logarithmic laws of the wall are imposed both for the case of the $2D$ and $3D$ simulations. This means that the computational domain starts from the first grid cell adjacent to the boundary, disregarding the details of the viscous sublayer solution. As told in Section 3.1, the $k-\epsilon$ model is very sensitive to the distance from the wall at which logarithmic laws of the wall are imposed. The analytical solutions of the algebraic models obtained in the case of external flows parallel and orthogonal to the street axis give estimates of the friction velocity u_* in function of the distance along the wall. We use these values (in the case of an external flow with arbitrary angle with respect to the street axis we refer to the estimates in the case of

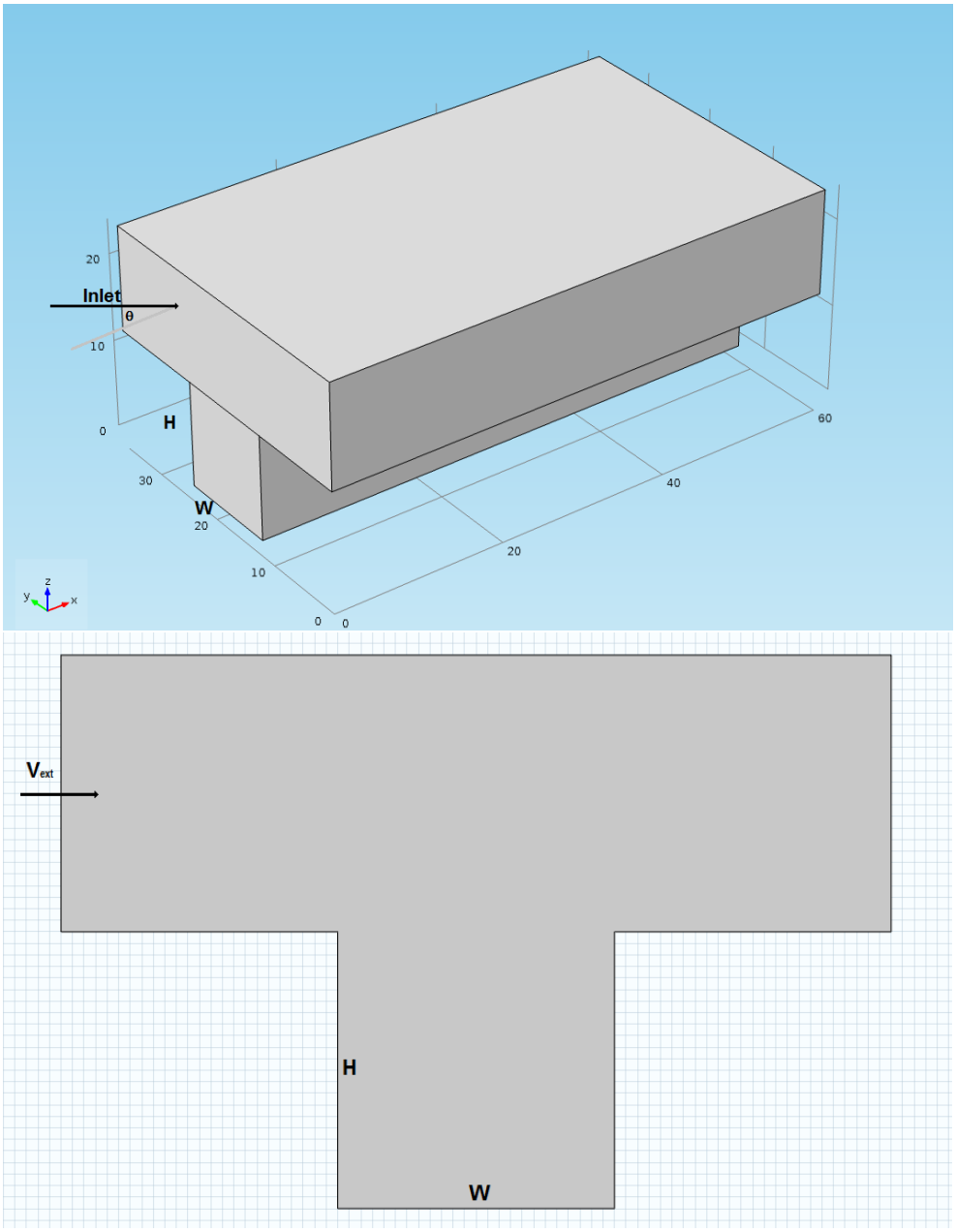

Figure 10: Symmetric canyon geometry with $H = W = 12m$. For the case of an external wind orthogonal to the street axis, the flow is two dimensional (bottom panel).

the orthogonal freestream situation) to determine the distance from the wall at which:

$$\frac{u_* y}{\nu} \sim 100.$$

For turbulent flows with Reynolds number of the order of 10^6 this is the stretched distance from the wall at which the logarithmic laws are valid [Wilcox, 1998]. The values of y goes from $\sim H \cdot 10^{-2}$ to $\sim H \cdot 10^{-3}$. We choose as the maximum dimension of the first cell adjacent to the wall the value of $y = H/100$ in the case of the parallel external flow, and $y = H/1000$ in the case of the arbitrary angle and orthogonal angle ($2D$ simulations) external flows. Solving the $2D$ models in the case of smaller y we have seen that the results remain unchanged. The imposed logarithmic laws are the first Equations in (3.11). The ϵ behaviour in the logarithmic region shows a rapid grow approaching the solid boundary. In order to overcome the propagation of significant numerical errors due to the discretization of derivatives in presence of the singular behaviour (first order polynomial finite elements will be used as the discretization elements), different layers of clustered grids of small dimension immediately adjacent to the boundary will be considered, for which the error in the determination of derivatives is contained. The cell dimension for the main flow region far from solid boundaries is of the order of l_0. In the case of the external flow parallel to the street axis, we consider a mean cell maximum dimension of diameter $H/15$; in the case of an external flow orthogonal to the street axis, we consider as the maximum mean cell dimension the maximum value of the wake thickness δ, calculated in the context of the algebraic Turbulence models, which is of the order of $H/100$. In the latter case there are different length scales, that corresponding to the main vortex recirculation in the canyon and those corresponding to secondary vortices. Thus we have to resolve for smaller mean scales than in the case of the parallel freestream flow. In Figure 11 we show the grid cases for the parallel and the orthogonal ($2D$ geometry) external flow situations, for freestream flow intensity of $1m/s$. The grid is constituted by free tetrahedral and free triangular cells.

The **inlet** conditions are specified at the roof vertical planes (or lines for $2D$ simulations) through which the flow is entering, according to the direction of the external wind (in the case of a parallel external flow, slip conditions are imposed on the lateral vertical roof planes). The inlet boundary conditions consists of a Dirichlet condition for the wind velocity, plus Dirichlet conditions on the turbulent quantities, expressed in terms of a turbulent length scale L_T and a turbulent intensity I_T:

$$k = \frac{3}{2}\big(|U| I_T\big)^2 \qquad ; \qquad \epsilon = C_\mu^{3/4} \frac{k^{3/2}}{L_T} \tag{3.18}$$

where $|U|$ is the external flow norm. Wind tunnel reference values for I_T

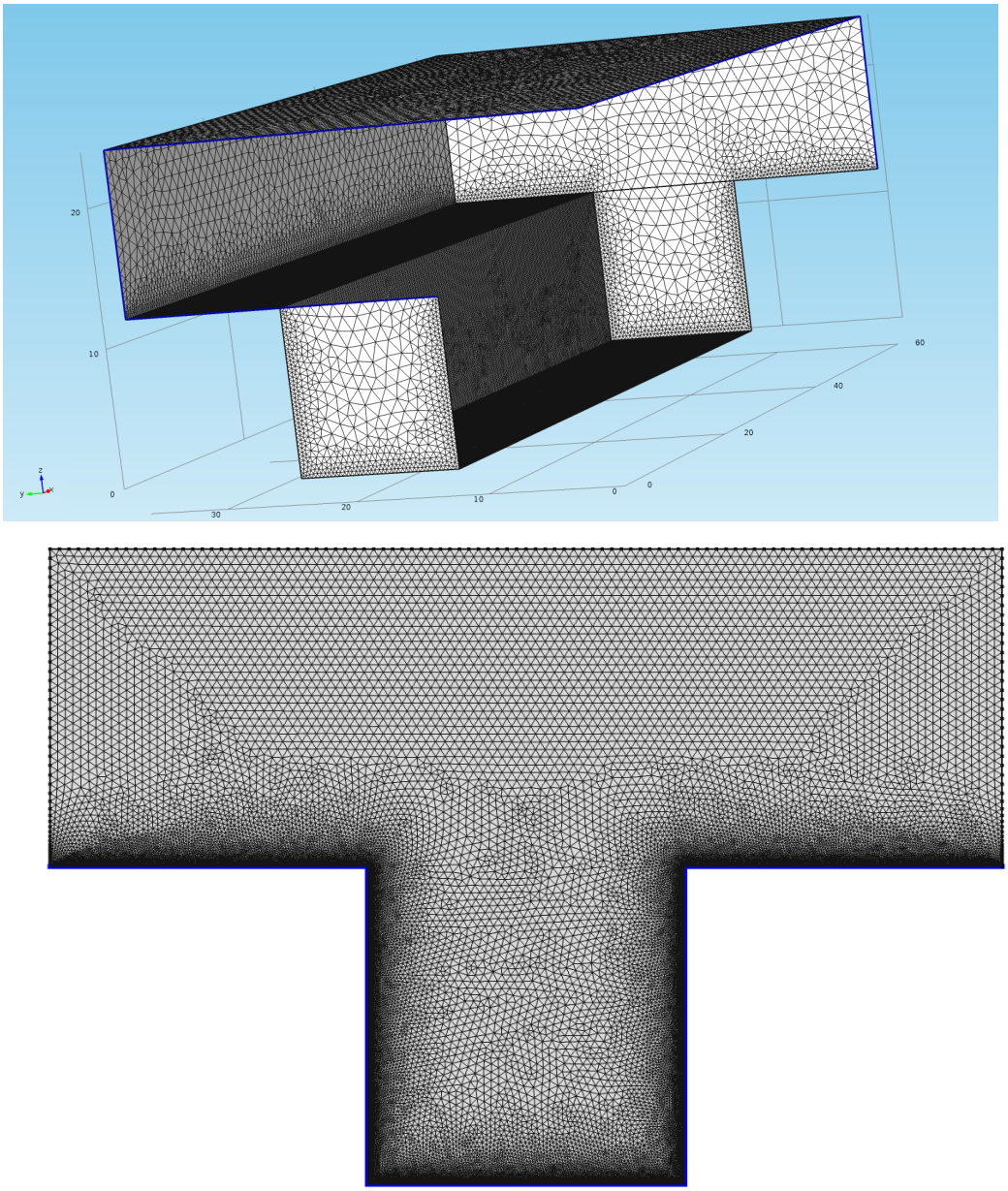

Figure 11: Grid cases for the parallel (upper panel) and the orthogonal ($2D$ geometry, bottom panel) external flow situations, as described in the text.

and L_T are [Wilcox, 1998]: $I_T = 0.05$; $L_T = 0.09H$.

The **outlet** conditions are specified at the roof vertical planes (or lines for $2D$ simulations) through which the flow is flowing out. We choose to specify a Dirichlet condition on the outflow velocity, equal to that for the inlet with opposite directions, for the front roof plane of the canyon, since we consider periodicity in the $x-$ longitudinal direction; a condition on the pressure and the viscous stress is imposed as an outflow condition for the lateral vertical roof planes:

$$p = p_0 \qquad ; \qquad \nu\left(\frac{\partial U_i}{\partial x_j} + \frac{\partial U_j}{\partial x_i}\right) n_j = \mathbf{0} \tag{3.19}$$

where n_j are the components of the normal vector to the boundary. This condition is stable, as it specifies the pressure level. Note that the pressure level p_0 is to be intended as the specification of the hydrodynamic pressure, and can be assumed to be equal to $1atm$ (the pressure variations due to the effect of gravity are included in the definition of the Hydrodinamic pressure). At these outlet boundaries, zero convective flux conditions are imposed on the turbulent quantities.

A **periodicity** boundary condition is imposed at the transversal canyon section planes: the flow at the downstream end is identical to the injected flow at the upstream entry to the canyon section. This enforce the prescription of an infinite canyon in the $x-$ direction.

A slip condition is imposed at the top horizontal plane of the domain, since we are not interested in resolving the flow details near this plane, which has been chosen sufficiently distant from the canyon so that the external flow is purely longitudinal there.

Discretization and solver procedure. We solve the $k - \epsilon$ equations in the context of a finite element discretization. As the finite dimensional subspaces of the Sobolev spaces in which the solutions u and p of the weak equations are defined, we choose first order $(P1 - P1)$ polynomial elements for both the velocity and pressure functions and for the turbulent variables. These finite dimensional subspaces are not *compatible*: they do not satisfy the $inf - sup$ Ladyzhenskaya – Babuška – Brezzi condition [Quarteroni, Valli, 2008], which implies that the basis functions for the pressure must be of lower order than the basis functions for the velocity. This is a necessary condition for the matrix associated to the discretization of a saddle-point problem to be non-singular; this also implies that no spurious pressure modes are allowed, which causes instabilities in the pressure calculation. Since we introduce a streamline diffusion stabilization (Galerkin Least Squares) in order to stabilize the convection-dominated Turbulence equations, it is possible to use equal-order interpolation. Crosswind diffusion [Quarteroni, Valli, 2008] is also added to the weak formulation of the

model, in order to introduce extra diffusion in the sharp turbulent-non turbulent layers, which present weak solutions with discontinuous derivatives [Wilcox, 1998] and would require a very dense mesh to be resolved. The discretized non-linear system can be solved by the application of the iterative Newton method, solving at each iteration step the corresponding linear algebraic system with direct LU factorization methods (in the case of $2D$ simulations) or with the $GMRES$ iterative procedure (in the case of $3D$ simulations), with Geometric Multigrid (GM) smoothers. After some tries, a pseudo-time advancing scheme has been introduced, since the stationary simulations showed very low convergence properties even in the $2D$ cases. The Newton linearization procedure is substituted by a Euler semi-implicit scheme for the time discretization. The pseudo-time step is chosen in function of the local CFL number for each element. The $GMRES$ procedure must be set up with an optimal number of iterations, in order to not fulfill the memory capacity of the calculator. Finally, the Turbulence model equations are solved through a sequentially-implicit method, solving the mean flow and the Turbulence model equations sequentially, with the discretization procedures just described. We have performed the simulations on a multi core parallel computing machine with 24 processors of $8GB$ RAM each, using a commercial code (COMSOL multyphysics) to generate the computational grid and implement the chosen Turbulence model and solvers in a finite element approach.

Wake simulations. For the purpose of validation, the geometry and dimensions of the vehicle are chosen to be the same as those of tested vehicles in previous wind-tunnel experiments. The geometry which has been considered for the shape of the vehicles is given by the so-called Ahmed body. The Ahmed body represents a simplified, ground vehicle geometry of a bluff body type. Its shape, constituted by a parallelepipedal central body, with a round front, a rear slant face and fixed cylindrical wheels, is simple enough to allow for accurate flow simulation, but retains some important practical features relevant to real vehicle bodies. The geometry was first defined by Ahmed [Ahmed, Ramm, 1984]; its aerodynamic properties are known from wind tunnel experiments [Ahmed, Ramm, 1984] [Lienhart, Becker, 2003]. In Figure 12 we show the case of Ahmed body geometry with a rear slant angle of $\alpha = 25\,^\circ$ (corresponding to a reduced geometry associated to a typical Sedan Vehicle (SV)). Dimensions are reduced, with respect to a real vehicle dimensions, by a factor of 4 (because wind tunnel experiments are run with reduced geometries). To obtain the same Reynolds number as real flow situations, velocities in our simulations must be multiplied by 4.

Several inclination angles of the back-side of the vehicles correspond, in terms of the associated turbulence field, to different vehicle classes. $\alpha = 30\,^\circ$ is a critical slant angle for which the topology of the flow is suddenly modified

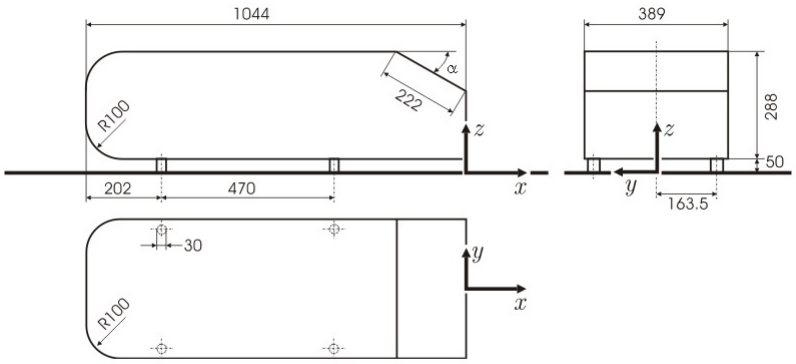

Figure 12: Ahmed body geometry for the case of rear slant angle of 25 °. Units are in mm.

and accompanied by an important decrease of the drag. The structure of the wake consists of a separation zone and counter-rotating vortices coming off the slant side edges, whose strength is mainly determined by the base slant angle. The maximum drag is found for a critical slant angle of $\alpha = 30\,^\circ$. Below this angle, strong counter-rotating vortices are present and the flow separates in the middle region of the top edge and reattaches on the slant, causing a slight increase in the form drag due to the low value of the pressure in the separation zone [Batchelor, 1967]. In this case the flow topology is unsteady. For angles above the critical angle, the counter-rotating vortices are weaker, causing a sudden drop in the induced drag [Batchelor, 1967], and the separation occurs along the entire top and the side edges and there is no reattachment. In this case the flow remains steady. In Figure 13 we show the flow topology of the Ahmed body for the two different slant angles considered in Ref. [Lienhart, Becker, 2003], i.e. $\alpha = 25\,^\circ$ and $\alpha = 35\,^\circ$, with an incoming longitudinal flow of velocity $40m/s$ (left panel); the evolution of the average drag coefficient C_D with the slant angle (right panel), as measured by Ahmed [Ahmed, Ramm, 1984] and by most recent wind tunnel experiments for the case of $\alpha = 25\,^\circ$ and $\alpha = 40\,^\circ$ (VKI2010 results [Tran, 2010]), are reported in the right panel. We can notice the discontinuity in the drag variation above the critical angle.

The drag coefficient is defined as:

$$C_D = \frac{F_D}{\frac{1}{2}\rho U_\infty^2 A} \tag{3.20}$$

where F_D is the drag force on the body, ρ is the air density, U_∞ is the intensity of the incoming flux and A is the projected area of the Ahmed body in longitudinal direction. It is an adymensional parameter describing drag

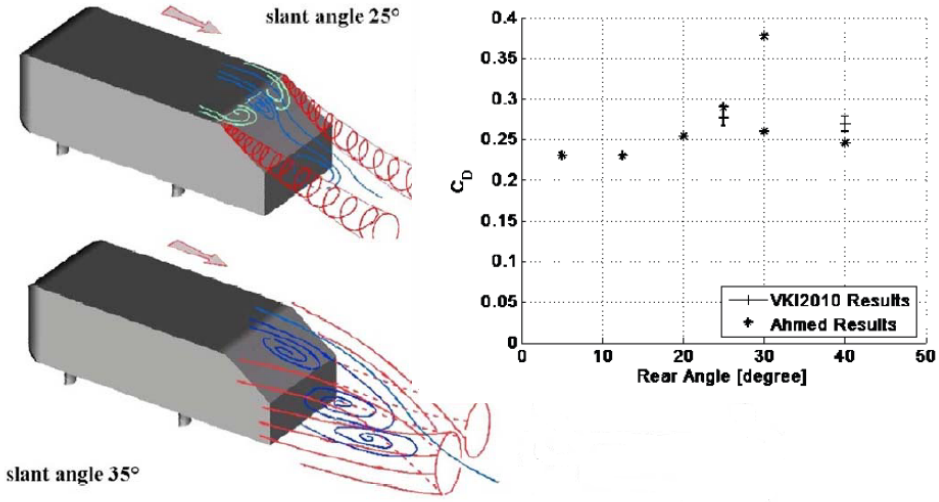

Figure 13: Flow in the wake of the Ahmed car body (left panel) [Lienhart, Becker, 2003], and drag coefficient versus slant angle (right panel) [Ahmed, Ramm, 1984] [Tran, 2010].

forces which depends only on the Reynolds number of the flow $C_D = f(Re)$ [Batchelor, 1967].

The topology of the flow generated by the Ahmed body for subcritical angle ($\alpha = 25\,^\circ$) is comparable with that generated by a SV, with reattachment due to the presence of a trunk at the rear, whereas the topology of the flow generated by the Ahmed body for supercritical angle $\alpha = 40\,^\circ$ is comparable with that generated by a Sport Urban Vehicle (SUV) or a LDV, with large detachment and large eddies or recirculating zones [Koike et al., 2004] [Jindal et al., 2005]. An Ahmed body with a zero rear slant angle is chosen as a simplified geometry for an HDV vehicle [Browand et al., 2009].

The geometry we adopted to describe different classes of vehicles, with respective longitudinal dimensions, are shown in Figure 14.

The domain is open road for extra-urban traffic and a urban canyon for urban traffic conditions.

The RANS Turbulence models overestimates the separation of the flow for the subcritical case, in which unsteady Turbulence is present; this is due to the fact that the assumption of equilibrium Turbulence for the formulation of statistical Turbulence models in terms of dimensional analysis (see Section 3.1 for details) leads to an overestimation of the eddy viscosity: unsteady RANS models are not able to resolve the unsteady Turbulence. LES Turbulence models should be applied in this case, which require more computational resources (typically, the discretization space of a LES model for the Ahmed body must contain $\sim 3 \cdot 10^6$ nodes, based on a Taylor length λ estimation, whereas a RANS model needs $\sim 5 \cdot 10^5$ nodes. Besides this,

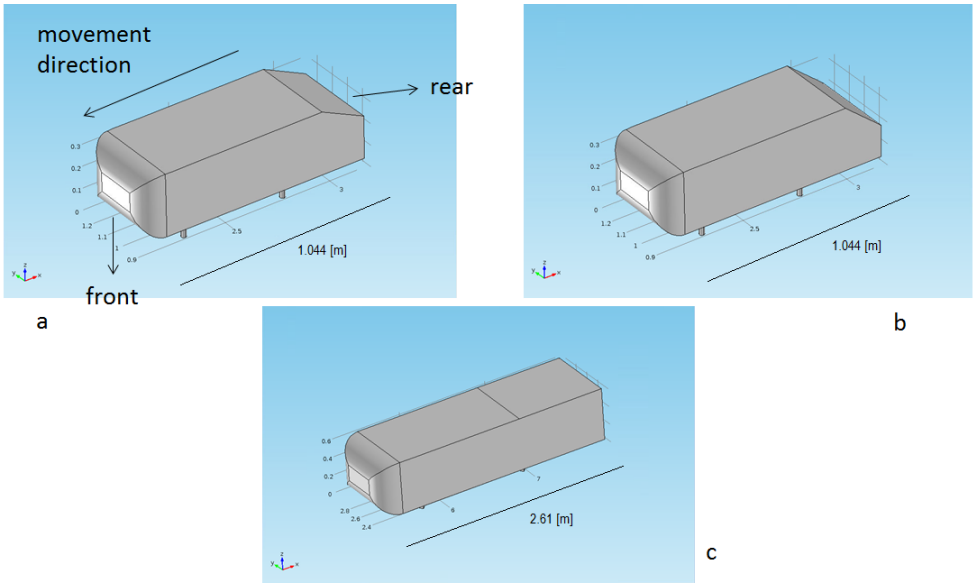

Figure 14: Ahmed body geometry for the case of: a) sedan vehicle (SV), $\alpha = 25\,°$; b) light duty vehicle (LDV), $\alpha = 40\,°$; c) heavy duty vehicle (HDV).

the boundary conditions must be specified in terms of specifical flow realizations for the LES case, and cannot be expressed in terms of mean quantities, such as I_T and L_T). Anyhow, even if the $k-\epsilon$ model is not able to predict the reattachment of the flow after the rear slant edge, it leads to contained errors ($\sim 6\%$) on the drag coefficient with respect to the $k-\omega$ model [Craft et al., 2001]. The supercritical case is associated with a steady Turbulence structure, and should be described by a calibrated $k-\omega$ model or more complex models (see Section 3.1 for details) in order resolve the scale of the large separation of the flow behind the body. We will use the $k-\epsilon$ Turbulence model for the Turbulence field description in the case of the subcritical angle geometry (SV) and in the case of HDV (in this case no counter-rotating vortices develop, the separation structure is simple and the $k-\epsilon$ model leads to good predictions of the measured velocity profiles [Browand et al., 2009]. We will use the $k-\omega$ calibrated Turbulence model for the supercritical case (LDV). We will compare the obtained velocity profiles (for the case of rear slant angles of $\alpha = 25\,°$ and $\alpha = 35\,°$) with the experimental profiles of Lienhart [Lienhart, Becker, 2003] and profiles those obtained by using more complex Turbulence models, reported in literature or occasionally implemented with CFD codes.

The RANS equations are written in the system of reference of the moving vehicle. For an accelerating vehicle, the non-inertial forces are considered as inserted in the hydrodinamic pressure (we consider only constant accelerations, given according to the representative values for European driving cycles reported in Table 5. In this case unsteady RANS model must be

applied, in order to resolve the unsteady mean-flow structures.

In order to calibrate the $k-\omega$ model by determining an appropriate value of ω_∞, we search for self-preserving solutions of the Turbulence equations valid in the far-wake region of an LDV vehicle, and compare them with the analytical solutions obtained using an algebraic model of Turbulence. In Section 4.1 we will find that the self-preserving solution for the longitudinal component of the velocity in the far-wake region of a vehicle moving with velocity U_∞ has the form of a defect law:

$$u(x,y,z) = U_\infty - U_\infty A\left(\frac{x}{h}\right)^{-3/4} f[\eta,\zeta] \tag{3.21}$$

where:

$$\eta = \frac{y}{\delta(x)} \quad ; \quad \zeta = \frac{z}{\delta(x)} \quad \text{with} \quad \delta(\mathrm{x}) = \gamma \mathrm{hA}\left(\frac{\mathrm{x}}{\mathrm{h}}\right)^{1/4};$$

γ is a constant related to the Turbulence intensity, h is the vehicle height and A is a constant depending on the draft on the vehicle (which is determined experimentally). We will prescribe, through the use of initial integral conditions on the vehicle wake, a form of A which contains the informations about vehicle far-wake interactions in a urban driving cycle. A solution of the form of Equation (3.21) has been obtained by Eskridge and Hunt [Eskridge et al., 1979], substituting it in the linearised equation for the conservation of the momentum with an algebraic model of Turbulence, and imposing no-slip conditions at $\eta \to \pm\infty$, $\zeta = 0$ (the road surface boundary) and $\zeta \to \infty$. In the context of the $k-\omega$ model calibration, we will use a far-wake solution of the algebraic Turbulence model equations which vanishes for $\eta \to \pm\infty$ (effectively, which vanishes at boundaries $y = \pm W/2$, as will be explained in Section 4.1) and$\zeta \to \infty$, and which matches with the logarithmic law of the wall for $\zeta \to 0$: we are supposing that the outer region of the boundary layer is being destroyed by the far-wake of the vehicle, which constitute the outer solution with which the inner viscous solution at the solid boundary must match in the context of a singular perturbation analysis. To obtain the corresponding solution of the $k-\omega$ model, we linearise the conservation equations, assuming that the velocity defect in the far-wake is small compared to the freestream velocity ($|u|, |v|, |w| \ll U_\infty$, i.e. the Oseen approximation):

$$\begin{cases} U_\infty \dfrac{\partial u}{\partial x} = \dfrac{\partial}{\partial y}\left[\nu_T \dfrac{\partial u}{\partial y}\right] + \dfrac{\partial}{\partial z}\left[\nu_T \dfrac{\partial u}{\partial z}\right] \\ U_\infty \dfrac{\partial k}{\partial x} = \nu_T\left[\left(\dfrac{\partial u}{\partial y}\right)^2 + \left(\dfrac{\partial u}{\partial z}\right)^2\right] - \beta^* \omega k + \dfrac{\partial}{\partial y}\left[\nu_T \sigma^* \dfrac{\partial k}{\partial y}\right] + \dfrac{\partial}{\partial z}\left[\nu_T \sigma^* \dfrac{\partial k}{\partial z}\right] \\ U_\infty \dfrac{\partial \omega}{\partial x} = \alpha \dfrac{\omega}{k} \nu_T\left[\left(\dfrac{\partial u}{\partial y}\right)^2 + \left(\dfrac{\partial u}{\partial z}\right)^2\right] - \beta \omega^2 + \dfrac{\partial}{\partial y}\left[\nu_T \sigma \dfrac{\partial \omega}{\partial y}\right] + \dfrac{\partial}{\partial z}\left[\nu_T \sigma \dfrac{\partial \omega}{\partial z}\right] \end{cases}$$

Terms containing the pressure p and the v and the w components of the velocity are considered to be small (of the first and of the second order in the small parameter u/U_∞ respectively) with respect to the terms containing u. Note that we do not need to introduce the λ constant in the $\{xy\}$ components of the Reynolds stress to take into account the asymmetry produced by the ground, as in [Eskridge et al., 1979], since this is accounted automatically by the matching procedure with the law of the wall. Let us search a self-preserving solution of the linearised equations of the form of Equation (3.21). We thus make the transformation of variables:

$$\begin{cases} \eta = \dfrac{y}{\delta(x)} \quad ; \quad \zeta = \dfrac{z}{\delta(x)} \quad \text{with} \quad \delta(\mathrm{x}) = \gamma \mathrm{hA} \left(\dfrac{\mathrm{x}}{\mathrm{h}}\right)^{1/4} \\ \dfrac{\partial}{\partial x} = \dfrac{\partial}{\partial x} - \dfrac{\delta'}{\delta}\eta\dfrac{\partial}{\partial \eta} - \dfrac{\delta'}{\delta}\zeta\dfrac{\partial}{\partial \zeta} \\ \dfrac{\partial}{\partial y} = \dfrac{1}{\delta}\dfrac{\partial}{\partial \eta} \\ \dfrac{\partial}{\partial z} = \dfrac{1}{\delta}\dfrac{\partial}{\partial \zeta} \end{cases}$$

and the substitutions:

$$\begin{cases} u = U_\infty - U_\infty A \left(\dfrac{x}{h}\right)^{-3/4} f[\eta, \zeta] \\ k = U_\infty^2 A^2 \left(\dfrac{x}{h}\right)^{-3/2} K[\eta, \zeta] \\ \omega = \dfrac{k^{1/2}}{\delta} = \dfrac{U_\infty}{x} W[\eta, \zeta] \\ \nu_T = \dfrac{k}{\omega} = U_\infty \gamma^2 h A^2 \left(\dfrac{x}{h}\right)^{-1/2} \dfrac{K}{W} \end{cases}$$

The $k - \omega$ equations become:

$$\begin{cases} \dfrac{\partial}{\partial \eta}\left(\dfrac{K}{W}\dfrac{\partial f}{\partial \eta}\right) + \dfrac{\partial}{\partial \zeta}\left(\dfrac{K}{W}\dfrac{\partial f}{\partial \zeta}\right) + \dfrac{1}{4}\left(\eta\dfrac{\partial f}{\partial \eta} + \zeta\dfrac{\partial f}{\partial \zeta}\right) + \dfrac{3}{4}f = 0 \\ \\ \sigma^*\left[\dfrac{\partial}{\partial \eta}\left(\dfrac{K}{W}\dfrac{\partial K}{\partial \eta}\right) + \dfrac{\partial}{\partial \zeta}\left(\dfrac{K}{W}\dfrac{\partial K}{\partial \zeta}\right)\right] - \beta^* KW + \dfrac{K}{W}\left[\left(\dfrac{\partial f}{\partial \eta}\right)^2 + \left(\dfrac{\partial f}{\partial \zeta}\right)^2\right] + \\ \dfrac{1}{4}\left(\eta\dfrac{\partial K}{\partial \eta} + \zeta\dfrac{\partial K}{\partial \zeta}\right) + \dfrac{3}{2}K = 0 \\ \\ \sigma\left[\dfrac{\partial}{\partial \eta}\left(\dfrac{K}{W}\dfrac{\partial W}{\partial \eta}\right) + \dfrac{\partial}{\partial \zeta}\left(\dfrac{K}{W}\dfrac{\partial W}{\partial \zeta}\right)\right] - \beta W^2 + \alpha\left[\left(\dfrac{\partial f}{\partial \eta}\right)^2 + \left(\dfrac{\partial f}{\partial \zeta}\right)^2\right] + \\ \dfrac{1}{4}\left(\eta\dfrac{\partial W}{\partial \eta} + \zeta\dfrac{\partial W}{\partial \zeta}\right) + W = 0 \end{cases} \tag{3.22}$$

The boundary conditions are:

- matching with the solutions in the logarithmic layer (3.11) for $\zeta \to 0$;
- $f = K = W = 0$ for $\eta \to \pm\infty$;
- $f, K \to 0$ and $W \to \omega_\infty$ for $\zeta \to \infty$

Here and in the sequel, homogeneous Dirichlet conditions for k, ϵ and ω are intended to correspond to small values of the turbulent quantities (in the context of RANS Turbulence modeling the Turbulence cannot be zero). For the Inlet Boundary conditions, the values are determined through Equations (3.18) and relation $\omega = \epsilon/(\beta^* k)$; for the Open Boundary conditions, reference values for the turbulence quantities are (see Ref. [Kuzmin et al., 2007]):

$$k_{OB} = 2.5{\cdot}10^{-3}[m^2/s^2] \quad ; \quad \epsilon_{OB} = 1.1{\cdot}10^{-4}[m^2/s^3] \quad ; \quad \omega_{OB} = \epsilon_{OB}/(\beta^* k_{OB}) \tag{3.23}$$

The same values can be chosen for the Open boundary conditions (i.e. for $\eta \to \pm\infty$ and $\zeta \to \infty$) for the self-similar variables K and W (the $x-$dependent factors cancels out in the self-similar forms of the equations (3.22)). We do not investigate the dependence of the solutions on the freestream value of W for $\eta \to \pm\infty$.

We consider the standard values of the closure coefficients, reported in Table 14. Problem (3.22) is a coupled system of non-linear Partial Differential Equations (PDE) in two dimensions. It is simpler than the complete $k-\omega$ problem, and can be integrated on a sufficiently wide rectangle to give the self-preserving forms of f, K, W.

By employing the realizability constraint [Wilcox, 1998]:

$$\nu_T \leq \frac{k}{\sqrt{6}\sqrt{S_{ij}S_{ij}}},$$

which ensures that the diagonal elements of the Reynolds stress tensor be nonnegative (S_{ij} is the mean strain rate tensor), expressed in the self-similar form:

$$\frac{K}{W} \leq \frac{\sqrt{2}K}{\sqrt{3}\sqrt{\left(\frac{\partial f}{\partial \eta}\right)^2 + \left(\frac{\partial f}{\partial \zeta}\right)^2}},$$

we avoid divisions by zero in the System (3.22). This is done by introducing the modified $\hat{W}$ function:

$$\hat{W} = \max\left(W, \frac{\sqrt{3}}{\sqrt{2}}\sqrt{\left(\frac{\partial f}{\partial \eta}\right)^2 + \left(\frac{\partial f}{\partial \zeta}\right)^2}\right)$$

Let us define the *spreading rate* (in the vertical direction) for the far-wake of the vehicle as the arithmetic average of the values of ζ where the velocity defect (at the centerline) is half its maximum value [Wilcox, 1998]. The process of the $k-\omega$ model calibration consists in comparing the spreading rate (in the vertical direction) calculated through the analytical solution of an algebraic model of Turbulence with that calculated through the numerical solution of the System (3.22), varying the value of the freestream value ω_∞. We choose the value that yields the closest spreading rate to that coming from the analytical solution. This is an extension of the calibration procedure reported in Ref. [Wilcox, 1998], formulated for the case of two-dimensional free-shear layers. Results will be shown in Sections 4.1 and 4.2. Finally, we implement the Durbin realizability constraint [Wilcox, 1998], which imposes an upper limit on the turbulent viscosity, in order to avoid the excessive production of Turbulence near the stagnation point on the front face of the vehicle.

We now schematically show the setting of boundary conditions, grid generation, discretization and solver procedure for the considered problems.

Boundary conditions and grid generation. At the **wall boundaries** of the canyon and at the vehicle surface, the logarithmic laws of the wall are imposed. The wall boundary is the road surface in the case of the open street geometry, and the road surface plus the canyon walls in the case of the street canyon geometry. These boundaries are moving with a velocity opposite to the vehicle velocity U_∞ (in the reference frame of the vehicle, in which it is fixed with zero velocity), so that we impose at the canyon boundaries:

$$U - U_\infty = \frac{u_*}{k}\log\left(\frac{u_* y}{\nu}\right) + C.$$

We use the u_* values given by the analytical solutions to determine the distance from the wall of the first grid cell. We choose as the maximum dimension of the first cell adjacent to the street surface a maximum value of $y = L/100$, where L is the length of the vehicle; for what concerns the vehicle surface, we multiply the u_* values by the draft coefficient for eache vehicle face, which is reported in the measurement data of Ref. [Lienhart, Becker, 2003] (for $U_\infty = 40m/s$) and Ref. [Browand et al., 2009]. This gives an indication of the friction for each face of the vehicle, for the different vehicle geometries, and leads to values of $y \sim L/500$. Different layers of clustered grids of small dimension immediately adjacent to the boundary has been considered. The maximum cell dimension Δx for the main flow region far from solid boundaries is determined as $\Delta x/\delta = 0.1$, where δ is the wake thickess calculated through the algebraic Turbulence model; this is an optimal measure to resolve the wake mean scales for the boundary-layer equations [Wilcox, 1998].

The domain dimension goes from distance $2L$ in front of the vehicle

to $7L$ behind it; considering the specific dimensions of the Ahmed body, this means that the domain extends to $\sim$ 21 times the vehicle heigth h behind the vehicle. We thus resolve all the near wake and a portion of the far wake region, which, according to Ref. [Eskridge et al., 1979], begins at $\sim 15h$ distance behind the vehicle. In Figure 15 we show the grid cases for the different geometries of the Ahmed body, for freestream flow velocity of $40m/s$. The grid is constituted by free tetrahedral cells. To demonstrate the grid independence on the results, we will perform an adaptive mesh refinement based on the equation residuals, which will be shown in Section 4.2. The fact that we are using first order Lagrange elements, while the equation residuals contain second derivative terms, is not a problem since the equations are convected dominated, and the viscous layers are nor resolved.

We note that a grid generation procedure based on a block partition of the domain, reducing the main grid dimensions in a domain region corresponding to a block containing the immediate near-wake of the vehicle, has lead to non convergent simulations, due to the bad quality of the generated meshes. In the reported cases the minimum aspect ratio of the mesh is ~ 0.5, with an average value of ~ 0.9.

The **inlet** conditions are specified at the front transversal plane of the street through which the flow is entering. The inlet boundary conditions consists of a Dirichlet condition for the wind velocity, plus Dirichlet conditions on the turbulent quantities, expressed in terms of a turbulent length scale L_T and a turbulent intensity I_T, as defined in Equations (3.18). We use the values:

$$I_T = \frac{u_{fw}}{U_\infty} \quad ; \quad L_T = \delta(x) \tag{3.24}$$

where u_{fw} is the maximum value (i.e. the value at the center-line for $z = \delta(x)$) of the far wake defect velocity $(u - U_\infty)$ of a preceding vehicle at the inlet, considering the inlet plane as positioned at a distance from a preceding vehicle determined by the considered driving condition statistics. In a same manner, $\delta(x)$ is the value of the far-wake thickness of a preceding vehicle at the inlet. In the case of non-interacting wake conditions the reference values of wind tunnel experiments can be considered, and the Dirichlet condition for the velocity is $u = U_\infty$. In the case of interacting wakes, the values of Turbulence intensity can reach the levels of 15%, and a reduced constant value for the inlet velocity is considered, as will be shown in Section 4.2.

The **outlet** conditions are specified at the bottom transversal planes of the canyon through which the flow is exiting. We choose to specify a Dirichlet condition on the pressure as an outflow condition ($p = p_0 = 1atm$), which has shown to lead to more convergent results than the pressure - no viscous stress condition in $2D$ test cases for the flow on the Ahmed body; zero convective flux conditions are imposed on the turbulent quantities.

Open boundary conditions are imposed at the top horizontal plane of

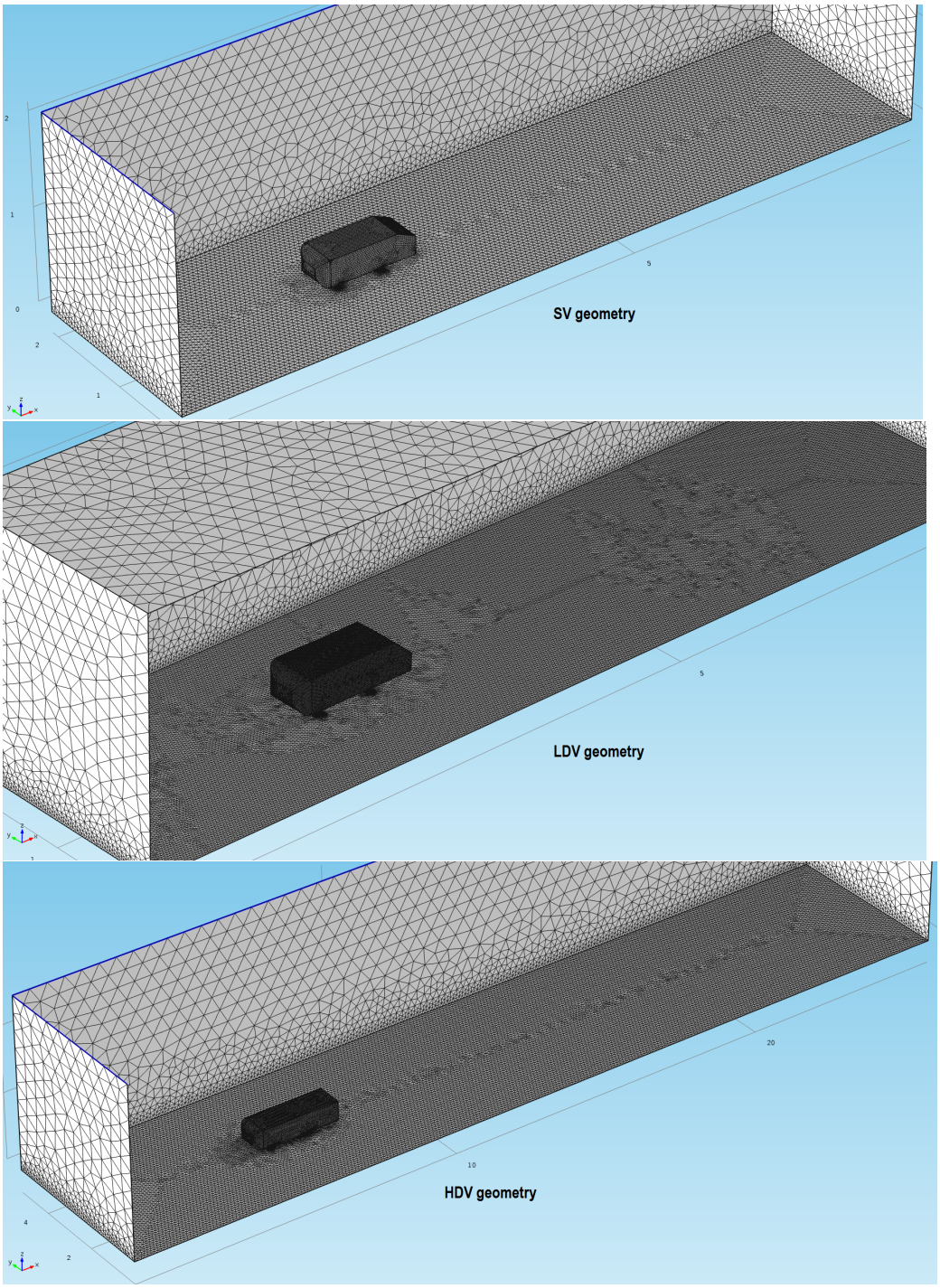

Figure 15: Grid cases for the different geometries of the Ahmed body, for freestream flow velocity of $40m/s$, as described in the text.

the canyon. In this case, a *non-friction* normal stress condition is imposed for the momentum equations, implying that the total stress in the tangential direction is zero:

$$[-pI_{ij} + 2(\nu + \nu_T)S_{ij}]n_j = -p_0 n_i,$$

where I_{ij} is the identity tensor. In the case of the $k-\epsilon$ model simulations, homogeneous Dirichlet conditions corresponding to (3.23) are prescribed for the Turbulence variables. In the case of the $k-\omega$ model simulations, Dirichlet conditions are imposed on the turbulent quantities, as previously discussed:

$$k = 0 \quad ; \quad \omega = \omega_\infty$$

In the case of the open street geometry, open boundary conditions are imposed on the side planes of the canyon, imposing non friction conditions for the total stress and homogeneous Dirichlet conditions for the Turbulent variables.

When the vehicle is moving with a constant acceleration, we consider unsteady RANS simulations, and an initial condition $U = U_v$ must be considered. An initial guess for the turbulent quantities, based on wind tunnel measurments, is [Kuzmin et al., 2007]:

$$k_{in} = \left(\frac{100\nu}{\delta}\right)^2 \quad ; \quad \epsilon_{in} = \frac{C_\mu k_{in}^{3/2}}{0.1\delta} \quad ; \quad \omega_{in} = \frac{\epsilon_{in}}{k_{in}}$$

We must note that the unsteady RANS Turbulence models cannot be applied to vehicles starting from zero velocity, cause the equations are singular for zero values of the turbulent quantities. Even if we prevent the division by zero by introducing upper limits on the mixing length, the models can only describe situations with non-zero Turbulence. For this reasons, when traffic statistics contain sectors with vehicle velocity starting from zero, we consider an initial small velocity (i.e. $U_\infty = 0.1m/s$). An initialization of the Turbulence model by analytical solutions of laminar boundary layer grow approximation [Batchelor, 1967] will be carried out in future investigations.

Discretization and solver procedure. We choose first order ($P1-P1$) piecewise polynomial elements for both the velocity and pressure functions and for the turbulent variables. We introduce a streamline diffusion stabilization (Galerkin Least Squares) in order to stabilize the convection-dominated Turbulence equations, and crosswind diffusion [Quarteroni, Valli, 2008], in order to introduce extra diffusion in the sharp turbulent-non turbulent layers, which present weak solutions with discontinuous derivatives [Wilcox, 1998] and would require a very dense mesh to be resolved. The discretized non-linear system is resolved, in the case of stationary simulations, by a pseudo-time advancing scheme, using an operator splitting Peaceman-Rutherford

scheme [Quarteroni, Valli, 2008] for each time step iteration. At each iteration step the corresponding linear algebraic system are solved with the $GMRES$ iterative procedure, with Geometric Multigrid (GM) smoothers. The pseudo-time step is chosen in function of the local CFL number for each element. The $GMRES$ procedure must be set up with an optimal number of iterations, in order to not fulfill the memory capacity of the calculator. The time dependent discretized equations are solved by a fractional step projection method [Quarteroni, Valli, 2008] based on a BDF differencing scheme and a pressure correction scheme, for the U and p variables, and a BDF Euler semi-implicit scheme for the turbulent variables. This method has shown faster convergence times than a Euler semi implicit method applied to all the valiables, which has been firstly applied. The choice of the time-step is a crucial point in obtaining convergent and accurate solutions. The discretized turbulent transport equations constitutes a stiff system: the time scale introduced by the rate of decay of Turbulence, $t_{diss} \sim k/\epsilon \sim 1/\omega$ varies on a wide spectrum of scales. We consider a time step based on the wave propagation and molecular diffusion Courant numbers. As the time integration algorithms introduced are unconditionally stable for both the momentum and the turbulent variables approximations, the problem is with accuracy and convergence time. We have found that, using the BDF differencing scheme in the initial stages of computation, and changing to a more accurate generalized alpha difference scheme, eventually lowering the time step, when the convergence properties of the solutions begin to get worse (observing the convergence plot while solving), a good final solution is obtained. Finally, the Turbulence model equations are solved through a sequentially-implicit method, solving the mean flow and the Turbulence model equations sequentially, with the discretization procedures just described.

3.5 Pollutant dispersion

Let us set up the operational and the numerical models for the dispersion of the Soot and the road dust component, starting from the dispersion Equation (3.14).

Operational models An empirical model derived on the basis of pollution measurements in canyon streets of San Jose and St. Louis is the *STREET model* by Johnson et al. (1973) [Berkowicz, Kearney, 2004]. The model assumes that the emission concentrations (in mg/m^3) from the local street traffic (C_s) are added to the pollution present in the air that enters from the roof level (C_b). The street contribution is given by:

$$C_s = \frac{K}{u+u_s}\sum_i \frac{Q_i}{\left[\left(y_i^2+z^2\right)^{1/2}+h_0\right]} \quad \text{for the } \textbf{leeward} \text{ side;}$$

$$C_s = \frac{K}{u+u_s}\frac{H-z}{H}\sum_i \frac{Q_i}{W} \quad \text{for the } \textbf{windward} \text{ side.}$$

K is an empirical constant ($K \sim 7$); u_s accounts for the mechanically induced air movement caused by the traffic flow ($u_s \sim 0.5m/s$); u is the magnitude of the roof-level wind speed component orthogonal to the street axis; h_0 accounts for the initial mixing of the pollutants $h_0 \sim 2m$; Q_i is the emission strength of the $i-$th traffic lane (in mg/ms); y_i and z are the horizontal and the vertical distances from the $i-$th traffic lane to the receptor point (thus the parametrization is $2-$ dimensional, and homogeneity in the longitudinal direction is considered; H and W are the height and the width of the canyon, respectively. The model is valid for external winds blowing at an angle of more than 30° to the street canyon axis: in this cases, a helical recirculation develops in the street [Berkowicz, Kearney, 2004], causing the pollutants emitted from traffic in the street to be primarily transported towards the upwind building (leeside), while the downwind side is primarily exposed to background pollution and pollution that has recirculated in the street. The model predicts thus that the concentrations on the leeward side of the street are higher than on the windward side. These are the most essential features of pollutant dispersion in street canyons and therefore the STREET model is still widely used. Besides this, the STREET model is based on the assumption that the dilution of pollutants emitted form the vehicles is proportional to the distance from the source to the receptor (see formula in Section 3.2), which is a valid assumption for the short source-receptor distances in street canyons [Berkowicz, Kearney, 2004].:

$$\sigma_z \sim \left(y_i^2+z^2\right)^{1/2}.$$

A puff in a direction determined by the vector component (y_i, z), advected by the ground level wind component in the helical recirculation, is being considered. If the roof level wind direction is at angle θ_∞ with respect to the street axis, then the street level wind in the helical recirculation zone forms an angle θ_∞ with the street axis too, but the transverse component is mirror reflected [Berkowicz, Kearney, 2004] (see also the results reported in Section 4.2). Outside the recirculation zone the wind direction is the same as at roof level. No diffusion in the longitudinal direction is considered in the empirical parametrization of the model. To modify this empirical model in order to take into account the deposition and resuspension processes, we can proceed in the following manner:

- **Soot dispersion** case: in Ref. [Rao, 1981] an analytical solution of a simplified gradient-transfer model is given, which estimates the decrease of the emission intensity Q moving along the direction of transportation due to the effect of deposition:

$$Q = Q_0 \exp\left[-\sqrt{\frac{2}{\pi}}\frac{v_d(z)}{V}\int_0^x \frac{dx}{\sigma_z \exp\left(H^2/2\sigma_z^2\right)}\right] \tag{3.25}$$

where Q_0 is the emission rate at the emission point (we are considering the case of one traffic lane), $v_d(z)$ is the deposition velocity at the height z of the emission point, and V is the advection velocity in the direction x. In our case, the plume is advected in a direction orthogonal to the street axis, $V = u + u_s$ and the integration is in the variable y. Considering the deposition at the road surface level $v_d(0)$ (the same used in Equation (2.3); we consider that the emission point is at $z = 0$) and the form for σ_z introduced previously, we have:

$$Q = Q_0 \exp\left[-\sqrt{\frac{2}{\pi}}\left(\frac{v_d(0)}{u+u_s}\right)\int_0^y \frac{\exp -\left(H^2/2y^2\right)}{y}\, dy\right]$$

We are not considering the deposition process for the background concentration c_b, whose value is assumed to be stationary. The integral in the last expression can be expressed in terms of the *incomplete Gamma* function ([Bateman, 1953]):

$$\Gamma(0,x) = \int_x^\infty e^{-t}t^{-1}\, dt.$$

Taking the substitution:

$$t \to \frac{A}{t'^2}$$

we have:

$$\Gamma(0,x) = 2\int_0^{\sqrt{A/x}} \frac{e^{-A/t'^2}}{t'}\, dt'.$$

We have thus:

$$Q = Q_0 \exp\left[-2\sqrt{\frac{2}{\pi}}\left(\frac{v_d(0)}{u+u_s}\right)\Gamma\left(0,\frac{H^2}{2y^2}\right)\right] \tag{3.26}$$

In Figure 16 we show the behaviour of the term $\exp\left[-\Gamma\left(0,\frac{1}{x^2}\right)\right]$. Its value is 1 near the emission point $y = 0$, and decays moving towards the canyon wall at the leeward side.

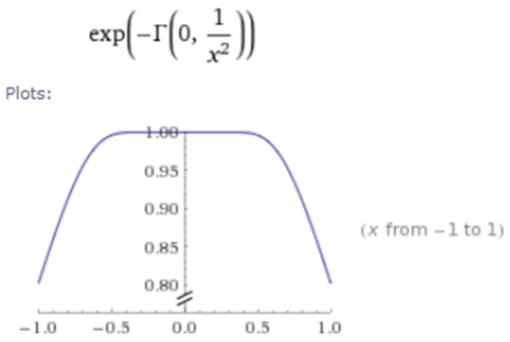

Figure 16: Behaviour of the term $\exp\left[-\Gamma\left(0, \frac{1}{x^2}\right)\right]$.

The modified contributions for the leeward and the windward side, corresponding to one traffic lane, are thus:

Leeward side :

$$C_s = \left(\frac{K}{u+u_s}\right) \frac{Q_0 \exp\left[-2\sqrt{\frac{2}{\pi}}\left(\frac{v_d(0)}{u+u_s}\right)\Gamma\left(0, \frac{H^2}{2y^2}\right)\right]}{\left[\left(y_i^2+z^2\right)^{1/2}+h_0\right]} \tag{3.27}$$

Windward side :

$$C_s = \left(\frac{K}{u+u_s}\frac{H-z}{H}\right) \frac{Q_0 \exp\left[-2\sqrt{\frac{2}{\pi}}\left(\frac{v_d(0)}{u+u_s}\right)\Gamma\left(0, \frac{2H^2}{W^2}\right)\right]}{W}$$

- **Road dust dispersion** case: the road dust emission source is distributed along all the width of the canyon. The appropriate emission rate (in mg/ms) is:

$$dQ = k_{res} P_s \, dy,$$

where the terms have the same meaning of those contained in the resuspension flux term in Equation (2.4). Here we have substituted c_s with P_d to avoid confusion with the street contribution term C_s. An integration over the street canyon width must be performed to consider the road dust emission charge at a distance y from the street axis (assumed at $y = 0$). In this model we cannot consider the deposition contribution to C_s (observe that $\partial C_s/\partial z|_{z=0}$ is zero except at $y = 0$).

We consider a stationary value of P_d, as in Equation (2.6), and neglect deposition. The value for the leeward contribution is given by:

$$C_s = \frac{K}{u+u_s} k_{res} P_s \int_0^y \frac{dy}{\left[\left(y^2+z^2\right)^{1/2}+h_0\right]}$$

The integral can be easily obtained by standard methods in terms of arctan and log functions. Considering that $h_0 = 2m$, we have the following modified contributions for the leeward and the windward side, corresponding to one traffic lane:

Leeward side :

$$C_s = \left(\frac{K}{u+u_s}\right) k_{res} P_s \left\{ \log\left(y+\sqrt{y^2+z^2}\right) - \log z - 2\frac{\left[\arctan\left(\frac{y}{\sqrt{z^2-4}}\right) - \arctan\left(\frac{2y}{\sqrt{z^2-4}\sqrt{y^2+z^2}}\right)\right]}{\sqrt{z^2-4}} \right\} \tag{3.28}$$

Windward side :

$$C_s = \left(\frac{K}{u+u_s}\frac{H-z}{H}\right)\frac{k_{res} P_s}{2}$$

Note that the solution for the leeward side is well defined: expanding the arctan in Taylor series around any finite point y we see that the singularity in $z = h_0$ is cancelled out. Besides this, the solution is real $\forall z$: when $z^2 < 4$, the arctan functions becomes $\arctan h$ functions and are purely imaginary for $y < 2$ (in the case $z = 0$, but this fact can be easily extended to all $z^2 < 4$, expressing the $\arctan h$ in terms of logarithms), and when $y > 2$ the real parts of the two arctan functions cancel out, as well as the singularity for $y = 2$. The only singularity is for $z = 0$ in the $\log z$ term, corresponding to the layer of concentration at the boundary. In Figure 17 we show the behaviour of the leeward solution for different values of z. We can see that increasing z the concentration values diminish; for a fix z, the concentration value increases with y, as should be expected.

The Equations (3.27) and (3.28) define an operational model, which we call **Model A**, which is valid in the hypothesis of the Street empirical model: i) canyon geometry; ii) external wind blowing at an angle $> 30°$ relative to the street axis (or, at least, presence on an helical wind recirculation in the canyon). We consider constant values of the parameters $v_d(0)$ and k_{res} across the canyon; these values must be determined as integral average values of this parameters across the street, and depend on the driving cycle. Results

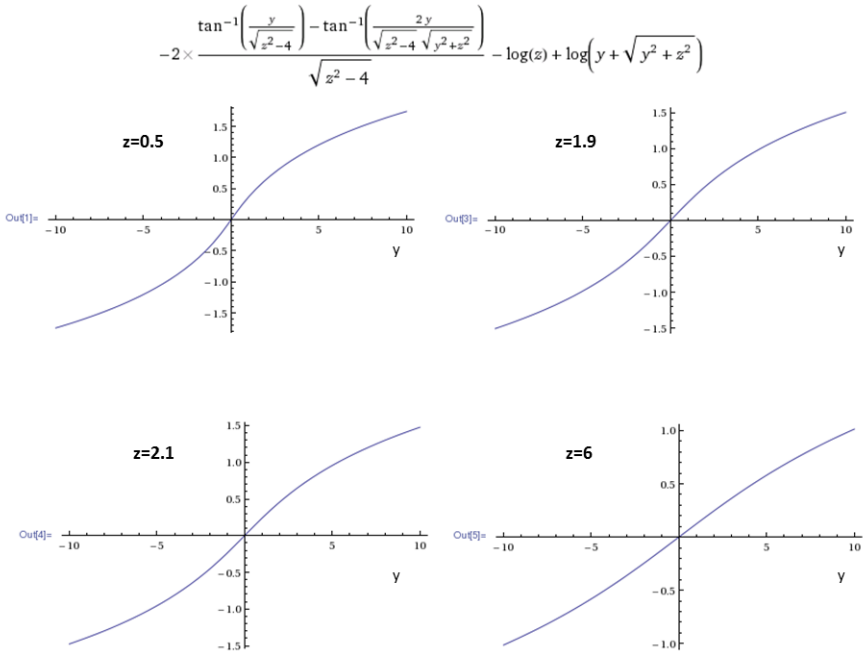

Figure 17: Behaviour of the leeward solution for different values of z: $z = 0.5, 1.9, 2.1, 6\,[m]$.

of the application of this model will be reported in Section 4.4. We must observe that this model requires very few computational resources, consisting in calculating the values of transcendental and special functions on the plane canyon domain.

Another operational model can be derived starting from the formulation of the *Operational Street Pollution Model* ($OSPM$) [Berkowicz, Kearney, 2004]. In $OSPM$ the concentrations of exhaust gases are calculated using a combination of a plume model, for the direct contribution of vehicle emitted pollutants, and a box model [Seinfeld, Pandis, 2006], that enables computation of the additional impact due to pollutants recirculated within the street by the vortex flow. This dispersion model makes use of a very simplified parameterization of flow and dispersion conditions in a street canyon, deduced from extensive analysis of experimental data and model tests. The direct contribution is calculated assuming that both the traffic and traffic emissions are uniformly distributed across the canyon, treating the emission field as a number of infinitesimal line sources aligned perpendicular to the wind direction at the street level, with thickness dy. The line sources are treated as infinite in the longitudinal direction; the problem is thus two dimensional, and a Gaussian solution is used to determine the contribution to the concentration at a point located at a distance y from the line source at

the ground level:

$$dC_s = \sqrt{\frac{2}{\pi}} \frac{dQ}{u_g \sigma_z(y)},$$

where u_g is the ground-level wind in the y direction, which advects the plume across the canyon, and $\sigma(z)$ is the vertical dispersion parameter at a downwind distance y. This contribution must be integrated along the wind path at the street level. The integration path depends on the extension of the recirculation zone. For a receptor on the leeward side, the direct contribution is calculated considering the emissions from traffic in the recirculation zone only. The total concentration at the leeward side must be computed as a sum of the direct contribution and the recirculation component C_r. For a receptor on the windward side, only contributions from the emissions outside the recirculation zone are taken into account. If the recirculation zone extends through the whole canyon, no direct contribution is given for the receptor on the windward side, and the only contribution is from the recirculation component. The latter contribution is calculated assuming a simple box model [Seinfeld, Pandis, 2006], i.e. a conservation of mass equation inside the volume of the whole canyon, assuming that the pollutants are perfectly mixed inside it : the inflow rate of the pollutants into the recirculation zone is equal to the outflow rate. In Ref. [Berkowicz, Kearney, 2004] the recirculation zone is assumed to have the form of a trapeze, on the sides of which the inflow and outflow fluxes must be calculated. When the vortex is totally immersed inside the canyon, the recirculation contribution is:

$$C_r = \frac{Q}{\sigma_{wt} W}, \tag{3.29}$$

where σ_{wt} is the canyon ventilation velocity, determined by the turbulence at the top of the canyon, which is expressed in terms of the roof-level wind speed u_t and the traffic produced turbulence σ_{tpt} as:

$$\sigma_{wt} = \left[\left(0.1 u_t\right)^2 + 0.4 \sigma_{tpt}^2 \right]^{1/2}$$

No dependence on the atmospheric stability is supposed. The dispersion parameter of the plume advected in the y direction is expressed in function of the mechanical Turbulence at the ground level:

$$\sigma_z(y) = \sigma_w \frac{y}{u_g} + h_0,$$

where σ_w is the vertical turbulent velocity fluctuation, parametrized as:

$$\sigma_w = \left[\left(0.1 u_g\right)^2 + \sigma_{tpt}^2 \right]^{1/2}$$

The value 0.1 corresponds to typical levels of mechanically induced turbulence [Berkowicz, Kearney, 2004]. The traffic produced Turbulence is described on the basis of the production-dissipation balance for turbulent kinetic energy generated by a single vehicle or a row of vehicles in a street canyon [Di Sabatino et al. I, 2003]. The number of vehicles producing Turbulence, the averaging volume in which Turbulence is produced and the length scale of dissipation of turbulent kinetic energy must be chosen depending on the particular traffic conditions. The results for the average values of traffic produced Turbulence are:

$$\begin{aligned}
\sigma_{tpt}^2 &= c_4 \cdot n_v \cdot C_D^{2/3} \cdot V^2 \cdot \frac{h^3}{S_c} \qquad \textbf{Light} \text{ Traffic Density} \\
\sigma_{tpt}^2 &= c_5 \cdot \left(n_v \cdot C_D\right)^{2/3} \cdot V^2 \cdot \frac{h^2}{S_c^{2/3}} \qquad \textbf{Intermediate} \text{ Traffic Density} \\
\sigma_{tpt}^2 &= c_6 \cdot C_D^{2/3} \cdot V^2 \cdot \frac{h^{4/3}}{S_c^{2/3}} \qquad \textbf{Heavy} \text{ Traffic Density}
\end{aligned} \tag{3.30}$$

where n_v is the number of vehicles per unit length, expressed in terms of the length of the street and the distance between the vehicles (given by traffic statistics); C_D is the average drag coefficient of the vehicles; V is the vehicle speed; h is the geometrical length scale of the vehicles (i.e. the frontal area of the vehicle, used in defining the drag coefficient); S_c is the cross-section area in the canyon in which traffic produced Turbulence is active (i.e. $W \cdot H$ in the case of Turbulence averaged over the whole canyon). Note that, in the case of heavy traffic density, the average drag coefficient of the vehicles is reduced from the single vehicle drag coefficient correspondent to the traffic velocity V, since the spacing between the vehicles decreases. This effect of wake interactions will be described in Section 4.1. The empirical constants in Equation (3.30) are determined from wind tunnel measurments [Kastner-Klein et al. II, 2003], in the case of Light and Intermediate traffic density. For the Heavy traffic density, we use a parametrization based on values introduced in [Berkowicz, Kearney, 2004] (where a parametrization constant b is introduced):

$$\begin{aligned}
c_4 &= 0.06 \\
c_5 &= 0.007 \\
c_6 &= \frac{b \cdot (S_c)^{2/3}}{C_D^{2/3} h^{4/3}}
\end{aligned} \tag{3.31}$$

where the average drag coefficient of the vehicles must be calculated considering the vehicle wakes interaction, as will be explained in Section 4.1. The parameter b is estimated to be equal to $b = 0.000126$.

Now we want to generalize the *OSPM* model, in order to take into account the deposition and resuspension processes, to consider open road and street canyon geometries, and to treat the cases in which the external wind at the roof level generates an helical recirculation inside the canyon or a longitudinal wind flux. To do this, we consider the solution of the dispersion Equation (3.14) as a superposition of different Puff solutions, with a structure depending on the street geometry and the wind flux at the street level. We obtain the Puff solutions by means of the *Green propagation* method [Morse, Feshbach, 1953]. Let us specialize this method to the case of the diffusion equation:

$$\frac{\partial C}{\partial t} - K_{xx}\frac{\partial^2 C}{\partial x^2} - K_{yy}\frac{\partial^2 C}{\partial y^2} - K_{zz}\frac{\partial^2 C}{\partial z^2} = S(x,y,z,t) \tag{3.32}$$

where the eddy diffusivity components are considered as constants for each Puff solution. Note that, for a Puff solution advected in the x direction with a constant velocity U (the same is valid considering advection in the y and z direction), Equation (3.14) reduces to Equation (3.32), changing to the characteristics coordinate $x \to \xi = x - Ut$. The distribution equation for the corresponding Green function $G(x-x_0, y-y_0, z-z_0, t-t_0)$ is:

$$-\frac{\partial G}{\partial t} - K_{xx}\frac{\partial^2 G}{\partial x^2} - K_{yy}\frac{\partial^2 G}{\partial y^2} - K_{zz}\frac{\partial^2 G}{\partial z^2} = \delta(x-x_0)\delta(y-y_0)\delta(z-z_0)\delta(t-t_0) \tag{3.33}$$

Now multiply Equation (3.32) by G and Equation (3.33) by C, subtract the resultant equations, and integrate over space and over time (from $t = 0$ to $t = t^+$), applying the Green formula for integration in a simply connected domain [Morse, Feshbach, 1953]

$$\int [\mathrm{div}(\nabla \mathrm{G})]\mathrm{C}\,\mathrm{dV}_0 = -\int \nabla \mathrm{G}\cdot\nabla \mathrm{C}\,\mathrm{dV}_0 + \int (\nabla \mathrm{G}\cdot \mathrm{n})\,\mathrm{C}\,\mathrm{dS}_0,$$

where dV_0 indicates integration in the (x_0, y_0, z_0) volume, dS_0 indicates integration on the boundary surface, and n is the unit vector normal to the

boundary. We obtain:

$$
\begin{aligned}
C(x,y,z,t) &= \int_0^{t^+} dt_0 \int dV_0 G(x-x_0, y-y_0, z-z_0, t-t_0) S(x_0, y_0, z_0, t_0) \\
&+ \int dV_0 [C(x_0, y_0, z_0, t_0) G(x-x_0, y-y_0, z-z_0, t-t_0)]_{t_0=0} \\
&+ K_{xx} \int_0^{t^+} dt_0 \int dS_0 \left[G \frac{\partial C}{\partial x_0} n_{x_0} - C \frac{\partial G}{\partial x_0} n_{x_0} \right] \\
&+ K_{yy} \int_0^{t^+} dt_0 \int dS_0 \left[G \frac{\partial C}{\partial y_0} n_{y_0} - C \frac{\partial G}{\partial y_0} n_{y_0} \right] \\
&+ K_{zz} \int_0^{t^+} dt_0 \int dS_0 \left[G \frac{\partial C}{\partial z_0} n_{z_0} - C \frac{\partial G}{\partial z_0} n_{z_0} \right]
\end{aligned}
\tag{3.34}
$$

The first term on the right hand side represents the propagation of the source term; the second term represents the influence of the initial conditions; the remaining terms represent the propagation of inhomogeneous boundary conditions. If we consider inhomogeneous boundary conditions applied only at the road surface ($z = 0$, $n = (0, 0, n_z)$), by choosing a Green function with the same homogeneous boundary conditions as C on the $x = c$ and $y = c$ boundaries (in a prism domain, where c is a generic constant) the third and the fourth terms on the right hand side vanish. To consider the deposition and the resuspension processes, we apply the boundary conditions (see Equations (2.3) and (2.4), with a stationary value for the road dust concentration, which enables to neglect the θ_0 term):

$$
\begin{aligned}
K_{zz} \frac{\partial C}{\partial z} &= -v_d(0) C \quad \text{for} \quad \textbf{Soot} \quad \text{dispersion} \\
K_{zz} \frac{\partial C}{\partial z} &= -v_d(0) C + k_{res} c_s \quad \text{for} \quad \textbf{road dust} \quad \text{dispersion}
\end{aligned}
\tag{3.35}
$$

These forms are valid when there is no advection of the Puff in the z direction; otherwise, the normal flux at the road surface must contain the advection term.

Starting from Equation (3.34) we set up the desired operational model, which we call **Model B**. We introduce it by distinguishing between the various dispersion cases.

1. **Soot dispersion - Open street geometry:** the solution for the pollutant concentration C (in mg/m^3) is constituted by a plume advected in the x direction. We consider a stationary solution of the dispersion

equation, written in the system of reference of the street:

$$V\frac{\partial C}{\partial x} - K_{yy}\frac{\partial^2 C}{\partial y^2} - K_{zz}\frac{\partial^2 C}{\partial z^2} = Q\delta(y)\delta(z - H_e) \tag{3.36}$$

The advection velocity V is the average traffic velocity (in the case of the open street we neglect the effect of a mean wind flow superposed to the traffic induced wind, because in this case the driving condition is usually extra-urban, and the average traffic velocity is much higher than the mean wind velocity); Q is the average emission rate of the vehicles (in mg/ms): we consider a linear emissive source at the canyon centerline ($y = 0$), at an height H_e. The canyon length is L: this model enables the description of the accumulation effect of the emitted pollutants in the direction of the traffic flow. If Turbulence is considered homogeneous in the street, the eddy diffusivity can be prescribed as:

$$\begin{aligned} K_{yy} &= \lambda\sigma_v^2\frac{L + h_0}{V} = \lambda\sigma_{tpt}^2\frac{L + h_0}{V} \\ K_{zz} &= \sigma_w^2\frac{L + h_0}{V} = \sigma_{tpt}^2\frac{L + h_0}{V} \end{aligned} \tag{3.37}$$

The λ constant takes into account the asymmetry produced by the ground, and it is expected from measurements in the wakes of cube obstacles that $1 \leq \lambda \leq 2$ [Eskridge et al., 1979]; anyhow, we assume that $\lambda = 1$, due to the lack of an empirical value obtained from vehicle wakes measurements. h_0 is associated to the initial (immediate) dispersion in the wakes of the vehicles ($h_0 = 2m$, as in $OSPM$ model). Another prescription, which would consider Turbulence accumulation in the x direction, could be:

$$\begin{aligned} K_{yy} &= \lambda\sigma_{tpt}^2\frac{x + h_0}{V} \\ K_{zz} &= \sigma_{tpt}^2\frac{x + h_0}{V} \end{aligned} \tag{3.38}$$

Note that the $OSPM$ prescription for the σ_z dispersion parameter is equivalent to:

$$K_{zz} = \frac{\sigma_w^2}{2}\frac{x}{V} + \frac{h_0^2}{2}\frac{V}{x} + h_0\sigma_w \tag{3.39}$$

Now we find the appropriate Green function corresponding to the Equation (3.36) with boundary condition (3.35) at the road surface. Note that, by taking the substitution $x \to Vt$, Equation (3.36) has the form of Equation (3.32). There are two possibilities:

- consider a Green function with boundary condition at the road surface:

$$\frac{K_{zz}}{v_d(0)}\frac{\partial G}{\partial z} = -G$$

In this case the solution to the dispersion equation is:

$$C(x,y,z,t) = \int_0^{t^+} dt_0 \int dV_0 GS + \int dV_0 [CG]_{t_0=0};$$

- consider a Green function with boundary condition at the road surface:

$$\frac{\partial G}{\partial z} = 0$$

In this case the solution to the dispersion equation is:

$$C(x,y,z,t) = \int_0^{t^+} dt_0 \int dV_0 GS + \int dV_0 [CG]_{t_0=0} - \int_0^{t^+} dt_0 \int dS_0 G v_d(0) C$$

The former possibility is easy to employ only when an homogeneous Neumann boundary condition is imposed on the z flux at the roof level (in a street canyon geometry) or at an inversion layer (in the open street geometry): in such a case, the Green function can be easily expressed as a series expansion in terms of eigenfunctions. Otherwise, we should solve for a transformed function H with an homogeneous Neumann boundary condition on the ground:

$$\frac{K_{zz}}{v_d(0)}\frac{\partial C}{\partial z} + C = H,$$

using the Laplace transform technique [Morse, Feshbach, 1953]. Since the latter conditions are physically acceptable only in few cases, we employ the second possibility. The Green function in the open street geometry with homogeneous Neumann condition at the road surface can be obtained using the Fourier transform and the method of images [Morse, Feshbach, 1953]. Solving Equation (3.33) with:

$$G(t-t_0, y-y_0, z-z_0) = \frac{1}{(2\pi)^2} \int e^{i[p_y(y-y_0)+p_z(z-z_0)]} \tilde{G}(t-t_0, p)\, dV_p,$$

considering the reciprocity property of the diffusion Green function, and the prescription (3.37) for the eddy diffusivity components (note that they are positive, so that the Fourier transformed Green function is a Gaussian function), we have:

$$G(x-x_0, y-y_0, z-z_0) = \\ \frac{1}{4\pi}\frac{\theta(x-x_0)V}{(x-x_0)\sqrt{K_{yy}K_{zz}}}e^{-\frac{V(y-y_0)^2}{4K_{yy}(x-x_0)}}\left[e^{-\frac{V(z-z_0)^2}{4K_{zz}(x-x_0)}} + e^{-\frac{V(z+z_0)^2}{4K_{zz}(x-x_0)}}\right] \tag{3.40}$$

where $\theta(x-x_0)$ is the Heaviside step distribution [Morse, Feshbach, 1953]. When considering the prescription (3.38) terms in x^2 appears in Equation (3.40). The Green function can be easily obtained also for the prescription (3.39). From Equation (3.34), we have for the general solution:

$$C(x,y,z) = \\ \frac{1}{4\pi}\int_0^L dx_0 \int dy_0 dz_0 \frac{\theta(x-x_0)}{(x-x_0)\sqrt{K_{yy}K_{zz}}}e^{-\frac{V}{4(x-x_0)}\left[\frac{(y-y_0)^2}{K_{yy}}+\frac{(z-z_0)^2}{K_{zz}}\right]}Q\delta(y_0)\delta(z_0-H_e) \\ + \frac{1}{4\pi}\int_0^L dx_0 \int dy_0 dz_0 \frac{\theta(x-x_0)}{(x-x_0)\sqrt{K_{yy}K_{zz}}}e^{-\frac{V}{4(x-x_0)}\left[\frac{(y-y_0)^2}{K_{yy}}+\frac{(z+z_0)^2}{K_{zz}}\right]}Q\delta(y_0)\delta(z_0-H_e) \\ +C_b - \frac{v_d(0)}{2\pi}\int_0^L dx_0 \int dy_0 \frac{\theta(x-x_0)}{(x-x_0)\sqrt{K_{yy}K_{zz}}}e^{-\frac{V}{4(x-x_0)}\left[\frac{(y-y_0)^2}{K_{yy}}+\frac{z^2}{K_{zz}}\right]}C(x_0,y_0,0) \tag{3.41}$$

where C_b is the background contribution at $x_0 = 0$. The integrals containing the step function can be considered making the substitution:

$$\xi = x-x_0 \;\rightarrow\; \int_0^L dx_0 \frac{\theta(x-x_0)}{(x-x_0)}\exp\left[-A/(x-x_0)\right] = \int_0^x d\xi \frac{1}{\xi}\exp\left[-A/\xi\right]$$

The solution can be expressed as:

$$C(x,y,z) = \\ \frac{Q}{4\pi\sqrt{K_{yy}K_{zz}}}\left\{\Gamma\left[0,\frac{V}{4x}\left(\frac{y^2}{k_{yy}}+\frac{(z-H_e)^2}{k_{zz}}\right)\right]+\Gamma\left[0,\frac{V}{4x}\left(\frac{y^2}{k_{yy}}+\frac{(z+H_e)^2}{k_{zz}}\right)\right]\right\}+C_b \\ -\frac{v_d(0)}{2\pi\sqrt{K_{yy}K_{zz}}}\int_0^L dx_0\int dy_0\,\frac{\theta(x-x_0)}{(x-x_0)}e^{-\frac{V}{4(x-x_0)}\left[\frac{(y-y_0)^2}{K_{yy}}+\frac{z^2}{K_{zz}}\right]}C(x_0,y_0,0) \tag{3.42}$$

One way to derive an operative solution is to neglect the surface contribution, considering a deposition parametrization as introduced in Equation (3.26):

$$C(x,y,z) = \\ \frac{Q_0\exp\left[-2\sqrt{\frac{2}{\pi}}\left(\frac{v_d(0)}{V}\right)\Gamma\left(0,\frac{H^2}{2y^2}\right)\right]}{4\pi\sqrt{K_{yy}K_{zz}}}\cdot \\ \left\{\Gamma\left[0,\frac{V}{4x}\left(\frac{y^2}{k_{yy}}+\frac{(z-H_e)^2}{k_{zz}}\right)\right]+\Gamma\left[0,\frac{V}{4x}\left(\frac{y^2}{k_{yy}}+\frac{(z+H_e)^2}{k_{zz}}\right)\right]\right\}+C_b \tag{3.43}$$

This approach introduces a description of the deposition process only across the street. This is a good approximation for an infinitely long street. Note that in this case the diffusion equation (3.36) could be substituted by a Poisson equation, making the problem of Green propagation of the source and the boundary terms more simple.

A more detailed method would be to solve by successive approximations the inhomogeneous Fredholm integral equation of the second kind [Morse, Feshbach, 1953] associated to Equation (3.42). Here we show the latter procedure. Consider the solution (3.42) with values on the road boundary $z = 0$:

$$C(x,y,0) = \frac{Q}{2\pi\sqrt{K_{yy}K_{zz}}}\Gamma\left[0,\frac{V}{4x}\left(\frac{y^2}{k_{yy}}+\frac{H_e^2}{k_{zz}}\right)\right]+C_b \\ -\frac{v_d(0)}{2\pi\sqrt{K_{yy}K_{zz}}}\int_0^L dx_0\int dy_0\,\frac{\theta(x-x_0)}{(x-x_0)}e^{-\frac{V}{4(x-x_0)}\frac{(y-y_0)^2}{K_{yy}}}C(x_0,y_0,0)$$

We underline here the fact that we are making a strong approximation: the surface boundary on which we impose the form for the deposition

flux extends to $-\inf < y < \inf$, with a constant value of $v_d(0)$ over the whole surface. This simplifies the calculations, but introduces a strong approximation which make the results useless if the receptor is in a point far away from the road. The results for a road surface extending to $-W/2 < y < W/2$ on which a deposition flux with a constant deposition velocity $v_d(0)$ is imposed (and imposing moreover an homogeneous Neumann condition on the remaining part of the $z = 0$ boundary), have been obtained too, but they are not in a closed form and different expansions are uniformly valid on different domain regions. We will treat this case in further investigations.

The last equation is an inhomogeneous Fredholm integral equation of the second kind of the type:

$$C(x,y,0) = f(x,y,0) - \lambda \int_0^L dx_0 \int dy_0\, K(x-x_0, y-y_0, 0) C(x_0, y_0, 0)$$

It's easy to see that the kernel term $K(x-x_0, y-y_0, 0)$ is continuous for $x > x_0 > 0$ and has a compact support (even if the y dimension extends to infinity), and that the constant λ is small compared to the maximum value of the kernel integrated on its support (M):

$$\lambda \cdot M \sim \frac{v_d(0)}{\sqrt{K_{zz} V}} \sim v_d(0) \sim 10^{-2},$$

where, for K_{zz}, the values corresponding to a light traffic density must be considered in the open street case (see Equations (3.30) and (3.40)), and $v_d(0) \sim 10^{-2}$(see Section 4.3); this means that the equation has a unique solution [Morse, Feshbach, 1953], and can be solved by the method of successive approximation:

$$C_i(x,y,0) = f(x,y,0) - \lambda \int_0^L dx_0 \int dy_0\, K(x-x_0, y-y_0, 0) C_{i-1}(x_0, y_0, 0)$$

We choose $C_0 = f$ and retain only the terms linear in $v_d(0)$, and substitute the surface value $C(x,y,0)$ inside the Equation (3.42), which propagates it on the whole domain. We introduce a further approximation, in order to make the results as simple as possible: the deposition contribution coming from the background concentration C_b is integrated over all the road surface domain, whereas the contribution coming from the line source $Q\delta(y)\delta(z-H_e)$ is propagated from the centreline of the street at the ground, considering as the source value the accumulated value at L . We obtain:

$$C(x,y,0) = \frac{Q}{2\pi\sqrt{K_{yy}K_{zz}}}\Gamma\left[0, \frac{V}{4x}\left(\frac{y^2}{k_{yy}} + \frac{H_e^2}{k_{zz}}\right)\right] + C_b$$
$$- 2C_b\frac{v_d(0)}{\sqrt{\pi V}\sqrt{K_{zz}}}\sqrt{x} - \frac{v_d(0)}{2\pi\sqrt{K_{yy}K_{zz}}}\Gamma\left[0, \frac{V}{4L}\left(\frac{H_e^2}{k_{zz}}\right)\right]\Gamma\left[0, \frac{V}{4x}\left(\frac{y^2}{k_{yy}}\right)\right]'$$

and finally:

$$C(x,y,z) =$$
$$\frac{Q}{4\pi\sqrt{K_{yy}K_{zz}}}\left\{\Gamma\left[0, \frac{V}{4x}\left(\frac{y^2}{k_{yy}} + \frac{(z-H_e)^2}{k_{zz}}\right)\right] + \Gamma\left[0, \frac{V}{4x}\left(\frac{y^2}{k_{yy}} + \frac{(z+H_e)^2}{k_{zz}}\right)\right]\right\} + C_b$$

$$- \frac{v_d(0)Q}{4\pi^2 K_{yy}K_{zz}}\Gamma\left[0, \frac{V}{4L}\left(\frac{H_e^2}{k_{zz}}\right)\right]\Gamma\left[0, \frac{V}{4x}\left(\frac{y^2}{k_{yy}} + \frac{z^2}{k_{zz}}\right)\right]$$

$$- 2\frac{v_d(0)C_b}{\sqrt{\pi V K_{zz}}}\left\{e^{-\frac{V}{4x}\frac{z^2}{K_{zz}}}\sqrt{x} - \frac{z}{2}\sqrt{\frac{\pi V}{K_{zz}}}\mathrm{Erfc}\left[\sqrt{\frac{\mathrm{Vz}^2}{4\mathrm{xK_{zz}}}}\right]\right\} \tag{3.44}$$

where we have integrated the Gaussian functions on the y coordinate, and used the fact that $\Gamma[1/2, x^2] \propto \mathrm{erf(x)}$. This is the solution for the Soot plume advected in the direction of the traffic flow in an open street, with constant dispersion parameters determined by the traffic produced Turbulence, considering the deposition and the resuspension processes.

2. **Road dust dispersion - Open street geometry:** in this case, we choose the same Green function as that in Equation (3.40), satisfying an homogeneous Neumann boundary condition. The solution of the dispersion Equation (3.36), without the source term, but with the second boundary condition in (3.35), representing a plume advected in the longitudinal direction by traffic velocity, is derived from Equation (3.34):

$$C(x,y,z,t) = C_{db} + k_{res}c_s\int_0^L dx_0\int dy_0[G] - v_d(0)\int_0^L dx_0\int dy_0[GC],$$

where C_{db} is the background road dust concentration in air. We are again assuming a stationary value of the road dust c_s, so that the boundary condition is not coupled with a budget equation for the road dust concentration dynamics. We have:

$$C(x,y,z) = C_{db} + \frac{2k_{res}c_s}{\sqrt{\pi V K_{zz}}}\left\{\sqrt{x}e^{-\frac{V}{4x}\frac{z^2}{K_{zz}}} - \frac{z}{2}\sqrt{\frac{\pi V}{K_{zz}}}\mathrm{Erfc}\left[\sqrt{\frac{\mathrm{Vz}^2}{4\mathrm{xK_{zz}}}}\right]\right\}$$
$$- \frac{v_d(0)}{2\pi\sqrt{K_{yy}K_{zz}}}\int_0^L dx_0 \int dy_0 \, \frac{\theta(x-x_0)}{(x-x_0)} e^{-\frac{V}{4(x-x_0)}\left[\frac{(y-y_0)^2}{K_{yy}}+\frac{z^2}{K_{zz}}\right]} C(x_0,y_0,0)$$

Solving the corresponding integral equation for the concentration at the road surface, and than substituting the solution inside the last equation, we obtain, at $O[z_0]$:

$$\begin{aligned} &C(x,y,z) = C_{db} + \\ &\frac{2}{\sqrt{\pi V K_{zz}}}\left[k_{res}c_s - v_d(0)C_{db} - 2\sqrt{L}\frac{k_{res}c_s v_d(0)}{\sqrt{\pi V K_{zz}}}\right]\cdot \\ &\left\{\sqrt{x}e^{-\frac{V}{4x}\frac{z^2}{K_{zz}}} - \frac{z}{2}\sqrt{\frac{\pi V}{K_{zz}}}\mathrm{Erfc}\left[\sqrt{\frac{\mathrm{Vz}^2}{4\mathrm{xK_{zz}}}}\right]\right\} \end{aligned} \tag{3.45}$$

This is the solution for the road dust plume advected in the direction of the traffic flow in an open street, with constant dispersion parameters determined by the traffic produced Turbulence, considering the deposition and the resuspension processes. Note that, due to the approximation of a constant deposition + resuspension flux applied to the whole surface boundary extending to $-\infty < y < \infty$, the solution is independetn from y; this is a valid approximation only if the receptor point is posed above the road boundary (i.e. between $-W/2 < y < W/2$).

3. **Soot dispersion - Canyon street geometry - No recirculation:** in this case the solution for the pollutant concentration C is constituted by a plume advected in the x direction, which is a stationary solution of the dispersion Equation (3.36). The advection velocity V is the sum of the average traffic velocity (the driving condition is usually intermediate or heavy traffic condition) and the mean velocity $\mathbf{U}_{//}$ relative to the longitudinal component of the wind flow generated thorough the canyon by the external wind flow (which will be defined in Section 4.1). If Turbulence is considered homogeneous in the street, the eddy diffusivity can be prescribed as:

$$\begin{aligned} K_{yy} &= \sigma_v^2\frac{L+h_0}{V} = \left[(\alpha\mathbf{U}_{//})^2 + \sigma_{tpt}^2\right]\frac{L+h_0}{V} \\ K_{zz} &= \sigma_w^2\frac{L+h_0}{V} = \left[(\alpha\mathbf{U}_{//})^2 + \sigma_{tpt}^2\right]\frac{L+h_0}{V} \end{aligned} \tag{3.46}$$

where $\alpha = 0.1$ as in the $OSPM$ parametrization.

Now we find the appropriate Green function for the street canyon geometry corresponding to the Equation (3.36) with the following boundary conditions:

$$\begin{cases} C = 0 \quad \text{for} \quad \text{y} = \pm \text{W}/2 \\ \\ C = 0 \quad \text{for} \quad \text{z} \to \infty \\ \\ \dfrac{\partial C}{\partial z} + \dfrac{v_d(0)}{K_{zz}} C = 0 \quad \text{for} \quad \text{z} = 0 \end{cases} \tag{3.47}$$

These are not perfect physical conditions; they are imposed for mathematical reasons in order to obtain simple solutions. We have chosen an homogeneous Dirichlet condition at the side walls, instead of a no-flux condition (homogeneous Neumann), because the latter would not allow a treatment of the deposition and resuspension fluxes through a Green propagation method as that introduced previously. The third condition implies a street canyon with infinite height: this allows us to avoid considerations on the correct boundary conditions to be imposed at the roof level, but it is a good approximation only if the receptor point is inside the canyon. The Green function with homogeneous Neumann boundary conditions at the road surface can be obtained by expansion in terms of eigenfunctions in the y direction, and using the Fourier transform and the method of images in the z direction[Morse, Feshbach, 1953]:

$$G(x - x_0, y - y_0, z - z_0) =$$
$$\frac{1}{W\sqrt{\pi K_{zz}}} \sum_{n=0}^{\infty} \left\{ \frac{\theta(x - x_0)\sqrt{V}}{(x - x_0)} e^{-\left[\frac{\pi^2 (2n+1)^2 K_{yy}}{W^2 V}(x - x_0)\right]} \cos\left[\frac{(2n+1)\pi}{W} y\right] \cos\left[\frac{(2n+1)\pi}{W} y_0\right] \cdot \right.$$
$$\left. \left[e^{-\frac{V(z - z_0)^2}{4K_{zz}(x - x_0)}} + e^{-\frac{V(z + z_0)^2}{4K_{zz}(x - x_0)}} \right] \right\} \tag{3.48}$$

Note that the Fourier series in Equation (3.48) is absolutely and uniformly convergent inside the canyon domain, and thus the summation can be interchanged with the integration operation in the context of the Green propagation method. The series is rapidly convergent, except for $x = x_0$. The solution is given by:

$$C(x,y,z) =$$
$$\frac{1}{W\sqrt{\pi V K_{zz}}}\sum_n\Bigg\{\int_0^L dx_0\int_{-W/2}^{W/2}dy_0\int dz_0\frac{\theta(x-x_0)}{\sqrt{x-x_0}}e^{-\left[\frac{\pi^2(2n+1)^2K_{yy}}{W^2V}(x-x_0)\right]}\cdot$$
$$\cos\left[\frac{(2n+1)\pi}{W}y\right]\cos\left[\frac{(2n+1)\pi}{W}y_0\right]\left[e^{-\frac{V(z-z_0)^2}{4K_{zz}(x-x_0)}}+e^{-\frac{V(z+z_0)^2}{4K_{zz}(x-x_0)}}\right]Q\delta(y_0)\delta(z_0-H_e)\Bigg\}$$
$$+C_b-\frac{2v_d(0)}{W\sqrt{\pi V K_{zz}}}\sum_n\Bigg\{\int_0^L dx_0\int_{-W/2}^{W/2}dy_0\frac{\theta(x-x_0)}{\sqrt{x-x_0}}e^{-\left[\frac{\pi^2(2n+1)^2K_{yy}}{W^2V}(x-x_0)\right]}\cdot$$
$$\cos\left[\frac{(2n+1)\pi}{W}y\right]\cos\left[\frac{(2n+1)\pi}{W}y_0\right]\left[e^{-\frac{Vz^2}{4K_{zz}(x-x_0)}}\right]C(x_0,y_0,0)\Bigg\}$$

The result, obtained by solving to the order $O(v_d(0))$ (observing that $\sqrt{VK_{zz}}\sim 1$ for both the cases of intermediate and heavy traffic conditions), is:

$$
\begin{aligned}
&C(x,y,z) = \\
&\frac{Q}{2\pi\sqrt{K_{yy}K_{zz}}}\sum_n\Bigg\{\frac{1}{2n+1}\cos\left[\frac{(2n+1)\pi}{W}y\right]e^{-\left[\frac{\pi(2n+1)\sqrt{K_{yy}}(z-H_e)}{W\sqrt{K_{zz}}}\right]}\cdot \\
&\left[1-\mathrm{erf}\left[\frac{\sqrt{\mathrm{V}}(\mathrm{z}-\mathrm{H_e})}{2\sqrt{\mathrm{K_{zz}}}\sqrt{\mathrm{x}}}-\frac{\pi(2\mathrm{n}+1)\sqrt{\mathrm{K_{yy}}}\sqrt{\mathrm{x}}}{\mathrm{W}\sqrt{\mathrm{V}}}\right]+\right. \\
&\left.e^{\left[\frac{2\pi(2n+1)\sqrt{K_{yy}}(z-H_e)}{W\sqrt{K_{zz}}}\right]}\left(\mathrm{erf}\left[\frac{\sqrt{\mathrm{V}}(\mathrm{z}-\mathrm{H_e})}{2\sqrt{\mathrm{K_{zz}}}\sqrt{\mathrm{x}}}+\frac{\pi(2\mathrm{n}+1)\sqrt{\mathrm{K_{yy}}}\sqrt{\mathrm{x}}}{\mathrm{W}\sqrt{\mathrm{V}}}\right]-1\right)\right]\Bigg\}+ \\
&\frac{Q}{2\pi\sqrt{K_{yy}K_{zz}}}\sum_n\Big\{\cdot\Big\}_{(z-H_e)\to(z+H_e)} \\
&+C_b-\frac{2v_d(0)C_b}{\pi^2\sqrt{K_{yy}K_{zz}}}\sum_n\Bigg\{\frac{(-1)^n}{(2n+1)^2}\cos\left[\frac{(2n+1)\pi}{W}y\right]e^{-\left[\frac{\pi(2n+1)\sqrt{K_{yy}}z}{W\sqrt{K_{zz}}}\right]}\cdot \\
&\left[1-\mathrm{erf}\left[\frac{\sqrt{\mathrm{V}}\mathrm{z}}{2\sqrt{\mathrm{K_{zz}}}\sqrt{\mathrm{x}}}-\frac{\pi(2\mathrm{n}+1)\sqrt{\mathrm{K_{yy}}}\sqrt{\mathrm{x}}}{\mathrm{W}\sqrt{\mathrm{V}}}\right]+\right. \\
&\left.e^{\left[\frac{2\pi(2n+1)\sqrt{K_{yy}}z}{W\sqrt{K_{zz}}}\right]}\left(\mathrm{erf}\left[\frac{\sqrt{\mathrm{V}}\mathrm{z}}{2\sqrt{\mathrm{K_{zz}}}\sqrt{\mathrm{x}}}+\frac{\pi(2\mathrm{n}+1)\sqrt{\mathrm{K_{yy}}}\sqrt{\mathrm{x}}}{\mathrm{W}\sqrt{\mathrm{V}}}\right]-1\right)\right]\Bigg\}- \\
&\frac{v_d(0)QW}{8\pi^3K_{yy}K_{zz}}\sum_n\Bigg\{\frac{1}{(2n+1)^2}\cos\left[\frac{(2n+1)\pi}{W}y\right]\cdot \\
&[I+II]_{z=0,x=L}\,e^{-\left[\frac{\pi(2n+1)\sqrt{K_{yy}}z}{W\sqrt{K_{zz}}}\right]}\cdot \\
&\left[1-\mathrm{erf}\left[\frac{\sqrt{\mathrm{V}}\mathrm{z}}{2\sqrt{\mathrm{K_{zz}}}\sqrt{\mathrm{x}}}-\frac{\pi(2\mathrm{n}+1)\sqrt{\mathrm{K_{yy}}}\sqrt{\mathrm{x}}}{\mathrm{W}\sqrt{\mathrm{V}}}\right]+\right. \\
&\left.e^{\left[\frac{2\pi(2n+1)\sqrt{K_{yy}}z}{W\sqrt{K_{zz}}}\right]}\left(\mathrm{erf}\left[\frac{\sqrt{\mathrm{V}}\mathrm{z}}{2\sqrt{\mathrm{K_{zz}}}\sqrt{\mathrm{x}}}+\frac{\pi(2\mathrm{n}+1)\sqrt{\mathrm{K_{yy}}}\sqrt{\mathrm{x}}}{\mathrm{W}\sqrt{\mathrm{V}}}\right]-1\right)\right]\Bigg\}
\end{aligned}
\tag{3.49}
$$

where I and II are the first two series on the right hand side; the second series is obtained from the first by taking $z-H_e \to z+H_e$. A solution of the integral equations in terms of an expansion in eigenfunctions could be obtained without employing a recurrence procedure and approximations to order $O(v_d(0))$, applying the Fredholm theorems for the solvability of integral equations and standard accelaration procedures for the resulting series [Morse, Feshbach, 1953]. We will treat this approach in future investigations. This is a cumbersome formula. The terms which not contain the erf functions can be summed via complex variable methods using the $tanh^{-1}$ function [Morse, Feshbach, 1953], but it's easy to observe that the erf function accelerates convergence (by making the numerators tending to zero) in such a way that it is possible to consider only the first term $n = 0$. (Taking fixed values of the independent variables, by a direct calculation it's possible to observe

that the term for $n = 1$ is reduced by a factor of $\sim 10^3$ with respect to the term for $n = 0$). This is the solution for the Soot plume advected in the direction of the traffic flow in a street canyon, with constant dispersion parameters determined by the traffic produced Turbulence and the longitudinal wind flow component, considering the deposition process, in the approximation of a canyon geometry extending to Infinity in height.

A more contained solution can be obtained by imposing the boundary conditions:

$$\begin{cases} C = 0 \quad \text{for} \quad \text{y} = \pm \text{W}/2 \\ \\ C = 0 \quad \text{for} \quad \text{z} \to \text{H} \\ \\ \dfrac{\partial C}{\partial z} + \dfrac{v_d(0)}{K_{zz}} C = 0 \quad \text{for} \quad \text{z} = 0 \end{cases} \tag{3.50}$$

The second condition introduces a finite dimension in the z direction, and we can expand the Green function in eigenfunctions also in that direction. It is presumable that a value $C \neq 0$ at the roof level has no effect on the values of concentration at a receptor point inside the canyon for the case of no wind recirculation. In the case of dispersion conditions which make the pollutant to disperse above the roof level, a simple parametrization, contained in the $OSPM$ model [Berkowicz, Kearney, 2004], of the effect of upstream concentrations can be added to the present results. We do not report it here. The Green function with homogeneous Neumann boundary conditions at the road surface and homogeneous Dirichlet conditions at the roof level is:

$$\begin{aligned} &G(x - x_0, y - y_0, z - z_0) = \\ &\frac{4}{WH} \theta(x - x_0) \sum_{n,m=0}^{\infty} \left\{ e^{-\frac{\pi^2}{V} \left[\frac{(2n+1)^2}{W^2} K_{yy} + \frac{(2m+1)^2}{4H^2} K_{zz} \right] (x - x_0)} \cdot \right. \\ &\left. \cos\left[\frac{(2n+1)\pi}{W} y \right] \cos\left[\frac{(2n+1)\pi}{W} y_0 \right] \cos\left[\frac{(2m+1)\pi}{2H} z \right] \cos\left[\frac{(2m+1)\pi}{2H} z_0 \right] \right\} \end{aligned} \tag{3.51}$$

The Fourier series are absolutely and uniformly convergent in the domain, since the coefficients are $O(n^{-2}), O(m^{-2})$ [Morse, Feshbach, 1953].

The solution is given by:

$$
\begin{aligned}
&C(x,y,z) = \\
&\frac{4Q}{VWH}\sum_{n,m=0}^{\infty}\left\{\cos\left[\frac{(2n+1)\pi}{W}y\right]\cos\left[\frac{(2m+1)\pi}{2H}z\right]\cos\left[\frac{(2m+1)\pi}{2H}H_e\right]\cdot\right. \\
&\left.\left[\frac{1-e^{-\frac{\pi^2}{V}\left[\frac{(2n+1)^2}{W^2}K_{yy}+\frac{(2m+1)^2}{4H^2}K_{zz}\right]x}}{\frac{\pi^2}{V}\left[\frac{(2n+1)^2}{W^2}K_{yy}+\frac{(2m+1)^2}{4H^2}K_{zz}\right]}\right]\right\}+C_b \\
&-\frac{8v_d(0)C_b}{\pi VH}\sum_{n,m=0}^{\infty}\left\{\frac{(-1)^n}{2n+1}\cos\left[\frac{(2n+1)\pi}{W}y\right]\cos\left[\frac{(2m+1)\pi}{2H}z\right]\cdot\right. \\
&\left.\left[\frac{1-e^{-\frac{\pi^2}{V}\left[\frac{(2n+1)^2}{W^2}K_{yy}+\frac{(2m+1)^2}{4H^2}K_{zz}\right]x}}{\frac{\pi^2}{V}\left[\frac{(2n+1)^2}{W^2}K_{yy}+\frac{(2m+1)^2}{4H^2}K_{zz}\right]}\right]\right\} \\
&-\frac{8v_d(0)Q}{VWH^2}\sum_{n,m=0}^{\infty}\left\{\cos\left[\frac{(2n+1)\pi}{W}y\right]\cos\left[\frac{(2m+1)\pi}{2H}z\right]\cos\left[\frac{(2m+1)\pi}{2H}H_e\right]\cdot\right. \\
&\left.\left[\frac{1-e^{-\frac{\pi^2}{V}\left[\frac{(2n+1)^2}{W^2}K_{yy}+\frac{(2m+1)^2}{4H^2}K_{zz}\right]L}}{\frac{\pi^2}{V}\left[\frac{(2n+1)^2}{W^2}K_{yy}+\frac{(2m+1)^2}{4H^2}K_{zz}\right]}\right]\cdot\left[\frac{1-e^{-\frac{\pi^2}{V}\left[\frac{(2n+1)^2}{W^2}K_{yy}+\frac{(2m+1)^2}{4H^2}K_{zz}\right]x}}{\frac{\pi^2}{V}\left[\frac{(2n+1)^2}{W^2}K_{yy}+\frac{(2m+1)^2}{4H^2}K_{zz}\right]}\right]\right\}
\end{aligned}
\tag{3.52}
$$

Note that, in the calculations of Equations (3.49) and (3.52), it was possible to remove the simplifying hypothesis that the deposition contributions from the term containing Q was limited to the centerline, by utilizing the orthogonality properties of the eigenfunctions in the integrations. Since the series in solution (3.52) are double series, there are no standard methods to accelerate their convergence; we note that they are rapidly convergent anyhow (although more slowly than the single series in Equation (3.49)), and only the $n = m = 0$ term can be considered. This is the solution for the Soot plume advected in the direction of the traffic flow in a street canyon, with constant dispersion parameters determined by the traffic produced Turbulence and the longitudinal wind flow component, considering the deposition process, in the approximation of a zero value of pollutant concentration at the roof level.

4. **Road dust dispersion - Canyon street geometry - No recirculation:**

   in this case, we choose the Green function with homogeneous Neumann boundary conditions at the road surface and homogeneous Dirichlet conditions at the roof level, written in Equation (3.51). The solution of the dispersion Equation (3.36), without the source term, but with

the second boundary condition in (3.35), representing a plume advected in the longitudinal direction by traffic velocity, is given by:

$$C(x,y,z,t) = C_{db} + k_{res} c_s \int_0^L dx_0 \int_{-W/2}^{W/2} dy_0 [G] - v_d(0) \int_0^L dx_0 \int_{-W/2}^{W/2} dy_0 [GC],$$

where C_{db} is the background road dust concentration in air. We are again assuming a stationary value of the road dust c_s, so that the boundary condition is not coupled with a budget equation for the road dust concentration dynamics. Solving to order $O[z_0]$, we have:

$$C(x,y,z) = C_{db} +$$
$$\left\{ \frac{8 k_{res} c_s}{\pi V H} - \frac{8 v_d(0) C_{db}}{\pi V H} - \frac{16 k_{res} c_s v_d(0)}{\pi V^2 H^2} \left[\frac{1 - e^{-\frac{\pi^2}{V}\left[\frac{(2n+1)^2}{W^2} K_{yy} + \frac{(2m+1)^2}{4H^2} K_{zz}\right] L}}{\frac{\pi^2}{V}\left[\frac{(2n+1)^2}{W^2} K_{yy} + \frac{(2m+1)^2}{4H^2} K_{zz}\right]} \right] \right\} \cdot$$
$$\sum_{n,m=0}^{\infty} \left\{ \frac{(-1)^n}{2n+1} \cos\left[\frac{(2n+1)\pi}{W} y\right] \cos\left[\frac{(2m+1)\pi}{2H} z\right] \left[\frac{1 - e^{-\frac{\pi^2}{V}\left[\frac{(2n+1)^2}{W^2} K_{yy} + \frac{(2m+1)^2}{4H^2} K_{zz}\right] x}}{\frac{\pi^2}{V}\left[\frac{(2n+1)^2}{W^2} K_{yy} + \frac{(2m+1)^2}{4H^2} K_{zz}\right]} \right] \right\} \tag{3.53}$$

This is the solution for the road dust plume advected in the direction of the traffic flow in a street canyon, with constant dispersion parameters determined by the traffic produced Turbulence and the longitudinal wind flow component, considering the deposition and the resuspension processes. We can consider again the $n = m = 0$ term only (even if we should consider the terms for $n = m = 1$ too to reach precision to the order 10^{-3}, as obtained in the case of Equation (3.49) considering the $n = m = 0$ term only).

5. **Soot and road dust dispersion - Canyon street geometry - Recirculation:** according to the *STREET* empirical model, when the external wind flows at an angle of more than 30° with respect to the canyon street axis, an helical recirculation develops in the street. In this situation, the formation of a wind vortex is observed from wind measurements [Nakamura, Oke, 1988], which causes concentration levels greater for the leeward than for the windward side of the canyon. We consider the case in which the wind vortex is totally immersed inside the canyon (*wakeinterference* and *skimmingflow* regimes, according to the definitions introduced in Ref. [Berkowicz, Kearney, 2004]). As we will show in Section 4, 1, these regimes correspond to external winds with an orthogonal component relative to the street axis greater in intensity than $1 m/s$, and to values of the geometric parameters of the canyon such that $H/W > 0.5$ (which are typical for most urban

situations). We have obtained analytical solutions for the wind velocity components (v, w) (the horizontal and the vertical components respectively) valid for these flow regimes (reported Section 4.1). We are using these solutions to set up an operational model for the determination of the pollutant concentration in the canyon recirculation case. As in the $OSPM$ model, the concentration is calculated as a combination of a plume model, for the direct contribution coming from the Soot and the road dust traffic emissions, and a box model, for the the additional impact due to pollutants recirculated within the street by the vortex flow. For a receptor on the leeward side, we construct the solution for the pollutant concentration C as the superposition of a plume advected in the x direction (which we call component 0), which take into account the deposition and the resuspension processes, plus two Gaussian segments [Seinfeld, Pandis, 2006] (components I and II) which take into account the advection of pollutants by the horizontal and the vertical components of the canyon vortex. The plume advected in the x direction is determined by the solutions (3.52) or (3.53), for the Soot and the road dust distribution respectively, in which the advection and the Turbulence parameters are determined by traffic velocity and by the mean longitudinal component of the external wind $\mathbf{U}_{//}$ as in Equation (3.46). The first Gaussian segment is a Gaussian solution of the dispersion equation:

$$v_{H_e}\frac{\partial C_I}{\partial y} - K_{xx}\frac{\partial^2 C_I}{\partial x^2} - K_{zz}\frac{\partial^2 C_I}{\partial z^2} = S_I \tag{3.54}$$

where the source term is:

$$S_I = \frac{\pi}{2}y^2\left(K_{yy}\frac{\partial C_0}{\partial y} + v_{H_e}C_0\right)\delta(x - L_r)\delta(y - y_I)\delta(z - H_e) \tag{3.55}$$

The source term represents a contribution from the concentration C_0, corresponding to the plume solution (component 0), in the form of a diffusive+advective flux in the y direction integrated over an hemispherical surface with radius y_I centred at $x = L_r$, $y = 0$, $z = H_e$, where L_r is the x coordinate of the receptor point and H_e is the height of the pollutant emission level ($H_e = 0$ for the road dust case). The meaning of this solution is the following: we start from the 0 component; at the centerline and around the emission level, we let it be dispersed for a small distance y_I, which corresponds to the lateral width of a vehicle, which determines the distance for which the near wake Turbulence override the influence of the recirculation wind; this flux, integrated over an hemispherical surface, constitutes the point source, at $(L_r, y_I, H_e$, for a Gaussian segment advected across the canyon by

a mean horizontal component of the vortex velocity at the level H_e, v_{H_e}; the segment component I is advected until the y_r coordinate of the receptor point. Since this segment is not advected through the whole canyon domain, the boundary conditions at $y = -W/2$ are not important, and we can consider a Green propagation function with homogeneous Neumann boundary conditions at $z = 0$ (the influence of the surface fluxes boundary conditions are already accounted for by the 0 component solution):

$$G_I(x - x_0, y - y_0, z - z_0) = \\ \frac{1}{4\pi} \frac{\theta(y - y_0) v_{H_e}}{(y - y_0)\sqrt{K_{xx} K_{zz}}} e^{-\frac{v_{H_e}(x-x_0)^2}{4K_{xx}(y-y_0)}} \left[e^{-\frac{v_{H_e}(z-z_0)^2}{4K_{zz}(y-y_0)}} + e^{-\frac{v_{H_e}(z+z_0)^2}{4K_{zz}(y-y_0)}} \right] \tag{3.56}$$

The solution C_I is easily found by propagating the S_I source. Note that this solution is valid only for $y > y_I$. The value of the mean component v_{H_e} is given by integrating the analytical solution for the horizontal component of the vortex canyon flow (reported in Section 4.1), at the H_e level, between $y_I \leq y \leq y_r$. The constant values of the turbulent parameters are:

$$\begin{aligned} K_{xx} &= \left[(\alpha \mathbf{U}_{//})^2 + \sigma_{tpt}^2 \right] \frac{L_r + h_0}{V} \\ K_{zz} &= \left[(\alpha v_{H_e})^2 + \sigma_{tpt}^2 \right] \frac{y_r + h_0}{v_{H_e}} \end{aligned} \tag{3.57}$$

The second Gaussian segment is a Gaussian solution of the dispersion equation:

$$w_{y_r} \frac{\partial C_{II}}{\partial z} - K_{xx} \frac{\partial^2 C_{II}}{\partial x^2} - K_{yy} \frac{\partial^2 C_{II}}{\partial y^2} = S_{II} \tag{3.58}$$

where the source term is:

$$S_{II} = \frac{\pi}{2}(z - H_e)^2 \left(K_{zz} \frac{\partial (C_0 + C_I)}{\partial z} + w_{y_r}(C_0 + C_I) \right) \delta(x - L_r) \delta(y - y_r) \delta(z - H_e - H_{II}) \tag{3.59}$$

The source term represents a contribution from the concentration $C_0 + C_I$, in the form of a flux in the z direction integrated over an hemispherical surface with radius H_{II} centred at $x = L_r$, $y = y_r$, $z = H_e$, where L_r is the x coordinate of the receptor point, y_r is the y coordinate of the receptor point, and H_e is the height of the pollutant emission level

($H_e = 0$ for the road dust case). The meaning of this solution is the following: we let disperse the 0 and II components for a small distance H_{II}, which has no direct physical meaning (we choose it to be equal to $2H_e$, if this distance is less than the distance from y_r to the canyon wall); this flux, integrated over an hemispherical surface, constitutes the point source, at $(L_r, y_r, H_e + H_{II}$, for a Gaussian segment advected vertically across the canyon by a mean vertical component of the vortex velocity at the level y_r, w_{y_r}; the segment component II is advected until the z_r coordinate of the receptor point. Since this segment is not advected through the whole canyon domain, the boundary conditions at $z = 0$ and $z = H$ are not important, and we can consider a Green propagation function with homogeneous Dirichlet boundary conditions at $y = -W/2$:

$$G_{II}(x - x_0, y - y_0, z - z_0) = \\ \frac{1}{4\pi} \frac{\theta(z - z_0) w_{y_r}}{(z - z_0)\sqrt{K_{xx} K_{yy}}} e^{-\frac{w_{y_r}(x-x_0)^2}{4K_{xx}(z-z_0)}} \left[e^{-\frac{w_{y_r}(y-y_0)^2}{4K_{yy}(z-z_0)}} - e^{-\frac{w_{y_r}(y+W+y_0)^2}{4K_{yy}(z-z_0)}} \right] \tag{3.60}$$

The solution C_{II} is easily found by propagating the S_{II} source. Note that this solution is valid only for $z > H_e + H_{II}$. The value of the mean component w_{y_r} is given by integrating the analytical solution for the vertical component of the vortex canyon flow (reported in Section 4.1), at the y_r level, between $H_e + H_{II} \leq z \leq z_r$. The constant values of the turbulent parameters are:

$$\begin{aligned} K_{xx} &= \left[(\alpha \mathbf{U}_{//})^2 + \sigma_{tpt}^2 \right] \frac{L_r + h_0}{V} \\ K_{yy} &= \left[(\alpha w_{y_r})^2 + \sigma_{tpt}^2 \right] \frac{H_r + h_0}{w_{y_r}} \end{aligned} \tag{3.61}$$

For a receptor on the windward side, we construct the solution for the pollutant concentration C as the superposition of a plume advected in the x direction (which we call component 0), which take into account the deposition and the resuspension processes, plus a contribution from the recirculation component. The plume advected in the x direction is determined by the solutions (3.52) or (3.53), for the Soot and the road dust distribution respectively, in which the advection and the Turbulence parameters are determined by traffic velocity and by the mean longitudinal component of the external wind $\mathbf{U}_{//}$ as in Equation (3.46). The contribution from the recirculation component C_r is determined using a box model as in the $OSPM$ model, considering a recirculation

zone which extends to the whole canyon. This contribution is expressed in Equation (3.29). If the recirculation zone is extended to the whole canyon domain (as in the *skimming flow regime*), only the recirculation term need to be considered [Berkowicz, Kearney, 2004]. In Figure 18 we show a graphic scheme of the **model B** in the case of the street canyon Soot emission with recirculation. The circles indicate a plume diffusion.

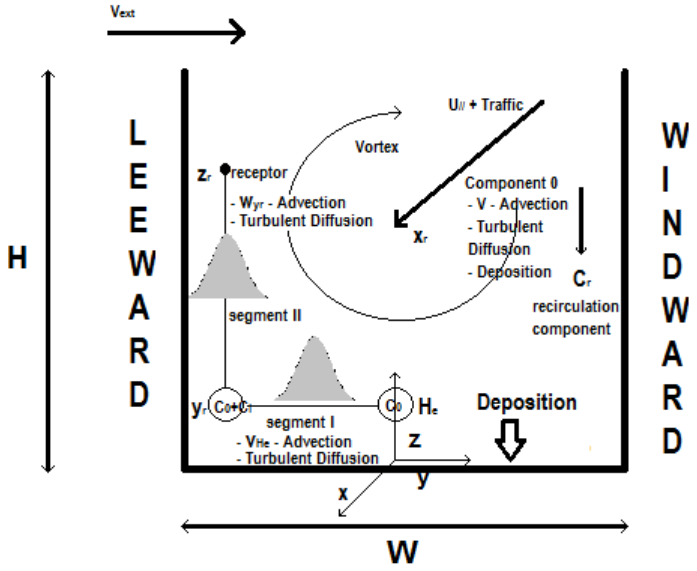

Figure 18: Graphic scheme of the **model B** in the case of the street canyon Soot emission with recirculation. The circles indicate a plume diffusion.

6. **Soot and road dust dispersion - Canyon street geometry - Canyon intersections:** in the case of the pollutant dispersion in canyon intersections, a simple approach can be employed by considering the flow as a 2−dimensional inviscid flow over a region between to straight solid boundaries intersecting at an angle α, in a plane parallel to the road surface. The problem is shown in Figure 19.

In Region **B** the inviscid flow can be described introducing the complex potential $\Omega(z)$ [Batchelor, 1967]:

$$\Omega(z) = \phi(x, y) + i\psi(x, y) = k\mathbf{U}_{\mathbf{A}//} z^n,$$

where $z = x + iy$, ϕ and ψ are the velocity potential and the stream function respectively, k is a constant, and $\alpha = \pi/n$ (note that the case in which

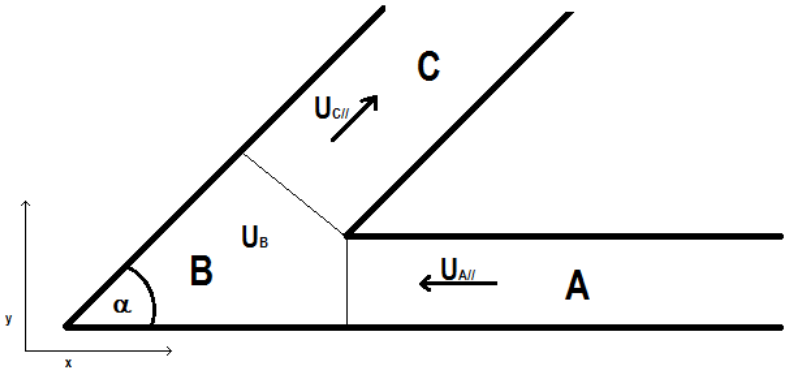

Figure 19: 2−dimensional inviscid flow between to straight solid boundaries intersecting at an angle α, representing the wind flow at an intersection between two canyons.

$\alpha = 2\pi$ corresponds to a canyon opening). A precise description of the inviscid flow in a canyon intersection should have to consider the conformal Schwarz–Christoffel mapping corresponding to the *elbow* geometry of Figure 19 [Batchelor, 1967]. The velocity components can be obtained as the gradient of the velocity potential; they generally vary with x and y. For example, in the case of $\alpha = \pi/2$, $u = \mathbf{U_{A//}}x$ and $v = \mathbf{U_{A//}}y$ (and $k = 1/2$). We can consider the dispersion process in Region **B** as the superposition of two 3−dimensional plume solutions, one advected by a velocity in the x direction with values u entering the intersection, the other by a velocity in the y direction with values v exiting the intersection (for angles different from $\alpha = \pi/2$, the exiting plume must be parallel to the side walls). The entering plume has an initial concentration determined by the dispersion in Region **A**. The exiting plume constitutes the initial concentration distribution C_b for dispersion in Region **C**. The Green propagation problem in Region **B** is generally simple: in the case of constant turbulent parameters and an angle $\alpha = \pi/2$, the Gaussian Green function of the entering plume in Region **B** is of the type:

$$G_B \propto \frac{\mathbf{U_{A//}}}{\log(x - x(0))} e^{-\frac{\mathbf{U_{A//}}(z-z_0)^2}{\log(x-x_0)}}$$

With turbulent parameters varying with polynomial laws in the direction of advection, the problem is exactly solvable. We do not develop a full treat-

ment of the solutions here, since it depends on the value of the intersections angles and on the laws of variance of the turbulent parameters.

Numerical models The numerical models consist in the solution of a discretized version of the unsteady dispersion equation (3.14):

$$\frac{\partial C}{\partial t} + U_j \frac{\partial C}{\partial x_j} = \frac{\partial}{\partial x_j}\left[\left(D + K_{jj}\right) \frac{\partial C}{\partial x_j} \right] \tag{3.62}$$

with the inhomogeneous Neumann boundary condition (2.3) for the flux at the road surface, in the case of Soot dispersion:

$$N = -v_d(0)C \tag{3.63}$$

and the inhomogeneous Neumann boundary condition (2.4) coupled with a balance equation for the road dust concentration at the road surface, in the case of road dust dispersion:

$$\begin{cases} N = -\dfrac{v_d(0)}{\theta_0} C(\theta_0 - c_s) + k_{res} c_s \\ \dfrac{\partial c_s}{\partial t} + v_v \dfrac{\partial c_s}{\partial x} = \dfrac{v_d(0)}{\theta_0} C(\theta_0 - c_s) - (k_{res} + f_x n_v) c_s + S(t), \end{cases} \tag{3.64}$$

Note that we are not considering a stationary value of the road dust concentration, as was done in the formulation of the operational models. The details of the deposition and resuspension fluxes modelization are reported in Section 2.3. We distinguish between the *near wake* and the *far wake-canyon* cases.

- *Near wake* case: the dispersion equation must be solved in the near wake zone of a single vehicle, in the system of reference of the vehicle, and must be coupled to the momentum conservation equation solved in the domain of Figure 15, with different Ahmed body geometries for different vehicle categories. The velocity components U_j in Equation (3.62) are thus the wind components obtained as a solution of the corresponding Turbulence models. Assuming an isotropic turbulent dispersion, the eddy diffusivity is given in terms of the eddy viscosity of the corresponding Turbulence model:

$$k - \epsilon \quad \text{model}: \quad \mathrm{K} = \nu_\mathrm{T} = \mathrm{C}_\mu \frac{\mathrm{k}^2}{\epsilon}$$
$$k - \omega \quad \text{model}: \quad \mathrm{K} = \nu_\mathrm{T} = \frac{\mathrm{k}}{\omega}$$

  In the case of Soot dispersion, the vehicle emission is introduced as an inhomogeneous Neumann flux on a small circle at the bottom of the vertical rear face of the Ahmed body, with a value of:

$$N_{emission} = v_{tp}Q,$$

where v_{tp} is the velocity of exiting exhaust fumes at the tailpipe (given by values in Ref. [EMEP/CORINAIR, 2007], multiplied by 4, since we are considering a reduced geometry), and Q is the vehicle Soot emission rate, dependent on the vehicle category and the driving cycle (calculated as shown in Section 2.1), transformed from mg/km to mg/m^3. In the case of road dust dispersion, the wear emissions are inserted through the $S(t)$ term (calculated as shown in Section 2.2) and as a Dirichlet boundary condition imposed on the tyres surface, depending on the vehicle category and the driving cycle, and transformed from emission data in mg/km to emission rates in mg/sm^2. We call this dispersion case **model C**.

- *Far wake-canyon* case: in this case the dispersion equation should be solved in the whole canyon domain for a multi-vehicle case, in a system of reference fixed in the canyon, considering the dispersion induced by the superposition of the vehicle wakes and by the components coming from the canyon wind recirculation. In order to simplify the problem, we consider the average wake effect of a series of vehicles, distributed along the road, in terms of their interacting far-wake solutions, and neglect the dispersion in the longitudinal x direction. The letter hypothesis is a good approximation if traffic is homogeneously distributed along the canyon, which permits to neglect the pollutant spreading in the downwake direction with respect to the spreading in the cross-wake and in the vertical directions. The problem is thus $2-$dimensional, and the dispersion equation is:

$$\frac{\partial C}{\partial t} + v\frac{\partial C}{\partial y} + w\frac{\partial C}{\partial z} = \frac{\partial}{\partial y}\left[K_y\frac{\partial C}{\partial y}\right] + \frac{\partial}{\partial z}\left[K_z\frac{\partial C}{\partial z}\right] \tag{3.65}$$

The advection velocity components v and w are expressed as a sum of the wind recirculation components v_r and w_r plus the components of the far-wake solutions averaged over all the vehicles along the canyon $\overline{v}_w$ and $\overline{w}_w$. The v_r and w_r components are given in terms of the self-preserving analytical solutions, derived in Section 4.1, depending on the intensity of the orthogonal component of the external wind and on the canyon geometry. These solutions are valid for situations in which the recirculation vortex is totally immersed inside the canyon. Note that, for an open street geometry or for situations with no wind recirculation, only the far-wake components of velocity must be considered in the dispersion Equation (3.65). The self preserving far-wake components for each vehicle have the form of Equation (3.21):

$$u_w(x,y,z) = U_\infty - U_\infty A\left(\frac{x}{h}\right)^{-3/4} f[\eta,\zeta]$$
$$v_w(x,y,z) = U_\infty c_v A^2\left(\frac{x}{h}\right)^{-3/2} g[\eta,\zeta]$$
$$w_w(x,y,z) = U_\infty c_w A^2\left(\frac{x}{h}\right)^{-3/2} h[\eta,\zeta]$$

where U_∞ is the vehicle velocity, c_v and c_w are constants, and the f, g, h are self-preserving functions in terms of the y and z variables scaled with the wake thickness (see Section 4.1 for the details). Now consider a distribution of N vehicles at the points $\{(x_j, y_j) : j = 1, \cdots, N\}$ along the canyon, separated by a distance Δx (determined by the driving conditions). Following Ref. [Eskridge et al., 1979], the effect of many vehicles can be obtained by summing the average wake effect of each vehicle as it takes on all positions between $x_j + \Delta x/2$ and $x_j - \Delta x/2$:

$$\begin{cases} \overline{u}_w(x,y,z) = U_\infty - \dfrac{1}{\Delta x}\displaystyle\sum_{j=1}^{N}\int_{x_j-\Delta x/2}^{x_j+\Delta x/2} dx\, U_\infty A_j\left(\frac{x_j}{h}\right)^{-3/4} f[\eta_j,\zeta_j] \\ \overline{v}_w(x,y,z) = \dfrac{1}{\Delta x}\displaystyle\sum_{j=1}^{N}\int_{x_j-\Delta x/2}^{x_j+\Delta x/2} dx\, U_\infty c_v A^2\left(\frac{x}{h}\right)^{-3/2} g[\eta,\zeta] \\ \overline{w}_w(x,y,z) = \dfrac{1}{\Delta x}\displaystyle\sum_{j=1}^{N}\int_{x_j-\Delta x/2}^{x_j+\Delta x/2} dx\, U_\infty c_w A^2\left(\frac{x}{h}\right)^{-3/2} h[\eta,\zeta] \end{cases} \tag{3.66}$$

As will be described in Section 4.1, we are introducing the effect of far wake interactions in the form of the constants A_j (and reduction of the values of U_∞ for each vehicle from its moving velocity), so that the Formula (3.66) can be applied not only to situations of non interacting vehicles, as in Ref. [Eskridge et al., 1979], but also to situations with intermediate and heavy traffic conditions. With this averaging procedure and the introduced hypothesis of homogeneous distributed traffic along the canyon, we effectively remove the x coordinate from the description of the dispersion process. substitution of σ_{tpt} parametrization.

The eddy diffusivity components K_y and K_z are given as a sum of recirculation components, K_r^y and K_r^z, plus average far-wake components for the multi-vehicle situation, K_w^y and K_w^z. We do not consider the contribution to the eddy diffusivity coming from the basic state atmosphere. This contribution is described in Ref. [Eskridge et al., 1979], in terms of the Obukhov length and the bulk Richardson number

[Seinfeld, Pandis, 2006]. Since the introduced parametrization needs measurement data on the temperature vertical profile to be specified, we neglect this term, whose influence will be treated in future investigations of specific cases with known atmospheric stratification data. The recirculation components are given as:

$$K_r^y = K_r^z = \omega_0 \delta^2, \tag{3.67}$$

where ω_0 is the mean value of the recirculation vorticity inside the canyon, and δ is the wake thickness relative to the recirculation flow. This is equivalent to the prescription that the eddy diffusivity associated to the wind recirculation be equal to the eddy viscosity of the associated algebraic Turbulence model, which will be treated in Section 4.1. Note that δ has different expressions in different regions of the canyon domain. The average far-wake components are given as:

$$\begin{cases} K_w^y = \dfrac{1}{\Delta x} \displaystyle\sum_{j=1}^{N} \int_{x_j - \Delta x/2}^{x_j + \Delta x/2} dx \, \overline{v'}^2 \delta(x) \\ K_w^z = \dfrac{1}{\Delta x} \displaystyle\sum_{j=1}^{N} \int_{x_j - \Delta x/2}^{x_j + \Delta x/2} dx \, \overline{w'}^2 \delta(x) \end{cases} \tag{3.68}$$

where $\overline{v'}^2$ and $\overline{w'}^2$ are the mean square turbulent velocity components of the far-wake solution, calculated by assuming that the Turbulence has also a self-preserving form (see Section 4.1 for the details), and $\delta(x)$ is the far-wake thickness. In the case of Soot dispersion, the vehicle emission is introduced as a point source at an height H_e above the centerline of the canyon. In the case of road dust dispersion, the wear emissions are inserted through the $S(t)$ term. The deposition and the resuspension fluxes are calculated averaging the contributions from each vehicle. The deposition velocity and the resuspension rates depend on near-wake turbulent quantities, integrated over the near wake road surface portion, as explained in Sections 2.3 and 4.3. Thus the near-wake effects on the dispersion at the canyon scale, for the multi-vehicle case, are confined to the determination of the deposition and the resuspension fluxes, whereas the advection and the eddy diffusivity components depend on far-wake and recirculation effects. We call this dispersion case **model D**. Note that we are considering a linear superposition of the recirculation and the wake flows in the dispersion dynamics, as in most of the canyon dispersion models in literature [Berkowicz, Kearney, 2004]. Possible non-linear interaction effects on the dispersion dynamics will be considered in future investigations, by means of approximated non-linear superposition principles (Darboux

transform [Rogers, Schief, 2002]) associated to the Turbulence equations.

The boundary condition for the side walls of the canyon is homogeneous Neumann condition (no flux), and the boundary condition for the roof level is homogeneous Dirichlet condition($C = 0$), for both **model C** and **model D**. For **model C**, the boundary condition for the front and bottom plane of the canyon (the inlet and the outlet boundaries relative to the wind flow problem) is a convective flux condition, i.e. the imposition that the diffusion flux across the boundary is zero.

The grid for **model C** is the same as that used in the simulation of the near-wake wind flow near the Ahmed body (see Figure 15). The grid for **model D** is the same as that used in the simulation of the $2-$dimensional wind flow generated by an external orthogonal wind in a canyon (see Figure 11, bottom panel).

We solve the dispersion equations in the context of a finite element discretization. In particular, for the road dust dispersion case, a weak formulation for the balance equation of the road dust concentration at the road boundary is also introduced. We choose piecewise linear finite elements as the discretization elements, corresponding to the order of the wind solution elements. We introduce a streamline diffusion stabilization (Galerkin Least Squares) in order to stabilize the convection-dominated equations.

The time dependent equations are solved by a BDF Euler semi-implicit method. The applications of this scheme to the discretized systems have shown to be stable despite the introduction of the stabilization terms for proper choices of the time step, avoiding the necessity to introduce operator splitting schemes, which would introduce the need to split the boundary conditions at the road surface as well. At each iteration step the corresponding linear algebraic system are solved with direct LU factorization methods (in the case of $2D$ simulations) or with the $GMRES$ iterative procedure (in the case of $3D$ simulations), with Geometric Multigrid (GM) smoothers. We consider a time step based on the wave propagation and molecular diffusion Courant numbers. Finally, in the case of road dust dispersion, the bulk concentration and the road surface balance equations are solved sequentially at each time step.

In Table 15 we recapitulate the introduced dispersion models, which consider the deposition and the resuspension processes, along with the methods adopted to obtain them, the reference to the Equations of their formulation, and their range of validity; the results will be shown in Section 4.4.

	Methods	Equations	Validity
Model A	*Street* model + modifications	(3.27) **Soot** (3.28) **road dust**	Street Canyon + recirculation
Model B	*OSPM* model + plume solutions	(3.43)-(3.44) **Soot** (3.45) **road dust**	Open street
		(3.49)-(3.52) **Soot** (3.53) **road dust**	Street Canyon-no recirculation + canyon intersections
	Gaussian segments + Box model	(3.54)-(3.58)-(3.29) **Soot** and **road dust**	Street Canyon+ recirculation + canyon intersections
Model C	Numerical	(3.62) +(3.63)**Soot** +(3.64)**road dust**	Near wake
Model D	Numerical	(3.65) +(3.63)**Soot** +(3.64)**road dust**	Street canyon

Table 15: Recapitulation of the dispersion models, along with the methods adopted to obtain them, the reference to the Equations of their formulations, and their range of validity

4 Results

In Section 4.1 we report the results of the analytical solutions of algebraic Turbulence models for the canyon and the vehicle geometries (Section 4.1), which are needed to calibrate the 2− equations Turbulence models and to set up the dispersion equations at the street canyon spatial scale. In Section 4.2 we show the results of the 2− equations Turbulence simulations, in order to validate the analytical solutions for the flow inside the street canyon and to obtain proper parameterizations of the deposition and the resuspension fluxes, reported in Section 4.3. These parametrizations are used to describe the corresponding physical processes in the tailpipe traffic emission models, introduced in Section 2.6 and 2.8, and in the dispersion models at the street canyon scale, described in Section 3.5. In Section 4.4 we report the results of the application of an operational dispersion model at the canyon scale (**model B**) to estimate the pollutant spatial concentrations, for the case of a congested urban traffic configuration.

4.1 Analytic solutions

Street canyon We describe the turbulent flow within the street canyon by the stationary RANS equations with the eddy viscosity hypothesis:

$$\begin{cases} v\frac{\partial u}{\partial y} + w\frac{\partial u}{\partial z} = \frac{\partial}{\partial y}\left[(\nu+\nu_T)\frac{\partial u}{\partial y}\right] + \frac{\partial}{\partial z}\left[(\nu+\nu_T)\frac{\partial u}{\partial z}\right] \\ v\frac{\partial v}{\partial y} + w\frac{\partial v}{\partial z} = -\frac{1}{\rho}\frac{\partial p}{\partial y} + \frac{\partial}{\partial y}\left[(\nu+\nu_T)\frac{\partial v}{\partial y}\right] + \frac{\partial}{\partial z}\left[(\nu+\nu_T)\frac{\partial v}{\partial z}\right] \\ v\frac{\partial w}{\partial y} + w\frac{\partial w}{\partial z} = -\frac{1}{\rho}\frac{\partial p}{\partial z} + \frac{\partial}{\partial y}\left[(\nu+\nu_T)\frac{\partial w}{\partial y}\right] + \frac{\partial}{\partial z}\left[(\nu+\nu_T)\frac{\partial w}{\partial z}\right], \end{cases} \tag{4.1}$$

where (u, v, w) and p are respectively the averaged vector field of velocity and the scalar field of pressure, ν is the air viscosity and ν_T the turbulent viscosity. Due to the hypothesis of stationarity and homogeneity along the x direction of the mean field (the x axis is aligned with the street axis), the terms containing $\frac{\partial}{\partial t}$ and $\frac{\partial}{\partial x}$ are zero. We must add the solenoidal condition for the incompressible averaged vector field of velocity. Here we do not consider thermal stratification, so the equations are not coupled to the energy balance equation. We can see from (4.1) that the equations for v and w do not depend on the u component. This means that the equations for the components of velocity transversal to the canyon are not coupled to the equation for the longitudinal component, so they can be solved indipendently in a two dimensional model. This indipendent two dimensional flow is generated by the component of the external wind field orthogonal to the street axis. Generally speaking, the equation for the u component is coupled to the equations for the transversal components. In the special case of an external wind flow parallel to the street axis (considering homogeneity in the x direction), the motion in the cross sectional-plane cannot survive the

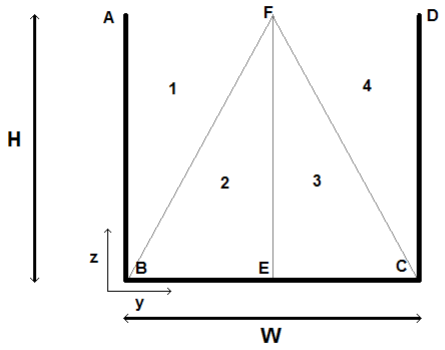

Figure 20: Domain geometry of the transversal plane of a symmetric canyon. H is the height of the side walls, W is the width of the street canyon. The domain decomposition for the solution at different scales is reported

viscous dissipation of energy, as there is not a supply of energy to the fluid by tangential stresses at the boundaries (tangential stresses in y and z directions are zero at the roof boundary). In this way the stationary solution is in the x direction ($v = 0$ and $w = 0$) and depends on the y and z coordinates only. The motion is unidirectional and the advective term in the first equation of (4.1) is identically zero. We can thus separate the analysis in two different cases: i) a parallel external wind and ii) an external wind orthogonal to the street axis. The case for an arbitrary angle of external flow relative to the street axis will be treated with the help of numerical considerations, as in Ref. [Soulhac et al., 2008].

External wind parallel to the street axis As expressed in the previous paragraph, in this case the flow is unidirectional and the problem is two dimensional. The governing equation is:

$$\frac{\partial}{\partial y}\left[(\nu + \nu_T)\frac{\partial u}{\partial y}\right] + \frac{\partial}{\partial z}\left[(\nu + \nu_T)\frac{\partial u}{\partial z}\right] = 0 \tag{4.2}$$

The geometry of the problem is shown in figure 20.

Equation (4.1) and (4.2) will be considered within the scheme of singular perturbation theory [Wilcox, 1998], using different asymptotic expansions, in suitable powers of a small parameter, for different stretching of coordinate variables (representing the different scales in the physical process); these asymptotic expansions are valid on different portions of the domain, but not uniformly on the whole domain. We recall from Section 3.1 that Turbulence sets up two different dominant scales in the boundary layer near a rigid boundary: the wall scale, scaling with distance from the wall as

$$y^+ = \frac{u_* y}{\nu},$$

and the wake scale, scaling as

$$\eta = \frac{y}{\delta}$$

The solution in the wall variables is logarithmically divergent far from the wall, and must match the wake solution for wake variables tending to zero [Wilcox, 1998]. For each scale and each term of asympthotic expansion, the existence of separated solutions is equivalent to the Helmotz hypothesis of existence of self-similar solutions for the boundary layer problem [Batchelor, 1967]. Let us start from the solution close to the three solid boundaries of the canyon (segments AB, BC and CD in figure 1). We scale the variables, for each segment of the rigid boundaries, and take the asympthotic expansions as reported in Table 16:

The sequence of asympthotic functions $\{1, \phi_1, \phi_2, \dots\}$ must be suitably chosen from the analysis of the equations. We assume that the main features of the solutions can be described by the first few terms of the asymptotic expansions defined in table 16. Let us consider the AB segment. We choose the parameter of the asymptotic expansion as

$$\phi_1 = \frac{\nu}{u_*(z_1^+)\delta(z_1^+)},$$

i.e. the inverse of the Reynolds number based on friction velocity. $\delta(z_1^+)$, the wake thickness, and $u_*(z_1^+)$ will be introduced in Section 4.1, in the context of the wake solution derivation. The sequence of asymptotic functions is given by the integer powers of ϕ_1, with $\phi_2 = \phi_1^2$. Clearly $u_* = O(1)$, the stress in y direction is $O(u_*^2) = O(1)$, and the stress in z direction is $O(\phi_1)$. Besides this, by requiring the existence of separated solutions to higher orders, we can see that terms like $\frac{u_*'}{u_*}$, where the prime stand for differentiation with respect to the variable on which the function depends, are $O(1)$ or limited variation functions (this is a general consequence of the procedure, and is valid for all the perturbation expansions we are considering in this paper). This ensure the validity of the perturbation. By substituting the formulas contained in table 16 and the change of variables transformation:

$$\begin{cases} \frac{\partial}{\partial y} = \frac{u_*(z_1^+)}{\nu} \frac{\partial}{\partial y_1^+} \\ \frac{\partial}{\partial z} = \frac{1}{H} \frac{\partial}{\partial z_1^+} + \frac{1}{H} \frac{u_*'(z_1^+)}{u_\tau(z_1^+)} y_1^+ \frac{\partial}{\partial y_1^+} \end{cases} \tag{4.3}$$

Segment **AB**	*Segment* **BE**
$y_1^+ = \dfrac{u_*(z)y}{\nu}$ $z_1^+ = \dfrac{z}{H}$	$y_2^+ = \dfrac{2y}{W}$ $z_2^+ = \dfrac{u_*(y)z}{\nu}$
$u = u_*(z_1^+)[u_0(y_1^+) + \phi_1 u_1(y_1^+, z_1^+) + \phi_2 u_2(y_1^+, z_1^+) + o(\phi_2)]$	$u = u_*(y_2^+)[u_0(z_2^+) + \phi_1 u_1(y_2^+, z_2^+) + \phi_2 u_2(y_2^+, z_2^+) + o(\phi_2)]$
$\nu_T = \nu[N_0(y_1^+) + \phi_1 N_1(y_1^+, z_1^+) + \phi_2 N_2(y_1^+, z_1^+) + o(\phi_2)]$	$\nu_T = \nu[N_0(z_2^+) + \phi_1 N_1(y_2^+, z_2^+) + \phi_2 N_2(y_2^+, z_2^+) + o(\phi_2)]$

Segment **EC**	*Segment* **CD**
$y_3^+ = \dfrac{2(W-y)}{W}$ $z_3^+ = \dfrac{u_*(y)z}{\nu}$	$y_4^+ = \dfrac{u_*(z)(W-y)}{\nu}$ $z_4^+ = \dfrac{z}{H}$
$u = u_*(y_3^+)[u_0(z_3^+) + \phi_1 u_1(y_3^+, z_3^+) + \phi_2 u_2(y_3^+, z_3^+) + o(\phi_2)]$	$u = u_*(z_4^+)[u_0(y_4^+) + \phi_1 u_1(y_4^+, z_4^+) + \phi_2 u_2(y_4^+, z_4^+) + o(\phi_2)]$
$\nu_T = \nu[N_0(z_3^+) + \phi_1 N_1(y_3^+, z_3^+) + \phi_2 N_2(y_3^+, z_3^+) + o(\phi_2)]$	$\nu_T = \nu[N_0(y_4^+) + \phi_1 N_1(y_4^+, z_4^+) + \phi_2 N_2(y_4^+, z_4^+) + o(\phi_2)]$

Table 16: Scaling of variables and asympthotic expansions chosen for the wall solutions with the boundaries divided in four segments

into equation (4.2) we obtain:

$$\frac{\partial}{\partial y_1^+}\left[(1+N_0+N_1\phi_1+N_2\phi_2+o(\phi_2))\,\frac{\partial}{\partial y_1^+}(u_0+u_1\phi_1+u_2\phi_2+o(\phi_2))\right]+$$
$$\phi_2\frac{\delta^2}{H^2}\frac{1}{u_*}\frac{\partial}{\partial z_1^+}\left[(1+N_0)\left(u_*'u_0+u_*\frac{\partial}{\partial z_1^+}u_0+u_*'y_1^+\frac{\partial}{\partial y_1^+}u_0+o(1)\right)\right]+$$
$$\phi_2\frac{\delta^2}{H^2}\frac{u_*'}{u_*^2}y_1^+\frac{\partial}{\partial y_1^+}\left[(1+N_0)\left(u_*'u_0+u_*\frac{\partial}{\partial z_1^+}u_0+u_*'y_1^+\frac{\partial}{\partial y_1^+}u_0+o(1)\right)\right]+o(\phi_2)=0 \tag{4.4}$$

If we retain only the zeroth order term of the expansion, and use the Prandtl law for the eddy viscosity far away from the boundary surface: $N_0 = ky_1^+$ for $y_1^+ \to \infty$ (with $k = 0.408$ the Von Karman constant), we obtain the law of the wall:

$$u \sim u_*(z_1^+)\left[\frac{1}{k}\ln y_1^+ + C\right] \qquad for \qquad y_1^+ \to \infty \tag{4.5}$$

where C is a constant of integration. The term $u_*(z_1^+)$ is determined by the matching with the wake solution. Equation (4.4) is also valid in the other segments of the canyon boundaries (with the appropriate coordinates), so the wall solutions have the same form in all the sections of the boundaries defined in Figure 20. We are interested only in the $y_1^+ \to \infty$ limit of the wall solutions, since we have to set up a boundary condition for the wake solution matching with the logarithmic law (4.5). A complete solution of the problem would require the use of the Van-Driest law of variation for the eddy viscosity near the surface [Wilcox, 1998], in order to resolve the viscous sublayer of the boundary, and to add the viscous and the wake solutions, after having performed the matching and having subtracted the overlapping part of the two solutions. The Van-Driest law has the form:

$$\nu_T = ku_*y\big(1-e^{-\frac{y^+}{B}}\big) \tag{4.6}$$

where B is Van-Driest constant. We will find in Section 4.1, in the context of the matching between the wall and the wake solutions, a way to derive an alternative form to the Van Driest law for the eddy viscosity, valid near the surface, as an asymphtotic expansion for the function N (defined in table 16) in powers of ky^+.

Let us consider the wake solution. In Equation (4.2) the viscosity of air can be neglected. In this case there are not small parameters which allow the study of a perturbative solution (in the study of the wake solution on a plate boundary, the small parameter is the deviation from the external velocity, and a perturbation analysis can be set up [Wilcox, 1998]). In this case the solution must vanish near the corners of the canyon in the wake solution too,

so the deviation from the external velocity is not small. Anyway, we search for separated solutions in suitable scaled coordinate variables, and perform the matching with the wall solutions and between the wake solutions in the four regions defined in Figure 20. We scale the variables, for each region of the domain, and search for separated solutions as reported in table 17:

Region **1**	*Region* **2**	*Region* **3**	*Region* **4**
$\eta_1 = \dfrac{y}{\delta_1(z)}$ $\zeta_1 = \dfrac{z}{H}$	$\eta_2 = \dfrac{2y}{W}$ $\zeta_2 = \dfrac{z}{\delta_2(y)}$	$\eta_3 = \dfrac{2(W-y)}{W}$ $\zeta_3 = \dfrac{z}{\delta_3(y)}$	$\eta_4 = \dfrac{W-y}{\delta_4(z)}$ $\zeta_4 = \dfrac{z}{H}$
$\frac{u}{U_\infty} = f_1(\eta_1)g_1(\zeta_1)$	$\frac{u}{U_\infty} = f_2(\zeta_2)g_2(\eta_2)$	$\frac{u}{U_\infty} = f_3(\zeta_3)g_3(\eta_3)$	$\frac{u}{U_\infty} = f_4(\eta_4)g_4(\zeta_4)$
$\nu_T = U_\infty \frac{W}{2}\eta_1 g_1(\zeta_1)$	$\nu_T = U_\infty H \zeta_2 g_2(\eta_2)$	$\nu_T = U_\infty H \zeta_3 g_3(\eta_3)$	$\nu_T = U_\infty \frac{W}{2}\eta_4 g_4(\zeta_4)$

Table 17: Scaling of variables, separated form for the wake solutions and turbulence modelization with the domain divided in four regions

Here δ is the wake thickness and U_∞ is the external velocity. We are supposing that turbulence sets up different self-similar solutions for each defined region of the domain, which are separated solutions in the newly scaled variables, each one performing its own matching with the wall solution of the corresponding segment. The eddy viscosity, in an algebraic model of turbulence, is usually given in two different ways (see Section 3.1):

- through Prandtl mixing-length hypothesis:
- Through Prandtl prescription for free-shear layer problems:

In our case the velocity u is perpendicular to the plane of the motion. For the solution near the canyon walls, we have already used the prescription (valid in region **1**):

$$\nu_T = y^2 \frac{\partial u}{\partial y} = k u_* y = \nu k y^+ \qquad for \qquad y^+ \to \infty$$

For the wake solution, far from the solid boundaries, a possible prescription for the eddy viscosity would be: $\nu_T = U_\infty \delta(z)$. This modelization for the wake eddy viscosity leads to unusual boundary value problems, which will be treated in the Appendix. The fact is that this prescription would be suitable if the wake thickness is a small parameter, and the wake solution matches to the external flow for $\eta = y/\delta \to \infty$. This will be the case for

the external wind perpendicular to the street axis, and will be treated in the next paragraph. Here, δ is a finite parameter, and the wake solution extends to the whole canyon domain. We have thus used the mixing-length prescriptions reported in Table 17, whose meaning will be clear in a moment. Consider region 1, and suppose that the component of the solution $g_1(\zeta_1)$ is the same component $u_*(z_1^+)$ of the wall solution: Turbulence changes the solutions form only in the direction orthogonal to the boundary. (The same argument applies to the other regions). By inserting the formulas in table 17 and the change of variable transformations into equation (4.2), we obtain:

$$H^2\eta_1 f_1^{''} + H^2 f_1^{'} + \left(\frac{g_1^{'}}{g_1}\right)^2 \delta_1^2\eta_1 f_1 + \frac{g_1^{''}}{g_1}\delta_1^2\eta_1 f_1 - 3\delta_1\delta_1^{'}\frac{g_1^{'}}{g_1}\eta_1^2 f_1^{'} - \delta_1\delta_1^{''}\eta_1^2 f_1^{'} - \delta_1\delta_1^{'}\frac{g_1^{'}}{g_1}\eta_1 f_1 + 3\delta_1^{'2}\eta_1^2 f_1^{'} + \delta_1^{'2}\eta_1^3 f_1^{''} = 0 \tag{4.7}$$

This equation is indipendent of the ζ_1 variable, and so a separated solution exists, if:

$$\begin{cases} \delta_1 = a_1\zeta_1 \\ \\ g_1 = \zeta_1^{b_1/a_1^2} \end{cases} \tag{4.8}$$

with a_1 and b_1 suitable constants, to be determined from the matching procedure and as eigenvalues of the boundary problem. Now the eddy viscosity prescription chosen becomes clear. We have:

$$\nu_T = U_\infty \frac{W}{2}\eta_1 g_1(\zeta_1) = HyU_\infty \frac{du_*}{dz}$$

This is equivalent to the mixing length hypothesis, with $l_{mix}^2 = Hy$, and the turbulent mixing given, in the wake region, by the derivative of the u_* component of velocity (the component of velocity dependent on y is responsible for the turbulent mixing near the solid boundary). There are two different scales for the mixing length, and the eddy viscosity still depends on the distance from the wall, as the wake zone extends to all the domain. Note that $u_* = g_1(\zeta_1)$ is dimensionless, and that its derivative is always positive, so that the absolute value in the mixing length hypothesis can be omitted. The equation for f_1 becomes:

$$\left[H^2\eta_1 + a_1^2\eta_1^3\right] f_1^{''} + \left[H^2 + \left(3a_1^2 - 3b_1\right)\eta_1^2\right] f_1^{'} + 2\left[\frac{b_1^2}{a_1^2} - b_1\right]\eta_1 f_1 = 0 \tag{4.9}$$

Equation (4.9) is valid for each f_i, $i = 1, \ldots, 4$, with constants $\{a_i, b_i\}$, $i = 1, \ldots, 4$, and with the substitution $H \to \frac{W}{2}$ from regions 1 and 4 to regions 2

and 3, if equation (4.8) is valid for each g_i, $i = 1, \ldots, 4$. Equation (4.9) is a Fuchsian equation with four regular singular points [Morse, Feshbach, 1953]. The method to find its solutions is given in the Appendix. Let us show now the matching procedure and the setting of boundary conditions. If we choose the values of the a_i parameters to be $a_1 = a_4 = \frac{W}{2}$ and $a_2 = a_3 = H$, we find that the segments **BF** and **CF**, with equations **BF** : $z = \frac{2H}{W} y$ and **CF** : $z = H\big(2 - \frac{2y}{W}\big)$, corresponds to the points:

$$\mathbf{BF}: \quad \eta_1 = \zeta_2 = 1 \qquad \mathbf{CF}: \quad \zeta_3 = \eta_4 = 1 \tag{4.10}$$

Regions **1**, **2** are given for $0 \leq y \leq \frac{W}{2}$, $0 \leq z \leq H$, with $y \leq \frac{W}{2}\frac{z}{H}$ for region **1**, and $y \geq \frac{W}{2}\frac{z}{H}$ for region **2**; regions **3**, **4** are given for $\frac{W}{2} \leq y \leq W$, $0 \leq z \leq H$, with $W - y \geq \frac{W}{2}\frac{z}{H}$ for region **3**, and $W - y \leq \frac{W}{2}\frac{z}{H}$ for region **4**. (We have found that with other algebraic turbulence models it's possible to perform the matching on polynomial segments. Details will be given elsewhere).

We set the boundary conditions for the f_i functions (with arguments ξ_i):

$$\begin{cases} f_i(1) = 1 \\ f_i'(0) \to \frac{1}{k\xi_i} \end{cases} \tag{4.11}$$

The second boundary condition ensure the matching with the law of the wall. The first condition enables the matching between the four regions. Note that the corner points **B** and **C** are on the segments corresponding to the points $\eta_1 = \zeta_2$; $\zeta_3 = \eta_4 = 1$, so that there the solution results correctly not logarithmically divergent, but vanishing with the g_i functions if:

$$\frac{b_i}{a_i^2} > 0 \tag{4.12}$$

In the point **F** the functions f_i, g_i are all equal to 1, so that $u = U_\infty$, as it should be. The condition of matching is now reduced to the fact that the g_i functions coincide on the segments **BF** and **CF**:

$$\begin{cases} \mathbf{BF}: \quad \left(\frac{z}{H}\right)^{b_1/a_1^2} = \left(\frac{2y}{W}\right)^{b_1/a_1^2} = \left(\frac{2y}{W}\right)^{b_2/a_2^2} \\ \qquad\qquad\qquad\qquad\qquad\qquad \Longrightarrow b_1 = b_4 = \frac{W^2}{4H^2} b_2 = \frac{W^2}{4H^2} b_3 \\ \mathbf{CF}: \quad \left(\frac{z}{H}\right)^{b_4/a_4^2} = \left(2 - \frac{2y}{W}\right)^{b_4/a_4^2} = \left(2 - \frac{2y}{W}\right)^{b_3/a_3^2} \end{cases} \tag{4.13}$$

The eigenvalues of the boundary value problem associated to Equation (4.9) and boundary conditions (4.11) are (see condition (6.5) in the Appendix):

$$b_1/a_1^2 = c \in \mathbb{N} > 0$$

Equation (4.9) can be rewritten in the form (6.1), and transformed into an hypergeometric equation, except at the point $\chi \to \infty$ for the case c an odd integer: in this case the monodromy representation of the hypergeometric equation is different from that of the Equation (6.1), and a proper analytic continuation for the solution of the hypergeometric equation needs to be implemented in order to obtain a solution of the original problem, as explained in the Appendix. In the case $c = 2n + 1$, with $n \in \mathbb{N} > 0$, a general solution is given by Equation (6.16), in the form of polynomials terms of degree $4n$, plus terms proportional to $\log \chi$, $\chi^2 \log \chi$, $\cdots \chi^{4n} \log \chi$, plus analogous terms containing $\sqrt{1+\chi^2}$. In the case $c = 2n$, with $n \in \mathbb{N} > 0$, a general solution is given by Equation (6.20), in the form of polynomials terms of degree $2n$, plus terms proportional to $\log \chi$, $\chi^2 \log \chi$, $\cdots \chi^{2n} \log \chi$. We see that only polynomials of even orders are generated. These solutions must be matched to the wall solutions of Equation (4.4). By considering an asymptotic expansion for the eddy viscosity near the wall of the form:

$$\nu_T = \nu\big[ky^+ + \phi_1 \cdot 0 + \phi_2 d(y^+)^3 + \cdots\big]$$

i.e. considering an expansion of the eddy viscosity in odd powers of y^+, we obtain, in the limit $y^+ \to \infty$, wall solutions in the form of polynomials of even orders and logarithmic terms multiplied by even powers of y^+. The matching procedure with the wake solutions, for $c \in \mathbb{N} > 0$, specifies the coefficients of the expansion $d, \cdots$. This prescription for the eddy viscosity near the wall, as an expansion of odd powers of y^+, is a correction to the empirical law of Van Driest (4.6), and can be used to obtain the wall solutions in the viscous region, for $y^+ \to 0$.

Let us show the matching procedures for the case $c = 1$ and $c = 2$. The solution of Equation (4.9) in the case $b_1/a_1^2 = c = 1$, is (see (6.17)):

$$A\left\{\sqrt{1+\left(\frac{W}{2H}\eta_1\right)^2} + \log\left[\frac{W}{2H}\eta_1\right] - \log\left[1+\sqrt{1+\left(\frac{W}{2H}\eta_1\right)^2}\right]\right\} + B \quad (4.14)$$

The matching with the law of the wall imposes:

$$\left[\frac{1}{k}\log(y_1^+) + C\right] - \big[A\log(\eta_1) + f_0\big] \longrightarrow 0 \quad for \quad y^+ \to \infty; \eta_1 \to 0 \quad (4.15)$$

where f_0 comprises all the constants of the solution (4.3) for $\eta_1 \to 0$. Hence:

$$A = \frac{1}{k}$$

The other boundary condition (the first condition in Equation (4.11)) is satisfied if:

$$B = 1 - \frac{1}{k}\left[\sqrt{1+\frac{W^2}{4H^2}} + \log\left(\frac{W}{2H}\right) - \log\left(1+\sqrt{1+\frac{W^2}{4H^2}}\right)\right]$$

Observing now that:

$$y_1^+ = \frac{u_* \delta_1}{\nu}\eta_1 = Re_{wake}\,\eta_1$$

where Re_{wake} is the Reynolds number based on friction velocity and wake dimensions, we obtain:

$$C = -\frac{1}{k}\log\left(Re_{wake}\right) + \frac{1}{k}\left(1 + \log\frac{W}{2H} - \log 2\right) + B$$

This means that matching imposes that the constant C of the viscous solution be dependent on wake scaling and variable along the wall. The solution (4.14), with the specified values of A and B, is valid starting from a point at a distance $y_1^+ \sim 30$ from the wall [Wilcox, 1998]. In order to have a uniformly valid solution on the whole domain, we have to subtract from the sum of the viscous solution and the wake solution (4.14) the part of the viscous solution which overlaps with the wake one for $y_1^+ \to \infty$. From Equation (4.15), it is clear that the term in $\log \eta_1$ disappears from the solution (4.14). A wall solution valid for $y_1^+ \to 0$ should be obtained from Equation (4.4) considering higher orders in the asymptotic expansion of ν_T ($\nu_T = \nu k y_1^+$ is valid only for $y_1^+ \to \infty$ [Wilcox, 1998]). We consider an approximation to the $O(\phi_2)$ order. As we have already seen, matching with the wake solution implies that $N_1 = 0$, $N_2 = d\left(y_1^+\right)^3$. Observing that:

$$\frac{\delta_1^2}{H^2}\frac{u_*''}{u_*} = \frac{\delta_1^2}{H^2}\frac{\left(u_*'\right)^2}{u_*^2} = \frac{W^2}{4H^2},$$

which means that separated solutions u_i of equation (4.4), i.e. depending only on the variable y_1^+, exist at all orders, we obtain, in the limit $y_1^+ \to \infty$, the solution at the $O(\phi_2)$ order:

$$u_2\left(y_1^+\right) = -\frac{W^2}{16H^2}\left(y_1^+\right)^2 - d\frac{\left(y_1^+\right)^2}{2k} + \frac{W^2}{16H^2 k}\left(y_1^+\right)^2 - \frac{W^2}{8H^2 k}\left(y_1^+\right)^2 \log\left(y_1^+\right) + D \tag{4.16}$$

The part of solution (4.16) proportional to $\log\left(y_1^+\right)$ has been inglobed into the u_0 solution. The wall solution, at $O(\phi_2)$ order of approximation, is:

$$u\left(y_1^+\right) = \left[\frac{1}{k}\log(y_1^+) + C\right] + \phi_2 u_2\left(y_1^+\right)$$

By matching with the wake solution $f(\chi) = f_{c=1}(\chi) + f_{c=2}(\chi)$ we can obtain the value of d. The wake solution, for the case $c = 2$, is (6.21):

$$f(\chi) = A\left\{-2-\log\left(\frac{W}{2H}\eta_1\right)+\left(\frac{W}{2H}\eta_1\right)^2\log\left(\frac{W}{2H}\eta_1\right)\right\}+B\left\{1-\left(\frac{W}{2H}\eta_1\right)^2\right\} \tag{4.17}$$

The term proportional to $\log\left(\frac{W}{2H}\eta_1\right)$ is summed to the corresponding term in the $f_{c=1}$ solution, so that matching requires that:

$$A = \frac{1}{2k}$$

B is determined in such a way to satisfy the condition $f(1) = 1$. Now, remembering that:

$$\phi_2 = \frac{1}{Re_{wake}^2}$$

we obtain, by matching with the wake solution with the solution at the order $O(\phi_2)$:

$$d = \frac{kW^2}{2H^2}\left(B + \frac{1}{4k} - \frac{1}{4}\right) \tag{4.18}$$

We can now solve Equation (4.4), with the prescription $\nu_T = \nu\left[ky^+ + \phi_1 \cdot 0 + \phi_2 d(y^+)^3\right]$, and sum its solution with the solution $f(\chi) = f_{c=1}(\chi) + f_{c=2}(\chi)$, subtracting the overlapping part for $y_1^+ \to \infty$, $\eta_1 \to 0$, in order to obtain the **uniformly valid solution** (for the whole domain of region **1**) $\mathbf{u}(\eta_\mathbf{1})$:

$$\begin{aligned}
&\mathbf{u}(\eta_\mathbf{1}) = \frac{1}{2k}\log\left(1+ky_1^+\right) + \frac{1}{4k^4\left(1+ky_1^+\right)}\cdot \\
&\left\{-\frac{W^2}{4H^2}k\left(1+ky_1^+\right)^2\left(3+k-ky_1^+ + k^2y_1^+\right) + d\left[6+18ky_1^+ + 6k^2\left(y_1^+\right)^2 - 2k^3\left(y_1^+\right)^3\right]-\right. \\
&\left.2\left(1+ky_1^+\right)\left[4d + k\left(\frac{W^2}{4H^2}\left[-1-k+k^2\left(y_1^+\right)^2\right]-k\right)\right]\log\left(1+ky_1^+\right)\right\}+ \\
&\frac{1}{2k}\left\{\sqrt{1+\left(\frac{W}{2H}\eta_1\right)^2} - \log\left[1+\sqrt{1+\left(\frac{W}{2H}\eta_1\right)^2}\right]\right\} - F_0
\end{aligned} \tag{4.19}$$

where $y_1^+ = Re_{wake}\eta_1$, and F_0 is the constant determined in the context of the matching processes. The depicted process to find uniformly valid solutions on the whole domain, with an increasing order of precision in the asymptotic expansion, is an iterative process for $c \in \mathbb{N} > 0$. Remember that an asymptotic expansion is not necessarily convergent, and an optimal

number of terms, corresponding to the different orders in the expansion, should be considered. We don't extend this analysis here. Turning back to the wake solutions for the four regions of the domain, valid starting from a distance $\sim$ 30 (until $\sim$ 100 for high turbulence flows) in the stretched variables orthogonal to the walls, we have (applying the change of variables for the four sections of the domain reported in Tables 17 and 30) the results shown in Table 18.

Region **1**
$0 \le y \le \dfrac{W}{2}\ ,\ 0 \le z \le H; \qquad y \le \dfrac{W}{2}\dfrac{z}{H}$

$$u(y,z) = U_\infty \frac{z}{H}\left\{\frac{1}{k}\sqrt{1+\left(\frac{y}{z}\right)^2} + \frac{1}{k}\log\left(\frac{y}{z}\right) - \frac{1}{k}\log\left(1+\sqrt{1+\left(\frac{y}{z}\right)^2}\right) + 1 \right.$$
$$\left. -\frac{1}{k}\left[\sqrt{1+\frac{W^2}{4H^2}} + \log\left(\frac{W}{2H}\right) - \log\left(1+\sqrt{1+\frac{W^2}{4H^2}}\right)\right]\right\}$$

Region **2**
$0 \le y \le \dfrac{W}{2}\ ,\ 0 \le z \le H; \qquad y \ge \dfrac{W}{2}\dfrac{z}{H}$

$$u(y,z) = U_\infty \frac{2y}{W}\left\{\frac{1}{k}\sqrt{1+\left(\frac{z}{y}\right)^2} + \frac{1}{k}\log\left(\frac{z}{y}\right) - \frac{1}{k}\log\left(1+\sqrt{1+\left(\frac{z}{y}\right)^2}\right) + 1 \right.$$
$$\left. -\frac{1}{k}\left[\sqrt{1+\frac{4H^2}{W^2}} + \log\left(\frac{2H}{W}\right) - \log\left(1+\sqrt{1+\frac{4H^2}{W^2}}\right)\right]\right\}$$

Region **3**
$\dfrac{W}{2} \le y \le W\ ,\ 0 \le z \le H; \qquad W-y \ge \dfrac{W}{2}\dfrac{z}{H}$

$$u(y,z) = U_\infty \frac{2(W-y)}{W}\left\{\frac{1}{k}\sqrt{1+\left(\frac{z}{W-y}\right)^2} + \frac{1}{k}\log\left(\frac{z}{W-y}\right) - \frac{1}{k}\log\left(1+\sqrt{1+\left(\frac{z}{W-y}\right)^2}\right) + 1 \right.$$
$$\left. -\frac{1}{k}\left[\sqrt{1+\frac{4H^2}{W^2}} + \log\left(\frac{2H}{W}\right) - \log\left(1+\sqrt{1+\frac{4H^2}{W^2}}\right)\right]\right\}$$

Region **4**
$\frac{W}{2} \le y \le W\ ,\ 0 \le z \le H; \qquad W-y \le \dfrac{W}{2}\dfrac{z}{H}$

$$u(y,z) = U_\infty \frac{z}{H}\left\{\frac{1}{k}\sqrt{1+\left(\frac{W-y}{z}\right)^2} + \frac{1}{k}\log\left(\frac{W-y}{z}\right) - \frac{1}{k}\log\left(1+\sqrt{1+\left(\frac{W-y}{z}\right)^2}\right) + 1 \right.$$
$$\left. -\frac{1}{k}\left[\sqrt{1+\frac{W^2}{4H^2}} + \log\left(\frac{W}{2H}\right) - \log\left(1+\sqrt{1+\frac{W^2}{4H^2}}\right)\right]\right\}$$

Table 18: Wake solutions for the four regions of the domain, after the matching with the respective laws of the wall

External wind orthogonal to the street axis As we have seen in the introduction of Section 4.1, the equations for v and w do not depend on the u component. This means that the equations for the components of velocity transversal to the canyon are not coupled to the equation for the longitudinal component, so they can be solved indipendently in a two dimensional model. This indipendent two dimensional flow is generated by the component of the external wind field orthogonal to the street axis V_∞. Let us consider the second and the third Equations in System (4.1). We can write them in a more convenient form introducing the vorticity vector:

$$\omega = \left(\frac{\partial v}{\partial z} - \frac{\partial w}{\partial y}\right)\mathbf{i},$$

which has only one component in the $\mathbf{i}$ direction, and introducing the stream function ψ (which automatically gives v and w for a divergenceless velocity):

$$vdz - wdy = d\psi \quad ; \quad \omega = -\frac{\partial^2 \psi}{\partial y^2} - \frac{\partial^2 \psi}{\partial z^2}$$

Taking the rot of these equations, and considering that ν_T can depend on y and z, we obtain:

$$\left(v - \frac{\partial \nu_T}{\partial y}\right)\frac{\partial \omega}{\partial y} + \left(w - \frac{\partial \nu_T}{\partial z}\right)\frac{\partial \omega}{\partial z} = \frac{\partial \nu_T}{\partial y}\left(\frac{\partial^2 w}{\partial y^2} + \frac{\partial^2 w}{\partial z^2}\right) - \frac{\partial \nu_T}{\partial z}\left(\frac{\partial^2 v}{\partial y^2} + \frac{\partial^2 v}{\partial z^2}\right)$$
$$+ \omega\left(\frac{\partial^2 \nu_T}{\partial y^2} + \frac{\partial^2 \nu_T}{\partial z^2}\right) + (\nu + \nu_T)\left(\frac{\partial^2 \omega}{\partial y^2} + \frac{\partial^2 \omega}{\partial z^2}\right) \tag{4.20}$$

Writing the vorticity form of the equations is suitable for the perturbation analysis we are going to apply: we consider that, in situations corresponding to the *wake interference* and the *skimming flow* regimes, described in Section 3.3, in which a uniform vorticity distribution ω_0 is extended to the whole canyon domain, the wake solutions relative to each wall boundary have the form of a defect law in the vorticity field:

$$\omega = \omega_0 - \omega_\tau F[\eta]$$

where ω_τ is the intensity of the small perturbation from the uniform vorticity inside the canyon, and η is the orthogonal coordinate to each wall boundary suitably scaled with the wake thickness. The perturbation is set up as an expansion in powers of ω_τ/ω_0, which is a small parameter, and far away from the boundary the perturbation vanishes and the vorticity tends to ω_0. The hypothesis that the main *freestream* steady solution, over which a perturbation analysis is set up, is constituted by a region of uniform vorticity ω_0 inside the canyon is derived by Physical reasons, which involve the action

of viscosity in an initial phase of the motion: in the steady state there exists a set of closed streamlines which do not enclose any wall boundary and on which the effect of viscous stresses is everywhere small (that is, none of these streamlines passes through a layer in which viscous and inertia forces are comparable). The vorticity will be approximlately constant along each one of these streamlines (the vorticity associated with a material element is constant for an inviscid flow [Batchelor, 1967]). Now the vorticity in this case of steady two-dimensional motion satisfies a diffusion equation, and it follows that if the vorticity has different values on different streamlines there will be a diffusive flux of vorticity across streamlines. Since there is no source or sink of vorticity, the only possible steady state is one of uniform vorticity ω_0. Arguments for this hypothesis will also be given by the analysis of the numerical results in Section 4.2.

We start from the description of the logarithmic layer adjacent to each wall segment. Similarly to the previous case, we consider different scalings of variables for the four segments **AB**, **BE**, **EC**, **CD** in Figure 20. Referring to the Segment **AB** (the extension to the other boundary segments is easy, employing the change of variables reported in Table 16), we introduce in Equation (4.20) the variables and expansions:

$$\begin{aligned} &y^+ = \frac{u_\tau(z) y}{\nu} \quad ; \quad z^+ = \frac{z}{H} \\ &\psi = \nu[f_0(y^+) + \phi_1 f_1(y^+, z^+)] \quad ; \quad \nu_T = \nu[N_0(y^+) + \phi_1 N_1(y^+, z^+)] \\ &\phi_1 = \frac{\nu}{u_\tau \delta} \end{aligned} \tag{4.21}$$

where δ is the thickness of the boundary layer, and the change of variables transformations are expressed in Equation (4.3). We obtain, to order $O(1)$, the Equation:

$$(1 + N_0)\frac{\partial^4 f_0}{\partial y^{+4}} + 2\frac{\partial N_0}{\partial y^+}\frac{\partial^3 f_0}{\partial y^{+3}} + \frac{\partial^2 N_0}{\partial y^{+2}}\frac{\partial^2 f_0}{\partial y^{+2}} = 0 \tag{4.22}$$

Using the Prandtl law for the eddy viscosity far away from the boundary surface [Wilcox, 1998]:

$$N_0 = k y^+ \quad \text{for} \quad \mathrm{y}^+ \to \infty$$

we obtain:

$$\frac{\partial^3 f_0}{\partial y^{+3}} = \frac{1}{k}\frac{1}{y^{+2}} \quad \longrightarrow \quad w = -\frac{\partial \psi}{\partial y} = -u_\tau \frac{\partial f_0}{\partial y^+} + O(\phi_1) = \frac{u_\tau}{k}\log y^+ + C \tag{4.23}$$

which is the logarithmic law of the wall. This wall solution should be matched with the wake solution, written as a defect law for the vorticity field; this

matching procedure should give the form for the friction velocity u_τ. Note that the z dependence of the w component of velocity near Segment **AB** should be of the form $w \propto z$, since the vertex **B** is a stagnation point for the local flow topology [Batchelor, 1967]. This dependence guarantees the matching between solutions relative to Segments **AB** and **BE**. Since we will obtain a defect law which does not match with the logarithmic behaviour, we will obtain the form for the friction velocity by another procedure, relating to integral conditions for the boundary layer [Batchelor, 1967] adjacent to the wall and on the request that the stagnation-point behaviour be satisfied. Remember that the form for u_τ is needed in order to determine the optimal boundary layer cell dimensions of the grid for the solution of the discretized problem, as explained in Section 3.4.

We now consider the wake solutions. As already told, we are considering solutions valid only when the wind recirculation vortex is extended to the whole canyon domain, i.e. the *wake interference* and the *skimming flow* regimes. These situations are the most relevant for the description of a urban geometry. We refer to the wind tunnel data in Ref. [Berkowicz, Kearney, 2004] and to our simulation results (see Section 4.2) to characterize these wind flow regimes, in terms of the external wind intensity, of its angle relative to the street axis, and of the ratio H/W. Anyhow, we point out here an analytical procedure to distinguish between the different regimes, which is also useful to determine precise values for the constant ω_0. As a first step, we find the solution for the two-dimensional inviscid flow relative to the canyon geometry, driven by an external wind component V_{ext} orthogonal to the street axis. This can be done through the methods of complex analysis, by taking a conformal transformation - the Schwarz-Christoffel transformation [Batchelor, 1967] - which transforms the canyon domain (in the z variable) to the upper half plane (in the ζ variable). The transformation is illustrated in Figure 21. The canyon vertices **A**, **B**, **C**, **D** are transformed into points on the real axis of the ζ plain, of coordinates ζ_A, ζ_B, ζ_C, ζ_D respectively. The transformation is:

$$z - z_0 = A \int d\zeta \sqrt{\frac{(\zeta - \zeta_A)(\zeta - \zeta_D)}{(\zeta - \zeta_B)(\zeta - \zeta_C)}},$$

where z_0 and $|A|$ and argA are arbitrary constants, which must be chosen in order to yield the correct origin, scale and orientation of the polygonal boundary in the z plane. We can choose $\zeta_A = -1/k$, $\zeta_D = 1/k$, $\zeta_B = -1$ and $\zeta_C = 1$, in order to reconduce the transformation to an elliptic integral of the second kind:

$$z - z_0 = kA \int d\zeta \sqrt{\frac{(1 - k\zeta)(1 + k\zeta)}{(1 - \zeta)(1 + \zeta)}} = kA\, E[\arcsin \zeta, k^2],$$

where E is the elliptic integral of the second kind [Andrews et al., 1999].

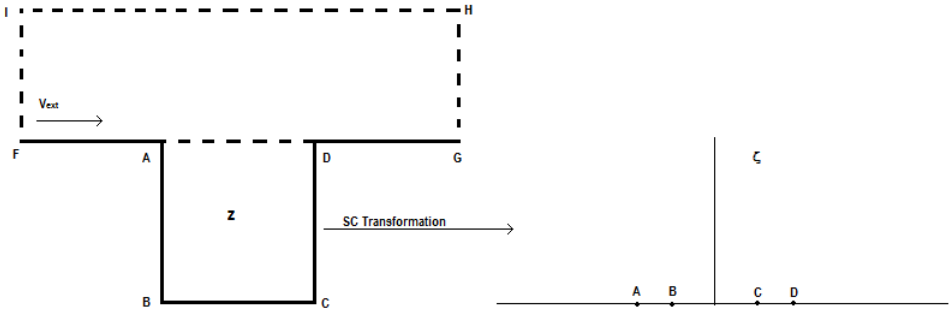

Figure 21: Illustration of the Schwarz-Christoffel transformation. V_{ext} is the external wind component orthogonal to the street axis.

Imposing the correspondence between the points $\zeta = \pm 1$ and the points $z = 0$ and $z = W$, using the properties of the elliptic functions, and inverting the relation, we have:

$$\zeta = \sin\left\{ E^{-1}\left[E[k^2]\frac{2}{W}\left(z - \frac{W}{2} \right), k^2 \right] \right\},$$

where E^{-1} is the elliptic function of the second order, and $E[k^2]$ is the complete elliptic integral of the second kind (corresponding to the real quarter period of the relative elliptic function). The elliptic function $\sin(E^{-1})$ is $1/k$ when its argument is $E(k^2) + E^{'}(k^2)$, where $E^{'}$ is the imaginary quarter period. Thus, in order to have $\zeta = 1/k$ when $z = W + iH$, we require that k is the value for which:

$$\frac{E^{'}(k^2)}{E(k^2)} = \frac{2H}{W}.$$

This value of k is obtained using the tables of elliptic integrals [Morse, Feshbach, 1953]. For example, when $W = 2H$, $k^2 = 0.5$. This completes the specification of the Schwarz-Christoffel transformation. Now, the inviscid flow for the canyon geometry is given by means of the complex potential Ω:

$$\Omega(z) = V_{ext}\zeta = V_{ext}\sin\left\{ E^{-1}\left[E[k^2]\frac{2}{W}\left(z - \frac{W}{2} \right), k^2 \right] \right\} \qquad (4.24)$$

The presence of boundary layer separation can be identified as an index for the distinction between the flow regimes inside the canyon: when the external

inviscid flow as an adverse pressure gradient which induces separation, the flow, which tends to the inviscid solution outside the canyon, recirculate inside the wake generated by the first vertical boundary, and the regime is *isolated roughness*. The presence of boundary layer separation induced by the external inviscid flow is indicated by the critical points of the inviscid solution [Batchelor, 1967]: if the inviscid solution has a point, inside the interval $0 \leq y \leq W$, for which $dV_\infty/dy = 0$, there is separation (this reasoning is analogous to the analysis conduced on boundary layers with accelerated external inviscid flows). The non-inviscid instabilities are responsible for second vortex flows inside the canyon, but the flow regime is determined by the nature of the external stream. The external flow V_∞ can be calculated as:

$$V_\infty = \frac{\partial}{\partial y} Re[\Omega(z)],$$

and the nature of its critical points depends on the intensity of V_{ext} and on the geometrical parameters H and W. This approach is based on numerical valuations of the elliptic integrals; we will develop it in further investigations.

Let us consider now the problem of the determination of the ω_0 constant. The vorticity is primarily generated at the boundary layer which forms along the streamlines at the canyon roof level (Segment **AD** in Figure 21). It is then convected inside the canyon, and the presence of the wall boundaries determine the regime of recirculation, and eventually generates second order vortices. In the roof level boundary layer, the v component of the velocity can be considered as a small departure from the external inviscid flow component V_∞. From mass conservation, the w component near the Segment **AD** can be expressed as:

$$w_{AD} \sim -z \frac{dV_\infty}{dy}$$

This could also be written as:

$$w_{AD} \sim \delta \Delta\omega$$

where $\Delta\omega$ is the variation of vorticity from the external value generated at the layer, and δ is the extension of the layer in which the vorticity is convected. If the convection of vorticity determine a uniform distribution inside the canyon domain, we can express the last equation as:

$$w_{AD} \sim -\omega_0 H$$

Now apply the integral form of the NS equations [Batchelor, 1967] to the control boundary S indicated by the dotted line in Figure 21:

$$\int \rho u_i u_j n_j dS = \int (-p n_i + S_{ij} n_j) dS \tag{4.25}$$

where we have omitted the external force terms. We choose a control surface such that there is no flux velocity across the **IH** segment, and the viscous forces are relatively small there. By applying the Bernoulli law for the pressure and the velocity of the undisturbed flow at the Segments **FI** and **GH**, and considering mass conservation, we see that these two segments give a zero contribution to Equation (4.25). At the Segments **FA**, **AD** and **DG** boundary layers are formed, but we assume that the Reynolds number of the flow is so large that the corresponding tangential stresses are small (they are proportional to the inverse of the square root of the Reynolds number). Equation (4.25) thus becomes:

$$\int_0^W dy\, \rho V_\infty w_{AD} = -\int_0^W dy\, \rho w_{AD}^2,$$

and considering that $w_{AD} \sim -\omega_0 H$:

$$\omega_0 HW = \int_0^W dy\, V_\infty = \int_0^W dy\, \frac{\partial}{\partial y} Re[\Omega(z)] \tag{4.26}$$

where $\Omega(z)$ is given in Equation (4.24) (where z is the complex variable $y+iz$, and $\Omega(z)$ must be specified at $z = H$). This gives the desired estimate for the value of ω_0. We now make the approximation that the external velocity remains constant at the roof level: $V_\infty = V_{ext} = \text{constant}$. According to this approximation, we have:

$$\omega_0 = \frac{V_\infty}{H} \tag{4.27}$$

We will use this value for ω_0.

For what concerns the defect layer solutions adjacent to each wall segment defined in Figure 20, we scale the variables and take perturbation expansions as reported in Table 19.

There are two small scales associated to each boundary segment i: the vorticity perturbation $\omega_{\tau i}$, which defines the parameter of the expansion $\phi_{1,i}$, and the wake thickness δ_i, which must be inserted, in order to define an appropriate turbulent viscosity. We scale the coordinate orthogonal to each boundary with the quantity Δ, which is a combination of the two small parameters. Note that:

$$\frac{\Delta\phi_1}{\delta} = 1$$

The stream function is defined as a perturbation, to order $O(\phi_1)$, of a stream function associated to a constant value of vorticity ω_0. We are searching for separated solutions, as in the previous case, so F will be a function of the variable η only. The prescription for the eddy viscosity is:

$$\nu_T = \alpha\delta^2\omega_0,$$

where α is a constant which determines the Turbulence intensity, and must be chosen by comperison with empirical data. This prescription is similar to that introduced in the Baldwin-Lomax algebraic Turbulence model [Wilcox, 1998]. We note that, in the case of the *isolated roughness* flow regime, this prescription is not valid, since the wake thickness is a finite parameter. An appropriate prescription should be: $\nu_T \propto U_r^2/\omega_0$, where U_r is the maximum velocity at the external streamlines of the wake recirculation behind the leeward wall. U_r can be defined starting from the fact that, for an inviscid flow with constant vorticity ω_0, the following relation is valid:

$$\frac{p}{\rho} = \text{const.} - \frac{1}{2}\mathrm{U}_\mathrm{r}^2 - \omega_0\psi,$$

which is derived from the fact that the the Bernoulli energy is constant along a streamline [Batchelor, 1967]. In boundary layer separation, the pressure inside the recirculation zone is equal to the pressure of the external flow V_∞. By applying the Bernoulli theorem, and considering the appropriate form of the stream function at the external streamline of the recirculation zone, we obtain the following prescription:

$$\nu_T = \alpha \min\left[\delta^2\omega_0, \frac{V_\infty^2}{\omega_0} + \omega_0\left(\frac{W}{2} - \delta\right)^2\right]$$

Details of the solutions for this algebraic Turbulence model will be treated in future investigations.

Introducing the change of variables and the expansions reported in Table 19 inside Equation (4.20) we obtain, in the case of the Segment **AB**, the following equation, retaining the terms to order $O(\Delta\phi_1)$:

$$\frac{\partial^4 F}{\partial\eta_1^4} + \frac{1}{\alpha H}\left[\Delta_1\frac{\delta_1'}{\delta_1} - \Delta_1\frac{\omega_{\tau 1}'}{\omega_{\tau 1}}\right]\frac{\Delta_1^2}{\delta_1^2}\eta_1^2\frac{\partial^3 F}{\partial\eta_1^3} - \frac{1}{\alpha H}\Delta_1\frac{\omega_{\tau 1}'}{\omega_{\tau 1}}\frac{\Delta_1^2}{\delta_1^2}\eta_1\frac{\partial^2 F}{\partial\eta_1^2} = 0 \quad (4.28)$$

Segment **AB**	*Segment* **BE**
$\eta_1 = \dfrac{y}{\Delta_1(z)}$	$\eta_2 = \dfrac{z}{\Delta_2(y)}$
$\zeta_1 = \dfrac{z}{H}$	$\zeta_2 = \dfrac{2y}{W}$
$\Delta_1(z) = \frac{\omega_0 \delta_{1,1}(z)}{\omega_{\tau 1}(z)}$	$\Delta_2(y) = \frac{\omega_0 \delta_{1,2}(y)}{\omega_{\tau 2}(y)}$
$\phi_{1,1} = \frac{\omega_{\tau 1}(z)}{\omega_0}$	$\phi_{1,2} = \frac{\omega_{\tau 2}(y)}{\omega_0}$
$\psi_1 = \omega_0 \Delta_1^2 \big[-\frac{1}{2}\eta_1^2 + \phi_{1,1} F(\eta_1, \zeta_1)\big]$	$\psi_2 = \omega_0 \Delta_2^2 \big[-\frac{1}{2}\eta_2^2 + \phi_{1,2} F(\eta_2, \zeta_2)\big]$
$\nu_T = \alpha_1 \delta_1^2 \omega_0$	$\nu_T = \alpha_2 \delta_2^2 \omega_0$

Segment **EC**	*Segment* **CD**
$\eta_3 = \dfrac{z}{\Delta_3(y)}$	$\eta_4 = \dfrac{W-y}{\Delta_4(z)}$
$\zeta_3 = \dfrac{2(W-y)}{W}$	$\zeta_4 = \dfrac{z}{H}$
$\Delta_3(y) = \frac{\omega_0 \delta_3(y)}{\omega_{\tau 3}(y)}$	$\Delta_4(z) = \frac{\omega_0 \delta_4(z)}{\omega_{\tau 4}(z)}$
$\phi_{1,3} = \frac{\omega_{\tau 3}(y)}{\omega_0}$	$\phi_{1,4} = \frac{\omega_{\tau 4}(y)}{\omega_0}$
$\psi_3 = \omega_0 \Delta_3^2 \big[-\frac{1}{2}\eta_3^2 + \phi_{1,3} F(\eta_3, \zeta_3)\big]$	$\psi_4 = \omega_0 \Delta_4^2 \big[-\frac{1}{2}\eta_4^2 + \phi_{1,4} F(\eta_4, \zeta_4)\big]$
$\nu_T = \alpha_3 \delta_3^2 \omega_0$	$\nu_T = \alpha_4 \delta_4^2 \omega_0$

Table 19: Scaling of variables, series expansions for the defect layer solutions and turbulence modelization with the domain divided in four regions, adjacent to the four segments **AB**, **BE**, **EC**, **CD**.

Equation (4.28) is dependent only on the η_1 variable, and thus separated solution exists, if the following conditions are valid:

$$\begin{cases} \dfrac{1}{\alpha H}\dfrac{\delta_1'}{\delta_1}\dfrac{\Delta_1^3}{\delta_1^2} = a \\ \\ \dfrac{1}{\alpha H}\dfrac{\omega_{\tau 1}'}{\omega_{\tau 1}}\dfrac{\Delta_1^3}{\delta_1^2} = b \end{cases} \tag{4.29}$$

with a and b constants. System (4.29) can be solved by eliminating the δ variable; considering the form of Δ_1 introduced in Table 19, we obtain the equation:

$$b\frac{\omega_{\tau 1}''}{\omega_{\tau 1}'} + (a-4b)\frac{\omega_{\tau 1}'}{\omega_{\tau 1}} = 0$$

A solution can be easily obtained by making the substitution: $\omega_{\tau 1}' = f(\omega_{\tau 1}) \rightarrow \omega_{\tau 1}'' = f'f$. The solutions, for both $\omega_{\tau 1}$ and δ_1, are:

$$\begin{cases} \omega_{\tau 1}(\zeta_1) = [(a-3b)(K_I\zeta_1 + K_{II})]^{b/(a-3b)} \\ \\ \delta(\zeta_1) = \dfrac{\alpha H}{\omega_0^3 K_I}[(a-3b)(K_I\zeta_1 + K_{II})]^{a/(a-3b)} \end{cases} \tag{4.30}$$

where K_I and K_{II} are constants of integrations. If we impose that $\omega_\tau \rightarrow 0$ and $\delta \rightarrow 0$ for $\zeta \rightarrow 0$, in correspondence with the stagnation point, we set $K_{II} = 0$, and impose particular constraints on the a and b values, in order to avoid that the Solutions (4.30) diverge, making the perturbation procedure useless. The Equation (4.28) becomes:

$$\frac{d^4F}{d\eta_1^4} + (a-b)\eta_1^2\frac{d^3F}{d\eta_1^3} - b\eta_1\frac{d^2F}{d\eta_1^2} = 0 \tag{4.31}$$

Introducing the function:

$$y(\eta_1) = \frac{d^2F}{d\eta_1^2},$$

and introducing the change of variable:

$$x = \frac{b-a}{3}\eta_1^3,$$

we transform Equation (4.31) into the Confluent Hypergeometric Function [Morse, Feshbach, 1953]:

$$xy'' + \left[\frac{2}{3} - x\right]y' - \frac{b}{3(b-a)}y = 0 \tag{4.32}$$

We now extend the analysis to the regions adjacent to the boundary segments defined in Figure 20. In Table 20 we report the form of the equations and of the solutions for the different regions. The respective variables and Turbulence modelizations have been introduced in Table 19.

Segment **AB**	*Segment* **BE**
$v = O[\Delta_1^2 \phi_{1,1}]$	$v = -\omega_0 \Delta_2 \eta_2 + \omega_0 \Delta_2 \phi_{1,2} \dfrac{\partial F}{\partial \eta_2}$
$w = \omega_0 \Delta_1 \eta_1 - \omega_0 \Delta_1 \phi_{1,1} \dfrac{\partial F}{\partial \eta_1}$	$w = O[\Delta_2^2 \phi_{1,2}]$
$\omega = \omega_0 - \omega_0 \phi_{1,1} \frac{\partial^2 F}{\partial \eta_1^2}$	$\omega = \omega_0 - \omega_0 \phi_{1,2} \frac{\partial^2 F}{\partial \eta_2^2}$
$\omega_{\tau 1} = [(a-3b)(K_I \zeta_1 + K_{II})]^{b/(a-3b)}$	$\omega_{\tau 2} = [(a-3b)(K_I \zeta_2 + K_{II})]^{b/(a-3b)}$
$\delta_1 = \frac{\alpha H}{\omega_0^3 K_I} [(a-3b)(K_I \zeta_1 + K_{II})]^{a/(a-3b)}$	$\delta_2 = \frac{\alpha W}{2\omega_0^3 K_I} [(a-3b)(K_I \zeta_2 + K_{II})]^{a/(a-3b)}$
$y(\eta_1) = \frac{d^2 F}{d\eta_1^2}; \quad x = \frac{b-a}{3} \eta_1^3$	$y(\eta_2) = \frac{d^2 F}{d\eta_2^2}; \quad x = \frac{a-b}{3} \eta_2^3$
$xy'' + \left[\frac{2}{3} - x\right] y' - \frac{b}{3(b-a)} y = 0$	$xy'' + \left[\frac{2}{3} - x\right] y' - \frac{b}{3(b-a)} y = 0$

Segment **EC**	*Segment* **CD**
$v = -\omega_0 \Delta_3 \eta_3 + \omega_0 \Delta_3 \phi_{1,3} \dfrac{\partial F}{\partial \eta_3}$	$v = O[\Delta_4^2 \phi_{1,4}]$
$w = O[\Delta_3^2 \phi_{1,3}]$	$w = -\omega_0 \Delta_4 \eta_4 + \omega_0 \Delta_4 \phi_{1,4} \dfrac{\partial F}{\partial \eta_4}$
$\omega = \omega_0 - \omega_0 \phi_{1,3} \frac{\partial^2 F}{\partial \eta_3^2}$	$\omega = \omega_0 - \omega_0 \phi_{1,4} \frac{\partial^2 F}{\partial \eta_4^2}$
$\omega_{\tau 3} = [(a-3b)(K_I \zeta_3 + K_{II})]^{b/(a-3b)}$	$\omega_{\tau 4} = [(a-3b)(K_I \zeta_4 + K_{II})]^{b/(a-3b)}$
$\delta_3 = \frac{\alpha W}{2\omega_0^3 K_I} [(a-3b)(K_I \zeta_3 + K_{II})]^{a/(a-3b)}$	$\delta_4 = \frac{\alpha H}{\omega_0^3 K_I} [(a-3b)(K_I \zeta_4 + K_{II})]^{a/(a-3b)}$
$y(\eta_3) = \frac{d^2 F}{d\eta_3^2}; \quad x = \frac{b-a}{3} \eta_3^3$	$y(\eta_4) = \frac{d^2 F}{d\eta_4^2}; \quad x = \frac{a-b}{3} \eta_4^3$
$xy'' + \left[\frac{2}{3} - x\right] y' - \frac{b}{3(b-a)} y = 0$	$xy'' + \left[\frac{2}{3} - x\right] y' - \frac{b}{3(b-a)} y = 0$

Table 20: Form of the equations and of the solutions for the four regions adjacent to the four segments **AB**, **BE**, **EC**, **CD**.

We note that the velocity components orthogonal to a given wall segment are of order of magnitude $O[\Delta^2\phi_1]$, and thus they can be neglected with respect to the parallel components in the region adjacent to a segment. The solution is the sum of the different components relative to each region. In the Region $\{0 \leq y \leq W/2; 0 \leq z \leq H/2\}$ the solution is given by:

$$\mathbf{u} = (v_{BE}, w_{AB}),$$

where the subscripts indicate the segment of reference of the corresponding solutions. In the Region $\{W/2 < y \leq W; 0 \leq z \leq H/2\}$ the solution is given by:

$$\mathbf{u} = (v_{EC}, w_{CD}),$$

We must add to the solution the influence of the freestream boundary condition at the Segment **AD**: $v = V_\infty$. This is done by introducing a solution for a constant vorticity ω_0 with the boundary contition at $z = H$ that $\partial\psi/\partial z|_{z=H} = V_\infty$, i.e.:

$$\psi_{AD} = -\frac{1}{2}\omega_0(H - z)^2 + V_\infty z$$

It is possible to use this solution due to the fact that we are considering a constant external freestream flow $V_\infty = V_{ext}$ over the canyon roof level. In the case we would consider a freestream flow obtained from the Equation (4.24), a perturbation analysis, considering a defect layer development at the roof level as a small perturbation from the freestream velocity, should be considered. In the Region $\{0 \leq y \leq W/2; H/2 < z \leq H\}$ the solution is given by:

$$\mathbf{u} = (v_{AD}, w_{AB})$$

In the Region $\{W/2 < y \leq W; H/2 < z \leq H\}$ the solution is given by:

$$\mathbf{u} = (v_{AD}, w_{CD})$$

Note that the terms of order Δ in the solutions have signs corresponding to the main vortex recirculation inside the canyon; in fact, removing the scaling, they are:

$$w_{CD} = -\omega_0(W - y); \quad v_{EC} = -\omega_0 z; \quad v_{EB} = -\omega_0 z; \quad w_{BA} = \omega_0 y$$

Anyhow these terms cannot be used in the determination of the solution valid on the whole domain without an ad-hoc partitioning of it. Consider for example the term $w_{BA} = \omega_0 y$: due to the way in which the stream functions have been constructed in each region adjacent to the wall segments (see Table 19), it vanishes for $y = 0$, but $w_{BA} \neq 0$ for $z = 0$. Besides this, considering both the contributions from w_{BA} and v_{EB} to order Δ in Region

$\{0 \leq y \leq W/2; 0 \leq z \leq H/2\}$, we would have $\omega = 2\omega_0$ (a factor of $\omega_0/2$ should be considered). The same problem arises for the other terms at order Δ. One way to avoid this incompatibility problem of the solutions at order Δ should be to insert an ad-hoc subdivision of the domain regions for the corresponding terms, using, for example above the bisector of the straight angle at the vertex **B**, the term $w_{BA} = \omega_0 y$ only, neglecting the v_{BE} term. This approximation is supported by the fact that, in the region of influence of a single wall boundary segment, the velocity component orthogonal to the boundary are of order $O(\Delta^2\phi_1)$. Thus the velocity components to leading order parallel to the other adjacent boundaries should not extend to the region of the considered boundary. (This is a similar procedure as that introduced in Ref. [Soulhac et al., 2008] to treat the case of an external freestream parallel to the street axis). This could introduce non-Physical effects, since in each region a component of velocity is neglected. We will introduce a more correct way to proceed, by using a main solution $\psi_{ms}(y, z)$, which substitute the incompatible components in each region. The perturbation term in the velocity solutions is proportional to δ, whereas the perturbation term in the vorticity defect law is proportional to ω_τ. Since we impose that these terms go to zero for $\zeta \to 0$, respecting the stagnation point behaviour, the perturbation terms are compatible with each other and can be used in their respective regions of definition. When ω_τ changes sign between two adjacent regions of the domain, a secondary recirculation can be established, depending on the intensity of the perturbation itself.

We illustrate here a procedure to solve the incompatibility of the terms at order Δ by introducing a main solution ψ_{ms} of the Equation:

$$\frac{\partial^2 \psi_{ms}}{\partial y^2} + \frac{\partial^2 \psi_{ms}}{\partial z^2} = -\omega_0,$$

valid for the whole domain, with the boundary condition that $\partial\psi/\partial z = V_\infty$ for $z = H$. The procedure consists in composing this solution with the contributions coming from the perturbation terms at order $O(\Delta\phi_1)$ reported in Table 21. When considering a boundary condition at $z = H$ given by a freestream flow obtained from the Equation (4.24), this procedure avoid in a first approximation the need to extend the perturbation analysis to the boundary layer which forms at the Segment **AD**. Applying a standard separation of variable approach to the Poisson equation for the stream functions,

we have obtained the following main solution ψ_{ms}:

$$\begin{aligned}\psi_{ms} =& \frac{1}{2}\omega_0\left[\left(\frac{W}{2}\right)^2 - \left(y-\frac{W}{2}\right)^2\right] \\ &+ \sum_{n=0}^{\infty}\left\{\left[\int_0^W dy' \, \frac{2V_\infty \cos[(2n+1)\pi(y'-W/2)]}{\pi(2n+1)\sinh[(2n+1)\pi(H/W)]}\right]\cdot \right. \\ &\left. \cosh\left[\frac{(2n+1)\pi z}{W}\right]\cos\left[\frac{(2n+1)\pi(y-W/2)}{W}\right]\right\}\end{aligned} \tag{4.33}$$

where V_∞ is obtained from the Equation (4.24). When V_∞ is constant, the Solution (4.33) becomes:

$$\begin{aligned}&\psi_{ms} = \frac{1}{2}\omega_0\left[\left(\frac{W}{2}\right)^2 - \left(y-\frac{W}{2}\right)^2\right] \\ &+ \frac{4V_\infty W}{\pi^2}\sum_{n=0}^{\infty}\left\{\frac{(-1)^n}{(2n+1)^2}\frac{\cosh[(2n+1)\pi z/W]}{\sinh[(2n+1)\pi(H/W)]}\cos\left[\frac{(2n+1)\pi(y-W/2)}{W}\right]\right\}\end{aligned} \tag{4.34}$$

We are interested in the velocity components. Taking the z derivative of Equation (4.34), we obtain:

$$v_{ms} = \frac{4V_\infty}{\pi}\sum_{n=0}^{\infty}\left\{\frac{(-1)^n}{2n+1}\frac{\sinh[(2n+1)\pi z/W]}{\sinh[(2n+1)\pi(H/W)]}\cos\left[\frac{(2n+1)\pi(y-W/2)}{W}\right]\right\} \tag{4.35}$$

This form for the v velocity component goes to zero at the canyon walls, and satisfies the freestream flow condition at the roof level. It is a solution of the Laplace equation valid on the whole domain; we consider v_{ms} as the v component of velocity in the regions above the bisectors at the point vertices **B** and **C**. For example, in the region above the bisector at the vertex **B**, i.e. for $z \geq y$, the velocity component v_{BE}, at order Δ, is incompatible, since $v_{BE} = -\omega_0 z$ does not vanish at $y = 0$. In this region the velocity components are thus: $\{v_{ms}, w_{AB} = \omega_0 y\}$ (note that the w_{AB} solves the Poisson equation, and takes into account the vorticity ω_0). In the region below the bisector at the vertex **B**, the v component is given by v_{BE}, and the w_{AB} component is incompatible. We cannot use the component $w_{ms} = -\partial\psi_{ms}/\partial y$ as a substitute for w_{AB} in this region, cause it is incompatible with our perturbation expansion analysis: in the region adjacent to the Segment **BC**, the stream functions must be, to leading order, of the form:

$$\psi \sim \frac{-1}{2}\omega_0 z^2,$$

which is not compatible with Equation (4.34). We thus introduce the stream function ψ_{msII}:

$$\psi_{msII} = \frac{1}{2}\omega_0\left[\left(\frac{H}{2}\right)^2 - \left(z - \frac{W}{2}\right)^2\right] + \frac{4W}{\pi^2}\left(V_\infty + \omega_0\frac{H}{2}\right)\sum_{n=0}^{\infty}\left\{\frac{(-1)^n}{(2n+1)^2}\frac{\sinh[(2n+1)\pi z/W]}{\cosh[(2n+1)\pi(H/W)]}\cos\left[\frac{(2n+1)\pi(y-W/2)}{W}\right]\right\} \tag{4.36}$$

which satisfies the freestream condition. Taking the y derivative of Equation (4.36), we obtain:

$$w_{msII} = \frac{4}{\pi}\left(V_\infty + \omega_0\frac{H}{2}\right)\sum_{n=0}^{\infty}\left\{\frac{(-1)^n}{2n+1}\frac{\sinh[(2n+1)\pi z/W]}{\cosh[(2n+1)\pi(H/W)]}\sin\left[\frac{(2n+1)\pi(y-W/2)}{W}\right]\right\} \tag{4.37}$$

This solution satisfies the no slip condition at the boundary $z = 0$, and satisfies free-slip conditions at the boundaries $y = 0$ and $y = W$. We substitute the w_{AB} component, in the region below the bisector at the **B** vertex, by w_{msII}. (Using this component away from the vertical boundaries, the boundary conditions at $y = 0$ and $y = W$ are not important in the form of the Solution (4.37)). We show in Figure 22 the different contributions, to leading order, for the different regions of the domain, to which the perturbation terms must be added. Note that, considering for example the region above the bisector at the **B** vertex, we could use the components $(v_{ms}, w_{ms} = -\partial\psi_{ms}/\partial y)$, instead of the components $(v_{ms}, w_{AB}$ (our perturbation analysis is not changed in this case). The same consideration can be made for the other segments.

We note that the Series (4.35) and (4.37) are fairly rapidly convergent, except for $z \to H$. Their convergence can be accelerated with the method of Kummer [Morse, Feshbach, 1953]. Noting that for large values of n the ratios of the hyperbolic functions in both the series expansions tends to the function:

$$e^{(2n+1)\frac{\pi}{W}(z-H)},$$

we add and subtract to the series (4.35) a term (which can be summed):

$$\sum_n \frac{1}{2n+1}\mathrm{Re}\left\{\mathrm{e}^{\mathrm{i}\frac{\pi}{\mathrm{W}}(2\mathrm{n}+1)[(\mathrm{y}-\mathrm{W}/2)-\mathrm{i}(\mathrm{z}-\mathrm{H})]}\right\} = \mathrm{Re}\left\{\mathrm{arctanh}\left[\mathrm{e}^{\mathrm{i}\frac{\pi}{\mathrm{W}}[(\mathrm{y}-\mathrm{W}/2)-\mathrm{i}(\mathrm{z}-\mathrm{H})]}\right]\right\},$$

and we add and subtract to the series (4.37) a term (which can be summed):

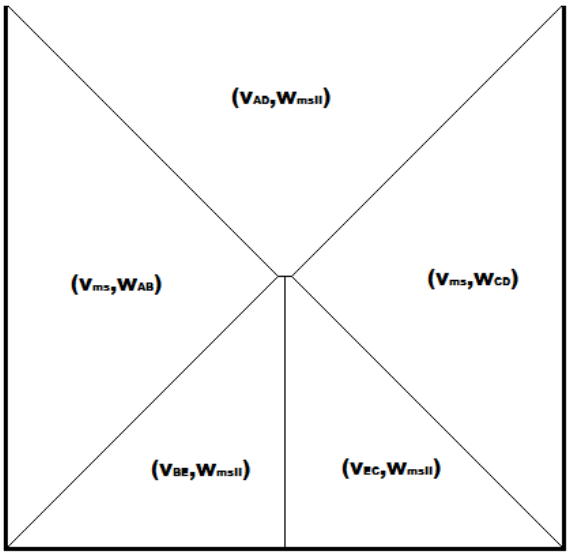

Figure 22: Different velocity components contributions, to leading order, for the different regions of the domain, to which the perturbation terms must be added

$$\sum_n \frac{(-1)^n}{2n+1} \mathrm{Im}\left\{ \mathrm{e}^{\mathrm{i}\frac{\pi}{\mathrm{W}}(2\mathrm{n}+1)[(\mathrm{y}-\mathrm{W}/2)-\mathrm{i}(\mathrm{z}-\mathrm{H})]} \right\} = \mathrm{Im}\left\{ \arctan\left[\mathrm{e}^{\mathrm{i}\frac{\pi}{\mathrm{W}}[(\mathrm{y}-\mathrm{W}/2)-\mathrm{i}(\mathrm{z}-\mathrm{H})]} \right] \right\}$$

The series expansions which remain are so rapidly convergent that only the first term needs to be included. The results are:

$$\begin{aligned} v_{ms} = {} & \frac{V_\infty}{\pi} \log\left\{ e^{-\frac{2\pi}{W}(H-z)} \sin^2\left[\frac{\pi}{W}\left(y - \frac{W}{2} \right) \right] + \left(e^{-\frac{\pi}{W}(H-z)} \cos\left[\frac{\pi}{W}\left(y - \frac{W}{2} \right) \right] + 1 \right)^2 \right\} \\ & - \frac{V_\infty}{\pi} \log\left\{ e^{-\frac{2\pi}{W}(H-z)} \sin^2\left[\frac{\pi}{W}\left(y - \frac{W}{2} \right) \right] + \left(1 - e^{-\frac{\pi}{W}(H-z)} \cos\left[\frac{\pi}{W}\left(y - \frac{W}{2} \right) \right] \right)^2 \right\} \\ & + \frac{4V_\infty}{\pi} e^{-\frac{\pi H}{W}} \frac{\sinh\left[\frac{\pi}{W}(z-H) \right]}{\sinh\left[\frac{\pi}{W} H \right]} \cos\left[\frac{\pi}{W}\left(y - \frac{W}{2} \right) \right] \end{aligned} \tag{4.38}$$

and

$$
\begin{aligned}
&w_{msII} = \\
&\frac{V_\infty + \omega_0 H/2}{\pi} \log\left\{ \left[e^{-\frac{\pi}{W}(H-z)} \sin\left[\frac{\pi}{W}\left(y - \frac{W}{2} \right) \right] + 1 \right]^2 + e^{-\frac{2\pi}{W}(H-z)} \cos^2\left[\frac{\pi}{W}\left(y - \frac{W}{2} \right) \right] \right\} \\
&- \frac{V_\infty + \omega_0 H/2}{\pi} \log\left\{ \left[1 - e^{-\frac{\pi}{W}(H-z)} \sin\left[\frac{\pi}{W}\left(y - \frac{W}{2} \right) \right] \right]^2 + e^{-\frac{2\pi}{W}(H-z)} \cos^2\left[\frac{\pi}{W}\left(y - \frac{W}{2} \right) \right] \right\} \\
&- 4\frac{V_\infty + \omega_0 H/2}{\pi} e^{-\frac{\pi H}{W}} \frac{\cosh\left[\frac{\pi}{W}(z-H) \right]}{\cosh\left[\frac{\pi}{W} H \right]} \sin\left[\frac{\pi}{W}\left(y - \frac{W}{2} \right) \right]
\end{aligned}
\tag{4.39}
$$

Let us return to the solution for the perturbation problem, introduced in Table 20. As already said, we choose $K_{II} = 0$. The appropriate boundary conditions are:

$$
\begin{cases}
y(\eta) = \dfrac{d^2F}{d\eta^2} \to 0 \quad \text{for } \eta \to \infty \\
y(\eta) = \dfrac{d^2F}{d\eta^2} \to -\dfrac{1}{k\eta} \quad \text{for } \eta \to 0
\end{cases}
\tag{4.40}
$$

The first of the conditions (4.40) corresponds to the request that the perturbation vanish at infinity, i.e. the solution tends to the solution with uniform vorticity ω_0 away from the boundary. The second condition is needed to set up a matching with the logarithmic law of the wall (4.23). We show now that the second condition cannot be satisfied by any solution of the Equation (4.32). The general form of the Hypergeometric Equation is:

$$
xy'' + [c - x]y' - dy = 0 \tag{4.41}
$$

where c and d are arbitrary real constants. In the case of Equation (4.32) (which is valid in all the regions of the domain adjacent to the wall boundaries):

$$
c = \frac{2}{3}; \quad d = \frac{1}{3}\frac{b}{b-a} \tag{4.42}
$$

The general solution of the Equation (4.41) in a neighbourhood of the origin (which is a regular singular point of the equation) extending to Infinity is [Morse, Feshbach, 1953]:

$$
y(x) = A\,{}_1F_1(d, c, x) + Bx^{1-c}\,{}_1F_1(d - c + 1, 2 - c, x),
$$

where ${}_1F_1$ is the Confluent Hypergeometric Function, expressed in a series expansion as:

$$ {}_1F_1(d,c,x) = \sum_{k=0}^{\infty} \frac{(a)_k}{(c)_k} \frac{x^k}{k!}, $$

(a further $1/\Gamma(c)$ factor must be introduced when c is a negative integer), and A and B are generic real constants. The two terms in the solution are linearly independent, except for the case $c = n \in \mathbb{N}$, in which the origin is a logarithmic point for the equation. In this case a term containing a logarithmic singularity must be present. For $d = -n \in \mathbb{N} > 0$, the series expansion of ${}_1F_1(d,c,x)$ is truncating, and the corresponding solution reduces to polynomials. Analytic continuations of the solutions can be obtained by means of the Kummer relation:

$$ {}_1F_1(d,c,x) = e^x \, {}_1F_1(c-d,c,-x) $$

In our case $c = 2/3$, so the origin is not a logarithmic point. In the case of the Confluent Hypergeometric Function there is no possibility to take an analytic continuation of a logarithmic behaviour at the point ∞, as was done in the case of the Hypergeometric solutions in the Appendix, since Infinity is an irregular singular point of the equation, and solutions in the form of uniformly convergent series expansions in a neighbourhood of ∞ do not exist. The only way to satisfy the boundary condition at 0 imposed in (4.40) is to search for solutions in the form of asymptotic expansions in powers of $1/x$ near the point ∞. Due to the Stokes phenomenon associated to the irregularity of the point at Infinity [Morse, Feshbach, 1953], two different asymptotic behaviours and two different asymptotic expansions correspond to the points $\pm\infty$. The asymptotic series are:

$$ \begin{cases} U_{1\Sigma} = x^{d-c} e^x \displaystyle\sum_{k=0}^{\infty} \frac{(1-d)_k (c-d)_k}{k!} \frac{1}{x^k} \\ U_{2\Sigma} = x^{-d} \displaystyle\sum_{k=0}^{\infty} (-1)^k \frac{(d)_k (d-c+1)_k}{k!} \frac{1}{x^k} \end{cases} \tag{4.43} $$

These series expansions are formal solutions of Equation (4.41), but, since they are divergent, they have to be intended as asymptotic expansions of effective solutions of (4.41) near the Infinity. A case in which the series expansions (4.43) are effective solutions of the Equation (4.41) is when the series are truncating, i.e. when the values of the parameters c and d are such that at least one of the terms $(1-d)_k, (c-d)_k, (d)_k, (d-c+1)_k$ is of the form $(-n)_k$, with $n \in \mathbb{N} > 0$. Exploring the various possibilities, it is easy to see that no solution of the form $x^{-1/3}$, which corresponds to the boundary condition at 0 imposed in (4.40), is available. Besides this, each value of d for which the series expansions defined in (4.43) truncate, remembering that $d = \frac{1}{3}\frac{b}{b-a}$, is associated to negative values of the exponents for the ω_τ and

the δ terms (see Equation (4.30)), thus introducing divergent solutions when $K_{II} = 0$.

We have thus seen that there is no possibility to match the defect layer solutions introduced in Table 20 with the logarithmic law of the wall (4.23). An appropriate algebraic Turbulence model which introduces a natural matching procedure will be studied in future investigations. We impose the new boundary conditions:

$$\begin{cases} y(\eta) = \dfrac{d^2F}{d\eta^2} \to 0 \quad \text{for } \eta \to \infty \\ \dfrac{dF}{d\eta} = 0 \quad \text{for } \eta = 0 \end{cases} \tag{4.44}$$

in which the condition at $\eta = 0$ is the no-slip boundary condition imposed on the velocity component parallel to the wall boundary. We are thus searching for solutions uniformly valid on the whole domain. The effect of the wall viscous layer, the determination of u_τ and of the turbulent intensity for the wake solution must anyhow be included in some way. We start from the Von-Karman integral relation [Batchelor, 1967], obtained by integrating the boundary layer equations for the stationary wall solutions with respect to the coordinate orthogonal to the wall:

$$u_\tau^2 = \frac{\partial U}{\partial x} U\delta + \frac{\partial (U^2\theta)}{\partial x} \tag{4.45}$$

where U is the freestream velocity outside the boundary layer, δ is the displacement thickness, which is intended to be the thickness of the defect layer adjacent to the viscous region, and θ is the momentum thickness. In our case, we can consider the displacement thickness as determined by the wake thickness parameter δ of our solutions, whose value is given in Equation (4.30). We can neglect the term containing the momentum thickness, since it can be shown that, to leading order, δ and θ are equal [Wilcox, 1998]. The relation (4.45) can thus be written as:

$$u_\tau^2 \sim \omega_0 V_\infty \delta = \frac{V_\infty^2}{H}\delta \tag{4.46}$$

In order to have an u_τ which varies linearly with ζ, thus defining wall solutions of the type of Equation (4.23) satisfying the stagnation point behaviour near the bottom vertices of the canyon, we should require that:

$$\delta \propto \zeta^2 \tag{4.47}$$

This is not a necessary imposition, since the approximation that the wall effect does not change the stagnation point inviscid law in the direction parallel to a given boundary is a strong one, especially when vorticity is present (anyhow, considering that the vorticity variation along a wall boundary is

negligibly small with respect to the orthogonal variation, this approximation can be made to leading order). A necessary constraint to be imposed to the solution is clearly that $u_\tau = 0$ for $\zeta = 0$. Now, in order to determine the turbulent intensity in the defect layer, we have to refer to empirical data. We use an empirical formula for the shear stress at the wall, introduced by Blasius [McComb, 1990]:

$$u_\tau^2 = 0.023 \cdot V_\infty^2 \left(\frac{\nu}{V_\infty \delta} \right)^{1/4} \tag{4.48}$$

This expression is valid for turbulent boundary layers, but is not clearly valid when a stagnation poin is present. We anyhow consider it valid far away from the stagnation point, at the centre of the wall boundary, at $\zeta = 1/2$ for the vertical segments or $\zeta = 1$ for the road surface segment. Applying the Condition (4.48) to Equation (4.46), we will find the value of the undefined constants in the solution for δ.

We now search for the appropriate solutions of the Equation (4.41), with the parameters defined in (4.42) and the variables defined in Table 20 for the different regions of the domain, satisfying the boundary conditions (4.44). We start from the observation that, in order to have non-diverging solutions for the functions ω_τ and δ, defined in (4.30), we must have:

$$a > 3b$$

This condition implies that:

$$d = \frac{b}{3(b-a)} < 0$$

The only solution of the Confluent Hypergeometric Equation that vanishes at Infinity is the solution which tends to Infinity as:

$$y(x) \to e^x x^{d-c} \quad \text{for} \quad \text{x} \to \infty,$$

only when $x < 0$. This solution is the Confluent Hypergeometric function of the third kind [Morse, Feshbach, 1953]:

$$y(x) = \frac{\Gamma(1-c)}{\Gamma(1-d)} e^{i\pi(d-c)} \, {}_1F_1(d,c,x) - \frac{\Gamma(c-1)}{\Gamma(c-d)} e^{i\pi d} x^{1-c} \, {}_1F_1(d-c+1, 2-c, x) \tag{4.49}$$

Applying the Kummer analytic continuation to this solution we obtain divergent solutions at Infinity. Recall that:

$$\begin{cases} x = \dfrac{b-a}{3}\eta^3 & \text{for} \quad \text{Segments} \quad \mathbf{AB - EC} \\ x = \dfrac{a-b}{3}\eta^3 & \text{for} \quad \text{Segments} \quad \mathbf{BE - CD} \end{cases}$$

so that different values of the constants mus be chosen for the two sets of segments, in order to have $x < 0$ in both cases. If we choose:

$$d = -\frac{1}{15} \longrightarrow a = 6b,$$

we have:

$$\begin{cases} \omega_\tau = (3bK_I\zeta)^{1/3} \\ \\ \delta = \dfrac{\alpha H}{\omega_0^3 K_I}(3bK_I\zeta)^2 \end{cases}$$

which satisfies Condition (4.47) (for the segments on the road boundary, H must be substituted with $W/2$). We must select values of the constants such that bK_I, in order to avoid complex values in the solution for ω_τ. When $b > 0$, selecting a positive value for α, we have:

$$\Delta_1(\zeta) > 0; \Delta_3(\zeta) > 0 \rightarrow \eta_1, \eta_3 > 0,$$

so that:

$$x = \frac{b-a}{3}\eta^3 = -\frac{5b}{3}\eta^3 < 0 \quad \text{for} \quad \text{Segments} \quad \mathbf{AB - EC}$$

For the other two segments, both in the cases of $b > 0$ or $b < 0$, we have to choose a negative value for α in order to have $x < 0$. This means that the perturbation contributions to the velocity components $\omega_0 \delta dF/d\eta$ for Segments **BE** and **CD** have an opposite sign with respect to the contribution for Segments **AB** and **EC**. This fact introduces secondary recirculations in the flow structure. This is the reason why we have inserted the constant α in the prescription for the eddy viscosity, without incorporating the intensity of Turbulence inside the definition of δ itself (since $\nu_T \propto \delta^2$). The magnitude of the constant α can be effectively set equal to 1. We have, in the case $b > 0$:

$$\Delta_2(\zeta) < 0; \Delta_4(\zeta) < 0 \rightarrow \eta_2, \eta_4 < 0,$$

so that:

$$x = \frac{a-b}{3}\eta^3 = \frac{5b}{3}\eta^3 < 0 \quad \text{for} \quad \text{Segments} \quad \mathbf{BE - CD}$$

Now we impose Equation (4.46):

$$\begin{cases} u_\tau^2 \sim \dfrac{9V_\infty^2}{\omega_0^3} K_I b^2 \zeta^2 \quad \text{for} \quad \text{Segments} \quad \mathbf{AB - CD} \\ u_\tau^2 \sim \dfrac{9WV_\infty^2}{2H\omega_0^3} K_I b^2 \zeta^2 \quad \text{for} \quad \text{Segments} \quad \mathbf{EB - EC} \end{cases}$$

These values of u_τ are those used in the context of the grid generation described in Section 3.4. Equation (4.48) gives (selecting the value $K_I = 1$):

$$\begin{cases} \text{Segments} \quad \mathbf{AB} - \mathbf{CD} : \\ 9\dfrac{H}{\omega_0^3} b^2 \zeta^2 \Big|_{\zeta=1/2} = (0.023)^{4/5} \left(\dfrac{\nu}{V_\infty}\right)^{1/5} \longrightarrow b = \sqrt{\dfrac{4}{9}\dfrac{V_\infty^3}{H^4}(0.023)^{4/5}\left(\dfrac{\nu}{V_\infty}\right)^{1/5}} \\ \\ \text{Segments} \quad \mathbf{BE} - \mathbf{EC} : \\ 9\dfrac{W}{2\omega_0^3} b^2 \zeta^2 \Big|_{\zeta=1} = (0.023)^{4/5} \left(\dfrac{\nu}{V_\infty}\right)^{1/5} \longrightarrow b = \sqrt{\dfrac{2}{9}\dfrac{V_\infty^3}{WH^3}(0.023)^{4/5}\left(\dfrac{\nu}{V_\infty}\right)^{1/5}} \end{cases} \tag{4.50}$$

Note that the values of b are small, and that the parameters ω_τ and δ defined in Equation (4.30) are small as a consequence; moreover, δ is smaller than ω_τ, due to the different value of the exponents, so that also Δ is small. These facts enforce our perturbation analysis.

Other choices for the parameter d can be made which respect the constraint $a > 3b$. For example, we can choose values of d such that the exponents of ω_τ and δ in Equation (4.30) are positive integers. This allows to choose values of b and K_I with opposite signs, introducing thus a change of sign of ω_τ between the different regions of the domain which let us to depict secondary recirculations also in the solution for ω. We must observe that the exponents of ω_τ and δ, when they are positive integers, have opposite parity:

$$\begin{cases} \dfrac{b}{a-3b} = 2n+1 \rightarrow \dfrac{a}{a-3b} = 4+6n \\ \dfrac{b}{a-3b} = 2n \rightarrow \dfrac{a}{a-3b} = 1+6n \end{cases}$$

where $n \in \mathbb{N} \geq 0$. It's easy to see that this fact introduces the necessity to change the sign of the perturbation contribution for the Regions adjacent to the Segments **BE** and **CD**.

We choose here $d = -\frac{1}{15}$. The Solution (4.49) becomes:

$$e^{-i\pi(11/15)} y(x) = A\left\{ \frac{\Gamma(1/3)}{\Gamma(16/15)}\, {}_1F_1\left(-\frac{1}{15}, \frac{2}{3}, x\right) + (-x)^{1/3} \frac{\Gamma(-1/3)}{\Gamma(11/15)}\, {}_1F_1\left(\frac{4}{15}, \frac{4}{3}, x\right) \right\} \tag{4.51}$$

where A is an arbitrary constant. Note that, since $x < 0$, this solution is always real. This function goes to $e^x x^{-11/15}$ for $x \to \infty$, thus it satisfies the first boundary condition in Equation (4.44). In order to satisfy the second boundary condition in Equation (4.44), let us write the Solution Equation

(4.51) in terms of the variable η:

$$\frac{d^2F}{d\eta^2} = A\left\{ \frac{\Gamma(1/3)}{\Gamma(16/15)}\,{}_1F_1\left(-\frac{1}{15}, \frac{2}{3}, \pm\frac{5}{3}b\eta^3\right) + \left[\mp\left(\frac{5}{3}b\right)^{1/3}\eta\right]\frac{\Gamma(-1/3)}{\Gamma(11/15)}\,{}_1F_1\left(\frac{4}{15}, \frac{4}{3}, \pm\frac{5}{3}b\eta^3\right)\right\} \tag{4.52}$$

where the different signs correspond to the different set of segments (remember that, for the Segments **BE** and **CD**, $\eta < 0$). Now we integrate in η, and obtain (using the standard techniques of integral representations of the confluent hypergeometric functions [Andrews et al., 1999]), choosing $A = 1$ and constant of integrations equal to 0:

$$\frac{dF}{d\eta} = \frac{\Gamma(1/3)}{\Gamma(16/15)}\eta\,{}_2F_2\left(-\frac{1}{15}, \frac{1}{3}; \frac{2}{3}, \frac{4}{3}; \pm\frac{5}{3}b\eta^3\right) \mp \left(\frac{5}{3}b\right)^{1/3}\frac{\Gamma(-1/3)}{2\Gamma(11/15)}\eta^2\,{}_2F_2\left(\frac{4}{15}, \frac{2}{3}; \frac{4}{3}, \frac{5}{3}; \pm\frac{5}{3}b\eta^3\right) \tag{4.53}$$

where ${}_2F_2(a, b; c, d; x)$ is the Generalized Hypergeometric Function, with series expansion around the origin:

$${}_2F_2(a, b; c, d; x) = \sum_{k=0}^{\infty}\frac{(a)_k(b)_k}{(c)_k(d)_k}\frac{x^k}{k!}$$

It is immediate to see that $dF/d\eta = 0$ for $\eta = 0$; the second boundary condition in Equation (4.44) is thus satisfied. We write the solution for the velocity field (v, w), dependent on the orthogonal component of the external flow V_∞, on $\omega_0 = V_\infty/H$ and on the constants H, W and b, in Table 21, with different expressions for the different regions of the domain adjacent to the wall segments. The symbol ${}_a(\cdot|\cdot)_b$ means that the expression at the right in the parenthesis must be used above the bisector, and the expression at the right below.

Region $\{0 \le y \le W/2; 0 \le z \le H/2\}$	
$v = {}_a(v_{ms}\| - \omega_0 z)_b - \dfrac{2 \cdot 3^2 \cdot b^2}{\omega_0^2 W} y^2 \dfrac{d}{d\eta_{BE}} F(\eta_{BE});$	$\eta_{BE} = -\dfrac{\omega_0^2 W^{2/3}}{2^{2/3} 3^{5/3} b^{5/3}} \dfrac{z}{y^{5/3}}$
$w = {}_a(\omega_0 y\|w_{msII})_b - \dfrac{3^2 \cdot b^2}{\omega_0^2 H} z^2 \dfrac{d}{d\eta_{AB}} F(\eta_{AB});$	$\eta_{AB} = \dfrac{\omega_0^2 H^{2/3}}{3^{5/3} b^{5/3}} \dfrac{y}{z^{5/3}}$
Region $\{W/2 < y \le W; 0 \le z \le H/2\}$	
$v = {}_a(v_{ms}\| - \omega_0 z)_b + \dfrac{2 \cdot 3^2 \cdot b^2}{\omega_0^2 W} (W-y)^2 \dfrac{d}{d\eta_{EC}} F(\eta_{EC});$	$\eta_{EC} = \dfrac{\omega_0^2 W^{2/3}}{2^{2/3} 3^{5/3} b^{5/3}} \dfrac{z}{(W-y)^{5/3}}$
$w = {}_a(-\omega_0 (W-y)\|w_{msII})_b - \dfrac{3^2 \cdot b^2}{\omega_0^2 H} z^2 \dfrac{d}{d\eta_{CD}} F(\eta_{CD});$	$\eta_{CD} = -\dfrac{\omega_0^2 H^{2/3}}{3^{5/3} b^{5/3}} \dfrac{(W-y)}{z^{5/3}}$
Region $\{0 \le y \le W/2; H/2 < z \le H\}$	
$v = {}_a(\omega_0 (H-z) + V_\infty\|v_{ms})_b$	
$w = {}_a(w_{msII}\|\omega_0 y)_b - \dfrac{3^2 \cdot b^2}{\omega_0^2 H} z^2 \dfrac{d}{d\eta_{AB}} F(\eta_{AB});$	$\eta_{AB} = \dfrac{\omega_0^2 H^{2/3}}{3^{5/3} b^{5/3}} \dfrac{y}{z^{5/3}}$
Region $\{W/2 < y \le W; H/2 < z \le H\}$	
$v = {}_a(\omega_0 (H-z) + V_\infty\|v_{ms})_b$	
$w = {}_a(w_{msII}\| - \omega_0 (W-y))_b - \dfrac{3^2 \cdot b^2}{\omega_0^2 H} z^2 \dfrac{d}{d\eta_{CD}} F(\eta_{CD});$	$\eta_{CD} = -\dfrac{\omega_0^2 H^{2/3}}{3^{5/3} b^{5/3}} \dfrac{(W-y)}{z^{5/3}}$

Table 21: Solution for the velocity field (v, w), with different expressions for the different regions of the domain adjacent to the wall segments **AB**, **BE**, **EC**, **CD**. The symbol ${}_a(\cdot|\cdot)_b$ means that the expression at the right in the parenthesis must be used above the bisector, and the expression at the right below.

where the terms $dF/d\eta$ are given in Equation (4.53), with the minus sign in the independent variable inside the Hypergeometric functions for the case of Segments **AB** and **EC**, and the plus sign for the case of Segments **BE** and **CD**. Note that the divergence of the solutions when the denominators of the η variables tend to zero in the terms containing η^2 is avoided by the fact that $d^2F/d\eta^2 \to 0$ for $\eta \to \infty$. The parameter b, for the different regions, is given by Equation (4.50).

External wind with arbitrary direction relative to the street axis Let us define the canyon longitudinal mean velocity $\mathbf{U}_{//}$ relative to the longitudinal component of the wind flow generated thorough the canyon by the external wind flow:

$$\mathbf{U}_{//} = \frac{1}{HW}\int_0^H dz \int_0^W dy\, u(y,z) \tag{4.54}$$

where $u(y,z)$ is the solution for the longitudinal velocity component generated by an external wind flow U_∞ parallel to the canyon axis, as defined in Table 18. In order to calculate this integral, the domain must be split in the four regions defined in Table 18, in which different forms of the solution are valid. For Region **1**, we have the contribution:

$$\begin{aligned}
&\frac{U_\infty}{HW}\int_0^H dz \int_0^{\frac{Wz}{2H}} dy\, \frac{z}{H}\left\{\frac{1}{k}\sqrt{1+\left(\frac{y}{z}\right)^2}+\frac{1}{k}\log\left(\frac{y}{z}\right)-\frac{1}{k}\log\left(1+\sqrt{1+\left(\frac{y}{z}\right)^2}\right)+1\right.\\
&\left.-\frac{1}{k}\left[\sqrt{1+\frac{W^2}{4H^2}}+\log\left(\frac{W}{2H}\right)-\log\left(1+\sqrt{1+\frac{W^2}{4H^2}}\right)\right]\right\}=\\
&\\
&\frac{U_\infty}{24HWk}\left[4H^2\mathrm{csch}^{-1}\left(\frac{2\mathrm{H}}{\mathrm{W}}\right)+\mathrm{W}\sqrt{4\mathrm{H}^2+\mathrm{W}^2}\right]+\frac{\mathrm{U}_\infty}{6\mathrm{k}}\left[\log\left(\frac{\mathrm{W}}{2\mathrm{H}}\right)-1\right]\\
&-\frac{U_\infty}{6Wk}\left[2H\mathrm{csch}^{-1}\left(\frac{2\mathrm{H}}{\mathrm{W}}\right)+\mathrm{W}\left(\log\left[2+\sqrt{4+\frac{\mathrm{W}^2}{\mathrm{H}^2}}\right]-1-\log 2\right)\right]\\
&+\frac{U_\infty}{6}-\frac{U_\infty}{6k}\left[\sqrt{1+\frac{W^2}{4H^2}}+\log\left(\frac{W}{2H}\right)-\log\left(1+\sqrt{1+\frac{W^2}{4H^2}}\right)\right]
\end{aligned} \tag{4.55}$$

It's easy to see that the contributions from Region **2** is obtained by taking the change $W \longleftrightarrow 2H$ in the contribution from Region **1**. The contribution from the other two regions is the same as the sum of the Region **1** and Region **2** contributions by symmetry.

In Section 4.2 we will compare the theoretical estimates of $\mathbf{U}_{//}$ with numerical estimates. The values of $\mathbf{U}_{//}$ are used to set up operational models for dispersion, as described in Section 3.5.

In the case of an external flow with arbitrary angle with respect to the street axis, the equation for the u component is coupled to the equations for the transversal components v and w, as is evident by observing the Equations of motion (4.1). The coupling term is given by:

$$v\frac{\partial u}{\partial y} + w\frac{\partial u}{\partial z},$$

which is not present in the unidirectional flow Equation (4.2) describing the case of external wind parallel to the street axis. The transverse components can be considered to be independent from the longitudinal one, and we can use the Solutions reported in Table 21 also to describe them in the case of an external flow with arbitrary angle relative to the street canyon axis; on the other hand, compared with the case of longitudinal freestream flow, the presence of the transverse component modifies the longitudinal component of the flow, and we cannot use the Solutions reported in Table 18 in the general case. In principle, it will be necessary, in order to describe the recirculation flow inside a street canyon in the general case, to modify the model for the longitudinal component, by taking into account the non-linear interactions with the transversal components of velocity. This can be accomplished by the method of Green propagation, but the details of the calculations, due to the different form of the equation in different regions of the domain, are very cumbersome. We will treat this case in future investigations. In the same manner as in Ref. [Soulhac et al., 2008], we have introduced the canyon longitudinal mean velocity $\mathbf{U}_{//}$ (see Equation (4.54), since it can be considered to be independent from the transversal components of velocity and to depend only on the component of the external velocity parallel to the street axis U_∞. This is shown in Ref. [Soulhac et al., 2008] by numerical simulations, and by applying to the integral form of the equation of motion. In fact, by considering the integral form of the NS equations (4.25) for the longitudinal component u integrated over the canyon surface, we can see that the flux of the coupling term through the canyon walls and the roof boundary is zero. Thus the integral forms of the equation for the case of an external flow parallel and with an arbitrary angle relative to the street axis are the same, and do not depend on the transversal dynamics. The definition of $\mathbf{U}_{//}$ comes as a solution of the integral equation for u. We have effectively chosen, in the formulation of dispersion operational models (see Section 3.5), to introduce an average effect of advection and turbulent dispersion along the canyon in terms of the quantity $\mathbf{U}_{//}$, whose Form (4.54) is valid for the case of external flow with arbitrary angles relative to the street axis, and depends only on the parallel component of the freestream velocity and on the geometry of the canyon. The advection and turbulent dispersion in the transversal directions are described by means of the Solutions reported in Table 21, obtained in the case of an external wind orthogonal to the street axis. As already said, these solutions depend only on the orthogonal

component of the freestream velocity.

Far-wake In Sections 3.3 and 3.4 we have pointed to the fact that a defect law solution for the longitudinal component of the velocity in the far-wake region of a moving vehicle has the form of a self-preserving solution. We now investigate this solution, extending the results obtained in Ref. [Eskridge et al., 1979]. Consider a vehicle travelling at a constant speed U_∞ in the $-x$ direction, and consider a system of coordinate fixed relative to the vehicle. Immediately behind the vehicle, the near-wake is composed by unsteady turbulent motions. However, several vehicle heights downstream ($x \geq h$, with h the vehicle height), the wake settles into a spatially homogeneous turbulent structure spreading in the cross-wake and vertical directions. The statistical averaged velocity can be expressed in the form of a deficit law (which is equivalent to applying the Oseen approximation [Batchelor, 1967] to the equations of motion for fluid flow behind an obstacle):

$$\overline{u} = [U_\infty + u, v, w] \tag{4.56}$$

where u, v and w are perturbation velocities, which are assumed to be small compared to U_∞. The wake thickness δ is assumed to be much smaller than the wake length L, so that a boundary-layer approximation [Batchelor, 1967], i.e. a perturbation analysis obtained by considering the derivatives in the x direction to be much smaller than the derivatives in the other directions, can be set up. From the continuity equation it follows that:

$$|v|, |w| \sim \frac{u\delta}{L}$$

Considering the defect law (4.56) as the first term in a perturbation expansion in powers of a small parameter ϕ_1, as done in previous paragraphs, we see that the orders of magnitude of the velocity components are:

$$u = O[\phi_1]; \quad v = O[\phi_1\delta; \quad v = O[\phi_1\delta$$

The Reynolds averaged NS equations, to leading order, are:

$$\begin{cases} U_\infty \dfrac{\partial u}{\partial x} = -\dfrac{1}{\rho}\dfrac{\partial p}{\partial x} + \dfrac{\partial}{\partial y}\left[\lambda\nu_T \dfrac{\partial u}{\partial y}\right] + \dfrac{\partial}{\partial z}\left[\nu_T \dfrac{\partial u}{\partial z}\right] \quad \text{at} \quad \mathrm{O}[\phi_1] \\ U_\infty \dfrac{\partial v}{\partial x} = -\dfrac{1}{\rho}\dfrac{\partial p}{\partial y} + \dfrac{\partial}{\partial y}\left[\lambda\nu_T \dfrac{\partial v}{\partial y}\right] + \dfrac{\partial}{\partial z}\left[\nu_T \dfrac{\partial v}{\partial z}\right] \quad \text{at} \quad \mathrm{O}[\phi_1 \cdot \delta] \\ U_\infty \dfrac{\partial w}{\partial x} = -\dfrac{1}{\rho}\dfrac{\partial p}{\partial z} + \dfrac{\partial}{\partial y}\left[\lambda\nu_T \dfrac{\partial w}{\partial y}\right] + \dfrac{\partial}{\partial z}\left[\nu_T \dfrac{\partial w}{\partial z}\right] \quad \text{at} \quad \mathrm{O}[\phi_1 \cdot \delta] \end{cases} \tag{4.57}$$

where λ is a constant which takes into account the asymmetry produced by the ground, and thus introduces in a simple manner anisotropy of the Reynolds stress tensor. It is expected that $1 \leq \lambda \leq 2$. As in Ref. [Eskridge et al., 1979], we take $\lambda = 1$. The boundary conditions to Equations (4.57) are:

$$u = v = w \to 0 \quad \text{for} \quad \mathrm{z} = 0,\, \mathrm{z} \to \infty,\, \mathrm{x} \to \infty,\, \mathrm{y} \to \pm\infty \tag{4.58}$$

Note that, from the third Equation in (4.35) and the boundary conditions for $z \to \infty$:

$$\frac{\partial p}{\partial z} \sim \frac{U_\infty u \delta}{L^2}; \quad \frac{\partial p}{\partial z} \to 0,$$

so that:

$$\frac{\partial p}{\partial x} \sim \left(\frac{\partial p}{\partial z}\right)\frac{\delta}{L} \sim \frac{U_\infty u \delta^2}{L^2},$$

and thus the pressure gradient term in the first Equation of (4.57) is $o(\phi_1)$ and can be neglected. We must note that this approximation is not valid for strong adverse external pressure gradients, which cause boundary layer separation and for which the perturbation analysis is not applicable and self-preserving solutions do not generally exist [Wilcox, 1998]. In any case, in the far-wake zone the effects of an adverse pressure gradient can be neglected. The longitudinal perturbation term u can be obtained by seeking a self-preserving solution of the corresponding equation, in terms of scaled variables with the wake thickness parameter:

$$u = AU_\infty u_0(\chi) f[\eta, \zeta]; \quad \text{with} \quad \chi = \frac{\mathrm{x}}{\mathrm{h}},\ \eta = \frac{\mathrm{y}}{\delta(\mathrm{x})},\ \zeta = \frac{\mathrm{z}}{\delta(\mathrm{x})} \tag{4.59}$$

where A is a constant, and with an algebraic Turbulence model prescription for the adimensional eddy viscosity:

$$\nu_T = \gamma \delta(\chi) u_0(\chi) \tag{4.60}$$

with γ a constant which determines the Turbulence magnitude within the wake (which is assumed to be equal to the Von Karman constant k in Ref. [Eskridge et al., 1979], by comparison with wind tunnel experiments). This is the Prandtl prescription for the wake boundary layer (3.6). Integrating the equations of motion for the u component with respect to x, y and z we find an integral constraint to the motion, which gives an initial condition for the development of the vehicle wake representing an integral property of the flow close to the vehicle:

$$\int_{-\infty}^{\infty}\int_{0}^{\infty} z U_\infty u \, dz dy = \overline{\mathrm{C}} \tag{4.61}$$

where C is a constant. A multiplication by z, and a consequent integration by part, has been introduced in order to consider the boundary condition at $z = 0$. The constant should be given in terms of the drag force on the vehicle, on the circulation intensity of the trailing vortices which develop behind the vehicle and on the external pressure gradient. In Ref. [Eskridge et al., 1979] it is shown how the two last contributions decays very quickly within one or two vehicle heights behind the vehicle. The constant C is chosen to be equal to the (the opposite of the) couple on the vehicle per unit mass:

$$\overline{C} = -\frac{Dh}{\rho} = -\frac{1}{2} U_\infty^2 \overline{A} h C_D \tag{4.62}$$

where D is the drag force on the vehicle surface, C_D is the drag coefficient (introduced in Equation (3.20)) and $\overline{A}$ is the cross-sectional area of the vehicle in the direction of motion. The choice (4.62) has been introduced in Ref. [Eskridge et al., 1979]. We will justify it in terms of the momentum integral equation when considering the case of interacting vehicles. The drag coefficient C_D for the Ahmed body is known from the experiments [Ahmed, Ramm, 1984] (see Figure 13), for different vehicle geometries and for a reference velocity. It is an adimensional coefficient, dependent only on the Reynolds number of the motion [Batchelor, 1967]. Its value is given in function of the vehicle velocity $C_D(U_\infty)$ by suitable parametrizations obtained through the numerical simulations in Section 4.2. Let us substitute the self-preserving form of the solution (4.59), with the corresponding change of variable, and the eddy viscosity form (4.60) inside the Equation of motion for the u component (4.57) and inside the integral Constraint (4.61). We obtain:

$$\frac{\partial^2 f}{\partial \eta^2} + \frac{\partial^2 f}{\partial \zeta^2} + \frac{\delta'}{H\gamma u_0} \eta \frac{\partial f}{\partial \eta} + \frac{\delta'}{H\gamma u_0} \zeta \frac{\partial f}{\partial \zeta} - \frac{u_0' \delta}{H\gamma u_0^2} f = 0 \tag{4.63}$$

and

$$\int_{-\infty}^{\infty} \int_{0}^{\infty} \zeta f[\eta, \zeta] \, d\zeta d\eta = \frac{\overline{C}}{A U_\infty^2 u_0 \delta^3} \tag{4.64}$$

The boundary conditions to Equation (4.63) are:

$$f \to 0 \quad \text{for} \quad \zeta = 0, \, \zeta \to \infty, \, \eta \to \pm\infty \tag{4.65}$$

The Equation (4.63) is not dependent on the variable x, and thus self-preserving solutions exists, if:

$$\begin{cases} \dfrac{\delta'}{H\gamma u_0} = c_1 \\ \\ \dfrac{u_0'\delta}{H\gamma u_0^2} = c_2 \\ \\ \dfrac{\overline{C}}{AU_\infty^2 u_0 \delta^3} = c_3 \end{cases}$$

with c_1, c_2 and c_3 constants. The solution of the system is given by:

$$\begin{cases} \delta \propto (\chi)^{1/4} \\ \\ u_0 \propto (\chi)^{-3/4} \end{cases}$$

and the Equation (4.63) becomes:

$$\frac{\partial^2 f}{\partial \eta^2} + \frac{\partial^2 f}{\partial \zeta^2} + c_1 \eta \frac{\partial f}{\partial \eta} + c_1 \zeta \frac{\partial f}{\partial \zeta} - c_2 f = 0 \tag{4.66}$$

The solution obtained in Ref. [Eskridge et al., 1979] corresponds to the choice:

$$u_0 \delta^3 = \gamma^3 h^3 A^4; \quad c_1 = \frac{1}{4}; \quad c_2 = -\frac{3}{4} \tag{4.67}$$

With this choice, we obtain the following forms:

$$\begin{cases} \delta = \gamma A h (\chi)^{1/4} \\ \\ u_0 = A(\chi)^{-3/4} \\ \\ \dfrac{\partial^2 f}{\partial \eta^2} + \dfrac{\partial^2 f}{\partial \zeta^2} + \dfrac{1}{4}\eta \dfrac{\partial f}{\partial \eta} + \dfrac{1}{4}\zeta \dfrac{\partial f}{\partial \zeta} + \dfrac{3}{4} f = 0 \end{cases} \tag{4.68}$$

The equation in (4.68) can be solved by separation of variables $f[\eta, \zeta] = f_1(\eta) f_2(\zeta)$:

$$\begin{cases} f_2'' + \dfrac{1}{4}\zeta f_2' + \dfrac{2}{4} f_2 = 0 \\ \\ f_1'' + \dfrac{1}{4}\eta f_1' + \dfrac{1}{4} f_1 = 0 \end{cases}$$

The first Equation is the adjoint of the Hermite differential function [Morse, Feshbach, 1953], whith the corresponding confluent hypergeometric function truncating to a

first order polynomial; the second is the equation for the Gaussian function. The solution is thus:

$$f[\eta,\zeta] = \Lambda_1\,\zeta\,e^{-\frac{(\eta^2+\zeta^2)}{8}} \tag{4.69}$$

where Λ_1 is a constant. This solution satisfies the boundary Conditions (4.65). The general solution Equation (4.66), with arbitrary values of c_1 and c_2, can be separated into Hermit differential equations, and by suitably choosing the values of the constants c_1 and c_2, we can generalize the Solution (4.69) as a series expansion in Hermite polynomials, choosing the eigenvalues such that only the odd order Hermite polynomials are solutions in the ζ direction (in order to satisfy the boundary condition at $\zeta = 0$. We do not go into details; we only note that the differential equations obtained by separating the variables in Equation (4.66) never a logarithmic point at the origin, so a matching with a logarithmic layer at the road boundary is not possible. The constant Λ_1 is obtained using the fact that the function f has a relative maximum at $(\eta,\zeta) = (0,2)$, and imposing the fact that $f \leq 1$ (since we are considering a perturbation of the freestream velocity). Imposing the integral Condition (4.64) to the solution (4.69), we obtain the value for A:

$$A^4 = \frac{\overline{C}}{\gamma^3 h^3 U_\infty^2 (32\pi)^{1/2}\Lambda_1} \tag{4.70}$$

The complete solution for the perturbation term is:

$$u = -U_\infty |A| \left(\frac{x}{h}\right)^{-3/4} 0.824\,\zeta\,e^{-\frac{(\eta^2+\zeta^2)}{8}} \tag{4.71}$$

In Figure 23 we show a plotting of the perturbation solution $|u|$ corresponding to an Ahmed body with 25° rear slant angle (sedan vehicle) moving at a velocity $U_\infty = 50km/h$. The profile corresponds to the solution at a variable height, equal to the height of the wake region ($\zeta = 1 \rightarrow z = \delta(x)$), and at different downstream locations (expressed in terms of the vehicle height h). We observe that far enough along the vehicle wake, at distances greater than $8h$, the perturbation is decreased to more than 1/10 of the freestream value.

By searching for similarity solutions for the perturbation components v and w in the same form as for the u component, satisfying the second and the third Equations in (4.57) and the continuity equation, we obtain:

$$\begin{cases} v = U_\infty \gamma A^2 \left(\dfrac{x}{h}\right)^{-3/2} 0.412\,\zeta\eta\,e^{-\frac{(\eta^2+\zeta^2)}{8}} \\ \\ w = U_\infty \gamma A^2 \left(\dfrac{x}{h}\right)^{-3/2} 0.206\,\zeta^2\,e^{-\frac{(\eta^2+\zeta^2)}{8}} \end{cases} \tag{4.72}$$

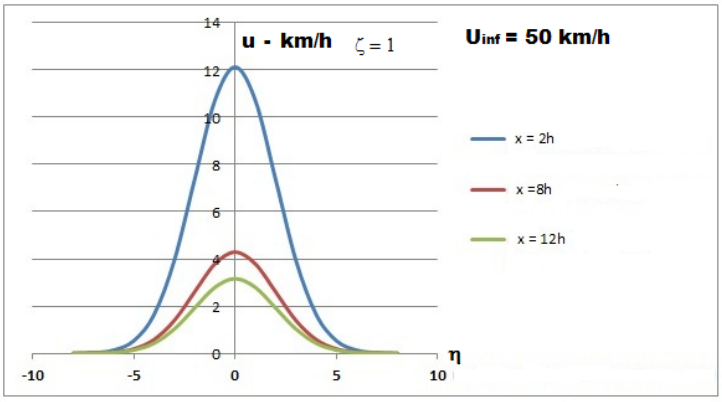

Figure 23: x component of perturbation velocity for an Ahmed body of rear slant angle of 25° degrees moving at $50km/h$. The z coordinate has been chosen to correspond to the height of boundary layer. The y coordinate is scaled in units of boundary layer thickness (η). Different profiles are reported for different distances behind the vehicle, in units of the height of the vehicle h

In Ref. [Eskridge et al., 1979], the Turbulence intensity is estimated by assuming that the Turbulence also has a self-preserving form:

$$(\overline{u'^2}, \overline{v'^2}, \overline{w'^2}) \propto U_\infty^2 \left(\frac{x}{h}\right)^{-3/2} F[\eta, \zeta],$$

and assuming moreover that $\overline{u'^2}$ is proportional to the shear stresses in the wake, and that the Turbulence is constant inside a core of radius $\eta^2+\zeta^2 = 12$. The result is:

$$(\overline{u'^2}, \overline{v'^2 w'^2}) = (a_1, a_2, a_3)\frac{1}{2}U_\infty^2 A^2 \gamma \Lambda_1 \left(\frac{x}{h}\right)^{-3/2} \left[\left(1-\frac{\zeta^2}{4}\right)+\frac{\eta^2\zeta^2}{16}\right]^{1/2} e^{-\frac{(\eta^2+\zeta^2)}{8}} \tag{4.73}$$

The values of the constants a_1, a_2, a_3 are obtained in Ref. [Eskridge et al., 1979] by comparison with empirical data:

$$a_1 = 0.35, \quad a_2 = 2.70, \quad a_3 = 0.23$$

We use the Form (4.73) for the Turbulence intensities, even if it should be reformulated considering the forms for the v and the w components (4.72), since it has been calibrated over empirical data.

We consider now the multi-vehicle case. As expressed in Section 3.5, the effect of a distribution of N vehicles at the points $\{(x_j, y_j) : j = 1, \cdots, N\}$ along the street, separated by a distance Δx (determined by the driving conditions) can be obtained by summing the average wake effect of each vehicle as it takes on all positions between $x_j + \Delta x/2$ and $x_j - \Delta x/2$, expressed in terms of the Solutions (4.71) and (4.72):

$$\begin{cases} \overline{u}_w(x,y,z) = U_\infty - \dfrac{1}{\Delta x}\displaystyle\sum_{j=1}^{N}\int_{x_j-\Delta x/2}^{x_j+\Delta x/2} dx\, U_\infty A\left(\frac{x_j}{h}\right)^{-3/4} 0.824\,\zeta_j\, e^{-\frac{(\eta_j^2+\zeta_j^2)}{8}} \\ \overline{v}_w(x,y,z) = \dfrac{1}{\Delta x}\displaystyle\sum_{j=1}^{N}\int_{x_j-\Delta x/2}^{x_j+\Delta x/2} dx\, U_\infty \gamma A^2\left(\frac{x_j}{h}\right)^{-3/2} 0.412\,\zeta_j\eta_j\, e^{-\frac{(\eta_j^2+\zeta_j^2)}{8}} \\ \overline{w}_w(x,y,z) = \dfrac{1}{\Delta x}\displaystyle\sum_{j=1}^{N}\int_{x_j-\Delta x/2}^{x_j+\Delta x/2} dx\, U_\infty \gamma A^2\left(\frac{x_j}{h}\right)^{-3/2} 0.206\,\zeta_j^2\, e^{-\frac{(\eta_j^2+\zeta_j^2)}{8}} \end{cases} \tag{4.74}$$

The mean eddy diffusivity contributions, formulated in the context of the pollutant dispersion as in Equation (3.68), and considering the form of the solutions for the Turbulence intensity given in Equation (4.73), are:

$$\begin{aligned} K_w^y =& \frac{1}{\Delta x}\sum_{j=1}^{N}\int_{x_j-\Delta x/2}^{x_j+\Delta x/2} dx \left\{\delta(x_j)\cdot \right. \\ & \left. \left(a_2\frac{1}{2}U_\infty^2 A^2\gamma\Lambda_1\left(\frac{x_j}{h}\right)^{-3/2}\left[\left(1-\frac{\zeta^2}{4}\right)+\frac{\eta^2\zeta^2}{16}\right]^{1/2} e^{-\frac{(\eta^2+\zeta^2)}{8}}\right)\right\} \end{aligned} \tag{4.75}$$

$$\begin{aligned} K_w^z =& \frac{1}{\Delta x}\sum_{j=1}^{N}\int_{x_j-\Delta x/2}^{x_j+\Delta x/2} dx \left\{\delta(x_j)\cdot \right. \\ & \left. \left(a_3\frac{1}{2}U_\infty^2 A^2\gamma\Lambda_1\left(\frac{x_j}{h}\right)^{-3/2}\left[\left(1-\frac{\zeta^2}{4}\right)+\frac{\eta^2\zeta^2}{16}\right]^{1/2} e^{-\frac{(\eta^2+\zeta^2)}{8}}\right)\right\} \end{aligned}$$

These Expressions for the main effect of many vehicles are valid only in the case on non-interacting vehicles. In the case of interacting vehicles, we employ a very simple procedure to insert in the perturbation solutions the effect of the vehicles far-wake interactions. This is done by modifying the initial integral condition (4.61)-(4.62), using the momentum equations in integral form. The Relations (4.61)-(4.62) can in fact be obtained by using the momentum Equation in integral form (4.25) for the u component of velocity, integrated over a control surface, shown in Figure 24 in a 2−dimensional projection, constituted by a rectangular parallelepiped, with the horizontal faces, indicated by S in Figure 24, parallel to the freestream,

and the vertical planes, indicated by A, orthogonal to the stream (frontal faces) and parallel to the stream (lateral faces).

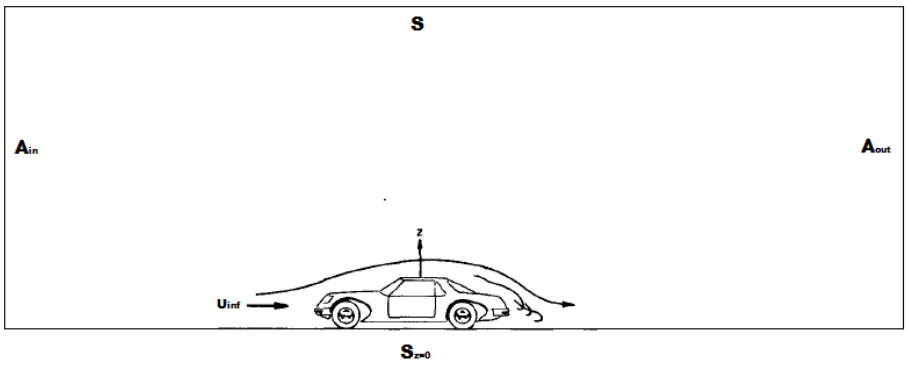

Figure 24: 2− dimensional projection of the control surface used to integrate the momentum Equation in integral form for determining an initial constraint on the far-wake development.

We consider the S faces to be sufficiently far enough from the body to lie outside the wake, except for the S_0 face, which is constituted by the road-surface boundary. The fluid within this control surface is acted on by forces at the control surface, and by forces at the body surface, whose resultant in the x direction is $-D$. The momentum integral equation gives:

$$D = \int (p_{in} + \rho u_{in}^2 - p_{out} - \rho u_{out}^2)\, dA - \rho \int u\mathbf{u} \cdot \mathbf{n}\, dS + \text{viscous forces at the control surface.} \tag{4.76}$$

We assume that all parts of the control surface are at large distances from the body, to ensure that viscous forces at the control surface are relatively small and in order to be able to approximate the values of u_{in}, u_{out}, p_{in} and p_{out} with the corresponding freestream values. Besides we assume that the Reynolds number of the flow is so large that the corresponding tangential stresses at the road surface S_0 are small (they are proportional to the inverse of the square root of the Reynolds number). Applying the conservation of mass flux across the control surface, we obtain:

$$D = \int [p_{in} + \rho u_{in}(u_{in} - U_\infty) - p_{out} - \rho u_{out}(u_{out} - U_\infty)]\, dA \tag{4.77}$$

It's easy to see that the integral over the part of the area of A outside the wake tends to zero, by application of the Bernoulli theorem. Far from the body the streamlines are nearly parallel, and the pressure variation across the wake is very small. The limiting form of the integral in (4.77), as the variables approach the corresponding free-stream values, but with u_{out} making the slowest approach, is thus:

$$-D = \int [\rho U_\infty (u_{out} - U_\infty)]\, dA \tag{4.78}$$

Remembering that $u_{out} - U_\infty$ is our perturbation term u, and introducing the effect of the boundary at the $z = 0$ surface, we obtain the Relation (4.61). The value of D is known from the values of the drag coefficient C_D for different vehicle geometries and velocities (4.62),whose value is given in function of the vehicle velocity $C_D(U_\infty)$ by suitable parametrizations obtained through the numerical simulations in Section 4.2. When considering the case of interacting vehicles, we can assume that a vehicle is moving in the far-wake zone of the preceding vehicle, and the initial constraint (4.61) must be expressed in terms of the far-wake solution for the preceding vehicle. The distance between two consecutive vehicles is given by the traffic statistics data. We consider the Face A_{in} in Fifure 24 as situated in the middle between two consecutive vehicles. In this case, the u_{in} value is given by the solution (4.71), specified at $x = \Delta x/2$, where Δx is the distance between the vehicles, and with the parameter A, defined in Equation (4.70), determined in function of the value of $C_D(U_\infty)$ for the preceding vehicle. The appropriate momentum Equation is now:

$$-D = \int [\rho U_\infty (u_{out} - U_\infty) - \rho u_{in}(u_{in} - U_\infty)]\, dA \tag{4.79}$$

Now we introduce the effect of the boundary condition at $z = 0$, and define the following quantities:

- u_{j-1}: the perturbation solution for a preceding vehicle;
- u_j: the perturbation solution for the considered vehicle;
- $U_{\infty j-1}$: the freestream velocity for a preceding vehicle;
- $U_{\infty j}$: the freestream velocity for the considered vehicle, which is given by the maximum value of $U_{\infty j-2} - U_{\infty j-1}$ at $x = \Delta x/2$ (U_∞ is the average traffic velocity)
- C_j: the constant introduced in (4.61), which determines the value of A in the solution (4.71). It is given in function of $C_D(U_{\infty j})$.

The integral constraint, in the case of interacting vehicles, for the vehicle j in a distribution of N vehicles, is given by:

$$\int_{-\infty}^{\infty}\int_{0}^{\infty} zU_{\infty j}u_j\,dzdy = \overline{\mathrm{C_j}} + \int_{-\infty}^{\infty}\int_{0}^{\infty} \mathrm{z[(U_{\infty j-1} + u_{j-1})u_{j-1}]\,dzdy} = \overline{\mathrm{C'_j}} \tag{4.80}$$

where $\overline{C'_j}$ is a modified constant. The integrals on the right can be calculate easily by considering the Gaussian self-preserving form of the solution for u_{j-1}. Using the Prescription (4.67) for the product $u_0\delta^3$, we obtain:

$$\overline{C'_j} = \overline{C_j} + \overline{C_{j-1}} + 16\sqrt{\pi}\gamma^3 H^3 \Lambda_1^2 U_{\infty j-1}^2 A_{j-1}^6 \left(\frac{\Delta x}{2h}\right)^{-3/4} \tag{4.81}$$

where Δx is the distance between two consecutive vehicles. The velocity and Turbulence solutions (4.71), (4.72) and (4.73) for the vehicle j are thus modified by considering an A_j given by using the modified constant $\overline{C'_j}$ in the Form (4.70):

$$A_j^4 = \frac{\overline{C'_j}}{\gamma^3 h^3 U_{\infty j}^2 (32\pi)^{1/2}\Lambda_1} \tag{4.82}$$

This procedure must be iterated for each vehicle in the distribution. The mean quantities (4.74) and (4.75) represent the case of non-interacting vehicles when using a unique value of the constant A for each vehicle, and the case of interacting vehicles when using the values A_j given in Equation (4.82). This method let us calculate the traffic produced turbulence in the case of interacting and non interacting vehicles, and the results should be compared with the empirical parametrizations (3.30).

We note here that the solutions (4.71), (4.72) and (4.73), obtained in correspondence to the boundary conditions (4.58), i.e. for the case of an open street geometry, can be used to describe the canyon geometry too. This is due to the fact that the self-preserving form of the solutions introduces a scaling of the variables with the wake thickness parameter δ; since this parameter is small compared to the street dimensions L, V and W, any finite boundary in the y direction is effectively moved to infinity. The fact is that the Gaussian solutions in Equation (4.71) decays rapidly moving in the y direction away from the street centerline, and is practically 0 for $|y| > 3$ (see Figure 23). Treating the canyon case with the imposition of no-slip or logarithmic boundary conditions at the canyon lateral walls (at $y = \pm W/2$) in the context of an algebraic Turbulence model would require a domain decomposition, as those introduced in the study of the canyon solutions in the previous paragraphs, in order to consider anisotropy of the Reynolds stress tensor. We will use the solutions (4.71), (4.72) and (4.73) to derive the convection and the eddy diffusivity terms in the formulation of

the dispersion models introduced in Section 3.5. The solutions of Equations (4.57) for the unsteady case, corresponding to the description of the far-wake development of an accelerating vehicle, can be treated through the method of the characteristics [Morse, Feshbach, 1953] (in the steady case no initial conditions for the parameter on the characteristics curves is given, so the method cannot be used). Anyhow, the presence of the algebraic eddy diffusivity complicates the procedure. We will treat this approach in future investigations. In this study, the effect of the vehicle acceleration enters only in the determination of the near-wake Turbulence and in the corresponding parametrization of the resuspension factor, obtained through numerical simulations.

Let us finally introduce a far-wake solution of the algebraic Turbulence model which matches with the logarithmic law of the wall for $\zeta \to 0$, in order to perform the $k-\omega$ model calibration, as explained in Section 3.4. The process of calibration consists in comparing the spreading rate in the z direction (defined as the arithmetic average of the values of ζ where the velocity defect at the centerline is half its maximum value) calculated through the analytical solutions with that calculated through the numerical solutions of the System (3.22), varying the value of the freestream parameter ω_0. We choose the value that yields the closest spreading rate to that coming from the analytical solution. Note that, since in the full 2− equations Turbulence simulations we are using the logarithmic law of the wall as the boundary condition applied to the first grid cell above the ground, we need to consider an analytical solution which matches with the law of the wall, and logarithmic boundary conditions above the ground for the system (3.22). We have already told that the Prandtl Prescription of the eddy viscosity for the wake boundary layer (4.60) cannot produce analytical solutions which matches with the logarithmic law of the wall. A Prandtl mixing length prescription of the same type as that introduced in Table 17 for the case of the canyon with a longitudinal freestream flow must be introduced. We thus make the positions:

$$\begin{cases} u = AU_\infty u_0(\chi) f[\zeta] g[y] \\ \nu_T = \gamma U_\infty u_0(\chi) \zeta \delta(\chi) \end{cases} \tag{4.83}$$

which substitute the Positions (4.59) and (4.60). Note that we have not introduced the scaling in the y variable, since we are not interested in the behaviour of the solution near the canyon vertical walls and in order to avoid the introduction of anisotropy of the eddy viscosity. We are imposing homogeneous Dirichlet boundary conditions at $y = \pm W/2$. Remember that the system (3.22) is integrated over a rectangle. As we have already told, a finite value of y corresponds effectively to an infinite value of η. Inserting

the Positions (4.83) inside the first equation of the System (4.57), we obtain:

$$\frac{1}{\delta^2}\left[\frac{f''}{f}+\frac{1}{\zeta}\frac{f'}{f}+\frac{\delta'}{h\gamma u_0}\frac{f'}{f}-\frac{u_0'\delta}{h\gamma u_0^2}\frac{1}{\zeta}\right]=\frac{g''}{g} \tag{4.84}$$

Separated solutions in the ζ and y variables exists only if the term on the right hand side is zero (otherwise, all the terms are mixed with functions of the χ variable, unless $\delta =$ constant, which is not physically acceptable). We can thus choose linear solutions for the component $g(y)$, and divide the domain in two symmetric parts, one for $0 \leq y \leq W/2$, for which:

$$g(y)=\frac{W/2-y}{W/2},$$

and one for $-W/2 \leq y \leq 0$, for which:

$$g(y)=\frac{W/2+y}{W/2}$$

With these choices $g = 1$ at the centerline. Anyhow, the choice of the function g is unimportant, since we are interested in the solutions in the ζ variable. Note that this is not equivalent to solve a $2-$dimensional problem, cause in two dimensions the Relation (4.64) and the Relations defining the constants (4.67) and the correspondin profiles for δ and u_0 should be changed. Now we can use the Relations (4.67) inside Equation (4.84), obtaining the equation:

$$zf''+[1-z]f'-3f=0, \quad \text{with} \quad \mathrm{z}=-\frac{1}{4}\zeta \tag{4.85}$$

This is a Confluent Hypergeometric equation with a logarithmic point at the origin [Morse, Feshbach, 1953]. The solution of Equation (4.85) which goes to zero at ∞ and has a logarithmic component for $z \to 0$ is the Confluent Hypergeometric function of the second kind $G(a,c,z)$:

$$G(a,c,z)=e^{i\pi a}\frac{\Gamma(c)}{\Gamma(a)}\left\{\frac{\Gamma(1-c)}{\Gamma(1-a)}\left[e^{-i\pi c}+\frac{\sin\pi(a-c)}{\sin\pi a}\right]{}_1F_1(a,c,z)\right.$$
$$\left.-2\frac{\Gamma(c-1)}{\Gamma(c-a)}z^{1-c}{}_1F_1(a-c+1,2-c,z)\right\}$$

where in our case $a = 3$, $c = 1$. The singularities in the Γ terms indicate a logarithmic divergence and the fact that the two Confluent Hypergeometric functions on the right hand side are not linearly independent for $c \in \mathbb{N}$; the function $G(a,c,z)$ must be calculated using de l'Hopital theorem, as done in the Appendix for the case of the Hypergeometric functions. In particular, we have:

$$G(a,c,z) \to 2\log z+2\psi(a)-i\pi \quad \text{for} \quad \mathrm{z}\to 0\,\text{and}\,\mathrm{a}=\mathrm{n}\in\mathbb{N}>0 \tag{4.86}$$

where $\psi(a)$ is the logarithmic derivative of $\Gamma(a)$. Note that, when the argument of the logarithm is $-z$, the pure imaginary term $-i\pi$ in the square bracket is cancelled out. If we apply the Kummer relation to the Solution (4.86), to find another linearly independent solution, we obtain a function truncating to a polynomial of the second order, which diverges at Infinity. The only other linearly independent solution which goes to zero at infinity is ${}_1F_1(a,c,z)$, when $z<0$, which is equal to 1 at $z=0$. The general solution for $f[\zeta]$ is thus:

$$f[\zeta] = \Lambda_1 G\left(3,1,-\frac{1}{4}\zeta\right) + \Lambda_2\, {}_1F_1\left(3,1,-\frac{1}{4}\zeta\right) \tag{4.87}$$

where Λ_1 and Λ_2 are constants to be determined in the context of the matching procedure with the logarithmic law at the wall, and imposing the condition that $f \leq 1$. Let us start from the matching step. Assuming that:

$$u_* = |A| U_\infty u_0,$$

(this is the value we have used to determine the first grid cell dimensions near the road boundary in our numerical simulations of the Ahmed body wake, as explained in Section 3.4), and introducing the wall scaled variable:

$$z^+ = \frac{u_* z}{\nu} = \frac{u_* \delta}{\nu}\zeta = \mathrm{Re}_\delta\, \zeta,$$

the matching, to leading order, becomes:

$$\left[\frac{1}{k}\log z^+ + C\right] - \left[-\Lambda_1(2\log\zeta - 2\log 4 + 2\psi(3)) - \Lambda_2\right] \to 0 \quad \text{for} \quad \mathrm{z}^+ \to \infty,\ \zeta \to 0 \tag{4.88}$$

Thus we have:

$$\begin{cases} \Lambda_1 = -\dfrac{1}{2k} \\ \\ C = -\dfrac{1}{k}\log \mathrm{Re}_\delta - \dfrac{1}{\mathrm{k}}\log 4 + \dfrac{1}{\mathrm{k}}\psi(3) - \Lambda_2 \end{cases} \tag{4.89}$$

which shows that C is a function of the Reynolds number based on the wake thickness parameter and the friction velocity in the case of the viscous sublayer associated to a vehicle far-wake. To determine the value of Λ_2, we observe that the term $-(1/2k)G(3,1,-\frac{1}{4}\zeta)$ has a relative maximum for $\zeta \sim 1.6$, with a value of ~ 0.8. Since the term ${}_1F_1(3,1,-\frac{1}{4}\zeta)$ is decreasing from $\zeta = 0$, and it has value 0.18 in $\zeta = 1.6$, we have:

$$f[\zeta] \leq 1 \longleftrightarrow 0.8 + \Lambda_2 \cdot 0.18 = 1 \to \Lambda_2 = 1.11 \tag{4.90}$$

The Solution (4.87) becomes:

$$f[\zeta] = -1.22\, G\left(3, 1, -\frac{1}{4}\zeta\right) + 1.11\, {}_1F_1\left(3, 1, -\frac{1}{4}\zeta\right) \tag{4.91}$$

In Figure 25 we compare the profile of the Solution (4.91), which we call $f_{\log}[\zeta]$, with the profile of the Solution (4.69) at the centerline ($\eta = 0$), which we call $f_0[\zeta]$.

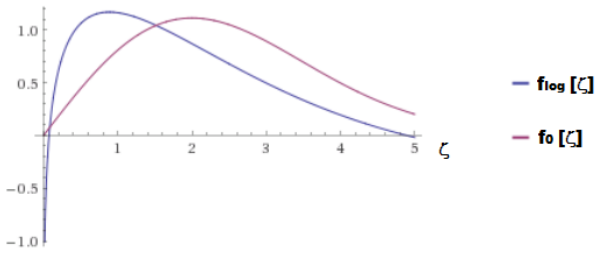

Figure 25: Plotting of the profiles of the Solution (4.91), $f_{\log}[\zeta]$, and of the Solution (4.69) at the centerline ($\eta = 0$), $f_0[\zeta]$.

The different behaviour of the two solutions near $\zeta = 0$ is clearly shown. We also note a translation of the maximum value of the perturbation term from $\zeta = 2$, in the case of the Solution $f_0[\zeta]$ (4.69) (the maximum is at the centerline ($\eta = 0$)), to $\zeta \sim 0.8$, in the case of the Solution $f_{\log}[\zeta]$ (4.91). The spreading rate in the z direction for the $f_{\log}[\zeta]$ solution is equal to 1.59. The spreading rate in the z direction for the $f_0[\zeta]$ solution is equal to 2.3. The spreading rate for the $f_0[\zeta]$ solution is thus 44.6% higher than that associated to the analytical solution which matches with the logarithmic law of the wall. We now show the results for the calibration of the $k-\omega$ Turbulence model. In Figure 26 we compare the profile of $f_{\log}[\zeta]$ with the profiles of the solution of the System (3.22) at the centerline ($\eta = 0$), which we call $f_\omega[\zeta]$, for different values of the freestream parameter ω_0.

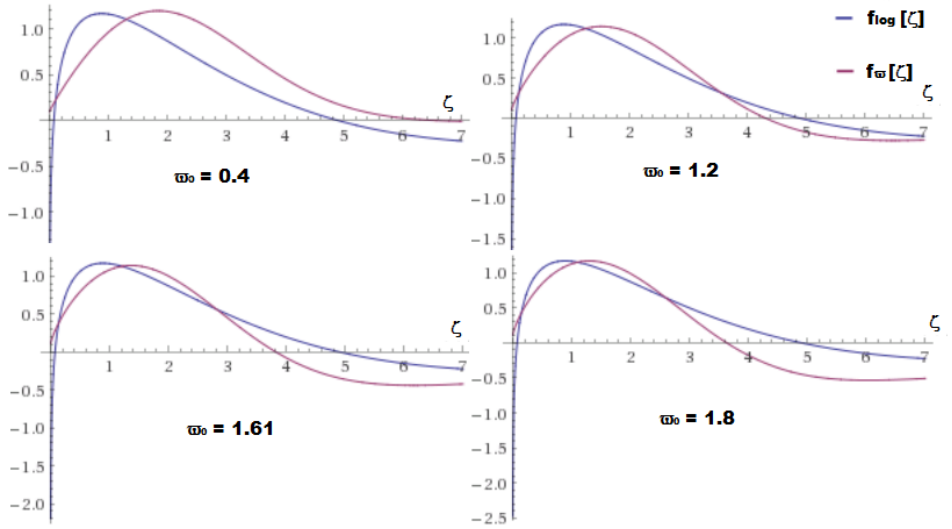

Figure 26: Plotting of the profiles of the Solution (4.91), $f_{\log}[\zeta]$, and of the solutions of the System (3.22) at the centerline ($\eta = 0$), $f_\omega[\zeta]$, for different values of the freestream parameter ω_0.

We have computated the solution of System (3.22) while taking a parametric sweep on the freestream value of the ω_0 parameter; in Figure 26 we show the plot of the solutions for four different values of ω_0. The case $\omega_0 = 0.4$ corresponds to the optimal choice for the ω_0 value, reported in Ref. [Wilcox, 1998], in the case of $2-$ dimensional free-shear far-wake structure (i.e. a wake structure without the solid boundary at $z = 0$). Note that the solution $f_\omega[\zeta]$ does not diverges logarithmically for $\zeta \to 0$. This is due to the fact that, according to the Matching (4.88)-(4.89), we impose a boundary condition at the road boundary:

$$f_\omega[\zeta] = -\frac{1}{2k}\log\left(\frac{100\nu}{u_\tau \delta} + \zeta\right) \quad \text{for} \quad \zeta \to 0,$$

considering the boundary as effectively placed in the logarithmic layer, at $z^+ \sim 100$. The influence of the different vehicle geometries is thus represented, in the search of a self-preserving solution for the far-wake structure solving the System (3.22), by the value of z at wich the logarithmic layer is placed (the parameters u_τ and δ in the boundary condition depend on the constant A, which depends on the drag coefficient C_D). We choose to consider the case of an Ahmed body with a 40° rear slant angle, representing an LDV geometry, which is the case considered in the simulations with the $k-\omega$ Turbulence model. In Table 22 we report the spreading rates calculated from the solutions corresponding to the values of ω_0 reported in Figure 26, showing the relative errors of the estimations with respect to the spreading rate calculated from the Solution $f_{\log}[\zeta]$.

Spreading Rate			
ω_0	$f_{\log}[\zeta]$	$f_{\omega}[\zeta]$	% error
0.4	1.59	2.2	38%
1.2	1.59	1.73	8%
1.61	1.59	1.59	0%
1.8	1.59	1.5	−5.6%

Table 22: Values of the spreading rate corresponding to the values of ω_0 reported in Figure 26, showing the relative errors of the estimations between the values calculated from the Solution $f_{\omega}[\zeta]$ and the value calculated from the Solution $f_{\log}[\zeta]$.

We thus calibrate the $k-\omega$ model, used for the Turbulence simulations in the case of strong boundary layer separation on the rear slant face of the Ahmed body, choosing a boundary condition for ω, at the top plane horizontal boundary of the domain, given by:

$$\omega_0 = 1.61$$

4.2 Turbulence simulations

Canyon simulations. In order to verify the theoretical assumptions and the analytical solutions introduced in Section 4.1, we compare here the corresponding results with the results of the numerical simulations, obtained within the procedures described in Section 3.4.

In Figure 27 we show the simulation results for the flow topology obtained in the case of a symmetric street canyon with aspect ratio $H/W = 1$, and $W = 12m$, for different values of the external angle $\theta_\infty = 0$, $\pi/6$, $\pi/3$, and a freestream wind intensity of $1m/s$. The external angle is defined as the angle between the freestream wind direction and the street axis; $\theta_\infty = 0$ corresponds to a wind parallel to the street.

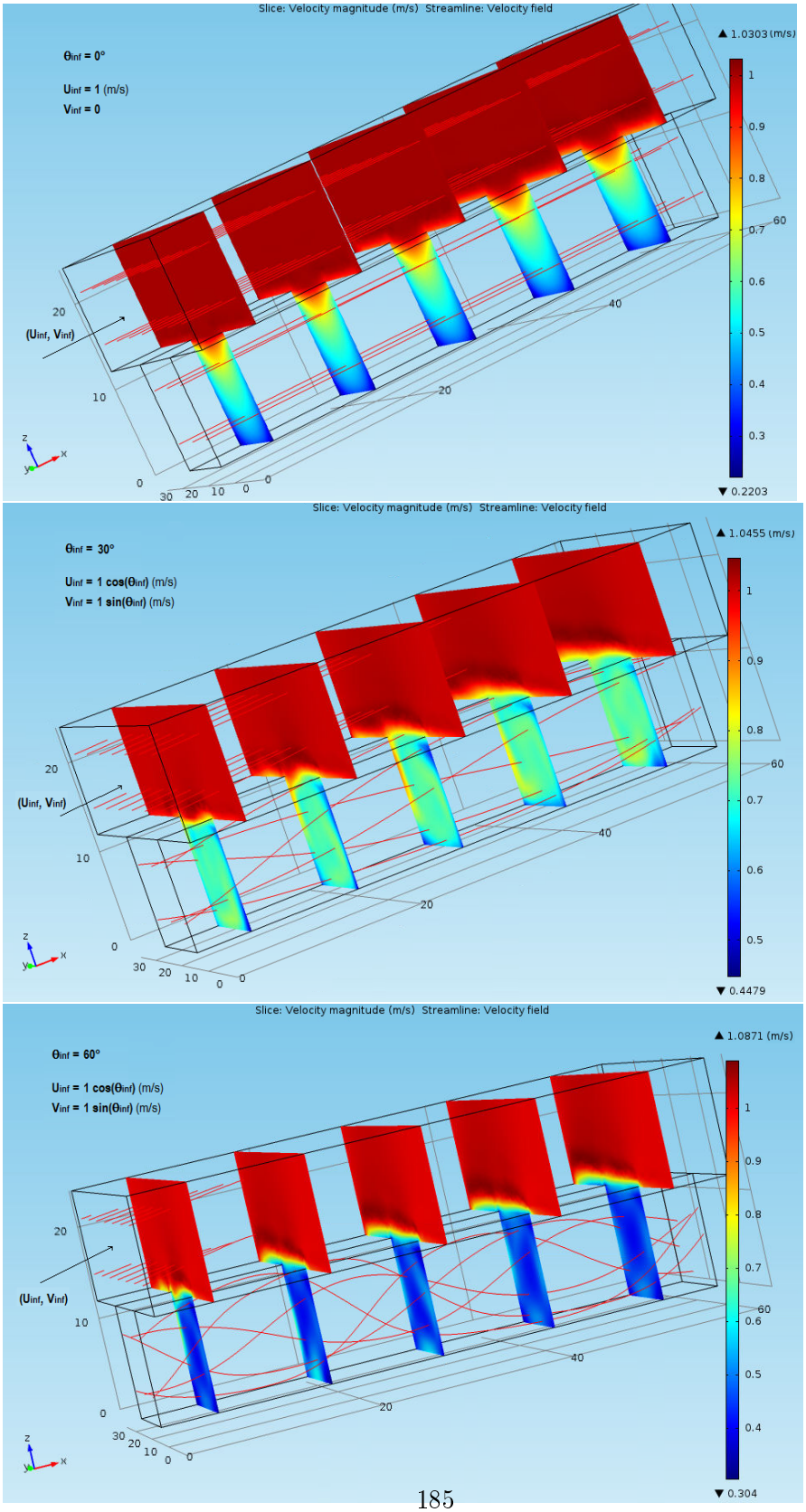

Figure 27: Plotting of the velocity magnitude (on the slice cross-sectional planes) and of the streamlines of the simulated velocity field, in the case of a symmetric street canyon with aspect ratio $H/W = 1$, and $W = 12m$, for different values of the external angle and a freestream wind intensity of $1m/s$. First panel: $\theta_\infty = 0$. Second panel: $\theta_\infty = \pi/6$. Third panel: $\theta_\infty = \pi/3$.

We see that for $\theta_\infty \neq 0$ the streamlines within the street tend to form an irregular helicoidal pattern: by direct observation of the streamlines topology we can see that the wind direction is closer to the axis of the street at the bottom of the street than it is at the top, confirming the simulation results reported in Ref. [Soulhac et al., 2008]. The helicoidal pattern is stronger and more defined in the case of $\theta_\infty = 60°$.

In Figures 28, 29 and 30 we show the velocity contour profiles, for the v and the w components on a transversal plane at the middle of the canyon domain, in the case of $H/W = 1$, for the values of the external angle $\theta_\infty = \pi/6$, $\pi/3$, $\pi/2$, and a freestream wind intensity of $|U_{fs}| = 1m/s$. The transversal and vertical velocity components are normalized with $V_\infty = |U_{fs}| \cdot \sin\theta_\infty$ as the reference velocity component.

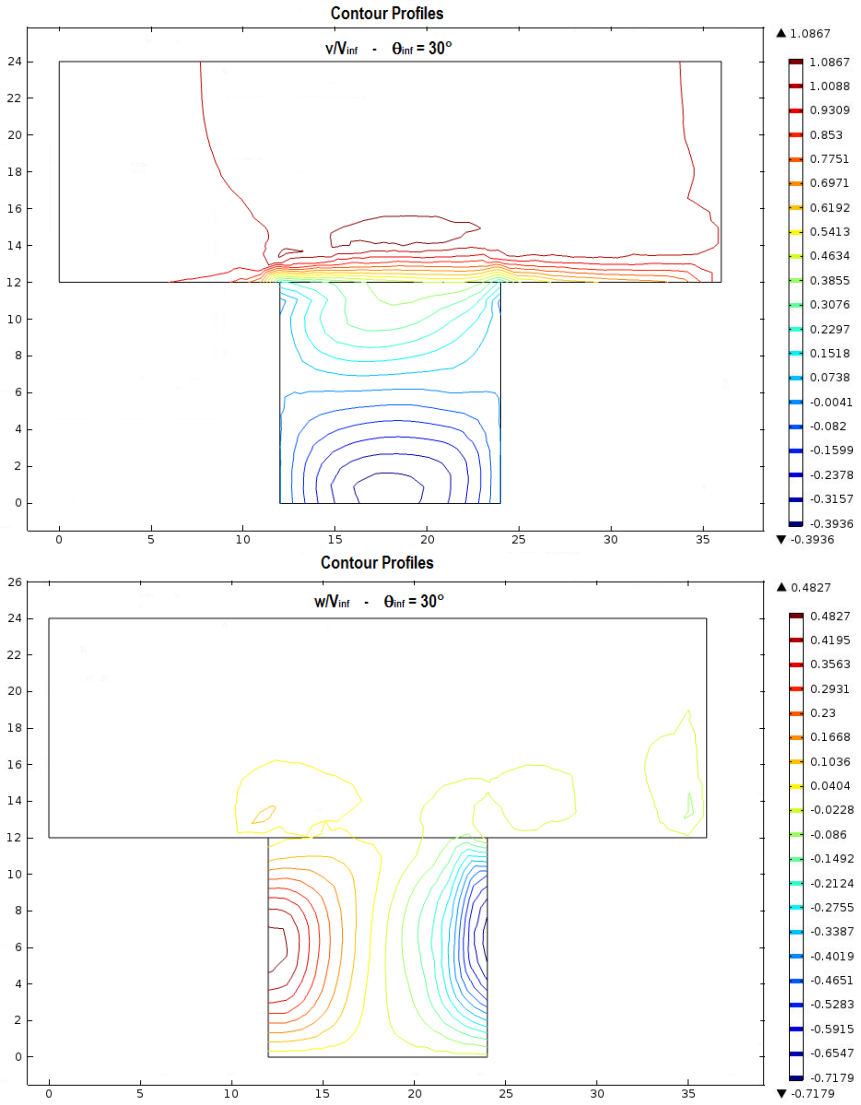

Figure 28: Plotting of the velocity contour profiles, for the v and the w components on a transversal plane at the middle of the canyon domain, in the case of $H/W = 1$, for the values of the external angle $\theta_\infty = \pi/6$, and a freestream wind intensity of $|U_{fs}| = 1m/s$. The transversal and vertical velocity components are normalized with $V_\infty = |U_{fs}| \cdot \sin\theta_\infty$ as the reference velocity component.

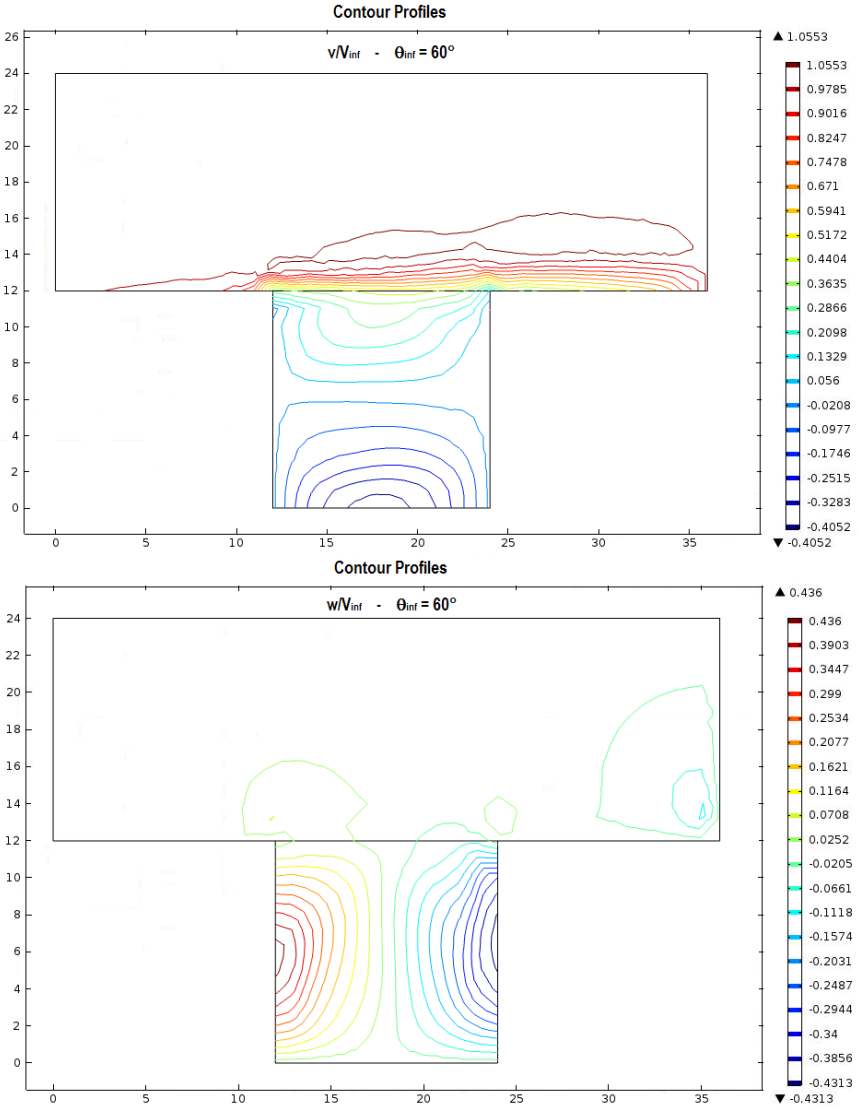

Figure 29: Plotting of the velocity contour profiles, for the v and the w components on a transversal plane at the middle of the canyon domain, in the case of $H/W = 1$, for the values of the external angle $\theta_\infty = \pi/3$, and a freestream wind intensity of $|U_{fs}| = 1m/s$. The transversal and vertical velocity components are normalized with $V_\infty = |U_{fs}| \cdot \sin\theta_\infty$ as the reference velocity component.

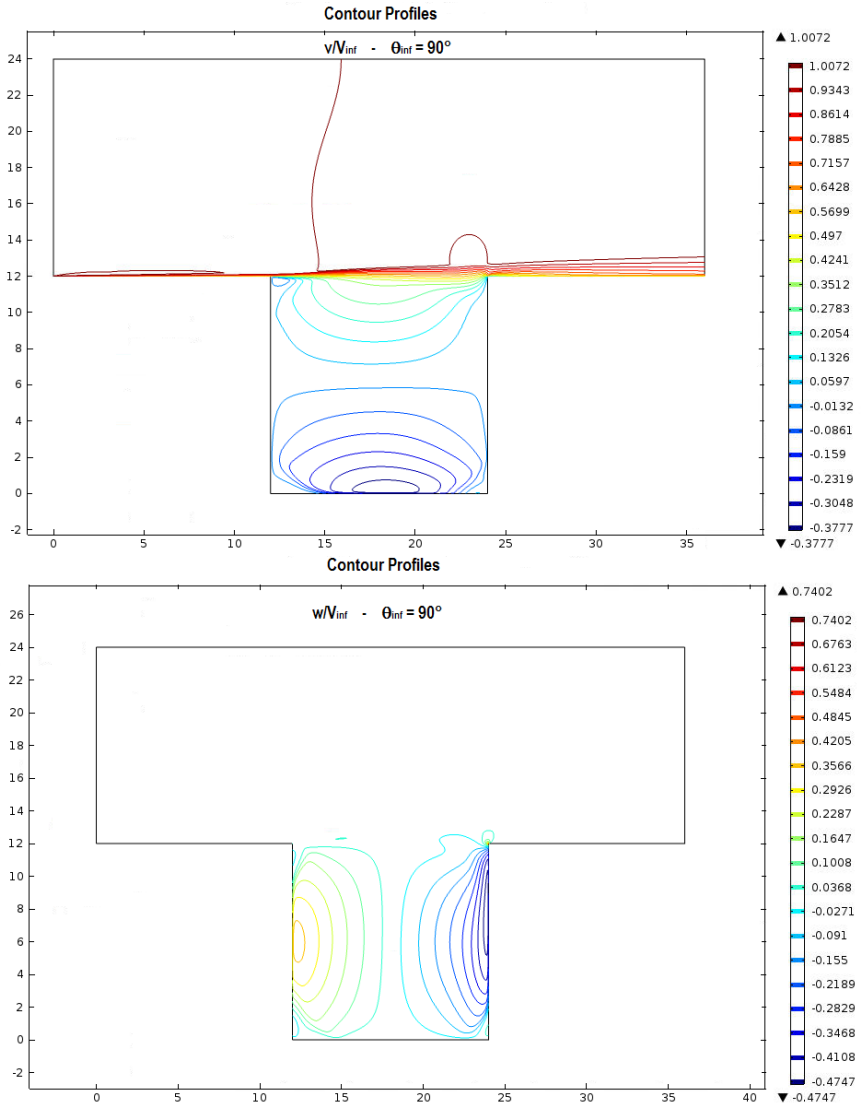

Figure 30: Plotting of the velocity contour profiles, for the v and the w components on a transversal plane at the middle of the canyon domain, in the case of $H/W = 1$, for the values of the external angle $\theta_\infty = \pi/2$, and a freestream wind intensity of $|U_{fs}| = 1m/s$. The transversal and vertical velocity components are normalized with $V_\infty = |U_{fs}| \cdot \sin\theta_\infty$ as the reference velocity component.

Observing the structure and the values associated to the contour lines for the normalized v and w velocity components, we can see that they tend to have the same form and distribution independently of the external wind direction. This confirms the assumption, introduced in Section 4.1, that there is no coupling between the two components v and w and the component u in the case of an homogeneous street canyon in the x direction. Therefore, for any freestream flow direction, the mean flow in the $y^{\smile}z$ plane is identical to that for a flow generated by an external wind orthogonal to the street axis. We must observe that, in the results for an external wind orthogonal to the street axis (Figure 30), the contour profiles for the normalized w component show a lower degree of uniformity than the other two cases. This is probably due to the fact that the imposition of inlet and outlet conditions on the cross-sectional planes above the roof level, for the cases $\theta_\infty = \pi/6$ and $\theta_\infty = \pi/3$, introduces spurious effects of non-homogeneity in the x direction, and a small coupling with the u component, which tends to homogenize the transversal and vertical components, weakening the effect of concentration of vorticity near the canyon vertices.

In Figures 31, 32 and 33 we show the velocity contour profiles and the vertical velocity profiles at the street axis for the longitudinal u component, on a transversal plane at the middle of the canyon domain, in the case of $H/W = 1$. The cases correspond to the values of the external angle $\theta_\infty = 0$, $\pi/6$, $\pi/3$ and to a freestream wind intensity of $|U_{fs}| = 1m/s$. The longitudinal component is normalized with $U_\infty = |U_{fs}| \cdot \cos\theta_\infty$ as the reference velocity component.

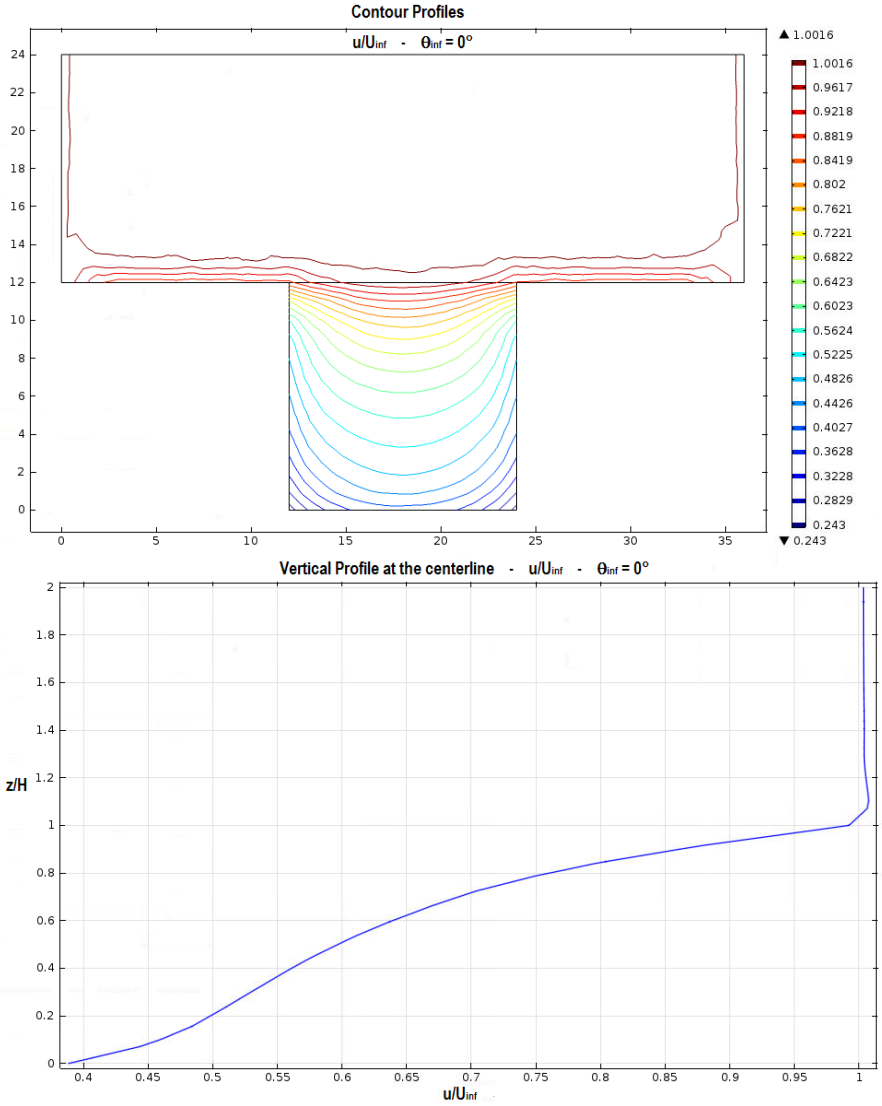

Figure 31: **First panel:** Plotting of the u/U_∞ velocity contour profiles, on a transversal plane at the middle of the canyon domain, in the case of $H/W = 1$, corresponding to the value of the external angle $\theta_\infty = 0$, and a freestream wind intensity of $|U_{fs}| = 1m/s$. **Second panel:** Plotting of the vertical velocity profiles at the street axis for the u/U_∞ component.

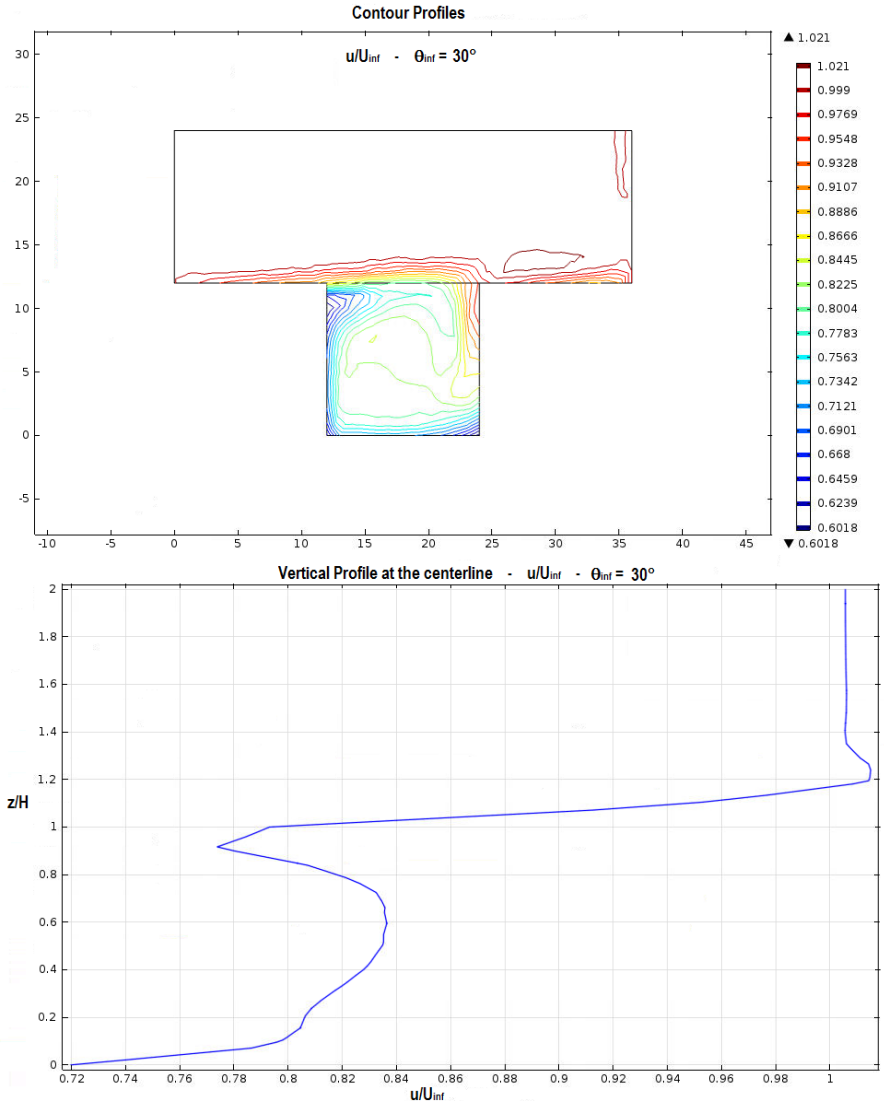

Figure 32: **First panel:** Plotting of the u/U_∞ velocity contour profiles, on a transversal plane at the middle of the canyon domain, in the case of $H/W = 1$, corresponding to the value of the external angle $\theta_\infty = 30°$, and a freestream wind intensity of $|U_{fs}| = 1m/s$. **Second panel:** Plotting of the vertical velocity profiles at the street axis for the u/U_∞ component.

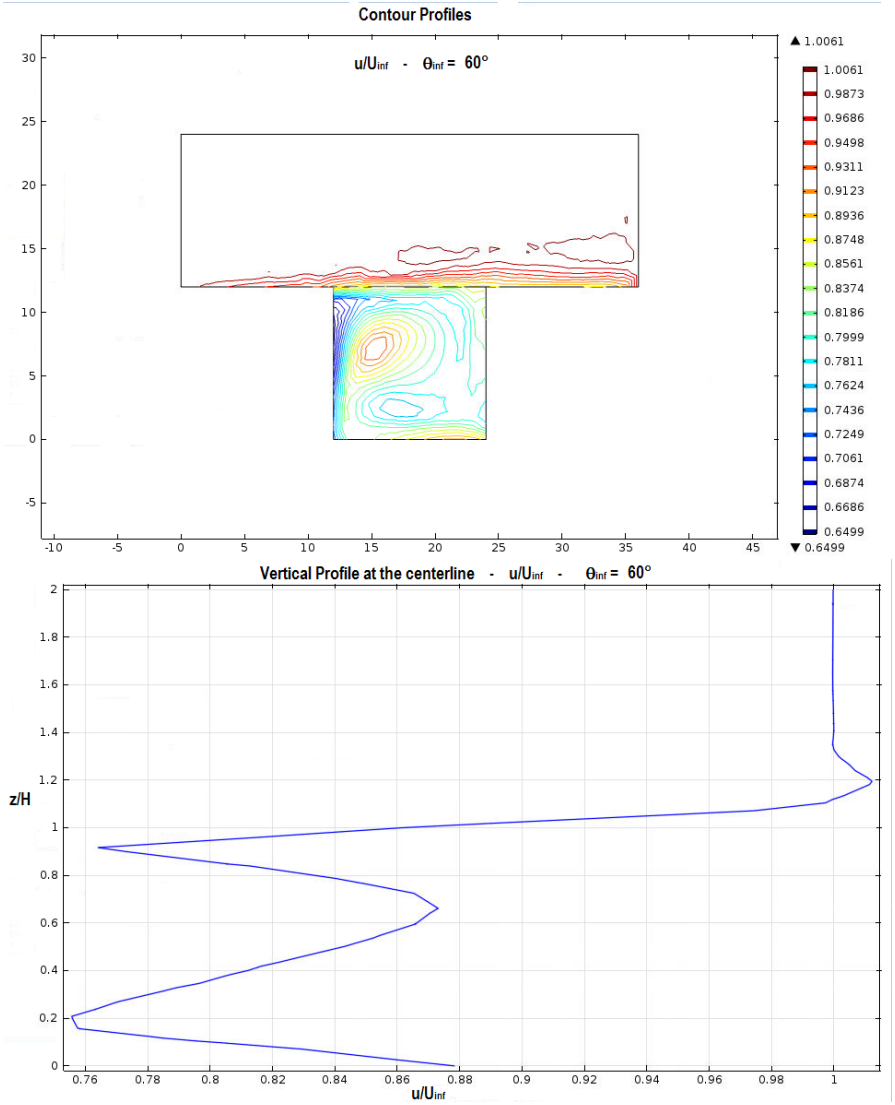

Figure 33: **First panel:** Plotting of the u/U_∞ velocity contour profiles, on a transversal plane at the middle of the canyon domain, in the case of $H/W = 1$, corresponding to the value of the external angle $\theta_\infty = 60°$, and a freestream wind intensity of $|U_{fs}| = 1m/s$. **Second panel:** Plotting of the vertical velocity profiles at the street axis for the u/U_∞ component.

The velocity contour profiles and the vertical velocity profiles of Figures 31, 32 and 33 clearly show that the flow behaviour of the longitudinal component u is greatly influenced by the non-linear interactions with the transversal and the vertical components, when the external freestream is not parallel to the street axis. Note that, due to the imposition of the logarithmic behaviour at the road boundary, the velocity does not go to zero for $z = 0$. Based on the hypothesis made in Section 4.1, we introduce the spatially averaged mean velocity component $\mathbf{U}_{//}$ (defined by Formula (4.54)). We have supposed that this quantity is independent of the freestream wind direction, depending only on the geometrical parameters of the canyon and on the longitudinal component of the external wind $U_\infty = U_{fs} \cos\theta_\infty$. In Figure 34 we show the simulation results for the values of $\mathbf{U}_{//}/U_\infty$, obtained by integrating the u values on a transversal plane at the middle of the canyon domain, as a function of the external angle θ_∞. We show the values for the case of $H/W = 1$, $|U_{fs}| = 1m/s$ and $\theta_\infty = 0$, 15, 30, 45, 60, 75 °.

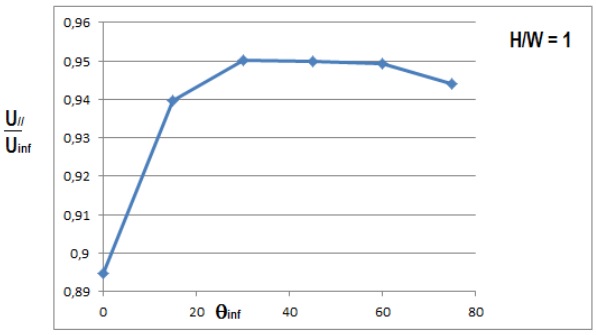

Figure 34: Values of $\mathbf{U}_{//}/U_\infty$, obtained by integrating the u values on a transversal plane at the middle of the canyon domain, as a function of the external angle θ_∞. The reported values correspond to the case of $H/W = 1$, $|U_{fs}| = 1m/s$.

We can observe that $\mathbf{U}_{//}/U_\infty$ is almost independent of the external wind direction (a spurious effect of dishomogeneity in the x direction is still present), in conformity with the hypothesis assumed in Section 4.1. This fact enforces the choice of the introduction of the parameter $\mathbf{U}_{//}$ in the operational dispersion models (see Section 3.5), which is used to express an average effect of advection and turbulent viscosity in the longitudinal direction for freestream flows with arbitrary angles relative to the street axis.

We now compare the simulation results with the analytical results obtained in Section 4.1. In Figure 35 we plot the longitudinal velocity con-

tours of the analytical solution obtained from Formula (4.17), in the case of $H/W = 1$ and $|U_{fs}| = 1m/s$, in the Regions **1** and **2** (defined in Figure 20). We do not show the profiles relative to the solution obtained from Formula (4.14): due to the fact that the solutions of Equation (4.9), for $c \in \mathbb{N} > 0$, are truncating, the effect of the logarithmic divergence for $\eta \to 0$ is too strong for the lower values of the eigenvalues c, causing an non-physical deflection of the contour lines near the boundaries. A complete solution in terms of an expansion in the eigenfunctions for $c \in \mathbb{N} > 0$ should be considered. This will be treated in future investigations. Here we are interested mainly in the quantity $\mathbf{U}_{//}$, which enters in the formulation of the operational dispersion models. We will show below that the values of $\mathbf{U}_{//}$ given in terms of the Solution (4.14), i.e. given by the Formula (4.55), are satisfactory, when compared to the values given by simulation results.

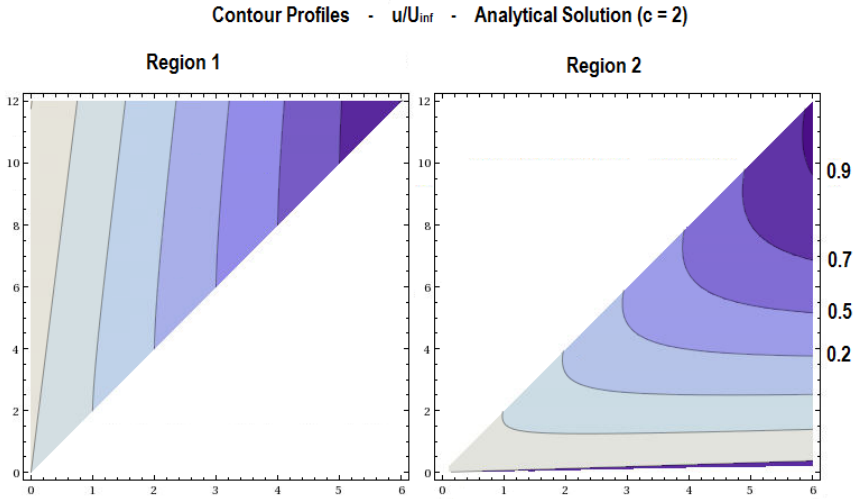

Figure 35: u/U_∞ contours of the analytical solution obtained from Formula (4.17) (corresponding to the eigenvalue $c = 2$), in the case of $H/W = 1$ and $|U_{fs}| = 1m/s$, in the Regions **1** and **2** (defined in Figure 20)

By comparing the contour profiles in Figure 35 with those obtained by means of numerical simulations, reported in Figure 31 (first panel), we see that an excessive deflection of the contour lines is still present in the analytical results for $c = 2$. To show how the things go when considering analytical solutions of the considered Turbulence model, introduced in Section 4.1, for higher values of c, we show in Figure 36 the longitudinal velocity contours in Region **1** for the case $c = 3$.

We can see how the contour curves and the relative values tend to agree more and more with the simulation data shown in Figure 31 (first panel) for increasing values of c. This confirms the validity of algebraic Turbulence model introduced in Section 4.1. An alternative way to proceed, in order

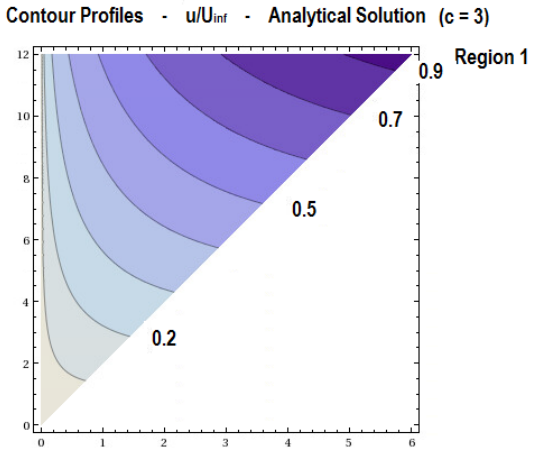

Figure 36: u/U_∞ contours of the analytical solution of Equation (4.9) for $c = 3$), in the case of $H/W = 1$ and $|U_{fs}| = 1m/s$, in the Region **1** (defined in Figure 20)

to avoid the influence of the logarithmic divergence at the walls extended to finite portions of the domain, would be to consider the Solution uniformly valid on the whole domain (4.19). We do not show this procedure here. In Table 23 we show the values of $\mathbf{U}_{///}/U_\infty$, given in terms of the Solution (4.14) ($c = 1$), i.e. given by the Formula (4.55), and compare them to the values given by simulation results, for the cases of aspect ratio $H/W = 0.5$, 1, 1.5, and $|U_{fs}| = 1m/s$, showing the relative errors of the analytical results with respect to the simulation data.

$\mathbf{U}_{///}/U_\infty$	Analytic Solution Equation(4.55)	Simulation Results	%error
$H/W = 0.5$	1.0329	0.9285	+11.24%
$H/W = 1$	0.9469	0.8948	+5.82%
$H/W = 1.5$	0.8997	0.8737	+2.98%

Table 23: Comparison of the values of $\mathbf{U}_{///}/U_\infty$, given by the Formula (4.55), with those given by simulation results, for the cases of aspect ratio $H/W = 0.5$, 1, 1.5, and $|U_{fs}| = 1m/s$, showing the relative errors of the analytical results with respect to the simulation data.

The values of $\mathbf{U}_{///}/U_\infty$ given in terms of the Formula (4.55) agree well with the values given by simulation results. The higher relative error has been found in the case of $H/W = 0.5$.

We now show the simulation results obtained for the case of an external flow V_∞ orthogonal to the street axis, in order to study the flow regimes

associated to street canyons of different aspect ratios. In Figures 37, 38 and 39 the results corresponding to different aspect ratios $H/W = 0.5, 1, 1.5$ (which are typical of Urban geometries) are shown, with different freestream wind intensities $V_\infty = 0.5, 1, 2, 3\, m/s$. The different colours correspond to different intensity of the velocity magnitude. The arrows show the direction of the velocity vector. The arrow length is proportional to the logarithm of the velocity intensity (in order to catch all the scales of the motion, which varies from those associated to the bulk velocity to those associated to the velocity near the stagnation points).

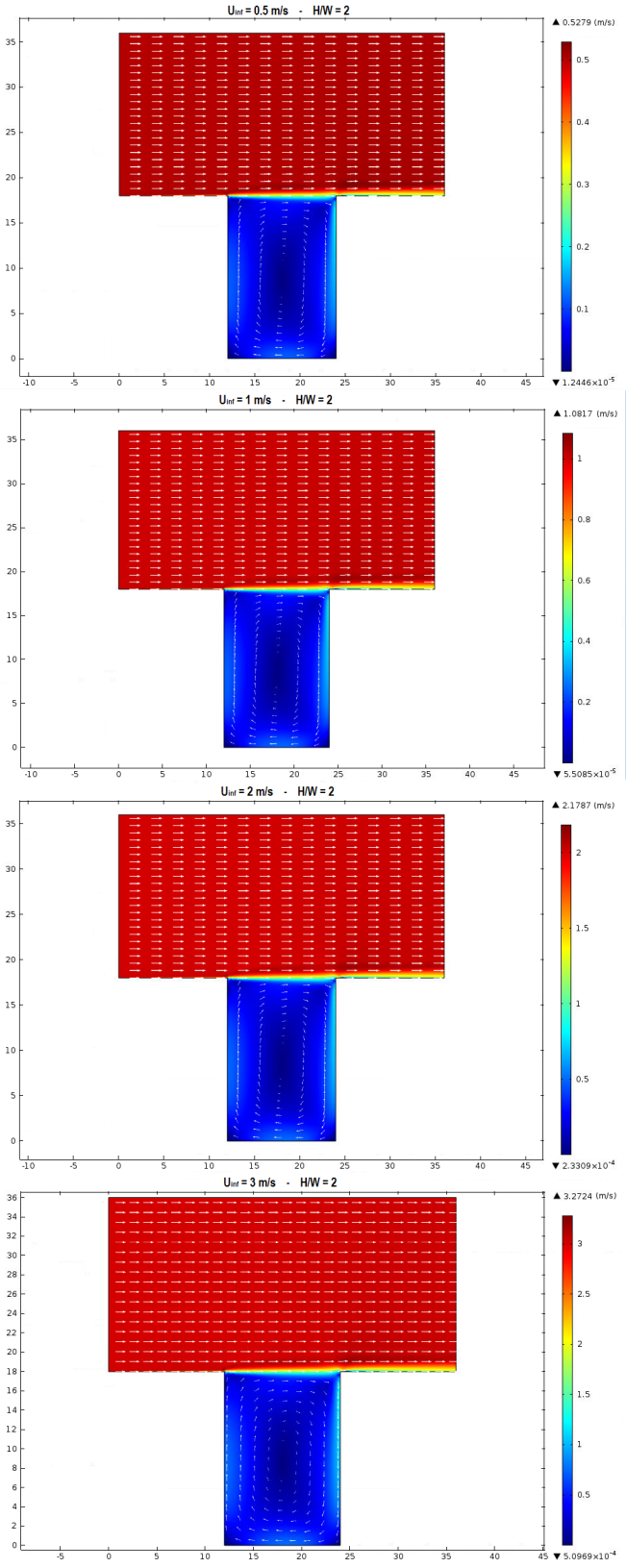

Figure 37: Velocity field structure for the transversal flow in the case of $H/W = 2$ and freestream velocity $V_\infty = 0.5$, 1, 2, $3\,m/s$. The different colours correspond to different intensity of the velocity magnitude. The arrows show the direction of the velocity vector. The arrow length is proportional to the logarithm of the velocity intensity.

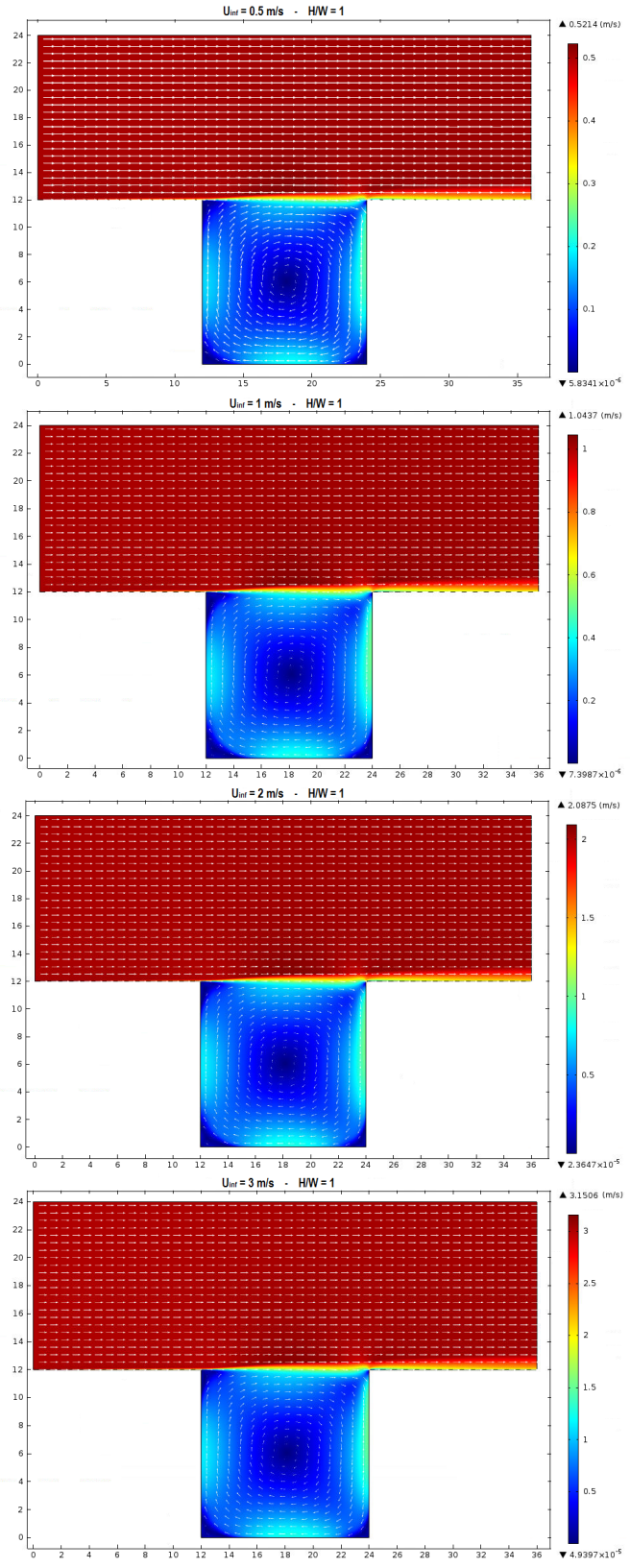

Figure 38: Velocity field structure for the transversal flow in the case of $H/W = 1$ and freestream velocity $V_\infty = 0.5,\ 1,\ 2,\ 3\,m/s$. The different colours correspond to different intensity of the velocity magnitude. The arrows show the direction of the velocity vector. The arrow length is proportional to the logarithm of the velocity intensity.

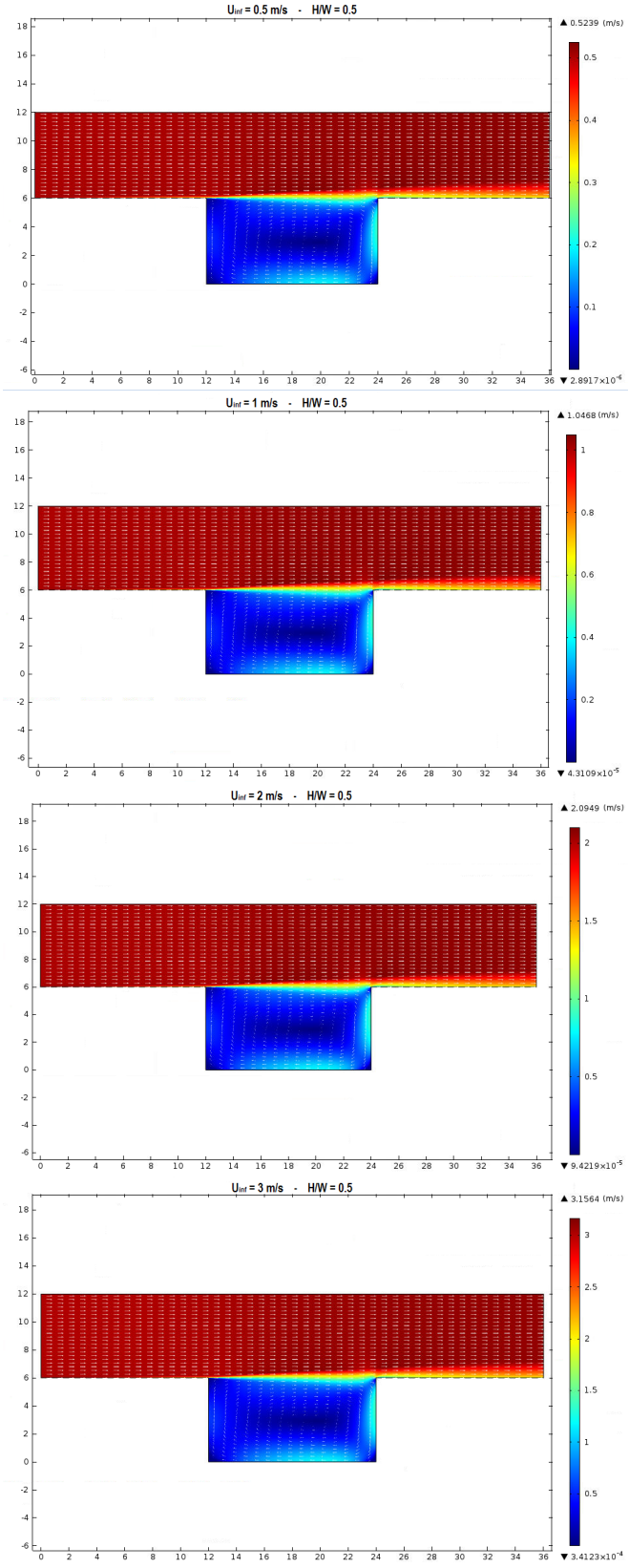

Figure 39: Velocity field structure for the transversal flow in the case of $H/W = 0.5$ and freestream velocity $V_\infty = 0.5$, 1, 2, $3\,m/s$. The different colours correspond to different intensity of the velocity magnitude. The arrows show the direction of the velocity vector. The arrow length is proportional to the logarithm of the velocity intensity.

We can see that in all the cases shown in Figures 37, 38 and 39 the vortex recirculation induced by the external flow is extended to the whole canyon domain (*wake interference* and *skimming flow* regimes). The bulk vorticity is displaced towards the windward side of the street in the case of $H/W = 0.5$;in this case a secondary vortex tends to form near the bottom vertex at the leeward side. This secondary recirculation is anyhow too weak with respect to that shown by wind tunnel results reported in Ref. [Berkowicz, Kearney, 2004]: this is probably due to the numerical stabilization we have added to the numerical formulation of the equations, as discussed in Section 3.4, which dissipates the secondary structures.

In Figures 40 and 41 we show the vertical profiles at the centerline and the horizontal profiles at an height $z = H/2$ of the vorticity ω, normalized with the quantity $\omega_0 = V_\infty/H$ (introduced in Equation (4.27)), for the cases of $H/W = 0.5$, 1, 1.5, and with $V_\infty = 1m/s$.

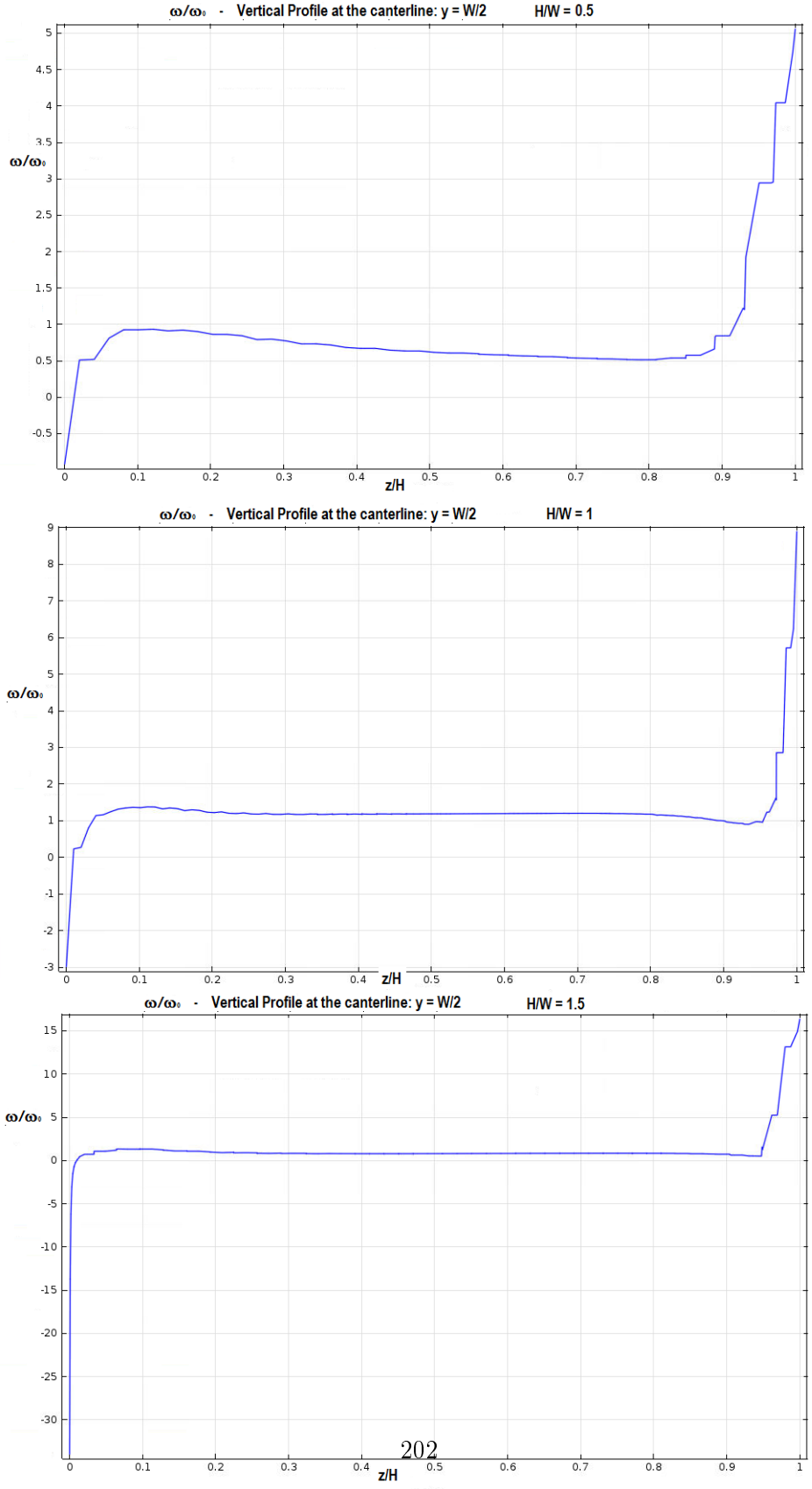

Figure 40: Vertical profiles of ω/ω_0 at the centerline $y = W/2$, with $\omega_0 = V_\infty/H$, in function of z/H, for the cases of $H/W = 0.5$, 1, 1.5, and with $V_\infty = 1m/s$.

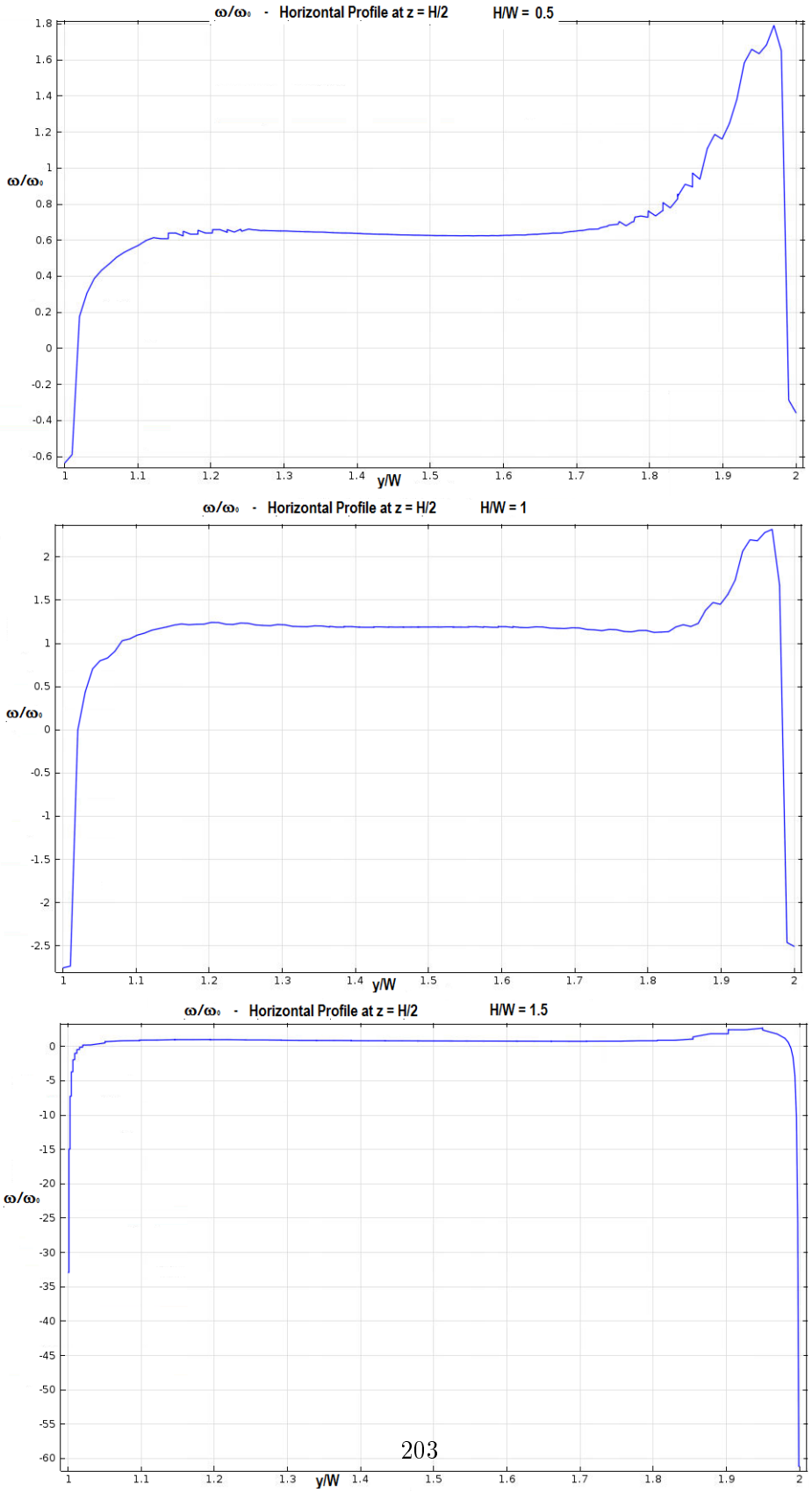

Figure 41: Horizontal profiles of ω/ω_0 at an height $z = H/2$, with $\omega_0 = V_\infty/H$, in function of y/W, for the cases of $H/W = 0.5$, 1, 1.5, and with $V_\infty = 1m/s$.

The profiles shown in Figures 40 and 41, in the cases of $H/W = 1$ and $H/W = 1.5$, clearly confirm the hypothesis that the vorticity field inside the canyon is constituted by a bulk constant value $\omega_0 = V_\infty/H$, plus perturbation terms near the solid boundaries. This is the hypothesis upon which we have based our perturbation analysis in Section 4.1. This hypothesis is not confirmed in the case of $H/W = 0.5$. Note that the perturbation terms are not small, compared with the magnitude of ω_0, at the boundary coordinates, due to the imposition of the logarithmic law boundary conditions at the canyon walls in the simulation models. This effect is not described by the analytical solutions obtained in Section 4.1, which are uniformly valid on the whole domain and do not diverge logarithmically at the wall boundaries. In order to validate the solutions obtained in Section 4.1 for the vorticity field in the case of an orthogonal external stream, reported in Table 20, we consider the perturbation contributions in the vertical and horizontal profiles given in Figure 40 and 41, for the case $H/W = 1$ (second panels), obtained from simulations, and compare them to the perturbation contributions at order ϕ_1 expressed in Table 20. The perturbation contributions from the simulation profiles $\omega_{p,sim}$ are given by the formula:

$$\frac{\omega}{\omega_0} \sim 1 + \omega_{p,sim}.$$

Observing the profiles reported in the second panels in Figures 40 and 41, we see that the constant value of the bulk vorticity throughout the canyon is not exactly $\omega_0 = V_\infty/H$. The perturbation contributions from the analytical solutions $\omega_{p,an}$ are calculated as:

$$\omega_{p,an} = -\omega_{\tau i} \frac{\partial^2 F}{\partial \eta_i^2},$$

where i is the index corresponding to the region of the domain, adjacent to a boundary segment, which influence the solution, and $\omega_{\tau i}$ and $\partial^2 F/\partial \eta_i^2$ are defined in Table 20 and Equation (4.52) respectively. In the case of the vertical profile at the centerline, only the contribution from the regions adjacent to the Segments **BE** and **EC** must be considered, the centerline is placed at an infinite distance with respect to the scaled variables η_{AB} and η_{CD} associated to the vertical segments. Analogously, in the case of the horizontal profile, only the contribution from the regions adjacent to the Segments **AB** and **CD** must be considered, the former near $y = 0$, the latter near $y = W$. In Figures 42, 43, 44 and 45 we report the vertical profiles (at $y = W/2$) and the horizontal profiles (at $z = H/2$) for $\omega_{p,sim}$ and $\omega_{p,an}$, in the case of $H/W = 1$ and $V_\infty = 1m/s$, in a neighbourhood of the respective walls.

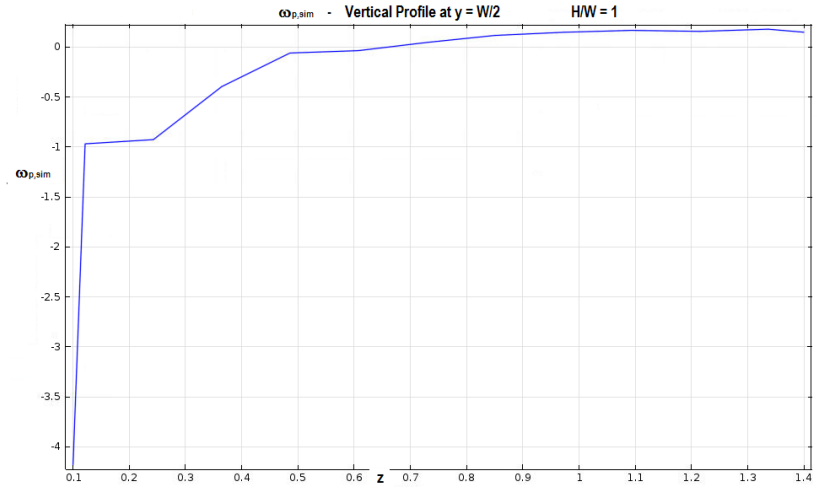

Figure 42: Vertical profile (at $y = W/2$) for $\omega_{p,sim}$, in the case of $H/W = 1$ and $V_\infty = 1m/s$, in a neighbourhood of the road surface.

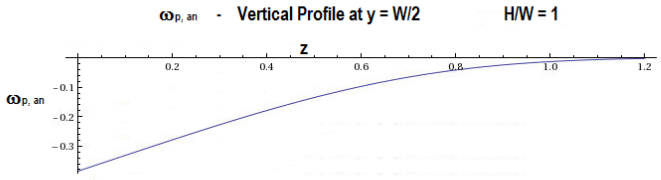

Figure 43: Vertical profile (at $y = W/2$) for $\omega_{p,an}$, in the case of $H/W = 1$ and $V_\infty = 1m/s$, in a neighbourhood of the road surface.

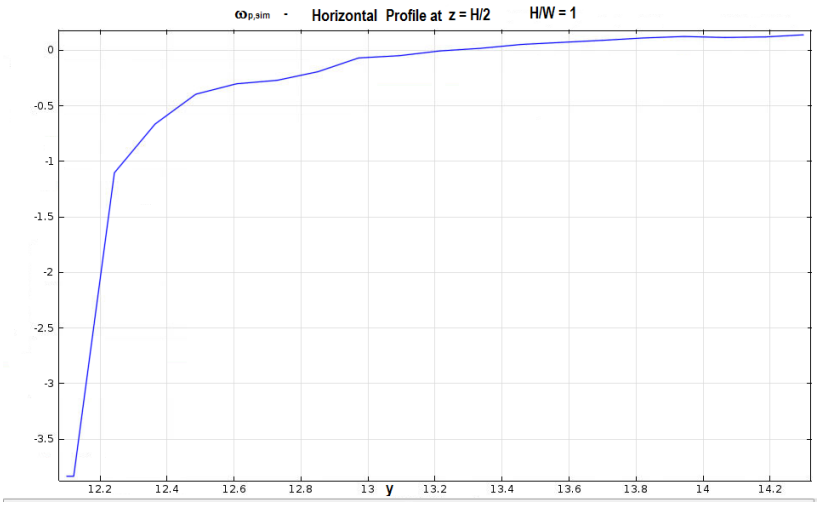

Figure 44: Horizontal profile (at $z = H/2$) for $\omega_{p,sim}$, in the case of $H/W = 1$ and $V_\infty = 1m/s$, in a neighbourhood of the leeward wall. The canyon domain in simulations begins at $y = W$.

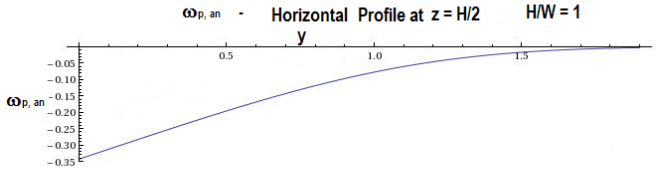

Figure 45: Horizontal profile (at $z = H/2$) for $\omega_{p,an}$, in the case of $H/W = 1$ and $V_\infty = 1m/s$, in a neighbourhood of the leeward wall.

We thus see, from the comparison between the simulation and the analytical profiles, in a neighbourhood of a wall segment, that our analytical solutions reproduce well the perturbation terms near a wall boundary. In particular, the way in which the perturbation goes to zero approaching the center of the domain is well reproduced, predicting a slower approach to the bulk value of vorticity for the horizontal profile; the behaviour near the wall boundary is well reproduced too, except for the effects of the logarithmic layer, which are present in the simulation results but not in the analytical solutions.

Wake simulations. In this Paragraph we show the simulation results for the Turbulence structure generated by vehicles of different categories, with an Ahmed body geometry, moving in an open street or in a canyon street, in correspondence to different driving cycles. We will derive some important parametrization of the flow characteristics, to be used in the models described in the text.

In Figures 46, 47 and 48 we show the wind field structure in the cases of Ahmed body geometry with a rear slant angle of 25°, corresponding to a Sedan vehicle, 40°, corresponding to an LDV, and 0°, corresponding to an HDV, in a street canyon geometry. These correspondences are in terms of the similarity of the topology of the generated Turbulence fields, as explained in Section 3.3, where the dimensions of the selected geometries are defined. We show the case of an external wind flowing at $U_\infty = 40m/s$ (which means that the vehicle is moving with a velocity $-U_\infty$), which is the case studied in the wind tunnel experiments in Ref. [Ahmed, Ramm, 1984]. The different colours refer to the different intensity of the velocity magnitude, plotted in the bulk domain, as well as on transversal planes and on a longitudinal plane at the centerline.

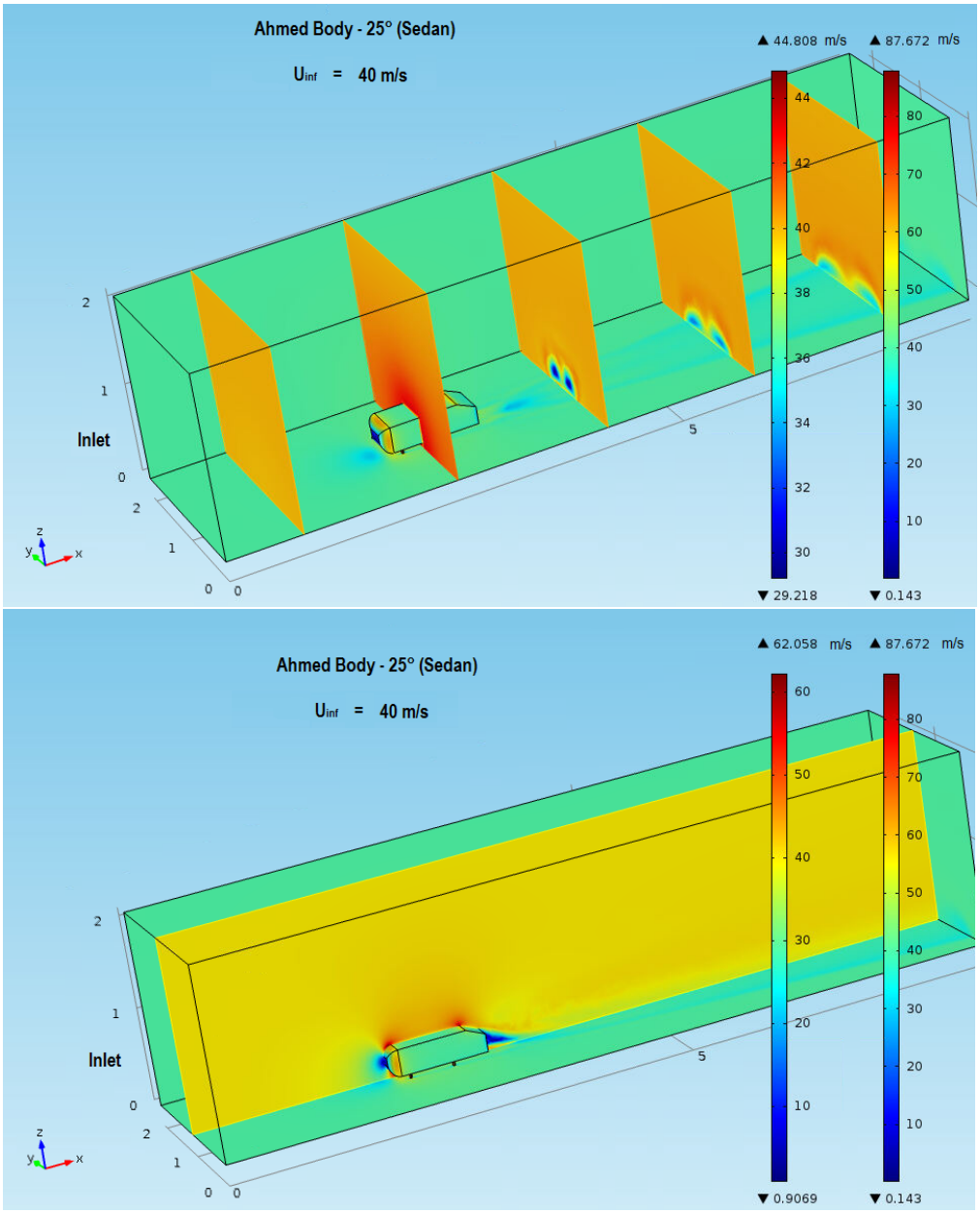

Figure 46: Wind field structure in the case of Ahmed body geometry with a rear slant angle of 25°, corresponding to a Sedan vehicle, for an external wind flowing at $40 m/s$ and a street canyon geometry. The different colours refer to the different intensity of the velocity magnitude, plotted in the bulk domain, as well as on transversal planes (first panel) and on a longitudinal plane at the centerline (second panel).

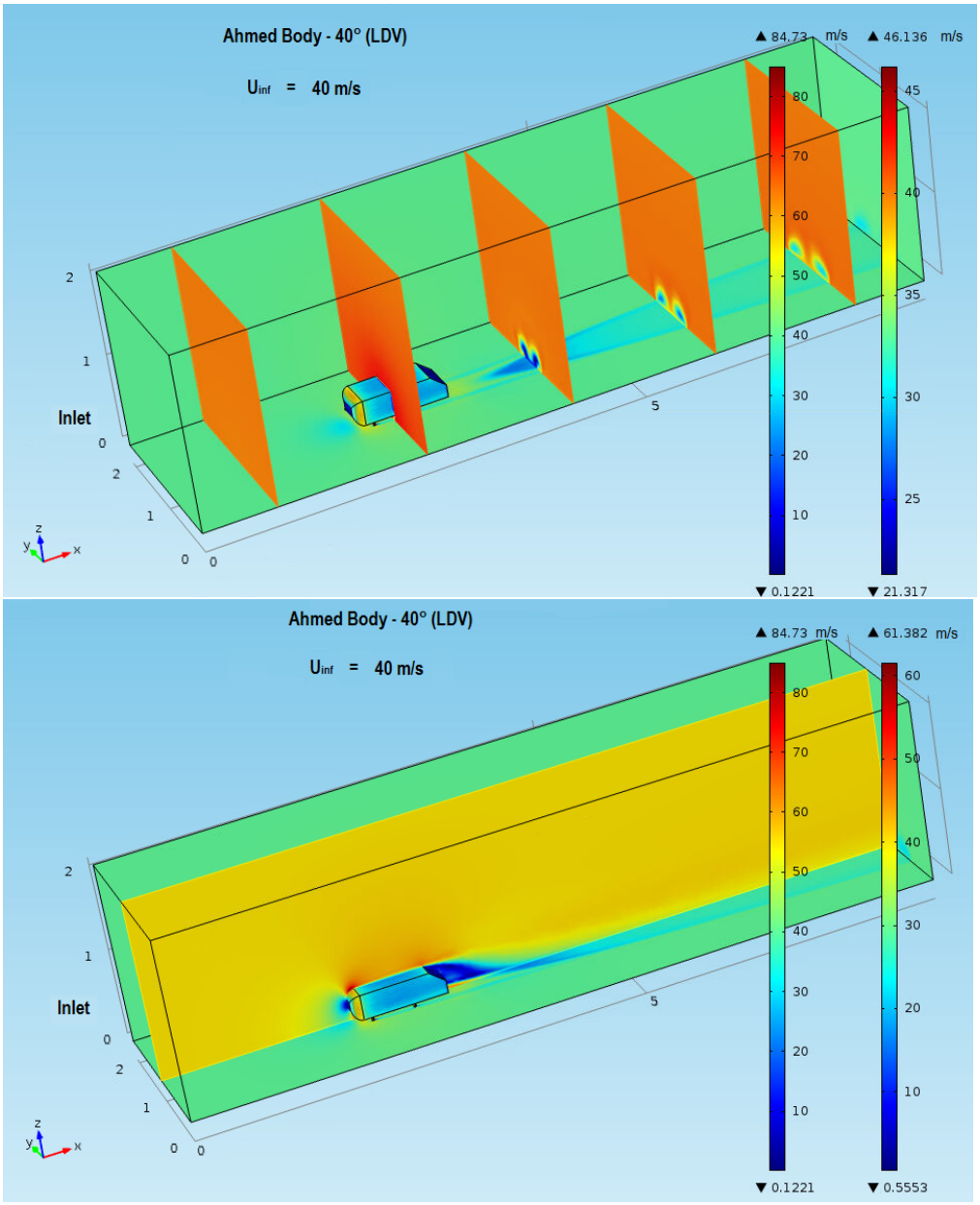

Figure 47: Wind field structure in the case of Ahmed body geometry with a rear slant angle of 40°, corresponding to an LDV, for an external wind flowing at $40 m/s$ and a street canyon geometry. The different colours refer to the different intensity of the velocity magnitude, plotted in the bulk domain, as well as on transversal planes (first panel) and on a longitudinal plane at the centerline (second panel).

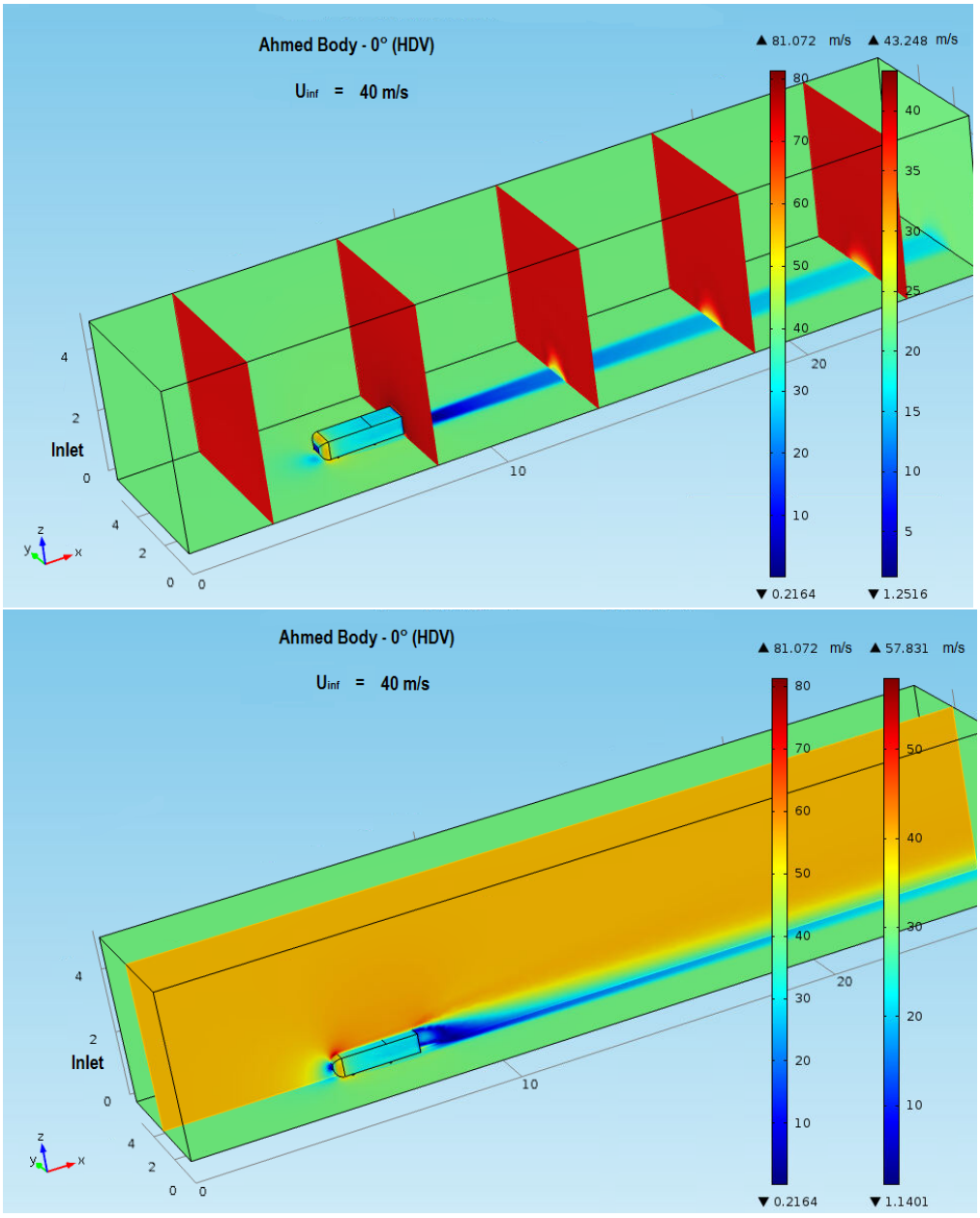

Figure 48: Wind field structure in the case of Ahmed body geometry with a rear slant angle of 0°, corresponding to an HDV, for an external wind flowing at $40 m/s$ and a street canyon geometry. The different colours refer to the different intensity of the velocity magnitude, plotted in the bulk domain, as well as on transversal planes (first panel) and on a longitudinal plane at the centerline (second panel).

We can see from Figures 46 and 47 that the topology of the simulated flow generated by the Ahmed body geometries with rear slant angles of 25° and 40° reproduces the characteristics of the Turbulence structure obtained from the wind tunnel experiments [Ahmed, Ramm, 1984], [Lienhart, Becker, 2003], described in Section 3.4 and in Figure 13: the structure of the wake consists of a separation zone and counter-rotating vortices coming off the slant side edges. In the case of the 25° rear slant angle, strong counter-rotating vortices are present and the flow separates in the middle region of the top edge and reattaches on the slant. In the case of the 40° rear slant angle, the counter-rotating vortices are weaker, and the separation occurs along the entire top and the side edges and there is no reattachment. In the case of the 0° rear slant angle and a geometry with augmented dimensions with respect to the Ahmed body studied in Ref. [Ahmed, Ramm, 1984], no counter-rotating vortices develop besides the vehicle, and the wake zone extends to the whole domain.

Note that we have chosen, to describe the LDV produced Turbulence field, an Ahmed body geometry with a rear slant angle of 40°; results for the 35° case (and a freestream velocity $U_\infty = 40m/s$) are reported in details in Ref. [Ahmed, Ramm, 1984] and [Lienhart, Becker, 2003], with the measured vertical profiles of the stream wise velocity at the rear slant face of the vehicles. Wind tunnel results of the 40° case are not reported in the literature we have studied, except for the values of the drag coefficient corresponding to this case, measured in Ref. [Tran, 2010]. We have chosen to simulate the Turbulence field generated by the 40° configuration, in order to reproduce the results reported in Ref. [Jindal et al., 2005], where a CFD approach with a RANS Turbulence model and an Immersed Boundary Method to resolve the vehicle boundaries has been employed to describe the flow topology generated by a vehicle with a detailed LDV geometry, in the case of $U_\infty = 30m/s$. In a preliminary analysis set up for only the $U_\infty = 30m/s$ case, and by varying the rear slant angle between the values $30° \leq \theta \leq 50°$, we have obtained that the value $\theta = 40°$ reproduces the correct extension of the main recirculation zone behind the rear face obtained in Ref. [Jindal et al., 2005]. In Figure 49 we show the streamlines of the mean velocity field in the center horizontal plane at the half height of the vehicle, as obtained by the numerical simulations in Ref. [Jindal et al., 2005] (left panel) and by our simulations with a calibrated $k - \omega$ Turbulence model in the case of $\theta = 40°$ (right panel).

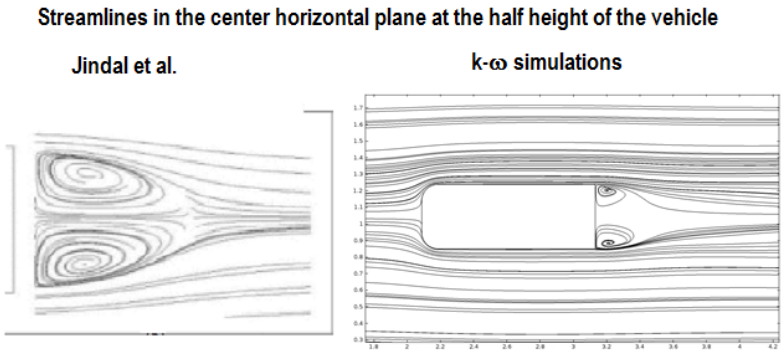

Figure 49: Streamlines of the mean velocity field in the center horizontal plane at the half height of the vehicle, as obtained by the numerical simulations in Ref. [Jindal et al., 2005] (left panel) and by our simulations with a calibrated $k-\omega$ Turbulence model in the case of $\theta = 40°$ (right panel).

We see that the streamwise extension of the main counter-rotating recirculation zones in the center horizontal plane, as obtained in Ref. [Jindal et al., 2005], is correctly reproduced by our simulation results when $\theta = 40°$. The Ahmed body geometry which represent the HDV case has been chosen according to the studies on Heavy vehicles generated Turbulence reported in Ref. [Browand et al., 2009], in which an Ahmed body with $\theta = 0°$ is considered, with dimensions reported in Figure 14.

In Table 24 we show the values of the drag coefficient C_D, defined in Formula (3.20), for the cases of $\theta = 25°$, $40°$, $0°$, and $U_\infty = 40m/s$, obtain by the simulation data, and compare them with the experimental data reported in Figure 13. In the case of $40°$ rear slant angle, we report the values obtained for different calibrations of the $k-\omega$ Turbulence model, corresponding to different freestream values ω_0.

We must observe that in Ref. [Browand et al., 2009] different geometries for the HDV vehicle are considered, in the context of wind tunnel measurments. In particular, a flat parallelepiped geometry (i.e. without the rounded front of the Ahmed body), with the dimensions we have reported in Figure 14, has been considered. A drag coefficient of $C_D = 1.17$ has been measured in this case (at a reference velocity). A Generic Conventional Model (GCM) geometry has been considered too, which is characterized by a front face of a realistic truck and a rounded rear face. The measured drag coefficient corresponding to this configuration (at a reference velocity) is $C_D = 0.62$.

Configuration	C_D simulated	C_D experimental	%error
$25°$ $(k-\epsilon)$	0.282	0.285	-1.05%
$40°$ $(k-\omega)$ $\omega_0 = 0$	0.631	0.26	$+142.69\%$
$40°$ $(k-\omega)$ $\omega_0 = 0.4$	0.404	0.26	$+55.38\%$
$40°$ $(k-\omega)$ $\omega_0 = \mathbf{1.61}$	0.253	0.26	-2.69%
$0°$ $(k-\epsilon)$	0.898	0.96	-6.46%

Table 24: Values of the drag coefficient C_D, for the cases of $\theta = 25°$, $40°$, $0°$, and $U_\infty = 40m/s$, obtain by the simulation data, compared with the experimental data reported in Ref. [Tran, 2010]

When a drag control study is conduced on the GCM geometry, the case in which flat flaps are added to the rear surface at the top and bottom side, when $U_\infty = 40m/s$, is associated to a drag coefficient of $C_D = 0.96$. This is the value to which we compare the result from our simulations.

Numerical accuracy of the simulation results is achieved by imposing to the iteration processes of the solvers to stop when the relative error between two successive iterates is smaller than 0.001. This typically guarantees iteration convergence for the slowly convergent discretized Turbulence systems [Wilcox, 1998]. In Figure 50 we show the convergence graph of the relative error between successive iterates in function of the iteration number, for the case of the $k-\omega$ simulation of the case $U_\infty = 40m/s$. Since we are solving the Turbulence model with a sequentially implicit method, the results for the two segregated groups of variables (u, p) (segregated group 1) and (k, ω) (segregated group 2) are shown. The $k-\omega$ simulations have been characterized by the slowest convergence rates between all our simulations. In order to accelerate the convergence process, we have in some cases (those characterized by too low convergence rates, both for stationary simulations with a pseudo-time advancing scheme and for unsteady simulations) initialized them with an initial solution obtained by a $k-\epsilon$ simulation for the same configuration.

In order to show the grid independence of the simulation results, we have repeated the computations, in the test cases of $U_\infty = 40m/s$ for the three vehicle geometries, with a refinement of the mesh based on the equation residuals, and we have compared the solutions with and without refinement. In Figures 51, 52 and 53 we report the refined meshes and the corresponding

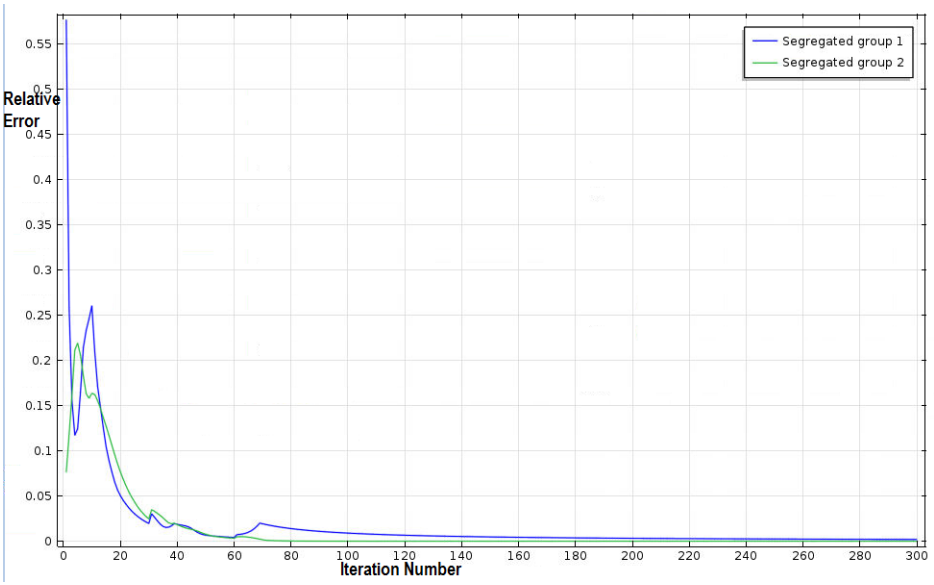

Figure 50: Convergence graph of the relative error between successive iterates in function of the iteration number for the two segregated groups of variables, relative to the case of the $k-\omega$ simulation of the case $U_\infty = 40m/s$.

wind field structures in the cases of rear slant angles of 25°, 40° and 0°, in a street canyon geometry. The different colours refer to the different intensity of the velocity magnitude, plotted in the bulk domain and on transversal planes.

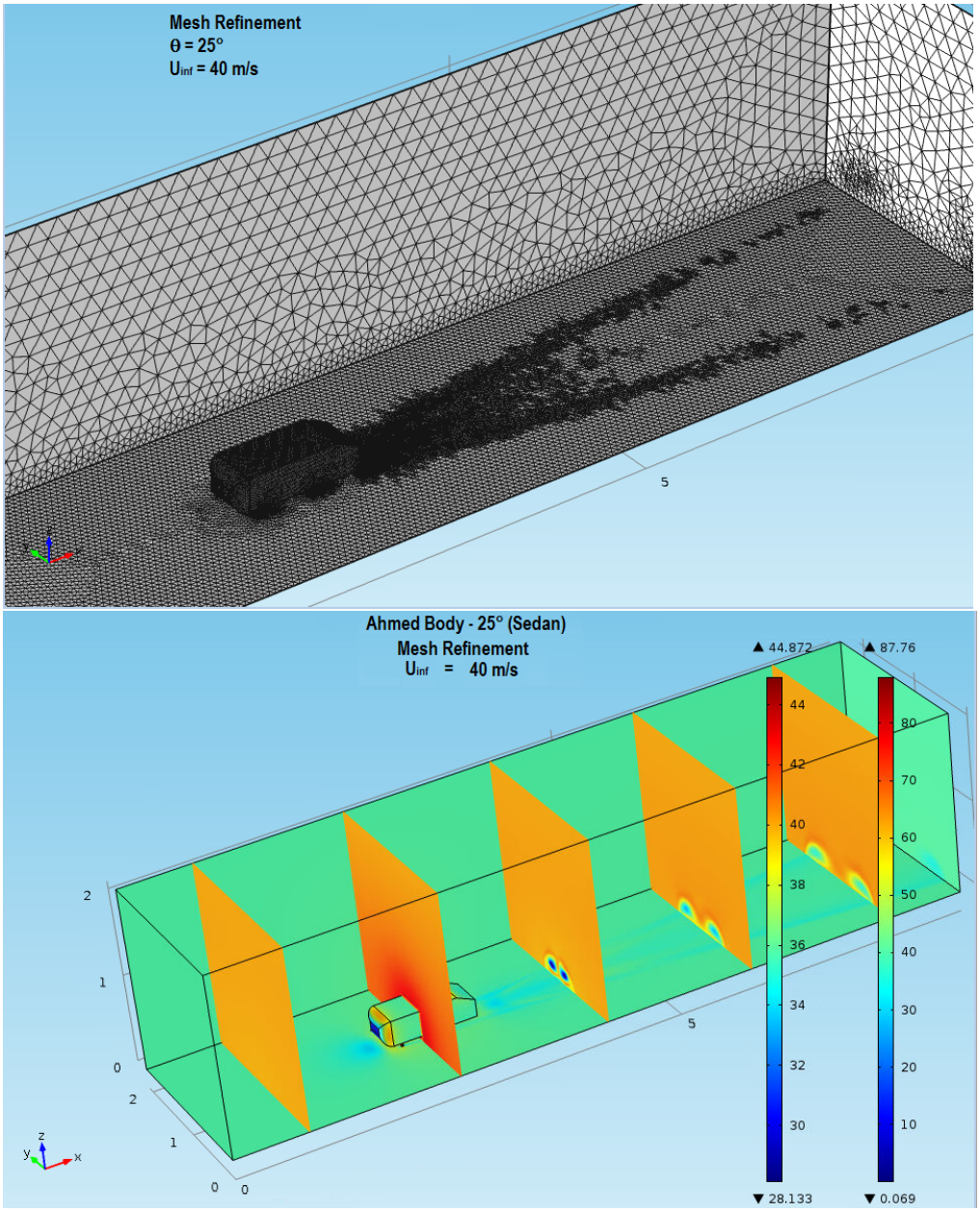

Figure 51: Refined mesh (first panel) and the corresponding wind field structure (second panel) in the case of a rear slant angles of 25°, in a street canyon geometry and $U_\infty = 40m/s$. The different colours refer to the different intensity of the velocity magnitude, plotted in the bulk domain and on transversal planes.

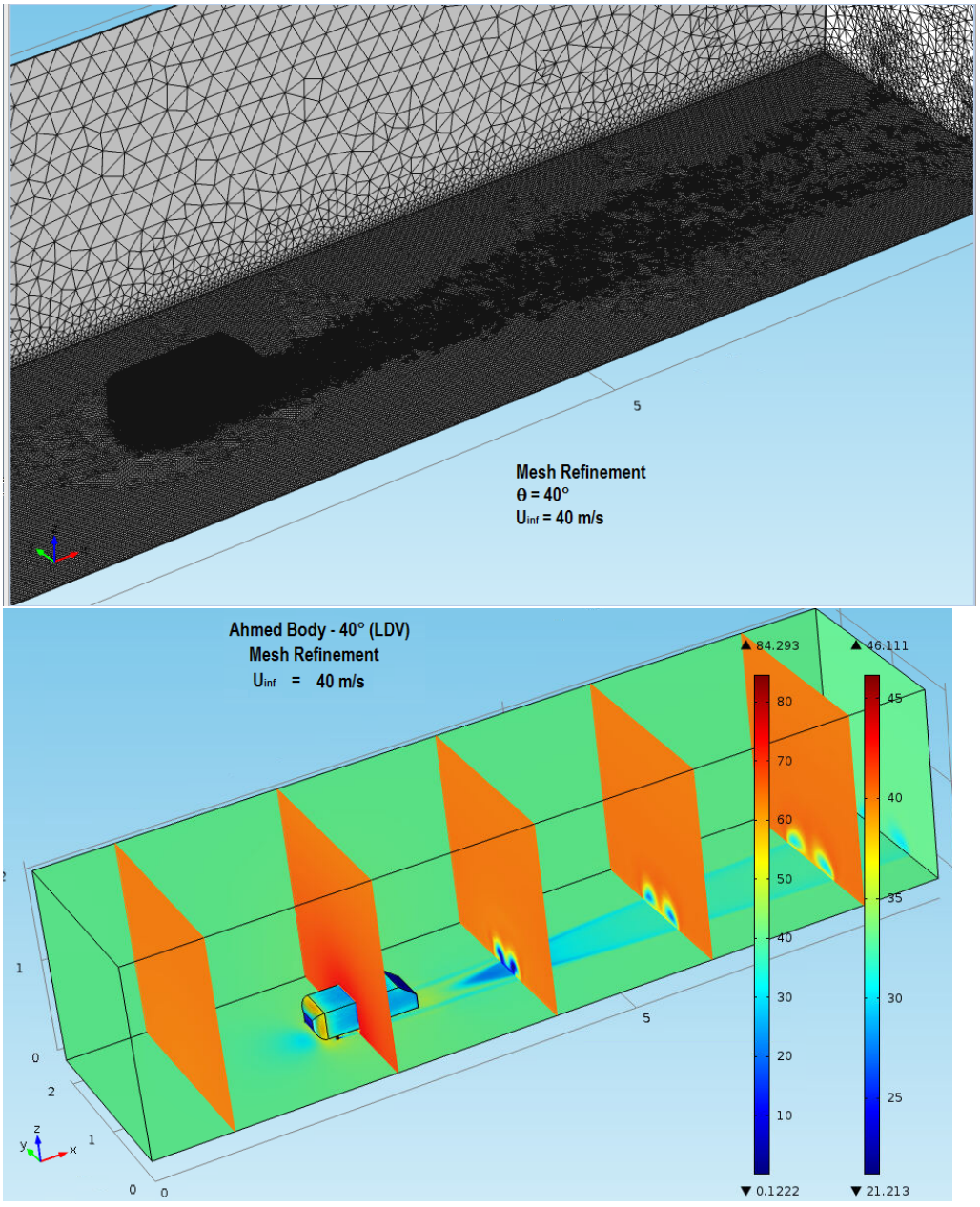

Figure 52: Refined mesh (first panel) and the corresponding wind field structure (second panel) in the case of a rear slant angles of 40°, in a street canyon geometry and $U_\infty = 40m/s$. The different colours refer to the different intensity of the velocity magnitude, plotted in the bulk domain and on transversal planes.

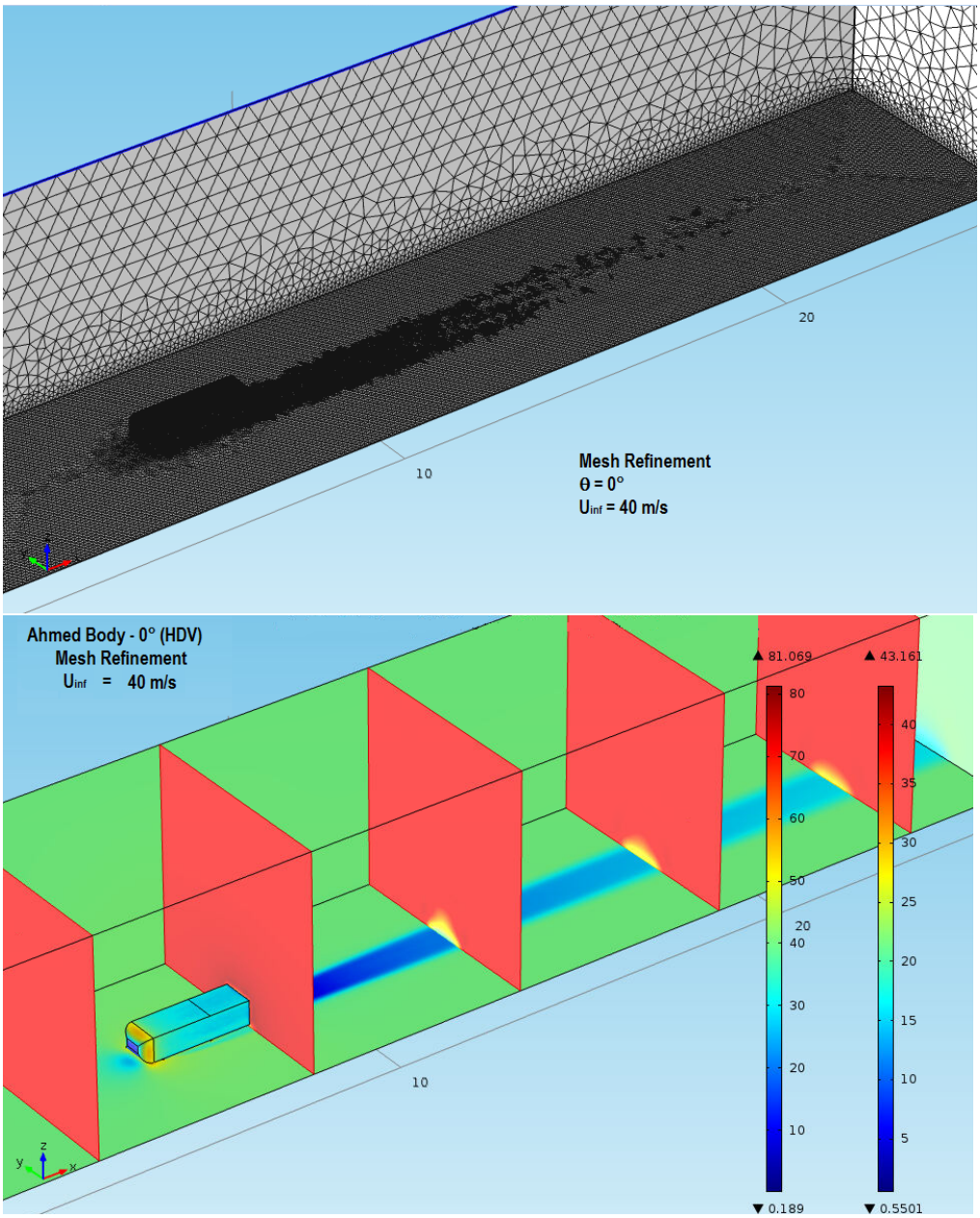

Figure 53: Refined mesh (first panel) and the corresponding wind field structure (second panel) in the case of a rear slant angles of 0°, in a street canyon geometry and $U_\infty = 40m/s$. The different colours refer to the different intensity of the velocity magnitude, plotted in the bulk domain and on transversal planes.

Observing the Figures 51, 52 and 53, it is evident how mesh refinement obviously reduces the numerical dissipation, but the flow topologies remain the same with respect to the original mesh cases. The minimal mesh sizes are merely halved by the refinement processes in all the three cases. We have taken the norm, on the whole domain, of the difference between the $|u|$ solutions obtained with and without the mesh refinement. The resulting values, for the three cases, is of the order of 10^{-2}. This norm is related to the solution error $e_h = f_{exact} - f_h$, where f_{exact} is the exact solution of the problem, and f_h is the solution obtained by a numerical simulation with an average mesh dimension h [Wilcox, 1998] without the refinement. Since we are using linear Lagrange elements as the discretization space, and since in all three cases the minimal mesh dimension is $\sim 10^{-3}$, a rough estimation of the order of magnitude of the error e_h is $e_h \sim h^{2/3}$, where h is the minimal mesh dimension. In Table 25 we show the values of the drag coefficient C_D obtained from the numerical solutions with the mesh refinement.

Configuration	C_D from simulation with refinement
25° $(k-\epsilon)$	0.289
40° $(k-\omega)$ $\omega_0 = \mathbf{1.61}$	0.252
0° $(k-\epsilon)$	0.911

Table 25: Values of the drag coefficient C_D, for the cases of $\theta = 25^\circ$, 40°, 0°, and $U_\infty = 40m/s$, obtain by the simulation data with mesh refinement.

Comparing these results with those reported in Table 24 show the grid insensitivity of the results.

We now validate the simulation results by comparing the vertical profiles of the streamwise component of velocity u, normalized with $U_\infty = 40m/s$, in a longitudinal plane at the middle of the canyon ($y = W/2$), with those obtained from wind tunnel measurements. The vertical profiles are taken at different positions along the rear slant face. Data for the cases of the Ahmed body with $\theta = 25^\circ$ and $\theta = 35^\circ$ are reported in Ref. [Lienhart, Becker, 2003]. For this reason, concerning the k_ω simulations, we report the results we have obtained for the $\theta = 35^\circ$ configuration. We have not found any report of vertical profiles for the case of the Ahmed body with $\theta = 0^\circ$ in literature. The graphical representation of the wind tunnel vertical profiles measured in Ref. [Lienhart, Becker, 2003] is taken from Ref. [Martinat et al., 2008]. In this representation, the vertical profiles are attached to the corresponding posi-

tions along the rear slant face at the mid longitudinal plane; profiles coming from simulations with different Turbulence models are reported as well. In particular, for the $\theta = 25°$ case, simulation results from the application of a $k - \omega$ model, a $k - \omega$ model with Menter cross-diffusion terms ($k - \omega\, SST$ model, see Section 3.1), and a 1−equation model (Spalart-Allmaras - SA model) are reported. In the $\theta = 35°$ case, simulation results from the application of a $k - \omega\, SST$ model, a $k - \epsilon$ model and a SA model are reported. We report the results of our simulations in a similar manner. The results are reported in Figures 54 and 55.

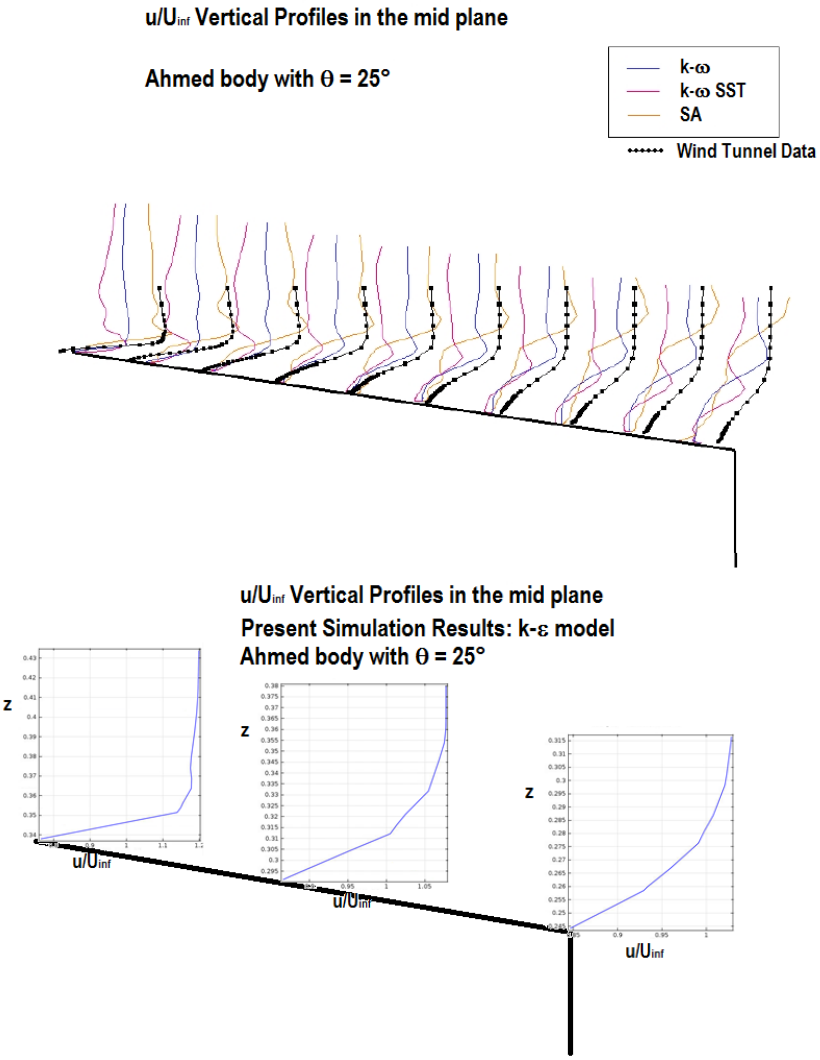

Figure 54: Vertical profiles of the u/U_∞ component of velocity, with $U_\infty = 40m/s$, in a longitudinal plane at the middle of the canyon ($y = W/2$), at different positions along the rear slant face. First panel: wind tunnel data for the case of the Ahmed body with $\theta = 25°$ [Lienhart, Becker, 2003] and data coming from simulations with $k-\omega$, $k-\omega\, SST$ and SA Turbulence models [Martinat et al., 2008]. Second panel: results from the present simulations, in the case of the $k-\epsilon$ model solved for the Ahmed body with $\theta = 25°$ configuration.

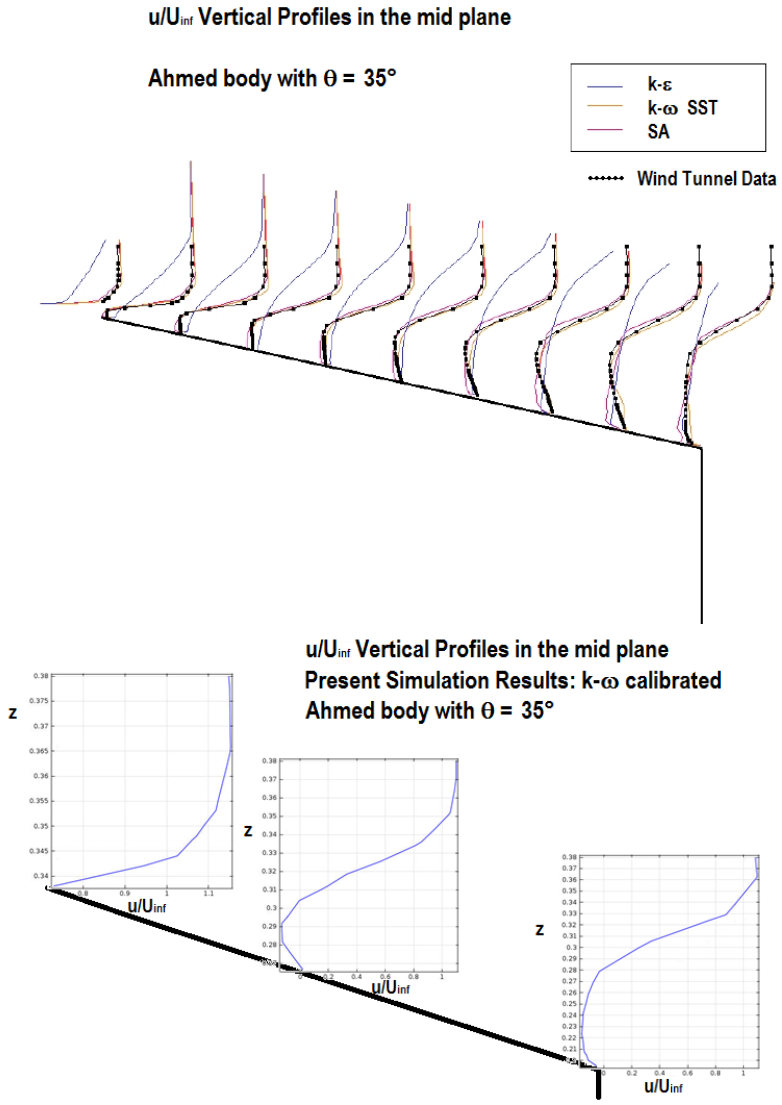

Figure 55: Vertical profiles of the u/U_∞ component of velocity, with $U_\infty = 40m/s$, in a longitudinal plane at the middle of the canyon ($y = W/2$), at different positions along the rear slant face. First panel: wind tunnel data for the case of the Ahmed body with $\theta = 35°$ [Lienhart, Becker, 2003] and data coming from simulations with $k-\epsilon$, $k-\omega\, SST$ and SA Turbulence models [Martinat et al., 2008]. Second panel: results from the present simulations, in the case of the calibrated $k-\omega$ model solved for the Ahmed body with $\theta = 35°$ configuration.

Comparing the wind tunnel vertical profiles with those obtained from our simulation results, we see that our computations perform well, especially in the case of the calibrated $k-\omega$ simulations. In particular, our calibrated $k-\omega$ simulations reproduces the experimental data as well as the $k-\omega\, SST$ simulations, which cost more in terms of computational resources. The $k\epsilon$ simulations mismatch the deflection of the vertical profiles, but are anyhow satisfactory when compared with the $k-\omega$ and the SA results obtained in Ref. [Martinat et al., 2008].

When considering the case of vehicles moving in an open street geometry, we must consider open boundary conditions at the lateral planes of the domain. In Figure 56 we report the wind field structure in the case of rear slant angles of 25° and $U_\infty = 40m/s$ in an open street geometry. The different colours in the first panel refer to the different intensity of the velocity magnitude, plotted in the bulk domain and on transversal planes. In the second panel, we show the directions of the velocity vector on a cross-sectional plane at a distance $L/2$ behind the vehicle. The length of the arrows is normalized.

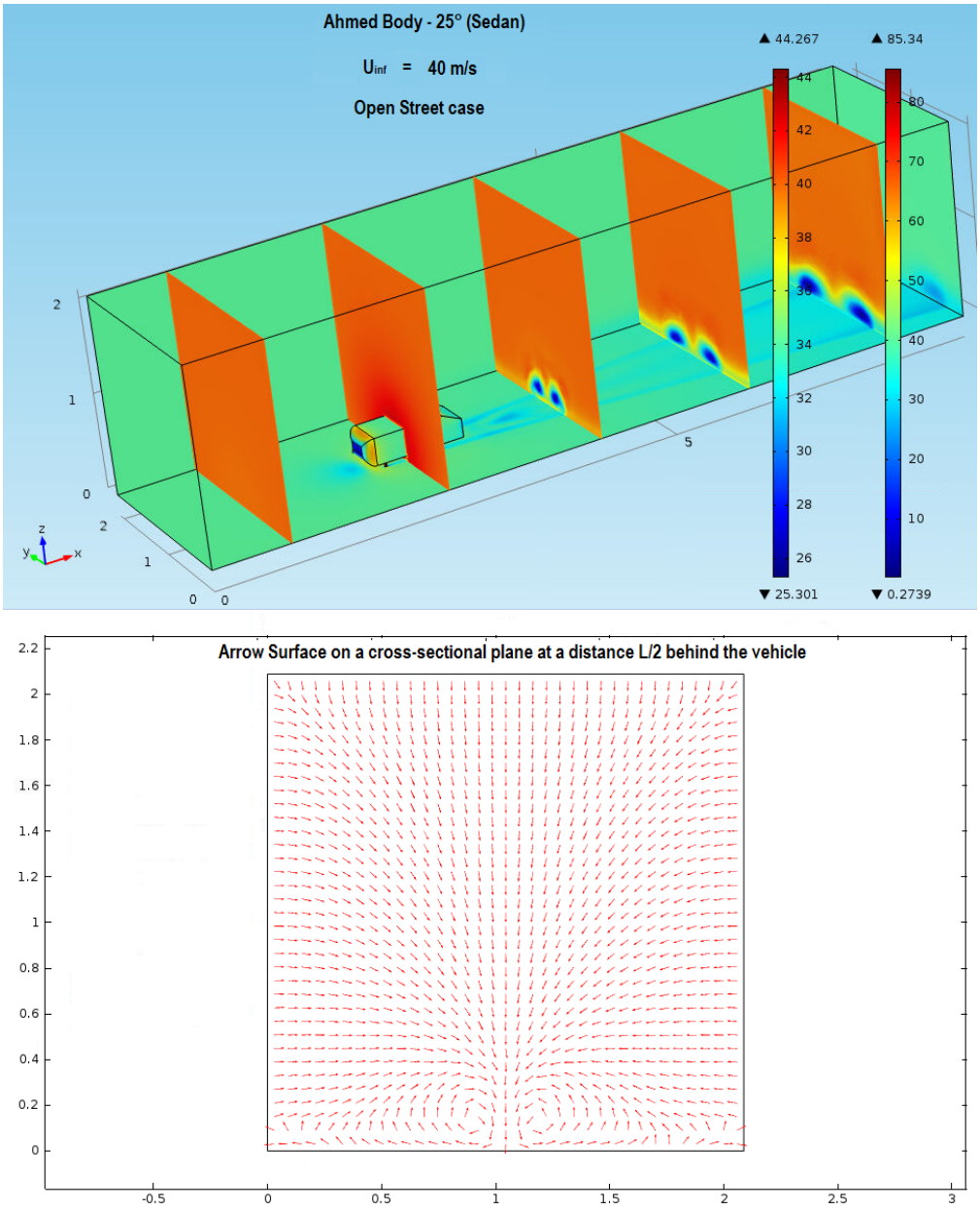

Figure 56: Wind field structure (first panel) in the case of a rear slant angles of 25°, in an open street geometry and $U_\infty = 40m/s$. The different colours refer to the different intensity of the velocity magnitude, plotted in the bulk domain and on transversal planes. Directions of the velocity vector (second panel) on a cross-sectional plane at a distance $L/2$ behind the vehicle. The length of the arrows is normalized.

We can see from Figure 56 that there is a suction effect at the open lateral walls, even if this effect is very small (the length of the arrows is normalized, and do not corresponds to the intensity of the velocity field). The draft coefficient in this case is:

$$C_{D,\text{open}} = 0.248,$$

so there is a reduction of the draft coefficient of a factor of 12% with respect to the result for the canyon street geometry (reported in Table 25), in the case of $U_\infty = 40 m/s$.

When considering the case of vehicles moving in a street canyon geometry, in an intermediate or in a heavy traffic situation, we must consider unsteady RANS simulations, taking into account the vehicles far-wake interactions (see Sections 3.3, 3.4 and 4.1 for the description of the approach). The driving cycles for typical urban driving conditions have been introduced in Figure 4 and Table 5. From the data in Ref. [André, 2004] we can deduce also the typical traffic density for each driving cycle; if N is the average number of vehicles which move within a particular traffic configuration for a distance L (N should be different for different European cities), then:

$$N = \frac{L}{L_v} = L n_v,$$

where L_v is the average distance between vehicles, and n_v is the average number of vehicles per unit length. The interaction with the far wake structure of a preceding vehicle, when a vehicle is placed at a position L_v behind a preceding vehicle, is determined by considering as an inlet condition a reduced value of the freestream velocity U_∞ and values of the Turbulence length scale L_T and of the Turbulent intensity I_T, given in Equation (3.24). The reduced value of the freestream velocity $U_{\infty,r}$ is determined as the maximum reduction, at a distance $L_v/2$ behind the preceding vehicle, of the traffic velocity, given by the self-preserving perturbation Solution U_p (4.71):

$$U_{\infty,r} = U_\infty - U_p = U_\infty - U_\infty |A| \left(\frac{L_v/2}{h} \right)^{-3/4} 0.824\, e^{-\frac{1}{8}}$$

where h is the vehicle height and A a constant which depends on the draft coefficient of the preceding vehicle and on the driving condition (see Equation (4.82)). Thus, the reduction of the freestream velocity is greater if the preceding vehicle is an HDV vehicle. The Turbulent intensity at the inlet boundary is given by:

$$I_T = \frac{U_p}{U_\infty},$$

and the Turbulent length scale is given by:

$$L_T = \gamma A h \left(\frac{L_v/2}{h} \right)^{1/4}$$

For example, considering the case of a congested urban driving condition, we can analyse the flow structure generated by a vehicle accelerating from the average speed of $10,2km/h$ to the running speed of $25,9km/h$, with a constant acceleration of $a = 0.87m/s^2$ (see the data reported in Figure 4). We consider now the simulation results corresponding to the case of a sedan vehicle preceded by an HDV; for this driving condition, an average value of $L_v = 16h$ is found, corresponding to a perturbation term $U_p \sim 0,13U_\infty$, with U_∞ varying in time from $10,2km/h$ to $25,9km/h$ (in a time $t = 5,012s$). The appropriate inlet conditions must be transformed accordingly. Remember that we are considering reduced spatial scales, so that $10,2km/h \rightarrow 11,3m/2$, $25,9km/h \rightarrow 28,7m/s$ (t and a must also be rescaled). In Figure 57 we report the unsteady wind field structure, at different instants of time, in the case of an accelerating Ahmed body with a rear slant angle of $25°$, with $U_\infty =$ varying from $9,86m/s$ to $25,03m/s$, which are the values of the freestream velocity reduced due to the far-wake interaction with a preceding HDV vehicle at a distance $L_v = 16h$. The domain is a canyon street geometry. The different colours refer to the different intensity of the velocity magnitude, plotted in the bulk domain and on transversal planes.

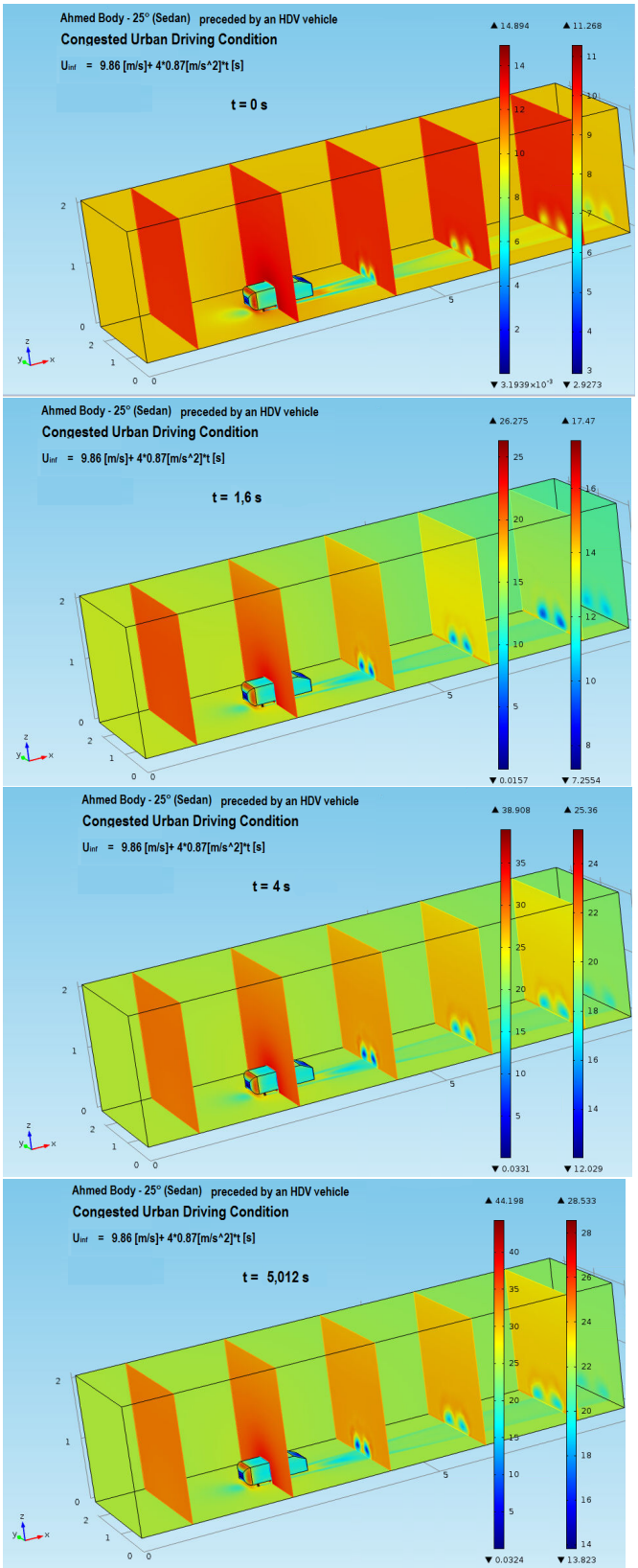

Figure 57: Unsteady wind field structure, at different instants of unreduced time t, in the case of an accelerating Ahmed body with a rear slant angle of 25°, preceded by an HDV vehicle in a congested Urban driving cycle, with U_∞ = varying from $9,86m/s$ to $25,03m/s$. The different colours refer to the different intensity of the velocity magnitude, plotted in the bulk domain and on transversal planes.

From the comparison between Figure 57 and Figure 46 (corresponding to the case without vehicle interaction) , we can observe that:

- The effect of an increased value of Turbulence intensity I_T in the case of interacting vehicles, which, in this case, goes from a non-interaction value of 0.05% to 13% ($U_p \sim 0,13U_\infty$), is to enhance boundary layer separation at the rear slant face (note the deceleration of the fluid velocity near this face). This clearly goes in the direction of augmenting the value of the drag coefficient, increasing the form drag [Batchelor, 1967].
- The retardation of the wake development with respect to the acceleration of the Inlet freestream velocity causes a weakening of the trailing vortex intensity, thus weakening the value of the induced drag [Batchelor, 1967] with respect to a stationary case with the same inlet condition.

In Figure 58 we show the variation of the drag coefficient C_D over time.

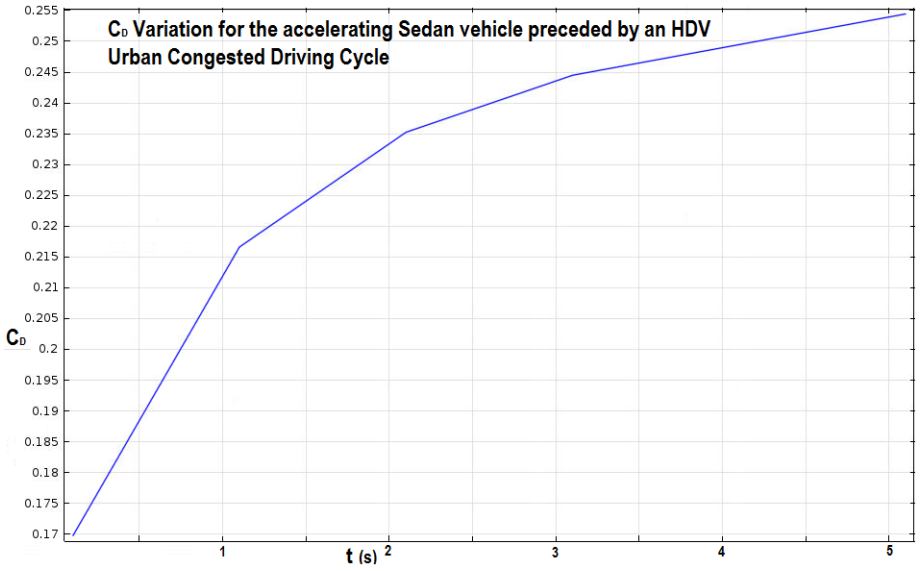

Figure 58: Variation of the drag coefficient C_D over unreduced time t in the case of an accelerating Ahmed body with a rear slant angle of 25°, preceded by an HDV vehicle in a congested Urban driving cycle, with U_∞ = varying from $9,86m/s$ to $25,03m/s$.

In Figure 58 we have not reported the initial value of C_D when $t = 0$, since it is equivalent to the value for a vehicle moving with a stationary velocity $U_\infty = 9.86m/s$ with an increased inlet turbulent intensity (we have found that $C_D = 0.265$ in this case), (the vehicle is not influenced by the unsteady effects at $t = 0$).

In Table 26 we show the near-wake configurations that we have simulated, according to the data on the typical driving cycles reported in Figure

4 and Table 5, in order to obtain the parametrization of the deposition velocities and the resuspension rates, to be used in the tailpipe emission model, described in Section 2.6, and in the dispersion models introduced in Section 3.5, whose results will be reported in Section 4.4. We have adopted the simplification that only the Congested Urban driving condition is considered with unsteady speeds and is characterized by vehicle wake interactions, whereas the other driving cycles are considered as a superposition of steady states of velocity with non-interacting vehicles (in the case of the Free Flow Urban driving cycle, an intermediate traffic condition with interacting wakes should be considered. An analysis based on the traffic density for this configuration shows that the appropriate values for I_T should be $\sim 3-6\%$. The proper extension to the simulation of intermediate traffic conditions characterized by unsteadiness and vehicle interactions will be considered in future investigations).

	U_∞ states [km/h]	$a\,[m/s^2]$	I_T	Geometry
Congested Urban	$0^* - 10.2 - 25.9$	0.87	$9 - 13\%$	Street Canyon
Free-flow Urban	$26.1 - 28 - 32.3 - 35.6$	Steady	0.05%	Street Canyon
Secondary Roads	$45.5 - 52.2 - 65$	Steady	0.05%	Open Street
Main Roads + Motorways	$75 - 86.1 - 115.6 - 123.8$	Steady	0.05%	Open Street

Table 26: Simulated near-wake configurations, according to the data reported in Figure 4 and Table 5. Only the Congested Urban driving condition is considered with unsteady speeds. *: since the Turbulence model cannot be run for $U_\infty = 0$, as explained in Section 3.4, we consider vehicles starting to move with a small velocity $\neq 0$.

The simulations for each driving configuration give values of deposition velocities and resuspension factors depending on the traffic velocities. We will thus derive simple parametrization laws for $v_{dep}(0)$ and k_{res} in function of U_∞. These laws are different for different vehicle geometries and different street geometries, and their forms depend on the fact that vehicle interactions and unsteadiness are considered or not.

To conclude this paragraph, we report the parametrization laws we have obtained for the function $C_D = f(U_\infty)$, considering only steady state configurations for simplicity. This function must be used in the context of the pollutant dispersion **model D**, introduced in Section 3.5, in order to express the interacting far-wake solutions which determine the advection terms and

the turbulent diffusivity for the dispersion process. It must also be used to determine the value of U_p and I_T for the interacting cases (according to Formulas (4.81) and (4.82)). We introduce the power law paramterization:

$$C_D = C_{D,ref}\left(\frac{v}{v_{ref}}\right)^n \tag{4.92}$$

where n is a constant exponent, $C_{D,ref}$ is the drag coefficient value calculated for the reference freestream velocity of $v_{ref} = U_\infty = 40m/s$, and $v = U_\infty$ varies depending on the traffic driving conditions. In Figures 59, 60, 61, 62, 63 and 64 we show the results of a linear fit of the numerical values of C_D according to the law:

$$\log_{10}\left(\frac{C_D}{C_{D,ref}}\right) = n\log_{10}\left(\frac{v}{v_{ref}}\right) + C,$$

which give the optimal values of the fitting parameter n in the different configurations.

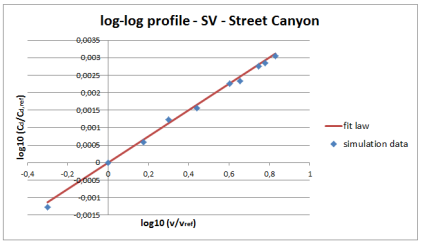

Figure 59: Linear fit of the $\log - \log$ profile law in the case of an Ahmed body with $\theta = 25°$ (Sedan vehicle) and for a street canyon geometry.

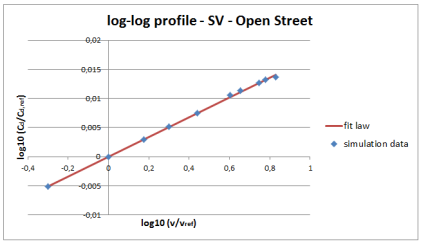

Figure 60: Linear fit of the $\log - \log$ profile law in the case of an Ahmed body with $\theta = 25°$ (Sedan vehicle) and for an open street geometry.

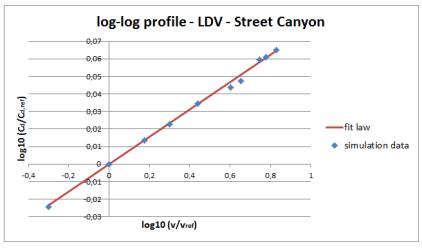

Figure 61: Linear fit of the $\log - \log$ profile law in the case of an Ahmed body with $\theta = 40°$ (LDV vehicle) and for a street canyon geometry.

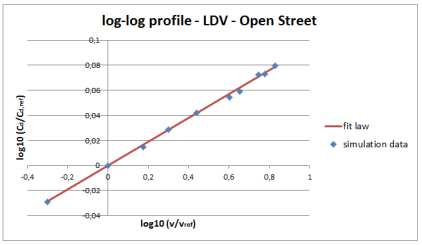

Figure 62: Linear fit of the $\log - \log$ profile law in the case of an Ahmed body with $\theta = 40°$ (LDV vehicle) and for an open street geometry.

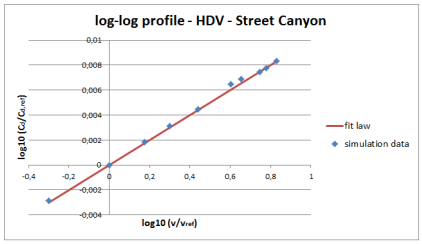

Figure 63: Linear fit of the $\log - \log$ profile law in the case of an Ahmed body with $\theta = 0°$ (HDV vehicle) and for a street canyon geometry.

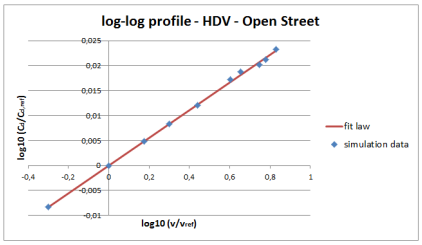

Figure 64: Linear fit of the $\log - \log$ profile law in the case of an Ahmed body with $\theta = 0°$ (HDV vehicle) and for an open street geometry.

The values of n and C, for the different configurations, with the corresponding errors introduced in the fitting procedure, are reported in Table 27, along with the values of $C_{D,ref}$ ($v_{ref} = 40m/s$ for all the configurations).

Sedan	Configuration	$C_{D,ref}$		
	Street Canyon	0.282	$n = 0.0037$	$\sigma_n = 6.44 \cdot 10^{-5}$
			$C = -5.222 \cdot 10^{-5}$	$\sigma_C = 3.56 \cdot 10^{-5}$
	Open Street	0.248	$n = 0.0169$	$\sigma_n = 0.000176$
			$C = 3.2789 \cdot 10^{-5}$	$\sigma_C = 9.7 \cdot 10^{-5}$
LDV	Configuration	$C_{D,ref}$		
	Street Canyon	0.253	$n = 0.0779$	$\sigma_n = 0.0014$
			$C = -0.00061$	$\sigma_C = 0.00082$
	Open Street	0.222	$n = 0.0951$	$\sigma_n = 0.0014$
			$C = -0.000612$	$\sigma_C = 0.000779$
HDV	Configuration	$C_{D,ref}$		
	Street Canyon	0.898	$n = 0.01$	$\sigma_n = 0.000153$
			$C = 0.00012$	$\sigma_C = 8.47 \cdot 10^{-5}$
	Open Street	0.797	$n = 0.0277$	$\sigma_n = 0.000359$
			$C = 4.67 \cdot 10^{-5}$	$\sigma_C = 0.000198$

Table 27: Values of n and C, for the different configurations, with the corresponding errors σ_n and σ_C introduced in the fitting procedure, along with the values of $C_{D,ref}$.

4.3 Deposition velocity and Resuspension factor estimates

In this Paragraph we show the parametrization law for quantitiees $v_{dep}(0)$ and k_{res} in function of U_∞. These laws are different for different vehicle geometries and different street geometries, and their forms depend on the fact that vehicle interactions and unsteadiness are considered or not.

We first recall the forms of $v_{dep}(0)$ and k_{res} introduced in Sections 2.3, sending back to that Section for the definition of the quantities which enter in the formulation:

$$v_{dep}(0) = \left[\frac{1}{ku_*} + \left(\frac{1}{v_d(z)} - \frac{1}{ku_*}\right)(1+50kSc)^{\frac{v_s}{ku_*}}\right]^{-1} \tag{4.93}$$

and

$$\begin{cases} k_{res,c} = \alpha_c \dfrac{u_* z_0 E_b}{(1-\theta_s)A^2} \\ k_{res,f} = \dfrac{u_* z_0 E_b E_f}{(1-\theta_s)d_c^2} \end{cases} \tag{4.94}$$

In particular, we have chosen $z^+ = 50$, so that:

$$\frac{ku_*}{D} = 50kSc$$

The values of the adhesion constants, set up in Section 2.6 through the comparison between the tailpipe emission model and the empirical results in Ref. [Empa, 2009], are given in Equations (2.7) and (2.8). The values of the geometrical parameters of the asphalts are given in Section 2.4 for different kinds of asphalts.

We make the assumption (which will be justified in a moment) that the average deposition and resuspension effects induced by each vehicle are determined mainly inside its near-wake. The quantities u_* and $E_b = Sc^{-2/3}$ are given by our numerical simulation data on the Turbulence structure in the near wake of the vehicles, observing that, in the logarithmic layer and depending on the Turbulence model used:

$$u_* = (0.09)^{1/4}\sqrt{k} \tag{4.95}$$

and

$$\begin{cases} \mathbf{k}-\epsilon \,\text{model}: \; E_b = \left(\dfrac{\nu}{D+D_T}\right)^{-2/3}; \; D_T = 0.09\dfrac{k^2}{\epsilon}\left(1-e^{-5/26}\right) \\ \\ \mathbf{k}-\omega \,\text{model}: \; E_b = \left(\dfrac{\nu}{D+D_T}\right)^{-2/3}; \; D_T = \dfrac{k}{\omega}\left(1-e^{-5/26}\right) \end{cases} \tag{4.96}$$

We define the following average values:

$$\begin{cases} \overline{v_d(0)} = \dfrac{1}{Wl_\omega} \displaystyle\int_\omega v_d(0)\, dxdy \\ \overline{u_* E_b} = \dfrac{1}{Wl_\omega} \displaystyle\int_\omega u_* Sc^{-2/3}\, dxdy \end{cases} \tag{4.97}$$

where the integrals are over the road surface in front, under and behind the vehicles, extending for the length of their developed near-wake (indicated as ω in the domain of integration), and l_ω is the longitudinal dimension of the domain (considered as 8 times the vehicle length behind the vehicle, and 1 time the vehicle length in front of it). These average values are intended to represent the main contributions to the deposition and the resuspension factors induced by each single vehicle.

We introduce the power law paramterizations:

$$\begin{cases} \overline{v_d(0)} = \overline{v_d(0)}_{ref} \left(\frac{v}{v_{ref}} \right)^n \\ \overline{u_* E_b} = \overline{u_* E_b}_{ref} \left(\frac{v}{v_{ref}} \right)^n \end{cases} \tag{4.98}$$

where n is a constant exponent, $\overline{v_d(0)}_{ref}$ and $\overline{u_* E_b}_{ref}$ are the average values of the deposition velocity and the resuspension contribution $u_* E_b$ calculated for a reference freestream velocity, and $v = U_\infty$ varies depending on the traffic driving conditions. In Figures 65-82 we show the results of linear fits of the numerical values of $\overline{v_d(0)}$ and $\overline{u_* E_b}$, for the different traffic configurations introduced in Table 26, according to the laws:

$$\begin{cases} \log_{10}\left(\dfrac{\overline{v_d(0)}}{\overline{v_d(0)}_{ref}} \right) = n \log_{10}\left(\dfrac{v}{v_{ref}} \right) + C \\ \\ \log_{10}\left(\dfrac{\overline{u_* E_b}}{\overline{u_* E_b}_{ref}} \right) = n \log_{10}\left(\dfrac{v}{v_{ref}} \right) + C \end{cases},$$

which give the optimal values of the fitting parameter n in the different configurations.

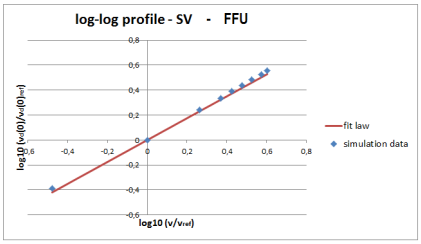

Figure 65: Linear fit of the $\log - \log$ profile law for the quantity $\overline{v_d(0)}$ in the case of an SV vehicle for the Free Flow Urban (FFU) driving condition.

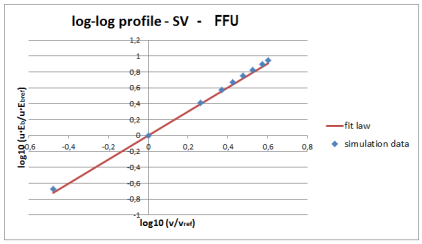

Figure 66: Linear fit of the $\log - \log$ profile law for the quantity $\overline{u_* E_b}$ in the case of an SV vehicle for the Free Flow Urban (FFU) driving condition.

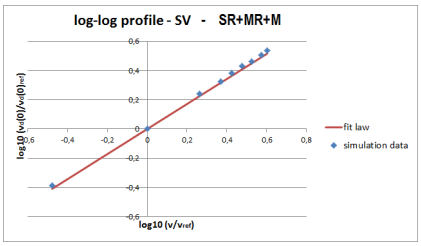

Figure 67: Linear fit of the $\log - \log$ profile law for the quantity $\overline{v_d(0)}$ in the case of an SV vehicle for the Secondary Roads (SR), Main Roads (MR) and Motorways (M) driving conditions.

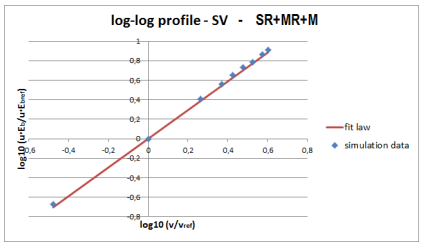

Figure 68: Linear fit of the $\log - \log$ profile law for the quantity $\overline{u_* E_b}$ in the case of an SV vehicle for the Secondary Roads (SR), Main Roads (MR) and Motorways (M) driving conditions

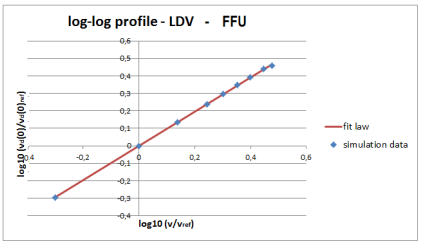

Figure 69: Linear fit of the $\log - \log$ profile law for the quantity $\overline{v_d(0)}$ in the case of an LDV vehicle for the Free Flow Urban (FFU) driving condition.

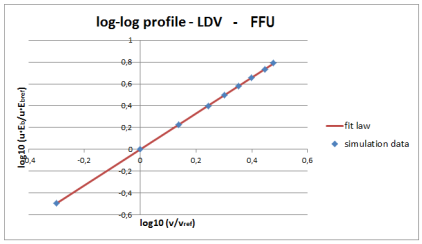

Figure 70: Linear fit of the $\log - \log$ profile law for the quantity $\overline{u_* E_b}$ in the case of an LDV vehicle for the Free Flow Urban (FFU) driving condition.

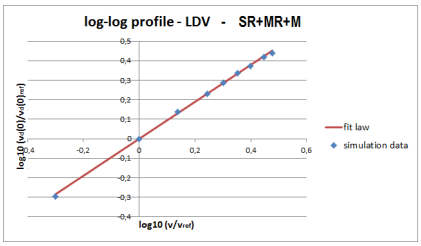

Figure 71: Linear fit of the $\log - \log$ profile law for the quantity $\overline{v_d(0)}$ in the case of an LDV vehicle for the Secondary Roads (SR), Main Roads (MR) and Motorways (M) driving conditions.

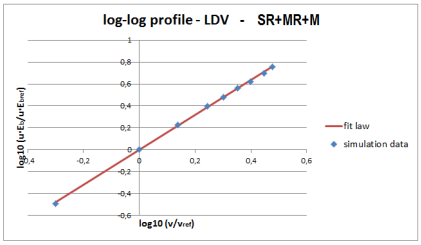

Figure 72: Linear fit of the $\log - \log$ profile law for the quantity $\overline{u_* E_b}$ in the case of an LDV vehicle for the Secondary Roads (SR), Main Roads (MR) and Motorways (M) driving conditions

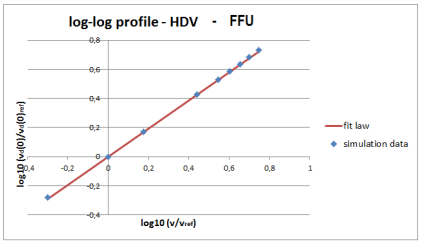

Figure 73: Linear fit of the $\log - \log$ profile law for the quantity $\overline{v_d(0)}$ in the case of an HDV vehicle for the Free Flow Urban (FFU) driving condition.

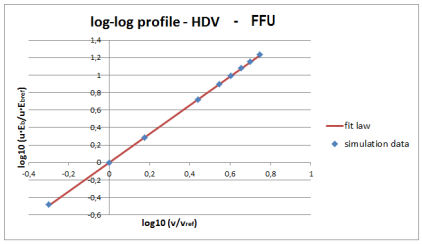

Figure 74: Linear fit of the $\log - \log$ profile law for the quantity $\overline{u_* E_b}$ in the case of an HDV vehicle for the Free Flow Urban (FFU) driving condition.

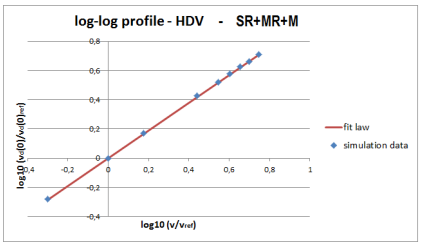

Figure 75: Linear fit of the $\log - \log$ profile law for the quantity $\overline{v_d(0)}$ in the case of an HDV vehicle for the Secondary Roads (SR), Main Roads (MR) and Motorways (M) driving conditions.

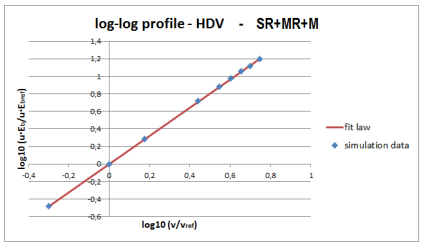

Figure 76: Linear fit of the $\log - \log$ profile law for the quantity $\overline{u_* E_b}$ in the case of an HDV vehicle for the Secondary Roads (SR), Main Roads (MR) and Motorways (M) driving conditions

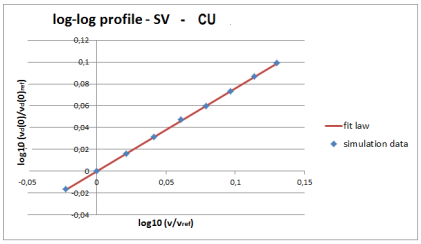

Figure 77: Linear fit of the $\log - \log$ profile law for the quantity $\overline{v_d(0)}$ in the case of an SV vehicle for the Congested Urban (CU) driving condition.

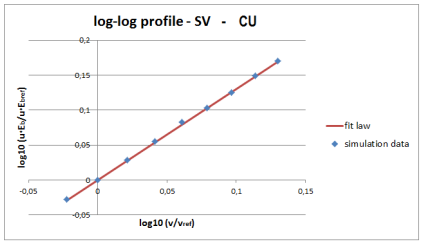

Figure 78: Linear fit of the $\log - \log$ profile law for the quantity $\overline{u_* E_b}$ in the case of an SV vehicle for the Congested Urban (CU) driving condition.

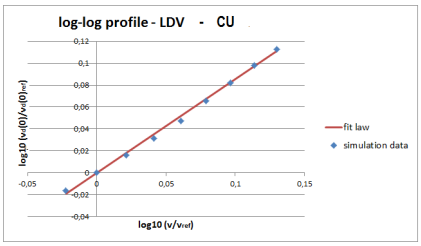

Figure 79: Linear fit of the $\log - \log$ profile law for the quantity $\overline{v_d(0)}$ in the case of an LDV vehicle for the Congested Urban (CU) driving condition.

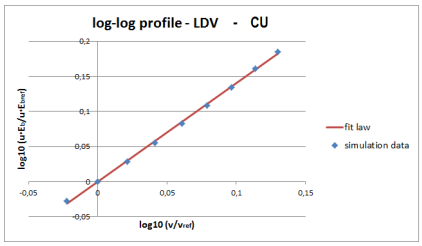

Figure 80: Linear fit of the $\log - \log$ profile law for the quantity $\overline{u_* E_b}$ in the case of an LDV vehicle for the Congested Urban (CU) driving condition.

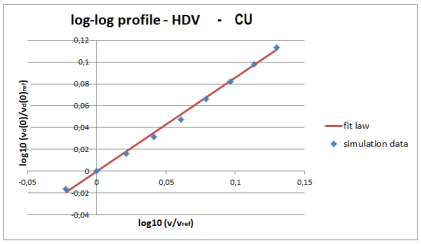

Figure 81: Linear fit of the $\log - \log$ profile law for the quantity $\overline{v_d(0)}$ in the case of an HDV vehicle for the the Congested Urban (CU) driving condition.

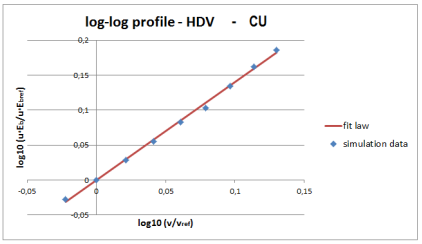

Figure 82: Linear fit of the $\log - \log$ profile law for the quantity $\overline{u_* E_b}$ in the case of an HDV vehicle for the the Congested Urban (CU) driving condition.

The values of n and C, for the different configurations, with the corresponding errors introduced in the fitting procedure, are reported in Tables 28 and 29, along with the values of $\overline{v_d(0)}_{ref}$, $\overline{u_* E_b}_{ref}$ and v_{ref} for all the configurations.

Sedan	Driving Cycle	$\overline{v_d(0)}_{ref}[m/s]$	$v_{ref}[m/s]$		
	FFU	0.0579	33.3	$n = 0.8774$	$\sigma_n = 0.0129$
				$C = 0.0182$	$\sigma_C = 0.0057$
	SR + MR + M	0.1800	133.3	$n = 0.8573$	$\sigma_n = 0.0089$
				$C = 0.0143$	$\sigma_C = 0.0040$
	CU	0.0292	11.1	$n = 0.7583$	$\sigma_n = 0.0041$
				$C = 0.0003$	$\sigma_C = 0.0003$
LDV	Driving Cycle	$\overline{v_d(0)}_{ref}[m/s]$	$v_{ref}[m/s]$		
	FFU	0.0371	33.3	$n = 0.9786$	$\sigma_n = 0.0043$
				$C = 0.0003$	$\sigma_C = 0.0014$
	SR + MR + M	0.1233	133.3	$n = 0.9485$	$\sigma_n = 0.0090$
				$C = 0.0028$	$\sigma_C = 0.0029$
	CU	0.016	11.1	$n = 0.8550$	$\sigma_n = 0.0175$
				$C = 0.0008$	$\sigma_C = 0.0013$
HDV	Driving Cycle	$\overline{v_d(0)}_{ref}[m/s]$	$v_{ref}[m/s]$		
	FFU	0.0768	33.3	$n = 0.9664$	$\sigma_n = 0.0032$
				$C = 0.0040$	$\sigma_C = 0.0022$
	SR + MR + M	0.2424	133.3	$n = 0.9478$	$\sigma_n = 0.0039$
				$C = 0.0036$	$\sigma_C = 0.0011$
	CU	0.0328	11.1	$n = 0.8572$	$\sigma_n = 0.0167$
				$C = 0.0007$	$\sigma_C = 0.0014$

Table 28: Values of n and C for the parametrization law of $\overline{v_d(0)}$, for the different configurations, with the corresponding errors σ_n and σ_C introduced in the fitting procedure, along with the values of $\overline{v_d(0)}_{ref}$ and v_{ref}. The values of velocities are referred to the reduced geometry of the Ahmed body.

Sedan	Driving Cycle	$\overline{u_* E_b}_{ref}[m/s]$	$v_{ref}[m/s]$		
	FFU	1.9149	33.3	$n = 1.5107$	$\sigma_n = 0.0185$
				$C = 0.0265$	$\sigma_C = 0.0083$
	SR + MR + M	14.5706	133.3	$n = 1.4748$	$\sigma_n = 0.0122$
				$C = 0.0195$	$\sigma_C = 0.0054$
	CU	1.08638	11.1	$n = 1.3010$	$\sigma_n = 0.0099$
				$C = 0.0011$	$\sigma_C = 0.0007$
LDV	Driving Cycle	$\overline{u_* E_b}_{ref}[m/s]$	$v_{ref}[m/s]$		
	FFU	1.18328	33.3	$n = 1.64583$	$\sigma_n = 0.0032$
				$C = 0.0001$	$\sigma_C = 0.0010$
	SR + MR + M	10.2051	133.3	$n = 1.5927$	$\sigma_n = 0.0145$
				$C = 0.0037$	$\sigma_C = 0.0047$
	CU	0.6019	11.1	$n = 1.4032$	$\sigma_n = 0.0162$
				$C = 0.00012$	$\sigma_C = 0.0012$
HDV	Driving Cycle	$\overline{u_* E_b}_{ref}[m/s]$	$v_{ref}[m/s]$		
	FFU	5.3129	33.3	$n = 1.6414$	$\sigma_n = 0.0038$
				$C = 0.0033$	$\sigma_C = 0.0027$
	SR + MR + M	44.3583	133.3	$n = 1.6082$	$\sigma_n = 0.0075$
				$C = 0.0026$	$\sigma_C = 0.0039$
	CU	2.6072	11.1	$n = 1.4014$	$\sigma_n = 0.026$
				$C = 0.0005$	$\sigma_C = 0.0019$

Table 29: Values of n and C for the parametrization law of $\overline{u_* E_b}$, for the different configurations, with the corresponding errors σ_n and σ_C introduced in the fitting procedure, along with the values of $\overline{u_* E_b}_{ref}$ and v_{ref}. The values of velocities are referred to the reduced geometry of the Ahmed body.

We must observe that the values of $\overline{v_d(0)}$ change of negligible quantities when the different Soot diameters, reported in Table 4, are considered. The values of $\overline{u_* E_b}$ are calculated for the road dust component only. In order to calculate the resuspension factors $k_{res,c}$ and $k_{res,f}$, the values of $\overline{u_* E_b}$ must be multiplies by the remaining terms in the Definitions (4.94). The remaining terms are constants which depends on the asphalt characteristics, and change, when changing the asphalt geometry and the asphalt state of maintenance, by the amount reported in Table 13.

By the observation of the values reported in the Tables 28 and 29, we conclude that:

- The deposition velocity $v_d(0)$ in the near wake region is about one order of magnitude grater than the deposition velocity in the far-wake zone (see the values reported in Table 7). This justifies our assumption of expressing the deposition velocity and the resuspension rate by considering the dynamics inside the near wake only;

- The greatest values of the resuspension factors are associated to the HDV vehicles. This cause the road dust to be resuspended mainly by the HDV produced Turbulence in the Urban driving conditions, as explained in Sections 2.5 and 2.6. The resuspension factors for the LDV vehicles are smaller then those for the SV vehicles, due to the different properties of boundary layer separation and wake recirculation associated to the relative Ahmed body configurations;

- When considering data on traffic flows in a particular urban situation, the types of roads, and so the types of driving conditions, are given for each road branch of the road network, together with the effective traffic velocities along the road branch. When the driving condition has been determined, the deposition velocities and the resuspension factors induced by each vehicle category can be determined by applying the parametrizations introduced in Tables 28 and 29, corresponding to the considered driving conditions, using the value of the traffic effective velocity. This was done in Section 2.8 in the context of the application of the tailpipe emission model to the case of the city of Milan, starting from traffic data given by *AMAT* and from emission inventories given by the *CORINAIR* emissive methodology;

- To the unsteady driving conditions ar eassociated more linear variation profiles of the resuspension factor variations.

To conclude, we note that, in order to represent more realistic driving conditions in the congested urban case, we should consider vehicles which accelerate and decelerate between two consecutive stops, using the values of acceleration given in Figure 4.

4.4 Fine Particulate spatial distributions

In this last Section we show the results of the application of some dispersion models introduced in Section 3.5 (see Table 15).

First of all, we show the results which characterize the deposition and the dispersion processes in the near wake zone behind the vehicles (application of **Model C**). For the case of Soot emission and deposition, we show in Figure 83 the results corresponding to an SV vehicle flowing at $50km/h$ in a canyon street (FFU driving condition) for $10s$ of (reduced) time. The Soot emission factor is given considering the hot emission contribution for a diesel Euro 4 sedan vehicle (see Section 2.1 for the description of the emission inventory methodology). The flux boundary condition corresponding to the emission is applied to a small circle near the left bottom corner of the vertical rear face of the vehicle. We plot the data of the deposition flux $v_d(0)C$ at different instant of times (at the surface), along the centerline of the street canyon, along a line parallel to the centerline and translated by an amount $w/2$ to the left (where w is the vehicle width), and along a transversal line at the surface at a distance $L/2$ behind the vehicle (where L is the vehicle length).

Observing the Figure 83 we can see that in this case the deposition process is mainly localized in the first meters behind the vehicle, approximately for a length of $\sim 4L$. This enforces our assumption that only the effects of the vehicle deposition in the near wake zone must be taken into account. The highest deposition flux is found in correspondence of the translated line parallel to the centerline (second panel). Note that this is the line which approximately follow the trailing vortex which develops behind the vehicle, on the side of the pollutant emission. The transversal profile (third panel) is clearly asymmetric, due to the presence of the pollutant emission flux at the left bottom vertex of the vertical rear face of the vehicle.

For the case of the road dust deposition and resuspension process, we show in Figure 84 the results corresponding to an HDV vehicle moving at $30km/h$ in a canyon street (CU driving condition) for $80s$ of (reduced) time, and to an SV vehicle, moving at $30km/h$, preceded by the HDV vehicle. The initial road dust concentration at the surface is $3[mg/m^2]$, and the wear emission factors are given considering the terms e_{tyre}, e_{brake} and $e_{asphalt}$ given by the *EMEP CORINAIR* methodology (see Section 2.2 for the description of the emission inventory methodology). The asphalt wear component is inserted in the $S(t)$ term which enters the boundary Condition (3.64), whereas the tyre and brake wear components are inserted as Dirichlet boundary conditions (properly transformed from the corresponding emission factors terms) imposed on the vehicle tyre surfaces (the base cylynder surfaces of the Ahmed body). We plot the data of the deposition - resuspension flux:

$$N_{dr} = \frac{v_d(0)}{\theta_0} C(\theta_0 - c_s) - (k_{res} + f_x n_v) c_s + S(t)$$

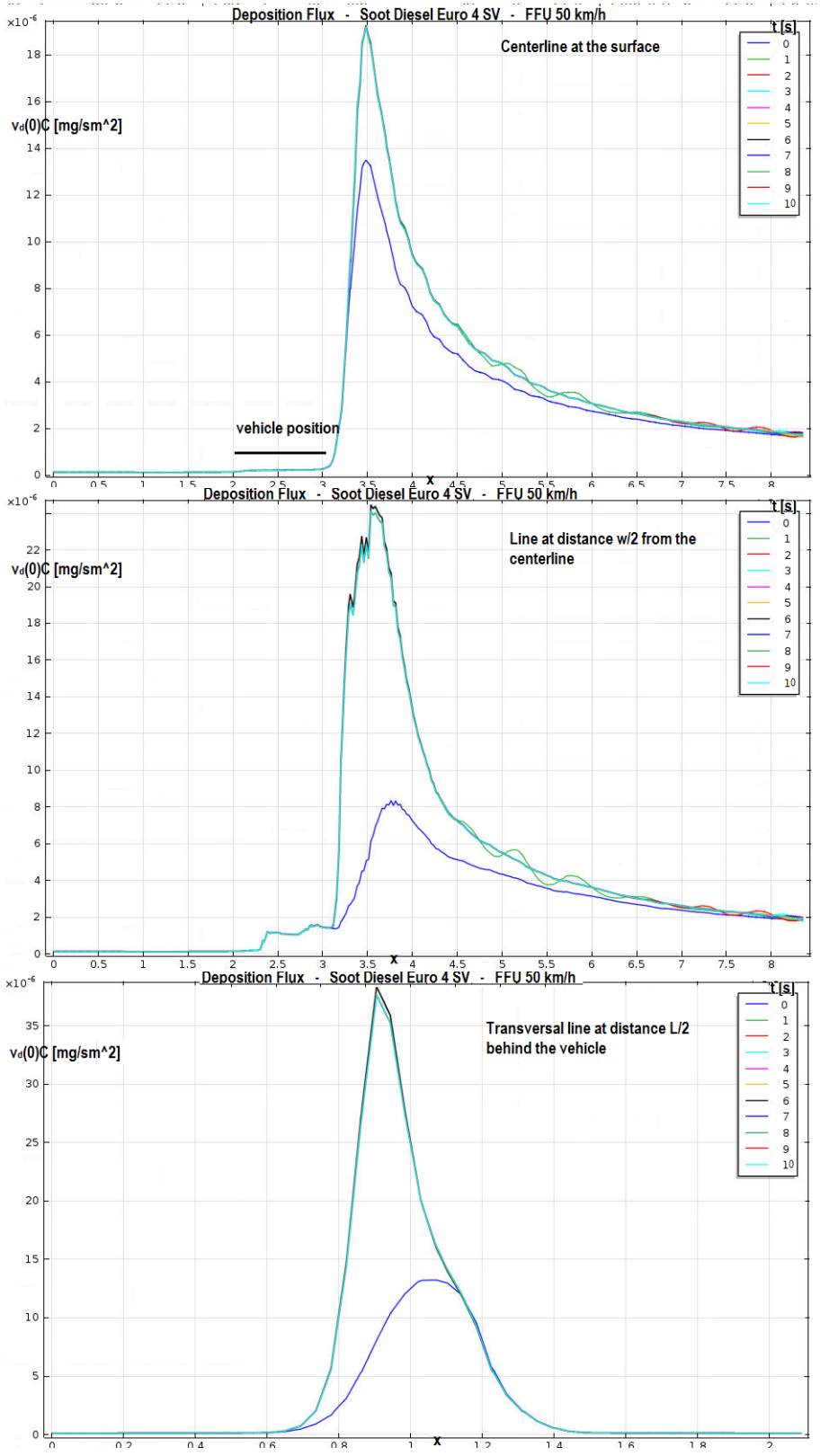

Figure 83: Deposition flux $v_d(0)C$ profiles at different instant of times (at the surface), along the centerline of the street canyon (first panel), along a line parallel to the centerline and translated by an amount $w/2$ to the left (second panel), and along a transversal line at the surface at a distance $L/2$ behind the vehicle (third panel).

at different instant of times (at the surface), along the centerline of the street canyon. We consider an $AC11$ asphalt in good condition (see Section 2.4 for details on the asphalt parameters and characteristics).

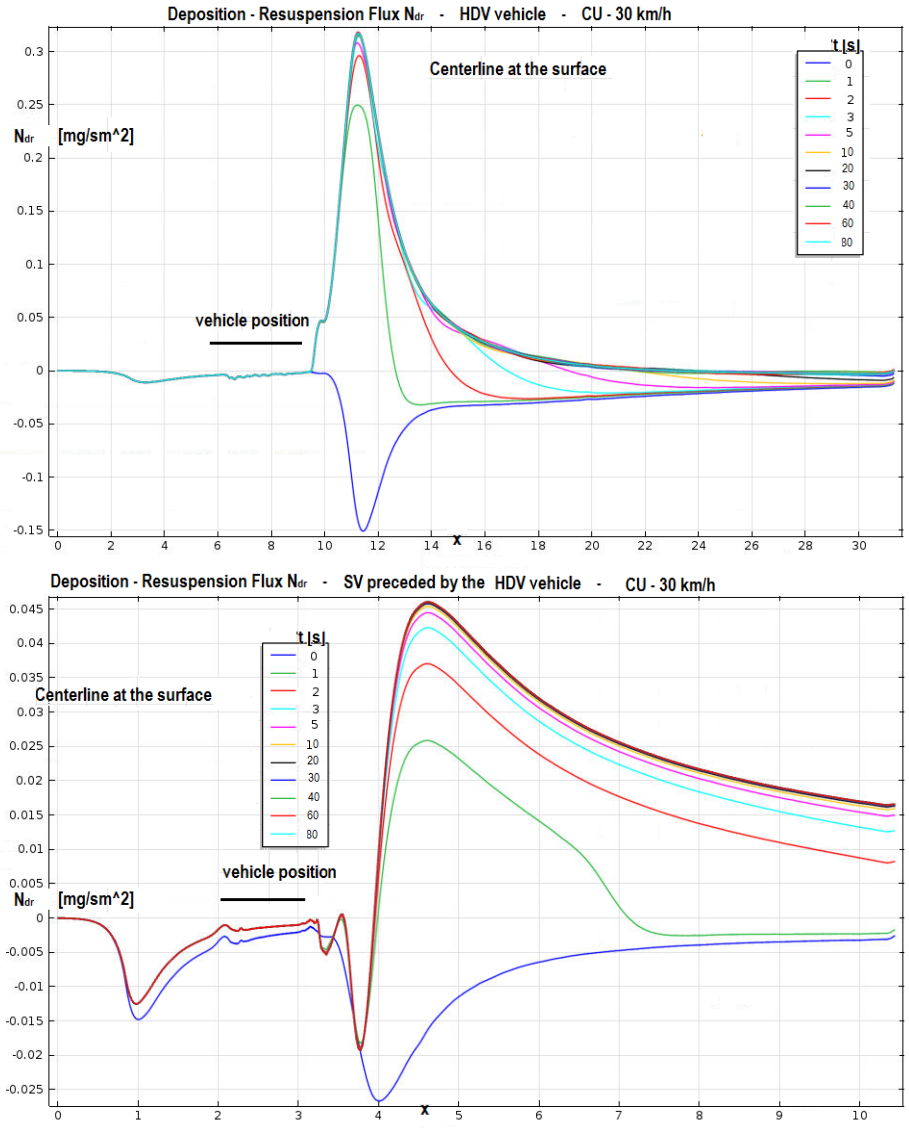

Figure 84: Deposition-Resuspension flux $N_{dr}C$ profiles at different instant of times (at the surface), along the centerline of the street canyon, for an HDV vehicle moving at $30km/h$ in CU driving conditions (first panel), and for an SV preceded by the HDV vehicle (second panel).

Observing the Figure 84 we can see that in this case the resuspension phenomenon is mainly localized in the immediate neighbourhoods of the vehicles front and rear faces. This enforces our assumption that only the effects of the vehicle resuspension in the near wake zone must be taken into account. The highest deposition and resuspension fluxes are found for the HDV case. According to the considerations made in Sections 2.5 and 2.6, the road dust is mainly resuspended and kept in a suspended state by the HDV produced Turbulence. We lastly note that the deposition and resuspension dynamics become stationary after $\sim 20s$ of reduced time.

As a final step of this dissertation, we apply the operational dispersion **model B** to the case of the Soot and road dust dispersion processes at the canyon scale in a urban situation, characterized by a canyon geometry with $W = H = 12m$ (skimming flow regime), an heavy traffic condition (CU driving cycle), and an external wind blowing with an intensity of $1m/s$ at an angle of $60°$ with respect to the street axis (presence of recirculation). The details of the applications of the other models, defined in Table 15, for the dispersion at the canyon scale will appear in future investigations. In particular, the results of the application of the numerical **model D** for the street canyon pollutant spatial distribution will be analysed in full details, comparing them with the results coming from the analytical operational models.

We consider a Urban canyon characterised by the same traffic conditions as the Zurich Weststrasse canyon street considered in Ref. [Empa, 2009], which presented a traffic flow with an average velocity of $\sim 30km/h = 8.33[m/s]$, a CU driving configuration, and a traffic density, in the rush hours, given by the number of vehicles per hour:

$$n_v = 1400[v/\text{hour}],$$

with a percentage of HDV vehicles on the total fleet composition equal to 12%. The length of the considered street branch is $L = 200m$. Let us determine firstly the values of the parameters which enter in the model formulation (see Equations (3.49), (3.52) and (3.53) for the base plume solutions corresponding to no recirculation, plus Equations (3.54), (3.58) and (3.29) for the Gaussian segments and the box model which describe the recirculation). We give them in the following list.

- **Emissions height and coordinates of the receptor points:** we consider a value of $H_e = 0.1[m]$ for the Soot emission and also for the starting height level at which the Gaussian segments for the road dust component start; the receptor point at the leeward side is at the point $(-5, +1.80)[m]$ in the cross-sectional coordinates (y, z), where $(y = 0, z = 0)$ corresponds to the road centerline. The receptor point at the downwind side is at the point $(+5, +1.80)[m]$. The street configuration extends for a length in the x direction $L = 200[m]$. The receptor is

considered to beat the middle of the canyon street, so $x_r = L/2 = 100[m]$

- **Turbulence parameters for the plume solutions:** the wind is flowing from left to right at the roof level, with $U_\infty = 1 \cdot \cos(\pi/3)$, $V_\infty = 1 \cdot \sin(\pi/3)$. The average velocity components of the canyon helical recirculation, given by our analytical solutions (see Equation (4.55) and Table 21, where the average transverse velocity components are given as integrals of the analytical solutions along the paths of the two gaussian segments, divided by their length), are:

$$\begin{cases} \mathbf{U}_{//} = 0.69072[m/s] \\ v_{He} = -0.3882[m/s] \\ w_{y_r} = 0.2947[m/s] \end{cases}$$

(Compare the results of the average transversal components with the contour values reported in Figure 29). The traffic produced Turbulence is given by the third formula in Equation (3.30):

$$\sigma^2_{tpt} = c_6 \cdot C_D^{2/3} \cdot V^2 \cdot \frac{h^{4/3}}{S_c^{2/3}}$$

Considering a traffic fleet composition with 12% percentage of HDV, the average drag coefficient, calculated from the values reported in Table 27 for the reference velocity of $30km/h$, is:

$$C_D = 0.4052$$

. Thus we have:

$$\sigma^2_{tpt} = 0.008743[m^2/s^2]$$

The dispersion coefficients for the plume solutions are (see the Definitions (3.46)):

$$K_{yy} = K_{zz} = 0.327591[m^2/s]$$

- **Turbulence parameters for the Gaussian segments:** the dispersion coefficients for the plume solutions are (in units $[m^2/s]$) (see the Definitions (3.57) and (3.61)):

$$\begin{aligned} &\text{First Segment}: \ \mathrm{K_{xx}} = 0.165417; \ \mathrm{K_{zz}} = 0.184827 \\ &\text{Second Segment}: \ \mathrm{K_{xx}} = 0.165417; \ \mathrm{K_{yy}} = 0.120674 \end{aligned}$$

The parameter y_I in Formula (3.55), which determines the starting level of the first Gaussian segment, is chosen to be $y_I = 0.5[m]$; the parameter H_{II} in Formula (3.59) is equal to $2H_e$ for both the Soot and the road dust dispersion cases.

- **Soot and road dust emissions and initial concentrations:** we consider for simplicity a fleet composed by diesel Euro 4 vehicles with DPF moving with constant velocity. Thus, considering the value for the Soot hot emissions averaged on the vehicle fleet (composed by 12% HDV), we have:

$$Q = 3.2\left[\frac{mg}{km}\right] \cdot \frac{1}{1000}\left[\frac{km}{m}\right] \cdot n_v = 1,244 \cdot 10^{-3}[mg/ms]$$

The Soot background concentration is given as a constant value, uniformly distributed across the canyon, taken from the data in Ref. [Vecchi et al., 2004], coming from measurements campaigns in the city of Milan:

$$C_b = 4.8 \cdot 10^{-3}[mg/m^3],$$

which is the value measured in correspondence of a winter situation. The value of the stationary road dust concentration is (see the discussion in Section 2.5:

$$C_s = 3[mg/m^2].$$

The value of the background concentration in atmosphere of a road dust component of the PM10 airborne concentration is taken from the measurements in Ref. [Vecchi et al., 2008], corresponding to a winter situation:

$$C_{db} = 8.84 \cdot 10^{-3}[mg/m^3].$$

- **Average deposition velocity and resuspension rate:** the average value of the deposition velocity, taken from Table 28 at the reference velocity of $v_{ref} = 30[km/h]$ and considering a fleet composed by a fraction of 12% HDV vehicles, is:

$$v_d(0) = 0.0616[m/s].$$

The average value of the resuspension factor, determined by the value of the $\overline{u_* E_b}$ factor, given in Table 29 at the reference velocity of $v_{ref} = 30[km/h]$ and considering a fleet composed by a fraction of 12% HDV vehicles, multiplied by the remaining factor in the definition of k_{res},

correspondent to an AC11 asphalt in good conditions of maintenance, is:

$$k_{res} = 0.00068[1/s].$$

We are now in a position to write the Solutions (3.52) and (3.53) for the base plume solutions, plus (3.54), (3.58) and (3.29) for the Gaussian segments and the box model. Considering $n = m = 0$ in the series expansions for the plume solutions (3.52) and (3.53), and a value of x corresponding to the longitudinal position of the receptor along the canyon $x = L_r = 100[m]$, we have for the Soot dispersion case:

Soot Plume :

$$\begin{aligned} C(y,z)_0[mg/m^3] =& (3.5215 \cdot 10^{-4}) \cos\left(\frac{\pi}{12}y\right) \cos\left(\frac{\pi}{24}z\right) \\ &+ 4.8 \cdot 10^{-3} - (6.3948 \cdot 10^{-4}) \cos\left(\frac{\pi}{12}y\right) \cos\left(\frac{\pi}{24}z\right) \\ &- (5.2607 \cdot 10^{-4}) \cos\left(\frac{\pi}{12}y\right) \cos\left(\frac{\pi}{24}z\right) \end{aligned} \tag{4.99}$$

For the road dust dispersion case we have:

Road dust Plume :

$$\begin{aligned} C(y,z)_0[mg/m^3] =& 8.84 \cdot 10^{-3} + (4.4119 \cdot 10^{-3}) \cos\left(\frac{\pi}{12}y\right) \cos\left(\frac{\pi}{24}z\right) \\ &- (1.1777 \cdot 10^{-3}) \cos\left(\frac{\pi}{12}y\right) \cos\left(\frac{\pi}{24}z\right) \\ &- (0.7912 \cdot 10^{-3}) \cos\left(\frac{\pi}{12}y\right) \cos\left(\frac{\pi}{24}z\right) \end{aligned} \tag{4.100}$$

Let us now determine the Gaussian segments Solutions (3.54), (3.58).

The source Term (3.55) for the first segment is:

Soot $\mathbf{S_I}$:

$$S_I[mg/sm^3] = \frac{\pi}{2} y^2 \left(K_{yy} \frac{\partial C_0}{\partial y} + v_{H_e} C_0 \right) \delta(x - L_r)\delta(y - y_I)\delta(z - H_e)$$
$$= 6.1239 \cdot 10^{-4} \cdot \delta(x - L_r)\delta(y - y_I)\delta(z - H_e) \tag{4.101}$$

For the road dust dispersion case we have:

Road dust $\mathbf{S_I}$:

$$S_I[mg/sm^3] = \frac{\pi}{2} y^2 \left(K_{yy} \frac{\partial C_0}{\partial y} + v_{H_e} C_0 \right) \delta(x - L_r)\delta(y - y_I)\delta(z - H_e)$$
$$= 1.7061 \cdot 10^{-3} \cdot \delta(x - L_r)\delta(y - y_I)\delta(z - H_e) \tag{4.102}$$

The first Gaussian segment GS_I is thus determined by propagating the source term S_I, using the propagator in Equation (3.56), distinguishing between the two dispersion cases, and considering values at the transversal plane at the receptor $x = L_r = 100[m]$:

Soot Gaussian Segment I :

$$GS_I = \frac{1.0819 \cdot 10^{-4}}{(y - 0.5)} \left[e^{-0.5251 \cdot \frac{(z - H_e)^2}{(y - 0.5)}} + e^{-0.5251 \cdot \frac{(z + H_e)^2}{(y - 0.5)}} \right] \tag{4.103}$$

Note that the solution GS_I is valid only for $y > 0.5[m]$, and can be used only to $y = y_r = 5[m]$. For the road dust dispersion case we have:

Road dust Segment I :

$$GS_I = \frac{0.3014 \cdot 10^{-3}}{(y - 0.5)} \left[e^{-0.5251 \cdot \frac{(z - H_e)^2}{(y - 0.5)}} + e^{-0.5251 \cdot \frac{(z + H_e)^2}{(y - 0.5)}} \right] \tag{4.104}$$

The source Term (3.59) for the second segment is:

Soot $\mathbf{S_{II}}$:

$$\begin{aligned} S_{II}[mg/sm^3] =& \frac{\pi}{2}(z-H_e)^2\left(K_{zz}\frac{\partial(C_0+C_I)}{\partial z}+w_{y_r}(C_0+C_I)\right)\cdot \\ & \delta(x-L_r)\delta(y-y_r)\delta(z-H_e-H_{II}) \\ & = 1.1328\cdot 10^{-4}\cdot\delta(x-L_r)\delta(y-y_I)\delta(z-H_e) \end{aligned} \tag{4.105}$$

For the road dust dispersion case we have:

Road dust $\mathbf{S_I}$:

$$\begin{aligned} S_{II}[mg/sm^3] =& \frac{\pi}{2}(z-H_e)^2\left(K_{zz}\frac{\partial(C_0+C_I)}{\partial z}+w_{y_r}(C_0+C_I)\right)\cdot \\ & = 0.2337\cdot 10^{-3}\cdot\delta(x-L_r)\delta(y-y_I)\delta(z-H_e) \end{aligned} \tag{4.106}$$

The second Gaussian segment GS_{II} is thus determined by propagating the source term S_{II}, using the propagator in Equation (3.60), distinguishing between the two dispersion cases, and considering values at the transversal plane at the receptor $x = L_r = 100[m]$:

Soot Gaussian Segment II :

$$GS_{II} = \frac{1.8803\cdot 10^{-5}}{(z-0.2)}\left[e^{-0.6105\cdot\frac{(y-5)^2}{(z-0.2)}} - e^{-0.6105\cdot\frac{(y-12+5)^2}{(z-0.2)}}\right] \tag{4.107}$$

Note that the solution GS_{II} is valid only for $z > 0.2[m]$, and can be used only to $z = z_r = 1.80[m]$. For the road dust dispersion case we have:

Road dust Segment II :

$$GS_{II} = \frac{3.8791\cdot 10^{-5}}{(z-0.2)}\left[e^{-0.6105\cdot\frac{(y-5)^2}{(z-0.2)}} - e^{-0.6105\cdot\frac{(y-12+5)^2}{(z-0.2)}}\right] \tag{4.108}$$

We can now obtain the pollutant concentration at the receptor at the leeward side by summing the contributions from the plume solution and the Gaussian segments at $(y_r = 5, z_r = 1.80)[m]$ (note that we have written the

Solutions (4.103), (4.104), (4.107) and (4.108) considering the variable y and the velocity component v_{H_e} as positive):

Soot Leeward Concentration :

$$C(y_r, z_r) = C_0(y_r, z_r) + GS_I(y_r, z_r) + GS_{II}(y_r, z_r) = 4.6425 \cdot 10^{-3}[mg/m^3] \tag{4.109}$$

Road dust Leeward Concentration :

$$C(y_r, z_r) = C_0(y_r, z_r) + GS_I(y_r, z_r) + GS_{II}(y_r, z_r) = 9.5761 \cdot 10^{-3}[mg/m^3] \tag{4.110}$$

We can observe that the Soot leeward concentration is reduced from the background value $C_b = 4.8 \cdot 10^{-3}$. This is clearly due to the deposition phenomenon. In the case of the road dust dispersion, due to the resuspension phenomenon and to the accumulation at the leeward side induced by the wind recirculation, the concentration level is increased, from the background value $C_b = 8.84 \cdot 10^{-3}$, by a factor of $\sim 8\%$. This should be compared with experimental data, and with results of the numerical simulations from **model D**. This will be treated in future investigations. The pollutant concentration at the receptor at the downwind side is obtained by summing the contributions from the plume solution and the recirculation contribution C_r, expressed in terms of a simple box model in Equation (3.29). If the recirculation zone is extended to the whole canyon domain (as in the *skimming flow regime* we are treating), only the recirculation term need to be considered [Berkowicz, Kearney, 2004]. Note that the source term for the case of the road dust dispersion can be expressed as:

$$Q = k_{res} c_s W$$

The results are:

Soot Downwind Concentration :

$$C(-y_r, -z_r) = C_r = 9.8854 \cdot 10^{-4}[mg/m^3] \tag{4.111}$$

Road dust Downwind Concentration :

$$C(y_r, z_r) = C_r = 7.551 \cdot 10^{-3}[mg/m^3] \tag{4.112}$$

The effect of the accumulation of the pollutants at the leeward side is thus evident. As a concluding remark, by applying the Formula for the average residence time τ of the pollutants defined in Equation (3.15), (Q is given by taking the integral of the concentration solutions over the canyon domain), we can easily find that:

$$\tau_{Soot} \sim 10^3[s]; \quad \tau_{Road\,dust} \sim 10[s].$$

An analysis of the mixing time values τ_M, defined in Equation (3.17), requires to describe the Turbulence structure in a more detailed way than was done within the operational **model B**. We will treat the mixing time study in the context of the application of **model D** in future investigations.

5 Conclusions

The modeling approach developed in Chapter 2 has allowed a quantitative estimate of the tailpipe contribution of the resuspension component to the total traffic-related PM10 emissions. Our results confirm previous experimental data [Empa, 2009] which attribute to the resuspension fraction approximately $\sim 50\%$ of total PM10 emissions.

We have shown that PM10 resuspension is influenced by asphalt porosity and its state of maintenance. This kind of quantitative information, applied to different urban and extra urban environments, is fundamental to outline more effective PM10 reduction scenarios.

We have provided evidence that a preventive policy of appropriate asphalt design and maintenance could be much more effective than other mitigation strategies based on partial traffic restrictions and/or occasional road washing to reduce traffic-dependent PM10 emissions in urban areas.

It should be reminded that, due to the lack of detailed experimental data on traffic emissions at kerbside, in roads characterized by different asphalt properties, our resuspension parametrization is necessarily simplified. Yet, it can provide important information on how the asphalt features influence resuspension phenomena.

In Chapter 3 a set of operational and simplified numerical models for the dispersion dynamics at the canyon scale has been introduced. These canyon-scale models allow us to describe the dispersion processes associated to complex urban traffic situations, characterised by vehicle wake interactions, which would be difficult to describe with numerical simulations for the dispersion dynamics associated to each single vehicle.

In Chapter 4 we have derived the analytical solutions required by the canyon-scale dispersion models, in order to describe the vehicle wake interactions effects and the effects of the flow recirculation inside the street canyon. The analytical solutions for the canyon recirculation flow structure, obtained by means of a singular perturbation analysis applied to different algebraic Turbulence models, have been validated by numerical simulations with $2-$equations Turbulence models. The analytical solutions for the far wake structure of a moving vehicle have been used to calibrate the Turbulence statistical models used in the near wake simulations in fluid flow situations with strong boundary layer separations, associated to particular vehicle geometries. Moreover, the far wake solutions have been used to define suitable inlet conditions for the near wake simulations when the effect of wake interaction with a preceding vehicle have to be taken into account, which is important when congested urban traffic configurations are described. The simulation results for the near wake Turbulence structure, for different vehicle categories and driving conditions, have been used to define suitable parametrizations of the deposition and resuspension fluxes, which are negligible away from the near wake zone, to be used in the canyon scale models.

Finally, we have applied the operational **model B** to the case of a congested urban traffic configuration in a canyon street, with wind flow recirculation inside the canyon. The validation of the results obtained by the application of **model B**, by comparison with measurements and with results from other canyon-scale models, will be treated in future investigations. We note that the set of canyon-scale dispersion models introduced in Chaprer 3 can describe a wide range of Urban dispersion situations and geometries. (We will extend the modelization to introduce the effects of a thermal stratification of the atmosphere, and to describe the *isolated roughness* canyon flow regime, in future investigations).

As we were interested only in PM10 mass concentrations, we have not considered all the particles' transformation processes which take place in the wakes of vehicles, as explained in the Chapter 2. In order to obtain particles number concentrations, which represent a more suitable indicator to be correlated with human health protection [Davidson et al., 2005], we should consider all the transformation processes and a turbulent flow description able to resolve the instantaneous flow, and not only its statistical mean. This would allow to describe the turbulent mixing which induces the faster transformation processes at the vehicle near wake scale. Large Eddy Simulations (LES) of turbulence field [Wilcox, 1998] and General Dynamic Equations (GDE) [Seinfeld, Pandis, 2006] for the description of number distribution evolution should be used, which will be carried out in future investigations.

6 Appendix - Turbulence analytic solutions

The equation (4.9) for the four regions has the form:

$$\chi\left(1+\chi^2\right)f^{''}+[1+(3-3c)\chi^2]f^{'}+2(c^2-c)\chi f=0 \qquad (6.1)$$

where:

Region **1**	*Region* **2**	*Region* **3**	*Region* **4**
$\chi=\dfrac{a_1\eta_1}{H}=\dfrac{W}{2H}\eta_1$	$\chi=\dfrac{2a_2\zeta_2}{W}=\dfrac{2H}{W}\zeta_2$	$\chi=\dfrac{2a_3\zeta_3}{W}=\dfrac{2H}{W}\zeta_3$	$\chi=\dfrac{a_4\eta_4}{H}=\dfrac{W}{2H}\eta_4$
$c=\dfrac{b_1}{a_1^2}=\dfrac{4b_1}{W^2}$	$c=\dfrac{b_2}{a_2^2}=\dfrac{b_2}{H^2}$	$c=\dfrac{b_3}{a_3^2}=\dfrac{b_3}{H^2}$	$c=\dfrac{b_4}{a_4^2}=\dfrac{4b_4}{W^2}$
$\begin{cases} f_1\left(\dfrac{W}{2H}\right)=1 \\ f_1^{'}(0)\rightarrow\dfrac{1}{k}\dfrac{1}{\chi} \end{cases}$	$\begin{cases} f_2\left(\dfrac{2H}{W}\right)=1 \\ f_2^{'}(0)\rightarrow\dfrac{1}{k}\dfrac{1}{\chi} \end{cases}$	$\begin{cases} f_3\left(\dfrac{2H}{W}\right)=1 \\ f_3^{'}(0)\rightarrow\dfrac{1}{k}\dfrac{1}{\chi} \end{cases}$	$\begin{cases} f_4\left(\dfrac{W}{2H}\right)=1 \\ f_4^{'}(0)\rightarrow\dfrac{1}{k}\dfrac{1}{\chi} \end{cases}$

Table 30: Change of variables and boundary conditions for the equation of the f_i functions in the four regions of the domain.

Equation (6.1) is a Fuchsian homogeneous second order differential equation with four regular singular points at $\{0,\pm i,\infty\}$ [Morse, Feshbach, 1953]. The exponents $\rho_{1,2}$ relative to each singular point are:

$$\begin{aligned} &0:\rho_{1,2}=0 \\ &\pm\, i:\rho_1=0,\ \rho_2=\frac{3}{2}c \\ &\infty:\rho_1=-c,\ \rho_2=2-2c \end{aligned}$$

Let us introduce the change of variable:

$$\xi=1+\chi^2 \qquad (6.2)$$

Equation (6.1) transforms into:

$$\sqrt{\xi-1}\left\{\xi(\xi-1)f^{''}+\left[\left(\frac{3}{2}c-1\right)+\left(2-\frac{3}{2}c\right)\xi\right]f^{'}+\frac{c^2-c}{2}f\right\}=0 \qquad (6.3)$$

The term in the brace bracket corresponds to an hypergeometric equation, whose corresponding solution can be represented in terms of the Riemann symbol [Morse, Feshbach, 1953]:

$$f(\xi) = P \left\{ \begin{matrix} 0 & 1 & \infty & \\ 0 & 0 & -\frac{c}{2} & \xi \\ \frac{3}{2}c & 0 & 1-c & \end{matrix} \right\} \tag{6.4}$$

where the first row contains the singular points of the equation, the first three elements of the other two rows are the characteristics exponents related to the corresponding singular points, and the last column contains the indipendent variable of the equation. The Riemann symbol represents a generic solution of the equation, and in particular is a shorthand representation of six linearly indipendent local series solutions (24 series representation if we consider Euler and Pfaff transformation, coming from the transformation properties of the Riemann symbol), two solutions uniformly convergent in a neighbourhood of each singular point. When the difference between the exponents corresponding to a singular point is an integer, the monodromy group generated by analytic continuation of the solution along closed paths around the singular point is isomorphic to the additive group in $\mathbb{C}$, and one of the two linearly indipendent solutions in the neighbourhood of the point contains a logarithmic term. Note that in the neighbourhood of the point $\xi = 1$ the solutions contains no poles: one solution is analytic, and a second linearly independent solution contains a logarithmic term. Thus it is possible to eliminate the term $\sqrt{\xi - 1}$ in Equation (3.5), for all points except at ∞ (in the case when c is an odd integer). In fact, for c an odd integer, the monodromy group for the hypergeometric Equation (3.6) is different from that for the Equation (6.1) (in particular, in this case the set of solutions of the hypergeometric Equation (6.4) in the neighbourhood of ∞ contains no logarithmic term, whereas the difference between the exponents relative to the point at ∞ of Equation (6.1) is always an integer for $c \in \mathbb{N}$. The mismatch is due to the elimination of the $\sqrt{\xi - 1}$ term in Equation (6.3): this term cancels the branch points of the solutions of Equation (6.4) near ∞). To treat the case of c an odd integer, we will perform proper analytic continuations of solutions of the Hypergeometric equation (6.4) near the point ∞. Note that the point $\xi = 1$ corresponds to the point $\chi = 0$. The boundary conditions reported in Table 30 can thus be satisfied for all values of c. The constraints on the solutions of Equation (6.1) are:

- Condition (4.12): $c > 0$;
- Matching with the solutions of the wall equations (4.4) to all orders in the asymptotic expansion. As shown in Section 2.1, these solutions have the form $(y^+)^n \log y^+$, when the terms in the asymptotic expansion for the eddy viscosity are given as a power expansion: $N_n = k(y^+)^n$. As will be seen later, this condition is satisfied for $c \in \mathbb{N}$.

- Given the boundary conditions valid on the segments **BF** and **CF**, reported in Table 30, the solution of Equation (6.4) must be valid both in $W/2H$ and in $2H/W$. These ratios cannot be both < 1. Generally, a series representation $f(\xi)$ of the solution of an hypergeometric equation is valid for $|\xi| < 1$. In the case of truncating solutions the hypergeometric series reduce to polynomials [Morse, Feshbach, 1953], uniformly valid on the whole complex plane. In our case, the solutions are truncating ones for $c \in \mathbb{N}$ even. For $c \in \mathbb{N}$ odd, suitable analytic continuations will be performed in order to have uniformly valid solutions in all the complex plane.

Summarizing, the eigenvalues of our boundary value problem are:

$$c \in \mathbb{N} > 0 \tag{6.5}$$

Let us introduce the general symbol:

$$P \left\{ \begin{array}{ccc} 0 & 1 & \infty \\ 0 & 0 & d \\ 1-h & h-d-e & e \end{array} \; \xi \right\} \tag{6.6}$$

When $d = -\frac{c}{2};\ e = 1-c;\ h = 1-\frac{3}{2}c$ this corresponds to the symbol in (6.4). A series solution of (6.6) valid for $|\xi| < 1$ (if $h-d-e > 0$ it is convergent in $\xi = 1$ too) is the Gauss hypergeometric function:

$${}_2F_1(d,e|h|\xi) = \frac{\Gamma(h)}{\Gamma(d)\Gamma(e)} \sum_{k=0}^{\infty} \frac{\Gamma(d+k)\Gamma(e+k)}{k!\Gamma(h+k)} \xi^k \equiv \frac{\Gamma(h)}{\Gamma(d)\Gamma(e)} \mathbf{{}_2F_1} \tag{6.7}$$

When $h = -n$, with n a positive integer, a factor of $\frac{1}{\Gamma(h)}$ must be inserted into (6.5), in order to avoid divergence. We will use the Pfaff transformation identity for the Gauss hypergeometric function:

$${}_2F_1(d,e|h|\xi) = (1-\xi)^{-d}\, {}_2F_1\left(d, h-e|h|\frac{\xi}{\xi-1}\right) \tag{6.8}$$

valid for $h \notin \mathbb{Z}_{\leq 0}$. Let us start from the case of $c \in \mathbb{N} > 0$ odd. In this case, the point 1 is logarithmic, and there are terminating hypergeometric series associated to the Riemann symbol (6.6) (since $e = 1-c$ is a negative integer [Morse, Feshbach, 1953]). In order to obtain an analytic continuation of a solution in a neighbourhood of ∞ which satisfies all the constraints of the problem, we express one of the solution in the neighbourhood of 1 through an analytical continuation as a combination of the two solutions around the

origin [Bateman, 1953]:

$$
\begin{aligned}
&(1-\xi)^{h-e-d}\,{}_2F_1(h-d,h-e|h+1-d-e|1-\xi) = \\
&\frac{\Gamma(h+1-d-e)\Gamma(e-d)}{\Gamma(1-d)\Gamma(h-d)}\,e^{-i\pi(h-e)}\,(-\xi)^{-d}\,{}_2F_1\left(d,d+1-h|d+1-e|\frac{1}{\xi}\right)+ \\
&\frac{\Gamma(h+1-d-e)\Gamma(d-e)}{\Gamma(1-e)\Gamma(h-e)}\,e^{-i\pi(h-d)}\,(-\xi)^{-e}\,{}_2F_1\left(e+1-h,e|e+1-d|\frac{1}{\xi}\right)
\end{aligned}
\tag{6.9}
$$

If $e-d=m\in\mathbb{Z}$ one (or both) of the terms on the right blows up (the solution contains a logarithmic term). The identity of Equation (6.9) is valid in $\xi=1$, with the terms which blows up in the two hypergeometric series on the right which cancel out; thus this is a valid analytic continuation. By considering the identity for the Γ function: $\Gamma(z)\Gamma(1-z)=\frac{\pi}{\sin(\pi z)}$, we arrive, after a little algebra, to the identity:

$$
\begin{aligned}
&(1-\xi)^{h-e-d}\,{}_{\mathbf{2}}\mathbf{F}_{\mathbf{1}}(h-d,h-e|h+1-d-e|1-\xi) = \\
&\frac{\pi}{\sin\pi(e-d)}\frac{1}{\Gamma(d+1-h)\Gamma(e+1-h)}\cdot \\
&\left[\frac{\sin\pi d}{\sin\pi(h-e)}e^{-i\pi(h-e)}\,(-\xi)^{-d}\,{}_{\mathbf{2}}\mathbf{F}_{\mathbf{1}}\left(d,d+1-h|d+1-e|\frac{1}{\xi}\right)-\right. \\
&\left.\frac{\sin\pi e}{\sin\pi(h-d)}e^{-i\pi(h-d)}\,(-\xi)^{-e}\,{}_{\mathbf{2}}\mathbf{F}_{\mathbf{1}}\left(e,e+1-h|e+1-d|\frac{1}{\xi}\right)\right]
\end{aligned}
\tag{6.10}
$$

The two terms on the right hand side of (6.10) are not linearly indipendent solutions at ∞ if $d-e=l\in\mathbb{Z}$. We impose this condition. The second term in (6.10) is thus an indeterminate form $\frac{0}{0}$, and its limit for $d-e\to l$, calculated by means of De L'Hopital theorem, gives a second linearly indipendent solutions at the point with a logarithmic term. Note that in the case of $c\in\mathbb{N}>0$ odd $d-e$ is not an integer. We will perform an analytic continuation for which $h\to h-d$; in this case $h-d-e=l=0$. Let us define the logarithmic solution at ∞ as the function:

$$
\begin{aligned}
&{}_{\mathbf{2}}\mathbf{U}_{\mathbf{1}} = (-1)^{l+1}l!\frac{\Gamma(e+1-h)}{\Gamma(h+1-d-e)}\frac{\Gamma(h-d)\Gamma(h-e)\sin\pi(h-e)}{\Gamma(d)\sin\pi d}\cdot \\
&\quad(1-\xi)^{h-e-d}\,{}_2F_1(h-d,h-e|h+1-d-e|1-\xi) = \\
&\quad\frac{l!}{\Gamma(d)\Gamma(d+1-h)}\frac{\partial}{\partial(e-d)}\left[e^{-i\pi(h-e)}\,(-\xi)^{-d}\,{}_{\mathbf{2}}\mathbf{F}_{\mathbf{1}}\left(d,d+1-h|d+1-e|\frac{1}{\xi}\right)-\right. \\
&\quad\left.\frac{\sin\pi(e)\sin\pi(h-e)}{\sin\pi(d)\sin\pi(h-d)}e^{-i\pi(h-d)}\,(-\xi)^{-e}\,{}_{\mathbf{2}}\mathbf{F}_{\mathbf{1}}\left(e,e+1-h|e+1-d|\frac{1}{\xi}\right)\right]\Bigg|_{d\to e+l}
\end{aligned}
\tag{6.11}
$$

When $h \to h - d = 1 - c$, the solution (6.11) is well defined, since the $\Gamma(h-d)\sin\pi(h-d)$ in the denominator is not divergent. Besides, the hypergeometric series resulting in the calculation of the limit in the right hand side of (6.11) will be truncating, which permit to satisfy the problem constraint. All these considerations are the reasons why we started from a solution in the neighbourhood of 1 of the form (6.9) (other solutions would be non-truncating or divergent). The result for Equation (6.11), in the limit $d \to e + l$, is:

$$
\begin{aligned}
&{}_{\mathbf{2}}\mathbf{U}_{\mathbf{1}} = \xi^{-d}\log\left(\frac{1}{\xi}\right){}_2F_1\left(d, d+1-h|1+l|\frac{1}{\xi}\right)+ \\
&\xi^{-d}\sum_{k=0}^{\infty}\frac{(d)_k(d+1-h)_k}{k!(1+l)_k}[\Psi(d+k)+\Psi(d+1-h+k)-\Psi(1+l+k)-\Psi(1+k)]\left(\frac{1}{\xi}\right)^k+ \\
&\xi^{-e}\frac{l!}{(1-d)_l(h-d)_l}\sum_{k=0}^{l-1}(-1)^{1+l-k}\frac{(e)_k(e+1-h)_k}{k!}\Gamma(l-k)\left(\frac{1}{\xi}\right)^k- \\
&\frac{l!}{\Gamma(1-l)}\frac{1}{(1-d)_l(h-d)_l}\left[\frac{\sin\pi(e)\sin\pi(h-e)}{\sin\pi(d)\sin\pi(h-d)}\right]'\xi^{-e}\sum_{k=0}^{\infty}\frac{(e)_k(e+1-h)_k}{k!(1-l)_k}\left(\frac{1}{\xi}\right)^k
\end{aligned}
\tag{6.12}
$$

where $(d)_n = \frac{\Gamma(d+n)}{\Gamma(d)}$, and Ψ is the logarithmic derivative of the Γ function. The details of calculations follow the derivation in [Andrews et al., 1999] for a logarithmic point at the origin, starting from the expressions of ${}_{\mathbf{2}}\mathbf{F}_{\mathbf{1}}$ given in Equation (6.7), and considering the properties of the Γ function, and the fact that [Andrews et al., 1999]:

$$
\lim_{d-e\to l}\frac{\Gamma'(1+e-d+k)}{[\Gamma(1+e-d+k)]^2} = (-1)^{l-k}\Gamma(l-k).
$$

The prime apex in the last term corresponds to the derivative of the function in the square bracket with respect to $e-d$, for $d \to e+l$. Note that in our case $h-d-e=0$, so this term vanishes. Now consider the following solution of (6.6) in the neighbourhood of ∞:

$$
\begin{aligned}
f_I(\xi) =&(-1)^{l+1}l!\frac{\Gamma(e+1-h)}{\Gamma(1+d-e)}\frac{\Gamma(d)\Gamma(h-e)\sin\pi(h-e)}{\Gamma(h-d)\sin\pi(h-d)}e^{-i\pi e}\cdot \\
&(-\xi)^{-d}{}_2F_1\left(d, d+1-h|d+1-e|\frac{1}{\xi}\right)
\end{aligned}
\tag{6.13}
$$

This solution is well defined, and is valid for $\xi > 1$. In $\xi = 1$ it blows up. In order to obtain an analytic continuation of f_I valid in the point $\xi = 1 \leftrightarrow \chi = 0$, we apply Pfaff transformation (6.8) to f_I (the same results

would be obtained by searching for the proper analytic continuations of the hypergeometric functions inside the square brackets in Equation (6.11)), and obtain:

$$f_I(\xi) = \Bigg\{ (-1)^{l+1} l! \frac{\Gamma(e+1-h)}{\Gamma(1+d-e)} \frac{\Gamma(d)\Gamma(h-e)\sin\pi(h-e)}{\Gamma(h-d)\sin\pi(h-d)} \cdot \frac{1}{(1-\xi)^{d-e}} {}_2F_1\left(d, h-e | d+1-e | \frac{1}{1-\xi}\right) \Bigg\} (\xi-1)^{-e} \tag{6.14}$$

The term in the brace bracket corresponds to the $\mathbf{{}_2U_1}$ function defined in Equation (6.11), with the substitutions:

$$d \longrightarrow h-d; \qquad \xi \longrightarrow \frac{\xi}{\xi-1}$$

This defines the desired analytic continuation. Expressing the $\mathbf{{}_2U_1}$ function as in Equation (6.12), with the previous substitutions, and noting that:

$$(\xi-1)^{-e}\left(\frac{\xi}{\xi-1}\right)^{d-h} = \xi^{d-h},$$

since $h-d-e=0$, we obtain the solution (after the change of variable (6.2) $\xi = 1+\chi^2$):

$$\begin{aligned} f_I(\chi) &= (1+\chi^2)^{d-h} \log\left(\frac{\chi^2}{1+\chi^2}\right) {}_2F_1\left(h-d, 1-d | 1 | \frac{\chi^2}{1+\chi^2}\right) + \\ &(1+\chi^2)^{d-h} \sum_{k=0}^{n} \frac{(h-d)_k (1-d)_k}{k!k!} [\Psi(1+n-k) + \Psi(1-d+k) - 2\Psi(1+k)] \left(\frac{\chi^2}{1+\chi^2}\right)^k + \\ &(1+\chi^2)^{d-h} (-1)^n n! \sum_{k=n+1}^{\infty} \frac{(k-n-1)!(1-d)_k}{k!k!} \left(\frac{\chi^2}{1+\chi^2}\right)^k \end{aligned} \tag{6.15}$$

where $n = d-h = c-1$, with $c \in \mathbb{N} > 0$. Note that, since $h-d=-n$, the hypergeometric function comparing in (6.15) is truncating to a polynomial of degree n. The terms:

$$\begin{aligned} &(1+\chi^2)^{d-h} \sum_{k=0}^{n} \frac{(h-d)_k (1-d)_k}{k!k!} [\Psi(1+n-k)] \left(\frac{\chi^2}{1+\chi^2}\right)^k + \\ &(1+\chi^2)^{d-h} (-1)^n n! \sum_{k=n+1}^{\infty} \frac{(k-n-1)!(1-d)_k}{k!k!} \left(\frac{\chi^2}{1+\chi^2}\right)^k \end{aligned}$$

are obtained by first subtracting a term $\Psi(h-d)\,{}_2F_1\left(h-d,1-d|1|\frac{\chi^2}{1+\chi^2}\right)$ to the second term in Equation (6.12) (with $d \to h-d$ and the variable substitution), in order to avoid the divergence in the term containing the factor $\Psi(-n+k)$, and noting that [Bateman, 1953]

$$\lim_{h-d\to -n}(h-d)_k\Psi(1+d-h-k) = (-1)^n n!(k-n-1)! \qquad for \qquad k \geq n+1$$

This term is erroneously omitted in the calculations reported in [Andrews et al., 1999]. The last series in Equation (6.15) is uniformly convergent for all the real values of χ, since its argument is always < 1 on the real line. This is a consequence of the chosen analytic continuation. This series can be calculated by standard methods in complex analysis [Bateman, 1953]. We choose the other solution $f_{II}(\chi)$, linearly indipendent from f_I, to be:

$$f_{II}(\chi) = {}_2F_1(d,e|h|1+\chi^2)$$

Note that, since $e = 1-c = -n$, this is a polynomial of degree n. The general solution of Equation (6.1), in the case $c \in \mathbb{N} > 0$ odd, is thus:

$$f(\chi) = Af_I(\chi) + Bf_{II}(\chi) \tag{6.16}$$

with A, B constants. In the special case of $c = 1$, $h-d = 0$, $d = -1/2$, $e = 0$, $h = -1/2$, and the general solution is:

$$\begin{aligned} f(\chi) =& A\left[\log\frac{\chi^2}{1+\chi^2} + \sum_{k=1}^{\infty}\frac{(3/2)_k}{k!k}\left(\frac{\chi^2}{1+\chi^2}\right)^k\right] + B = \\ & A\left[\log\frac{\chi^2}{1+\chi^2} - 2\sqrt{1+\chi^2}\left\{\frac{1}{\sqrt{1+\chi^2}} + \right.\right. \\ & \left.\left.\frac{1}{\sqrt{1+\chi^2}}\log\left[\frac{1}{2}\left(\frac{1}{\sqrt{1+\chi^2}}+1\right)\right] - 1\right\}\right] + B = \\ & A\left[\sqrt{1+\chi^2} + \log\chi - \log(1+\sqrt{1+\chi^2})\right] + B \end{aligned} \tag{6.17}$$

where we have renamed the constants A and B. It's easy to see, by direct substitution, that Equation (6.17) is a solution of Equation (6.1) with $c = 1$. For $c = 1, 3, 5, \cdots, 2n+1$, Equations (6.15) and (6.16) gives polynomials terms of degree $4n$, since $e = 1-c = -2n$, plus terms proportional to $\log\chi$, $\chi^2\log\chi$, $\cdots\chi^{4n}\log\chi$, plus analogous terms containing $\sqrt{1+\chi^2}$.

Let us consider now the case of $c \in \mathbb{N} > 0$ even. In this case, for $c = 2n$, $d = -n$, $e = 1-2n$, $h = 1-3n$, $h-d = 1-2n$, $h-e = -n$. The solutions and analytic continuations in Equations (6.9), (6.11) and (6.13) contains divergent terms and cannot be used. The monodromy group is a

non-trivial subgroup of the additive group in $\mathbb{C}$, the points $\xi = 1$ and $\xi = \infty$ are logarithmic points, whereas the point ξ is not logarithmic(due to the truncating properties of the hypergeometric series). In this case it's possible to choose a power series solution at the origin, and express it in a valid analytic continuation as a combination of linearly independent solutions near the point 1, which contains a logarithmic term. Let us define the logarithmic solution at $\xi = 1$ of the Equation (6.6) as the function:

$$
\begin{aligned}
{}_{\mathbf{2}}\mathbf{u_1} = (-1)^{m+1} m! \frac{\Gamma(d+1-h)\Gamma(e+1-h)}{\Gamma(2-h)} \frac{\sin \pi d \, \sin \pi e}{\sin \pi(h-d) \, \sin \pi(h-e)} \cdot \\
\xi^{1-h} \, {}_2F_1(d+1-h, e+1-h|2-h|\xi) = \\
\frac{m!}{\Gamma(h-d)\Gamma(h-e)} \frac{\partial}{\partial(h-e-d)} \Bigg[{}_{\mathbf{2}}\mathbf{F_1}\Big(d, e|d+e+1-h|1-\xi\Big) - \\
\frac{\sin \pi d \, \sin \pi e}{\sin \pi(h-d) \, \sin \pi(h-e)} \, e^{i\pi d} (\xi - 1)^{h-d-e} \cdot \\
{}_{\mathbf{2}}\mathbf{F_1}\Big(h-d, h-e|h+1-d-e|1-\xi\Big) \Bigg] \Bigg|_{(h-e-d)\to m}
\end{aligned}
\tag{6.18}
$$

where $h - e - d = m = 0$ in our case. We have introduced in (6.18) the factor $e^{i\pi d}$ in order to have real solutions in the variable χ. Note that, since the variable ξ tends to 1 from above (when $\chi \to 0$), formula (6.18) should be written in the variable $\xi - 1$ around the point 1. Our procedure is valid anyway for $c \in \mathbb{N}$ even. Solution ${}_{\mathbf{2}}\mathbf{u_1}$ contains no divergent term and is well defined. The result for Equation (6.18), in the limit $h - d - e \to m$, is:

$$
\begin{aligned}
&{}_{\mathbf{2}}\mathbf{u_1} = \\
&\frac{m!}{(1+e-h)_m (1+d-h)_m} \sum_{k=0}^{m-1} (-1)^{m-k} \frac{(d)_k (e)_k}{k!} \Gamma(m-k) \big(1-\xi\big)^k + \\
&(1-\xi)^m \sum_{k=0}^{\infty} \frac{(d+m)_k (e+m)_k}{k!(1+m)_k} [\Psi(1+k) + \Psi(1+m+k)] \big(1-\xi\big)^k - \\
&\log\big(\xi - 1\big)(1-\xi)^m \, {}_2F_1\big(d+m, e+m|1+m|1-\xi\big) - \\
&\sum_{k=0}^{n} \frac{(d+m)_k (e+m)_k}{k!(1+m)_k} \Psi(1+n-k) \big(1-\xi\big)^k - \sum_{k=0}^{2n-1} \frac{(d+m)_k (e+m)_k}{k!(1+m)_k} \Psi(2n-k) \big(1-\xi\big)^k - \\
&\sum_{k=n+1}^{2n-1} (-1)^n n! (k-n-1)! \frac{(1-2n)_k}{k!(1+m)_k} \big(1-\xi\big)^k - \\
&\sum_{k=2n}^{\infty} (-1)^{2n-1} (2n-1)! (k-2n)! \frac{(-n)_k}{k!(1+m)_k} \big(1-\xi\big)^k
\end{aligned}
\tag{6.19}
$$

where $h - d - e = m$, $c = 2n$. The same passages as those described for the case $c \in \mathbb{N}$ odd have been applied here. The first term on the right hand side of Equation (6.19) is not present, since $m = 0$. The second term is a truncating series, since $d + m = -n$ and $e + m = 1 - 2n$. The hypergeometric function in the third term truncates to a polynomial of degree n in the variable $1 - \xi$. The second sum in the fourth term vanishes for $n + 1 \leq k \leq 2n$. Finally, the last series vanishes. We have seen that all the terms are truncating to polynomials, so that no problems of convergence impose. We identify the general solution of (6.1), in the case $c \in \mathbb{N}$ even, to be (with the substitution $\xi = 1 + \chi^2$):

$$f(\chi) = A\,\mathbf{2u_1}(1+\chi^2) + B\,{}_2F_1(d, e|d+e+1-h|-\chi^2) \tag{6.20}$$

Let us specify to the case $n = 1$. In this case $d = e = -1$, and:

$$\frac{(-1)_k}{k!}\frac{(-1)_k}{k!} = \binom{1}{k}\binom{1}{k}$$

The solution (6.20) is thus:

$$\begin{aligned} f(\chi) =& A\left\{\sum_{k=0}^{1}\binom{1}{k}\binom{1}{k}\left[2\Psi(1+k) - 2\Psi(2-k)\right](-\chi^2)^k - \log\left(\chi^2\right){}_2F_1\left(-1,-1|1|-\chi^2\right)\right\} + \\ & B\left\{\,{}_2F_1(-1,-1|1|-\chi^2)\right\} = \\ & A\left\{-2 + \left(1-\chi^2\right) - \log(\chi) + \chi^2\log(\chi)\right\} + B\left\{1-\chi^2\right\} \end{aligned} \tag{6.21}$$

It's easy to see, by direct substitution, that Equation (6.21) is a solution of Equation (6.1) with $c = 2$. For $c = 2, 4, 6, \cdots, 2n$, Equations (6.19) and (6.20) gives polynomials terms of degree $2n$, since $d = -n$, plus terms proportional to $\log\chi$, $\chi^2\log\chi$, $\cdots\chi^{2n}\log\chi$.

Let us now consider a form for the eddy viscosity according to the Prandtl prescription for free-shear layer problems (valid for Region **1**):

$$\nu_T = U_\infty \delta_1(z)$$

We said in Section 4.1 that this prescription leads to unusual boundary value problems, which now will be shown. Inserting this form for the eddy viscosity, together with the same changes of variables as those introduced in Table 17, into Equation (4.2), we obtain:

$$H^2 f_1'' + \delta_1\delta_1'\frac{g_1'}{g_1}f_1 + \delta_1^2\frac{g_1''}{g_1}f_1 - \delta_1\delta_1''\eta_1 f_1' - 2\delta_1\delta_1'\frac{g_1'}{g_1}\eta_1 f_1' + \delta_1'^2\eta_1 f_1' + \delta_1'^2\eta_1^2 f_1'' = 0 \tag{6.22}$$

A separated solution exists if:

$$\begin{cases} \delta_1 = a_1 \zeta_1 \\ \\ g_1 = \zeta_1^{\frac{\frac{b_1}{2}}{a_1^2}} \end{cases} \tag{6.23}$$

with a_1 and b_1 suitable constants, to be determined from the matching procedure and as eigenvalues of the boundary problem respectively. The equation for f_1 becomes:

$$\left(1 + \frac{a_1^2 \eta_1^2}{H^2}\right) f_1'' + \left(\frac{a_1^2}{H^2} - 2\frac{b_1}{H^2}\right) \eta_1 f_1' + \frac{1}{H^2} \frac{b_1^2}{a_1^2} f_1 = 0 \tag{6.24}$$

Equation (6.24) is valid for each $f_i,\ i = 1, \ldots, 4$, with constants $\{a_i, b_i\},\ i = 1, \ldots, 4$, and with the substitution $H \to \frac{W}{2}$ from regions 1 and 4 to regions 2 and 3, if equation (6.23) is valid for each $g_i,\ i = 1, \ldots, 4$. It can be written in the form:

$$\left(1 + \xi^2\right) f'' + (1 - 2c) \xi f' + c^2 f = 0 \tag{6.25}$$

where:

$$\xi = \frac{a_1 \eta_1}{H} = \frac{W}{2H} \eta_1 \quad , \quad c = \frac{b_1}{a_1^2} = \frac{4 b_1}{W^2}$$

Equation (6.25) is a Gegenbauer equation with imaginary argument, i.e. a Fuchsian equation with three regular singular points at $\{\pm i, i\infty\}$ and particular conditions on the characteristic exponents [Morse, Feshbach, 1953]. Let us introduce the change of variable:

$$\xi = i\chi \tag{6.26}$$

and represent the solution in term of the Riemann symbol [Morse, Feshbach, 1953]:

$$f(\chi) = P \left\{ \begin{array}{cccc} -1 & 1 & \infty & \\ 0 & 0 & -c & \chi \\ \frac{1+2c}{2} & \frac{1+2c}{2} & -c & \end{array} \right\} \tag{6.27}$$

We recall the fact that the difference between the exponents corresponding to a singular point is an integer, the monodromy group generated by analytic continuation of the solution along closed paths around the singular point is isomorphic to the additive group in $\mathbb{C}$, and one of the two linearly indipendent solutions in the neighborhood of the point contains a logarithmic term. Omographic transformations of the indipendent variables are symmetries of the Riemann symbol, which induce a transformation of the singular points without changing the monodromy group of the equation. Two linearly indipendent solutions near one of the points ± 1 for the symbol (6.27)

are Gegenbauer functions of the first and second kind T_α^β and V_α^β, with $\alpha = c;\ \beta = -(\frac{1+2c}{2})$. When α is an integer and β is not, the T series solutions truncate to Gegenbauer polynomials, and the V solutions have branch points at ± 1. When β is an integer, the T solutions are proportional to derivative of Legendre functions of the first kind, which has logarithmic singularities in one of the two points ∓ 1. The V solution is proportional to derivatives of Legendre functions of the second kind, which have logarithmic singularities at both points ± 1 [Morse, Feshbach, 1953]. All these considerations are not useful now, because we need logarithmic divergence of the solution near the origin, which is a regular point of the equation (6.27). The usual way of writing the Gegenbauer solutions in terms of $\frac{1}{\chi^2}$ [Morse, Feshbach, 1953] in order to see their behaviour for imaginary arguments are not useful here. It is not guaranteed that such a solution exists, as we are searching a particular form of the solution in the region of oscillation of solutions of a Sturm-Liouville problem: it may be that the spectrum of eigenvalues for the particular boundary value problem is empty or collapse to a finite set of points. We start from the identities:

$$\begin{aligned} f(\chi) &= P\left\{\begin{array}{cccc} -1 & 1 & \infty & \\ 0 & 0 & -c & \chi \\ \frac{1+2c}{2} & \frac{1+2c}{2} & -c & \end{array}\right\} = P\left\{\begin{array}{cccc} 0 & 1 & \infty & \\ 0 & 0 & -c & \frac{1-\chi}{2} \\ \frac{1+2c}{2} & \frac{1+2c}{2} & -c & \end{array}\right\} \\ &= P\left\{\begin{array}{cccc} 0 & 1 & \infty & \\ 0 & 0 & -\frac{c}{2} & 1-\chi^2 \\ \frac{1+2c}{2} & \frac{1}{2} & -\frac{c}{2} & \end{array}\right\} \end{aligned} \tag{6.28}$$

The second symbol corresponds to a solution of the hypergeometric equation with argument $\frac{1-\chi}{2}$, whereas the third to a solution of the hypergeometric equation with argument $1-\chi^2$. The second identity is obtained by taking the change of variable $\frac{1-\chi}{2} \to 4\frac{1-\chi}{2}\left(1-\frac{1-\chi}{2}\right)$ in the hypergeometric equation to which the second symbol is associated, and noting that, due to the particular form of the exponents of the singular points, the terms containing square root of variables disappears. We note that in the third symbol the point $\chi = 0$ corresponds to the singular point $1-\chi^2 = 1$ of the associated hypergeometric equation. The quadratic transformation introduced has conformally changed the base space of the fundamental group associated to the original equation, by concentrating the two singular points ± 1 into one and introducing a new singular point at the origin with a different monodromy group. We have now to search a solution with logarithmic divergence for $\chi \to 0$, which converges uniformly for suitable intervals of variation of the variables, and which is real when expressed in terms of the original variable ξ. There are two ways of doing this:

- to express the solution represented by the third symbol in (6.28) around the point 1 in terms of two linearly indipendent solutions around the

point ∞. One of the two indipendent solutions at the point ∞ must contain a logarithmic term, as the difference between the exponents relative to that point is zero;

- to express the solution represented by the third symbol in (6.28) around the point 1 in terms of two linearly indipendent solutions around the point 0, and impose that $\frac{1+2c}{2}$ be an integer > 0 (in order to match condition (4.12)).

We choose here to follow the second procedure, as the first one gives conditions on the eigenvalues incompatible with condition (4.12). Let us introduce the variable $1 - \chi^2 = \phi$ and the symbol:

$$P \left\{ \begin{array}{cccc} 0 & 1 & \infty & \\ 0 & 0 & d & \phi \\ 1-h & h-d-e & e & \end{array} \right\} \tag{6.29}$$

When $d = e = -\frac{c}{2}$; $h = \frac{1-2c}{2}$ this corresponds to the third symbol in (6.28). A series solution of (6.29) valid for $|\phi| < 1$ is the Gauss hypergeometric function.

Let us express one of the solution in the neighbourhood of 1 in (6.29) through an analytical continuation as a combination of the two solutions around the origin [Bateman, 1953]:

$$\begin{array}{l} {}_2F_1(d, e|1+d+e-h|1-\phi) = \\ \frac{\Gamma(1+d+e-h)\Gamma(1-h)}{\Gamma(d+1-h)\Gamma(e+1-h)}\, {}_2F_1\big(d, e|h|\phi\big) + \\ \frac{\Gamma(1+d+e-h)\Gamma(h-1)}{\Gamma(d)\Gamma(e)}(\phi)^{1-h}\, {}_2F_1\big(d+1-h, e+1-h|2-h|\phi\big) \end{array} \tag{6.30}$$

If $1 - h = m \in \mathbb{Z}$ one (or both) of the terms on the right blows up (the solution contains a logarithmic term). By considering the identity for the Γ function: $\Gamma(z)\Gamma(1-z) = \frac{\pi}{\sin(\pi z)}$, we arrive, after a little algebra, to the identity:

$$\begin{array}{l} \mathbf{{}_2F_1}(d, e|1+d+e-h|1-\phi) = \frac{\pi}{\sin(\pi h)} \frac{1}{\Gamma(d+1-h)\Gamma(e+1-h)} \cdot \\ \left[\mathbf{{}_2F_1}\Big(d, e|h|\phi\Big) - (\phi)^{1-h} \mathbf{{}_2F_1}\Big(d+1-h, e+1-h|2-h|\phi\Big) \right] \end{array} \tag{6.31}$$

The two terms on the right hand side of (6.30) are not linearly indipendent solutions at the origin if $h = 1 + m \in \mathbb{Z}$. We impose this condition. The second term in (6.31) is thus an indeterminate form $\frac{0}{0}$, and its limit for $h \to 1 + m$, calculated by means of De L'Hopital theorem, gives a second

linearly indipendent solutions at the point with a logarithmic term. Let us define the logarithmic solution at the origin as the function:

$$
\begin{aligned}
{}_{\mathbf{2}}\mathbf{U_1} &= (-1)^{n+1} n! \frac{\Gamma(d+1-h)\Gamma(e+1-h)}{\Gamma(1+d+e-h)}\, {}_2F_1(d,e|1+d+e-h|1-\phi) \\
&= \frac{1}{n!\Gamma(d)\Gamma(e)} \frac{\partial}{\partial h} \left[{}_{\mathbf{2}}\mathbf{F_1}\big(d,e|h|\phi\big) - (\phi)^{1-h}\, {}_{\mathbf{2}}\mathbf{F_1}\big(1+d-h, 1+e-h|2-h|\phi\big) \right] \Bigg|_{h\to 1+m}
\end{aligned}
\tag{6.32}
$$

We now recall equation (6.28) and condition (4.12): a physical imposition on the eigenvalues is that $c > 0$; so we have $1 - h = \frac{1}{2} + c > 0$. Let us now call $1 - h = n, n \geq 1, n \in \mathbb{Z}$. As a consequence, $h = 1 - n \in \mathbb{Z}_{\leq 0}$. The eigenvalues are $c = n - \frac{1}{2} = \frac{1}{2}, \frac{3}{2}, \ldots$. The result for equation (6.32), for the limit $h \to 1 - n$, is:

$$
\begin{aligned}
{}_{\mathbf{2}}\mathbf{U_1} =& (d)_n (e)_n \phi^n \ln\phi\, {}_2F_1\big(d+n, e+n|1+n|\phi\big) + n! \sum_{k=0}^{n-1} (-1)^{1+n-k} \frac{(d)_k (e)_k}{k!} \Gamma(n-k)\phi^k + \\
& (d)_n (e)_n \phi^n \sum_{k=0}^{\infty} \frac{(d+n)_k (e+n)_k}{k!(1+n)_k} [\Psi(d+n+k) + \Psi(e+n+k) - \Psi(n+k+1) - \Psi(k+1)]\phi^k
\end{aligned}
\tag{6.33}
$$

where $(d)_n = \frac{\Gamma(d+n)}{\Gamma(d)}$, and Ψ is the logarithmic derivative of the Γ function. The last series is convergent for $|\phi| \leq 1$.

Now we express the ${}_{\mathbf{2}}\mathbf{F_1}$ function contained in the definition of ${}_{\mathbf{2}}\mathbf{U_1}$ (for $1 - h = n$), expressed in a neighbourhood of 1, as a suitable linear combination of two local solutions in the other singular points of the equation (we choose the first of such 20 relations reported in [Bateman, 1953]), obtaining, after a little algebra:

$$
\begin{aligned}
{}_{\mathbf{2}}\mathbf{U_1} &= -1^{n+1} n! \frac{\Gamma(d+1-h)\Gamma(1-e)}{\Gamma(d+1-e)} (-\phi)^{-d}\, {}_2F_1\left(d, d+1-h|d+1-e|\frac{1}{\phi}\right) \\
&\quad - n!\pi \frac{e^{-i\pi e}}{\sin(\pi e)\Gamma(h)}\, {}_2F_1(d,e|h|\phi)
\end{aligned}
\tag{6.34}
$$

A first approach to find a solution which goes to zero logarithmically when $\phi = 1 - \chi^2$ is the following. Take the change $\phi \to \phi - 1$ in the identity (6.34).

Then we have:

$$
\begin{aligned}
{}_{\mathbf{2}}\mathbf{U}_{\mathbf{1}} &= (-1)^{n+1} n! \frac{\Gamma(d+1-h)\Gamma(e+1-h)}{\Gamma(1+d+e-h)}\, {}_2F_1(d,e|1+d+e-h|2-\phi) \\
&= -1^{n+1} n! \frac{\Gamma(d+1-h)\Gamma(1-e)}{\Gamma(d+1-e)}(1-\phi)^{-d}\, {}_2F_1\left(d, d+1-h|d+1-e|\frac{1}{\phi-1}\right) \\
&- n!\pi \frac{e^{-i\pi e}}{\sin(\pi e)\Gamma(h)}\, {}_2F_1(d,e|h|\phi-1)
\end{aligned}
\tag{6.35}
$$

The ${}_{\mathbf{2}}\mathbf{U}_{\mathbf{1}}$ written in (6.35) is a solution for the equation in question with a singular poin at 2. Now apply the Pfaff transformation to the first term in the second line:

$$
\begin{aligned}
{}_{\mathbf{2}}\mathbf{U}_{\mathbf{1}} &= (-1)^{n+1} n! \frac{\Gamma(d+1-h)\Gamma(e+1-h)}{\Gamma(1+d+e-h)}\, {}_2F_1(d,e|1+d+e-h|2-\phi) \\
&= -1^{n+1} n! \frac{\Gamma(d+1-h)\Gamma(1-e)}{\Gamma(d+1-e)}(1-\phi)^{-d}\left(\frac{2-\phi}{1-\phi}\right)^{-d} {}_2F_1\left(d, h-e|d+1-e|\frac{1}{2-\phi}\right) \\
&- n!\pi \frac{e^{-i\pi e}}{\sin(\pi e)\Gamma(h)}\, {}_2F_1(d,e|h|\phi-1)
\end{aligned}
\tag{6.36}
$$

The hypergeometric function in the second line of equation (6.36), with its constant of multiplication, corresponds to the ${}_{\mathbf{2}}\mathbf{U}_{\mathbf{1}}$ with $e \to h-e$ and $\phi \to \frac{1-\phi}{2-\phi}$, so we obtain:

$$
\begin{aligned}
{}_{\mathbf{2}}\mathbf{U}_{\mathbf{1}} &= (1-\phi)^{-d}\left(\frac{2-\phi}{1-\phi}\right)^{-d}\Bigg\{(d)_n(h-e)_n\left(\frac{1-\phi}{2-\phi}\right)^n \ln\left(\frac{1-\phi}{2-\phi}\right)\, {}_2F_1\big(d+n, h-e+n|1+n|\frac{1-\phi}{2-\phi}\big) \\
&+ n!\sum_{k=0}^{n-1}(-1)^{1+n-k}\frac{(d)_k(h-e)_k}{k!}\Gamma(n-k)\left(\frac{1-\phi}{2-\phi}\right)^k + (d)_n(h-e)_n\left(\frac{1-\phi}{2-\phi}\right)^n \cdot \\
&\sum_{k=0}^{\infty}\frac{(d+n)_k(h-e+n)_k}{k!(1+n)_k}[\Psi(d+n+k)+\Psi(h-e+n+k)-\Psi(n+k+1)-\Psi(k+1)]\left(\frac{1-\phi}{2-\phi}\right)^n\Bigg\} \\
&- n!\pi \frac{e^{-i\pi e}}{\sin(\pi e)\Gamma(h)}\, {}_2F_1(d,e|h|\phi-1)
\end{aligned}
\tag{6.37}
$$

For $n \geq 1$ we have a complete set of solutions, and the general solution can be given by a linear superposition of these base solutions. We don't go further in the treatment of this solution: by substituting $\phi = 1-\chi^2$ we obtain uniformly convergent series on all the values of the variable. Remembering

that $\xi = i\chi$, these series diverge on the real axis. Besides this, the behaviour at the origin is not logarithmic, but has to be matched with higher order terms of the perturbation expansion of the viscous solution.

We proceed now to find another solution with logarithmic behaviour at the origin. Let's start from identity (6.34), written for a solution of our hypergeometric equation (6.29) with the translation of singular point $1 \to -1$. It's easy to see that this is a solution of our original equation if we set $h \to -h$ and change the variable $\phi \to -\phi$.

$$\begin{aligned}
{}_{\mathbf{2}}\mathbf{U_1} &= (-1)^{n+1} n! \frac{\Gamma(d+1+h)\Gamma(e+1+h)}{\Gamma(1+d+e+h)}\, {}_2F_1(d,e|1+d+e+h|-1+\phi) \\
&= -(1)^{n+1} n! \frac{\Gamma(d+1+h)\Gamma(1-e)}{\Gamma(d+1-e)} (\phi)^{-d}\, {}_2F_1\left(d, d+1+h|d+1-e|-\frac{1}{\phi}\right) \\
&- n!\pi \frac{e^{-i\pi e}}{\sin(\pi e)\Gamma(-h)}\, {}_2F_1(d,e|-h|-\phi)
\end{aligned} \tag{6.38}$$

Take the change $\phi \to \phi - 1$ in the identity (6.38). Then we have:

$$\begin{aligned}
{}_{\mathbf{2}}\mathbf{U_1} &= (-1)^{n+1} n! \frac{\Gamma(d+1+h)\Gamma(e+1+h)}{\Gamma(1+d+e+h)}\, {}_2F_1(d,e|1+d+e+h|-2+\phi) \\
&= -(1)^{n+1} n! \frac{\Gamma(d+1+h)\Gamma(1-e)}{\Gamma(d+1-e)} (\phi-1)^{-d}\, {}_2F_1\left(d, d+1+h|d+1-e|\frac{1}{1-\phi}\right) \\
&- n!\pi \frac{e^{-i\pi e}}{\sin(\pi e)\Gamma(-h)}\, {}_2F_1(d,e|-h|1-\phi)
\end{aligned} \tag{6.39}$$

Now send $\phi \to 2\phi$ and $h \to 2h$, in order for ${}_{\mathbf{2}}\mathbf{U_1}$ to be a solution of the original hypergeometric equation, and apply the Pfaff transformation to the first term in the second line:

$$\begin{aligned}
{}_{\mathbf{2}}\mathbf{U_1} &= (-1)^{n+1} n! \frac{\Gamma(d+1+2h)\Gamma(1-e)}{\Gamma(1+d-e)} e^{-i\pi d}(2\phi-1)^{-d} \frac{2\phi^{-d}}{(2\phi-1)^{-d}}\, {}_2F_1(d,-2h-e|1+d-e|\frac{1}{2\phi}) \\
&- n!\pi \frac{e^{-i\pi e}}{\sin(\pi e)\Gamma(-2h)}\, {}_2F_1(d,e|-2h|1-2\phi)
\end{aligned} \tag{6.40}$$

The complex exponential factors can be absorbed in the definition of the solution ${}_{\mathbf{2}}\mathbf{U_1}$, as in our original case $d = e$. The hypergeometric function in the first line of equation (6.40) (sending $2\phi \to \phi$ and $2h \to h$), with its constant of multiplication, corresponds to the ${}_{\mathbf{2}}\mathbf{U_1}$ with $e \to -h - e$ and $\phi \to \frac{\phi-1}{\phi}$. Recall that $h = 1 - n$, with $n \geq 1$. Now we have $-h = n - 1$,

so $-h = 0, 1, 2, \ldots$. When $-h = 0$ we can apply the result (6.33). We have already seen that in this case the solution has a $\phi^2 \ln \phi^2$ local behaviour, so it can be used to obtain a matching with the second order solution of the viscous case. When $-h \geq 1$ we have the result:

$$
\begin{aligned}
{}_{\mathbf{2}}\mathbf{U_1} &= \phi^{-d}\Bigg\{ {}_2F_1\big(d, e|n-1|\frac{\phi-1}{\phi}\big) \ln\left(\frac{\phi-1}{\phi}\right) \\
&+ \left(\frac{\phi-1}{\phi}\right)^{2-n} \sum_{k=0}^{n-3} (-1)^{n-2-k} \frac{(d+2-n)_k (e+2-n)_k}{k!} \Gamma(n-2-k) \left(\frac{\phi-1}{\phi}\right)^k \\
&+ \sum_{k=0}^{\infty} \frac{(d)_k (e)_k}{k!(n-1)_k} [\Psi(d+k) + \Psi(e+k) - \Psi(n-1+k) - \Psi(k+1)] \left(\frac{\phi-1}{\phi}\right)^k \Bigg\} \\
&- n! \frac{\pi}{\sin(\pi e)\Gamma(n-1)} \, {}_2F_1(d, e|n-1|1-\phi)
\end{aligned}
\tag{6.41}
$$

To have a logarithmic behaviour at the origin, it is necessary to have the condition:

$$
1 + h = 2 - n = 0 \;\longrightarrow\; n = 2 \;\longrightarrow c = n - \frac{1}{2} = \frac{3}{2} \tag{6.42}
$$

For $n \geq 3$ the finite sums in (6.41) give divergent terms in $\frac{1}{\xi}$ (when the substitution has been done). Solutions for eigenvalues $n < 2$ would be useful to extend the matching with higher orders viscous solutions, and to obtain uniformly convergent solutions on the domain. Such a procedure should help to set up an expansion law for the eddy diffusivity near the walls of the canyon as a power series in y^+, as done previously for the case of the application of the Prandtl mixing-length hypothesis to the modelization of the eddy viscosity. Unfortunately, wake solutions for $n < 1$ are not physical. We now set $n = 2, c = \frac{3}{2} \rightarrow d = e = -\frac{3}{4}, \phi = 1 + \xi^2$ into equation (6.41):

$$
\begin{aligned}
{}_{\mathbf{2}}\mathbf{U_1} &= [2(1+\xi^2)]^{3/4} \frac{\Gamma(-7/4)}{\Gamma(-3/4)} \Bigg\{ {}_2F_1\left(-\frac{3}{4}, -\frac{3}{4}|1|\frac{\xi^2}{1+\xi^2}\right) \ln\left(\frac{\xi^2}{1+\xi^2}\right) \\
&+ \sum_{k=0}^{\infty} \frac{(-\frac{3}{4})_k (-\frac{3}{4})_k}{k!k+1!} \left[2\Psi\left(-\frac{3}{4}+k\right) - \Psi(2+k) - \Psi(1+k)\right] \left(\frac{\xi^2}{1+\xi^2}\right)^k \Bigg\} \\
&+ \frac{4}{\sqrt{2}} \pi \, {}_2F_1\left(-\frac{3}{4}, -\frac{3}{4}|2| - 1 - 2\xi^2\right)
\end{aligned}
\tag{6.43}
$$

The last hypergeometric function is uniformly convergent for $-1 - 2\xi^2 \leq 1$. Remembering that $\xi = \frac{W}{2H}\eta_1$ in region **1** and $\xi = \frac{2H}{W}\zeta_2$ in region **2**, we see that this last term must be analytically continued through the Pfaff

transformation in order to be valid for both the regions on the whole real line, unless $W = 2H$. We set the general solution as:

$$
\begin{aligned}
f(\xi) =& K_1 \Bigg[2(1+\xi^2)^{\frac{3}{4}} \frac{\Gamma(-7/4)}{\Gamma(-3/4)} \Bigg\{ {}_2F_1\big(-\frac{3}{4}, -\frac{3}{4}|1|\frac{\xi^2}{1+\xi^2}\big) \ln\left(\frac{\xi^2}{1+\xi^2}\right) \\
&+ \sum_{k=0}^{\infty} \frac{(-\frac{3}{4})_k (-\frac{3}{4})_k}{k!k+1!} \left[2\Psi\left(-\frac{3}{4}+k\right) - \Psi(2+k) - \Psi(k+1) \right] \left(\frac{\xi^2}{1+\xi^2}\right)^k \Bigg\} \\
&+ \frac{4}{\sqrt{2}} \pi [2(1+\xi^2)]^{\frac{3}{4}} \, {}_2F_1\left(-\frac{3}{4}, \frac{11}{4}|2|\frac{1+2\xi^2}{2+2\xi^2}\right) \Bigg] + \\
& K_2 \left[(1+\xi^2)^{\frac{3}{4}} \, {}_2F_1\left(-\frac{3}{4}, \frac{5}{4}|1|\frac{1}{1+\xi^2}\right) \right] \\
&= K_1 f_I(\xi) + K_2 f_{II}(\xi)
\end{aligned}
\tag{6.44}
$$

which is uniformly valid on all the real line. The matching with the law of the wall must be imposed. This is a general form for the solution of the Turbulence model with a Prandtl prescription for free-shear layer. It cannot be expressed in a closed form. We have found that this form is also important for a possible extension of the canyon solution to an analytic form for the case of a freestream wind with arbitrary angle with respect to the street axis, whose treatment will be studied in future investigations.

References

[AMAT, 2008] Agenzia Mobilità e Ambiente Srl, 2008, *Dati di traffico. Versione 0.2.* http://www.ama-mi.it/.

[AMAT, 2010] Agenzia Mobilità e Ambiente Srl, 2010, *Monitoraggio ECOPASS. Indicatori sintetici.* http://www.ama-mi.it/.

[Ahmed, Ramm, 1984] Ahmed S.R., Ramm G., 1984, *Some Salient Features of the Time-Averaged Ground Vehicle Wake.* SAE-Paper 840300.

[Amato et al., 2009] Amato F. et al., 2009, *Spatial and chemical patterns of PM10 in road dust deposited in urban environment.* Atmospheric Environment **43**, 1650–1659.

[Amato et al., 2009] Amato F. et al., 2009, *Evaluating urban PM10 pollution benefit induced by street cleaning activities.* Atmospheric Environment **43**, 4472–4480.

[André, 2004] André M., 2004, *The ARTEMIS European driving cycles for measuring car pollutant emissions.* Science of the Total Environment **334–335**, 73-84.

[Andrews et al., 1999] Andrews G.E., Askey R., Roy R. 1999, *Special Functions.* Cambridge University Press.

[Automobile Club Italia, 2006] Automobile Club Italia, *Auto-Trend. Analisi statistica sulle tendenze del mercato auto in Italia.* http://www.aci.it.

[Automobile Club Italia, 2010] Automobile Club Italia, *Auto-Trend. Analisi statistica sulle tendenze del mercato auto in Italia.* http://www.aci.it.

[Avella, Faedo, 2008] Avella F., Faedo D., 2008, *Progetto Parfil. Caratterizzazione dell'emissione di inquinanti non convenzionali di autovetture a benzina e diesel.* Final report. Stazione sperimentale per i combustibili. I - 20097 San Donato Milanese MI.

[Batchelor, 1967] Batchelor G.K., 1967, *An Introduction to Fluid Dynamics.* Cambridge University Press.

[Bateman, 1953] Bateman H., 1953, *Higher Trascendental Functions.* Cambridge University Press. McGraw-Hill book company, Inc.

[Blades, Kearney, 2004] Blades C., Kearney E., 2004, *Asphalt Paving Principles.* Cornell local roads program. New York LTAP center.

[Berkowicz, Kearney, 2004] Berkowicz R., Hertel O., Larsen S.E., Sorensen N.N., Nielsen M., 1997, *Modeling Traffic Pollution in Streets.* Ministry of Environment and Energy. National Environment Research Institute.

[Browand et al., 2009] Browand et al., 2009, *The Aerodynamics of Heavy Vehicles II: Trucks, Buses, and Trains.* Lecture Notes in Applied and Computational Mechanics. Volume 41. Springer-Verlag Berlin Heidelberg.

[CAFE, 2005] CAFE, 2005, *The Communication on Thematic Strategy on Air Pollution and the Directive on "Ambient Air Quality and Cleaner Air for Europe".* Impact Assessment, COM (2005) 446 final.

[Craft et al., 2001] Craft T.J. et al., 2001, *Computational study of flow around the Ahmed car body.* 9^{th} ERCOFTAC workshop on refined turbulence modeling, Darmstadt University of Technology, Germany.

[Davidson et al., 2005] Davidson C.I., Phalen R.F., Solomon, P.A.(2005), *Airborne particulate matter and human health: A review.* Aerosol Science and Technology **39**, 737–749.

[Davidson, 2004] Davidson P.A., 2004, *Turbulence - an introduction for scientists and engineers.* Oxford University Press.

[De Leeuw, 2002] De Leeuw, F., 2002, *A set of emission indicators for long-range transboundary air pollution.* Environmental Science and Policy **5**, 135-145.

[Di Sabatino et al. I, 2003] Di Sabatino S. et al., 2003, *The Modelling of Turbulence from Traffic in Urban Dispersion Models – Part I: Theoretical Considerations.* Environmental Fluid Mechanics **3**: 129–143.

[Kastner-Klein et al. II, 2003] Kastner-Klein P. et al., 2003, *The Modelling of Turbulence from Traffic in Urban Dispersion Models – Part II: Evaluation Against Laboratory and Full-Scale Concentration Measurements in Street Canyons.* Environmental Fluid Mechanics **3**: 145–172.

[Dunbar, 1976] Dunbar D.R., 1976, *Resuspension Of Particulate Matter.* EPA-450/2-76-031, U. S. Environmental Protection Agency, Research Triangle Park, NC.

[Durbin, 1995] Durbin P.A., 1995, *Separated Flow Computations with the k-ϵ -v2 Model.* AIAA Journal, V33, N4, PP659-664.

[EEA, 2006] European Environment Agency, 2006, *Air Quality and ancillary benefits of climate change policies.* EEA Technical Report N. 4-2006, Copenhagen.

[EEA, 2007] European Environment Agency, 2007, *Air Pollution in Europe 1990-2004.* EEA Report N. 2-2007, Copenhagen.

[EMEP/CORINAIR, 2007] 2007, *EMEP/CORINAIR emission inventory guidebook.* http://www.eea.europa.eu/publications/EMEPCORINAIR5.

[Empa, 2009] Empa, 2009, *PM10 emission factors of abrasion particles from road traffic.* August 2009.

[Eskridge et al., 1979] Eskridge et al., 1979, *Highway Modeling. Part I: Prediction of Velocity and Turbulence Fields in the Wake of Vehicles.* Journal of Applied Meteorology. Vol. 18, No. 4.

[Eskridge et al., 1979] Eskridge et al., 1979, *Highway Modeling. Part II: Advection and Diffusion of SF6 Tracer Gas.* Journal of Applied Meteorology. Vol. 18, No. 4.

[Giovannini, Grechi, 2003] Giovannini F., Grechi D., 2003, *Emissioni PM10 non-exhaust. Il ruolo critico e misterioso del risollevamento.* VIII Expert Panel. Emissioni da traffico stradale. Roma, 5 novembre 2003.

[Hardiman, 2004] Hardiman, 2004, *Application of packing theory on grading design for porous asphalt mixtures.* Civil Engineering Dimension **6**, 57–63.

[Hedalen, 1994] Hedalen T., 1994, *Road Wear e Particle Size Distributions.* SINTEF Report No. STF36A94011. SINTEF, Oslo, Norway (in Norwegian).

[Hotchkiss, Harlow, 1973] Hotchkiss R.S., Harlow F.H., 1973, *Air pollution transport in street canyons.* EPA-R4-73-029.

[Hussain, Lee, 1980] Hussain M., Lee B.E., 1980, *An investigation of wind forces on three-dimensional roughness elements in a simulated atmospheric boundary layer flow: Part II Flow over large arrays of identical roughness elements and the effect of frontal and side aspect ratio variations.* Report BS 56, Dept. Building Science, University of Sheffield.

[Jindal et al., 2005] Jindal S., Khalighi B., Iaccarino G., 2005, *Numerical Investigation of Road Vehicle Aerodynamics Using Immersed Boundary RANS Approach.* SAE 2005-01-0546.

[Kalman et al., 2009] Kalman B. et al., 2009, *Sustainable Pavements for European New Member States.* Sixth Framework Programme. Sustainable Surface Transport.European Commision.

[Keskinen et al., 2010] Keskinen J. et al., 2010, *Combustion aerosols: fine particles from traffic.* A tutorial presented at the IAC 2010, Helsinki, Finland.

[Koike et al., 2004] Koike M., Nagayoshi T., Hakamoto M., 2004, *Research on Aerodynamic Drag Reduction by Vortex Generators.* Mitsubishi motors technical review 2004, no.16.

[Kumar et al., 2011] Kumar P., Ketzel M., Vardoulakis S., Pirjola L., Britter R., 2011, *Dynamics and dispersion modelling of nanoparticles from road traffic in the urban atmospheric environment — A review.* Journal of Aerosol Science **42**, 580–603.

[Kuzmin et al., 2007] Kuzmin D. et al, 2007, *On the Implementation of the $k-\epsilon$ Turbulence Model in Incompressible Flow Solvers Based on a Finite Element Discretization.* International Journal of Computing Science and Mathematics, vol. 1, no. 2–4, pp. 193–206.

[Lienhart, Becker, 2003] Lienhart H., Becker S., 2003, *Flow and Turbulence Structure in the Wake of a Simplified Car Model.* SAE 2003 World Congress, SAE Paper 2003-01-0656, Detroit, Michigan, USA.

[Logan et al., 1995] Logan B. E. et al., 1995, *Clarification of clean-bed filtration models.* Journal of Environmental Engineering **121**, 869-873.

[Marcazzan et al., 2001] Marcazzan G. M. et al., 2001, *Characterisation of PM10 and PM2.5 particulate matter in the ambient air of Milan (Italy).* Atmospheric Environment **35**, 4639-4650.

[Martinat et al., 2008] Martinat et al., 2008, *Numerical Simulation of the Flow in the Wake of Ahmed Body Using Detached Eddy Simulation and URANS Modeling.* S.-H. Peng and W. Haase (Eds.): Adv. in Hybrid RANS-LES Modelling, NNFM 97, pp. 125–131.

[McComb, 1990] McComb W.D., 1990, *The Physics of Fluid Turbulence.* Clarendon Press. Oxford.

[Morse, Feshbach, 1953] Morse P.M., Feshbach H., 1953, *Methods of Theoretical Physics.* McGraw-Hill book company, Inc.

[Nakamura, Oke, 1988] Nakamura Y., Oke T.R., Madler L., Li N., 2006, *Wind, temperature and stability conditions in an E-W oriented canyon.* Atmospheric Environment, 22, 2691 - 2700.

[Nel et al., 2006] Nel A., Xia T., Madler L., Li N., 2006, *Toxic potential of materials at the nanolevel.* Science **311**, 622-627.

[Ouchlyama, Tanaka, 1984] Ouchlyama N., Tanaka T., 1984, *Porosity Estimation for Random Packings of Spherical Particles.* Ind. Eng. Chem. Fundam. **23**, 490-493.

[Patra et al., 2008] Patra A. et al., 2008, *On street observations of particulate matter movement and dispersion due to traffic on an urban road.* Atmospheric Environment **42** (2008) 3911–3926.

[Penttinen et al., 2001] Penttinen P., Timonen K.L., Tiittanen P., Mirme A., Ruuskanen J., Pekkanen J.(2001), *Number concentration and size of particles in urban air: Effects on spirometric lung function in adult asthmatic subjects.* Environmental Health Perspectives **109**, 319–323.

[Pey et al., 2009] Pey J., Querol X., Alastuey A., Rodríguez S., Putaud J.P., Van Dingenen R., 2009, *Source apportionment of urban fine and ultrafine particle number concentration in a Western Mediterranean city.* Atmospheric Environment **43**, 4407-4415.

[Pope, Dockery, 2006] Pope C.A., Dockery D.W., 2006, *Health effects of fine particulate air pollution: Lines that connect.* Journal of the Air and Waste Management Association **56**, 709–742.

[Pryor et al., 2008] Pryor S.C. et al., 2008, *A review of measurement and modelling results of particle atmosphere–surface exchange.* Tellus (2008), 60B, 42–75.

[Quarteroni, Valli, 2008] Quarteroni A., Valli A., 2008, *Numerical Approximation of Partial Differential Equations.* Springer Series in Computational Mathematics ISSN 0179-3632.

[Rao, 1981] Rao K.S., 1981, *Analytical solution of a gradient-transfer for plume deposition and sedimentation.* NOAA-ERL ARL-109.

[Rogers, Schief, 2002] Rogers C., Schief W.K., 2002, *Backlund and Darboux transformations. Geometry and Modern Applications in Soliton Theory.* Cambridge University Press.

[Sayers, Karamihas, 1998] Sayers M.W., Karamihas S.M., 1998, *The little book of profiling. Basic Information about Measuring and Interpreting Road Profiles.* University of Michigan, Ann Arbor, Transportation Research Institute.

[Seinfeld, Pandis, 2006] Seinfeld J.H., Pandis S.N., 2006, *Atmospheric Chemistry and Physics.* John Wiley & Sons, Inc.

[Slinn, 1982] Slinn W.G.N., 1982, *Predictions for Particle Deposition to Vegetative Canopies.* Atmospheric Environment Vol. **16**, No. 7, pp. 1785-1794.

[Soulhac et al., 2008] Soulhac L., Perkins R.J., Salizzoni P., 2008, *Flow in a Street Canyon for any External Wind Direction.* Boundary-Layer Meteorol (2008) 126:365–388.

[SPENS, 2009] DG RESEARCH, *Recommendations for modified binder usage in pavement.* SIXTH FRAMEWORK PROGRAMME Sustainable Surface Transport.

[Stone, Donaldson, 1998] Stone V., Donaldson K.,(1998), *Small particles - big problem.* The Aerosol Society Newsletter **33**, 12–14.

[Stull, 1989] Stull R.B., 1989, *An Introduction to Boundary Layer Meteorology.* Kluwer Academic Publishers, Dordrecht, 666 pp.

[Tran, 2010] Tran H.P., 2010, *Experimental Study of the Aerodynamics of an Ahmed Body, Including Passive Drag Control.* Phd thesis.

[Wilcox, 1998] Wilcox D.C., 1998, *Turbulence Modeling for CFD.* DCW Industries Inc.

[Wong et al., 2003] Wong C.P., Chan T.L., Leung C.W.(2003), *Characterisation of diesel exhaust particle number and size distributions using mini-dilution tunnel and ejector-diluter measurement techniques.* Atmospheric Environment **37**, 4435–4446.

[Vecchi et al., 2004] Vecchi R. et al., 2004, *The role of atmospheric dispersion in the seasonal variation of PM1 and PM2.5 concentration and composition in the urban area of Milan (Italy).* Atmospheric Environment **38**, 4437-4446.

[Vecchi et al., 2008] Vecchi R. et al., 2008, *A mass closure and PMF source apportionment study on the sub-micron sized aerosol fraction at urban sites in Italy.* Atmospheric Environment **42**, 2240-2253.

List of Publications

Report pubblication
Antonio Ballarin Denti, Maria Chiesa, Abramo Agosti, Fabio Boschetti: "Relazioni tra emissioni inquinanti e loro concentrazioni atmosferiche: conseguenze sulle politiche locali di miglioramento della qualità dell'aria". CRASL - Centro di ricerche per l'ambiente e lo sviluppo sostenibile della Lombardia. Dicembre 2011.

Publications under review
Abramo Agosti, Fausto Borgonovi and Antonio Ballarin Denti: *Traffic-dependent resuspension of fine particulate matter: role of vehicle and asphalt parameters and mitigation strategies.* Submitted to the 'International Journal of Environment Pollution (IJEP)' in date 23/07/2012. Currently in review.

Abramo Agosti: *Analytical solutions of algebraic turbulence models for Canyon geometry.* Submitted to the 'Boundary Layer Meteorology Journal (BLM)' in date 07/01/2013. Currently in review.

Publications in preparation Abramo Agosti, Fausto Borgonovi: *Two-Equation turbulence models simulations of the Ahmed Body wake and estimations of pollutant Deposition and Resuspension rates.* To be submitted to the 'Boundary Layer Meteorology Journal (BLM)' presumably at the end of January.

Acknowledgement

We acknowledge useful discussions with A. Ballarin Denti, A. Marzocchi and G. Valli. Financial Support from a grant from Università Cattolica D3.2-2010 for the additional year of the Phd research is also acknowledged.